

Transverse, Single-Spin Asymmetries for Charged Hadrons and for Muons from
Open-Heavy-Flavor Decays in Polarized Proton-Proton and Proton-Nucleus
Collisions in PHENIX

BY

JEONGSU BOK, B.S., M.S.

A dissertation submitted to the Graduate School

in partial fulfillment of the requirements

for the degree

Doctor of Philosophy

Major Subject: Physics

New Mexico State University

Las Cruces New Mexico

May 2019

Jeongsu Bok

Candidate

Physics

Major

This Dissertation is approved on behalf of the faculty of New Mexico State University, and it is acceptable in quality and form for publication:

Approved by the Dissertation Committee:

Dr. Vassili Papavassiliou

Chairperson

Dr. Stephen Pate

Committee Member

Dr. Marc Schlegel

Committee Member

Dr. Chris Churchill

Committee Member

DEDICATION

to Soohyun

ABSTRACT

TRANSVERSE, SINGLE-SPIN ASYMMETRIES FOR CHARGED HADRONS
AND FOR MUON FROM OPEN-HEAVY-FLAVOR DECAYS IN POLARIZED
PROTON-PROTON AND PROTON-NUCLEUS COLLISIONS IN PHENIX

BY

JEONGSU BOK, B.S., M.S.

Doctor of Philosophy

New Mexico State University

Las Cruces, New Mexico, 2019

Dr. Vassili Papavassiliou, Chair

Transverse single-spin asymmetry (TSSA) phenomena have gained substantial attention in several decades because they provide valuable information on the spin structure of the nucleon.

Production of heavy flavor is dominated by gluon-gluon fusion in the leading order perturbative Quantum Chromodynamics calculation at RHIC energies, and the transverse single-spin asymmetry in heavy-flavor production is sensitive to

the tri-gluon correlations in the twist-3 collinear factorization framework. Study of this asymmetry for single muons from heavy flavor decays in the PHENIX experiment serves as a clean probe for this process. This thesis shows a study of transverse single-spin asymmetries of μ^- and μ^+ from open heavy-flavor decays in polarized $p+p$ collisions at $\sqrt{s} = 200$ GeV at forward and backward rapidity ($1.4 < |y| < 2.0$) over the transverse momentum of $1.25 < p_T < 5$ GeV/ c and the Feynman-x (x_F) range of $-0.2 < x_F < 0.2$ in the PHENIX experiment at RHIC.

In addition, TSSA in the process $p+p \rightarrow h+X$ has been described by twist-3 spin-dependent three-parton correlation functions, or twist-3 fragmentation functions in the QCD collinear factorization approach. Studying the TSSA for inclusive hadron production in $p+A$ collisions gives new insight on the underlying mechanism because different contributions to the TSSA are affected differently by the saturation effect in large nuclei. This thesis reports a study on the TSSA of charged hadron production at forward and backward ($1.4 < |y| < 2.4$) rapidity for $1.25 < p_T < 7.0$ GeV/ c and $0.2 < x_F < 0.2$ from $p+p$, $p+Al$, and $p+Au$ collisions at $\sqrt{s_{NN}}=200$ GeV.

CONTENTS

LIST OF TABLES	xviii
LIST OF FIGURES	xxxvii
1 Introduction	1
1.1 Spin Structure of the Nucleon	1
1.2 Transverse Single Spin Asymmetry	2
1.3 TSSA for Light Hadron Production	6
1.4 TSSA in $p + A$ Collisions	8
1.5 TSSA for Heavy Flavor	10
2 Experimental Setup	11
2.1 Relativistic Heavy Ion Collider	11
2.2 Polarized Proton Acceleration for RHIC	12
2.2.1 Polarized Ion Source to RHIC	12
2.2.2 Control of Polarized Beam	15
2.3 PHENIX Experiment	17
2.3.1 PHENIX Detector Overview	18
2.3.2 PHENIX Muon Arms	18
2.3.3 Inner Detectors	25
2.3.4 Event Triggering	30

2.3.5	Minimum Bias Trigger	31
2.3.6	MUID LL1 Trigger	32
2.3.7	MuTrg LL1 Trigger	32
2.3.8	Centrality	35
3	Data Analysis (I) : Heavy Flavor A_N	36
3.1	Single Muon Measurements	36
3.2	Transverse Single Spin Asymmetry	38
3.2.1	Maximum Likelihood Method	38
3.2.2	Inclusive and Background Asymmetry Estimations	39
3.2.3	A_N vs. p_T	43
3.2.4	A_N vs. x_F	57
3.2.5	Systematic Uncertainty	65
3.3	Simulation to Convert Theory Calculations for A_N of D Meson into A_N of Muon	81
3.3.1	Additional Test with Flat A_N Input	88
3.4	Results	90
3.5	Discussion and Outlook for the Heavy Flavor A_N	96
4	Data Analysis (II) : Charged Hadron A_N	97
4.1	Analysis Method	97
4.2	Raw A_N for Charged Hadrons	101
4.2.1	Raw A_N in $p + p$ Collisions	101

4.2.2	Raw A_N in $p + \text{Au}$	106
4.2.3	Measured A_N from $p + \text{Au}$ Data for Different Centrality Range	109
4.3	Estimation of Initial Charged Hadron (π^\pm, K^\pm) Spectra	115
4.3.1	$p + p$ Collisions	115
4.3.2	$d + \text{Au}$ Collisions	122
4.3.3	$p + \text{Au}$ Collisions	127
4.3.4	$p + \text{Al}$ Collisions	128
4.4	Fraction of Particles in Reconstructed Momentum Bins	129
4.5	Momentum Migration	136
4.5.1	Toy Simulation to Test the Unfolding Procedure	139
4.5.2	Unfolding Result	143
4.6	Systematic Uncertainty	148
4.6.1	Analysis Method	148
4.6.2	Difference between Unfolded and Measured Asymmetries .	155
4.6.3	Contribution from Other Spices	155
4.6.4	Uncertainty in the Migration Matrix	155
4.6.5	Result with Systematic Uncertainties	169
4.7	$p + \text{Al}$ Results in 4 x_F Bins	188
4.7.1	Raw A_N from $p + \text{Al}$ Data	188
4.7.2	Unfolded Result from $p + \text{Al}$ data	190

4.8 Additional Systematic Uncertainty to Cover the K/π Ratio for Direct Comparison of $p + p$ and $p+A$ Data.	190
4.9 A-dependence of A_N for Positively Charged Hadrons at $0.1 < x_F < 0.2$	196
4.10 Comparison of Modulations	200
4.11 Discussion and Outlook for the Charged Hadron A_N in $p^\uparrow+p$ and $p^\uparrow+A$	201
REFERENCES	203
REFERENCES	211

LIST OF TABLES

1	A part of the trigger list for Run15 $p + p$ collisions at $\sqrt{s} = 200$ GeV.	31
2	The light hadron background fraction (f_h) in p_T bins, (–) charge	41
3	The background fraction (f_h) in x_F bins, (–) charge	41
4	The background fraction (r) in p_T bins, (+) charge	42
5	The background fraction (r) in x_F bins, (+) charge	42
6	J/ψ fraction in p_T bins, (–) charge	43
7	J/ψ fraction in p_T bins, (+) charge	44
8	J/ψ fraction in x_F bins, (–) charge	44
9	J/ψ fraction in x_F bins, (+) charge	45
10	Number of (–) tracks in different Gaps after all the track quality cuts.	45
11	Number of (+) tracks in different Gaps after all the track quality cuts.	46
12	p_T dependence of A_N^B (blue beam), A_N^Y (yellow beam) and A_N (combined) in forward rapidity. (–) charge	49
13	p_T dependence of A_N^B (blue beam), A_N^Y (yellow beam) and A_N (combined) in backward rapidity. (–) charge	50

14	p_T dependence of physics asymmetries A_N^B (blue beam), A_N^Y (yellow beam) and A_N (combined). The physics asymmetries were obtained by using Eq. 8 and 9 with $A_N(\text{Inclusive}) = A_N(\text{Gap4})$ and $A_N(\text{Background}) = A_N(\text{Gap3})$. (-) charge	51
15	p_T dependence of A_N^B (blue beam), A_N^Y (yellow beam) and A_N (combined) in forward rapidity. (+) charge	54
16	p_T dependence of A_N^B (blue beam), A_N^Y (yellow beam) and A_N (combined) in backward rapidity. (+) charge	55
17	p_T dependence of physics A_N^B (blue beam), A_N^Y (yellow beam) and A_N (combined). The physics asymmetries were obtained by using Eq. 8 and 9 with $A_N(\text{Inclusive}) = A_N(\text{Gap4})$ and $A_N(\text{Background}) = A_N(\text{Gap3})$. (+) charge	56
18	x_F dependence of A_N^B (blue beam), A_N^Y (yellow beam) and A_N (combined). (-) charge	59
19	x_F dependence of Physics A_N^B (blue beam), A_N^Y (yellow beam) and A_N (combined). The physics asymmetries were obtained by using Eq. 8 and 9 with $A_N(\text{Inclusive}) = A_N(\text{Gap4})$ and $A_N(\text{Background}) = A_N(\text{Gap3})$. (-) charge	60
20	x_F dependence of A_N^B (blue beam), A_N^Y (yellow beam) and A_N (combined). (+) charge	63

21	x_F dependence of Physics A_N^B (blue beam), A_N^Y (yellow beam) and A_N (combined). The physics asymmetries were obtained by using Eq. 8 and 9 with $A_N(\text{Inclusive}) = A_N(\text{Gap4})$ and $A_N(\text{Background}) = A_N(\text{Gap3})$.	
	(+) charge	64
22	Sources of $\delta A_N^{\text{syst.}}$ for μ^- as a function of p_T .	66
23	Sources of $\delta A_N^{\text{syst.}}$ for μ^+ as a function of p_T .	67
24	Sources of $\delta A_N^{\text{syst.}}$ for μ^- as a function of x_F .	68
25	Sources of $\delta A_N^{\text{syst.}}$ for μ^+ as a function of x_F .	68
26	Simulation results for A_N of μ^- ($ x_F < 0.2$) as a function of p_T from theory input for D mesons ($\bar{D}^0, D^- \rightarrow \mu^-$).	85
27	Simulation results for A_N of μ^+ ($ x_F < 0.2$) as a function of p_T from theory input for D mesons ($D^0, D^+ \rightarrow \mu^+$).	86
28	Simulation results for A_N of μ^- (μ^+) in $1.25 < p_T < 5.0$ GeV/ c as a function of x_F from theory input for D mesons ($\bar{D}^0, D^- \rightarrow \mu^-$ or $D^0, D^+ \rightarrow \mu^+$).	87
29	Fit results of the cosine modulation for simulation of $A_N(D \rightarrow \mu)$ using $A_N(D) = 0.1$ for low p_T muons ($p_T < 1.0$ GeV/ c).	89
30	Results for A_N of heavy-flavor μ^- as a function of p_T .	93
31	Results for A_N of heavy-flavor μ^+ as a function of p_T .	94
32	Results for A_N of heavy-flavor μ^- as a function of x_F .	95
33	Results for A_N of heavy-flavor μ^+ as a function of x_F .	95

34	Number of hadron tracks in p_T bins after all the track quality cuts from $p + p$ data. (–) is negatively charged tracks and (+) is positively charged tracks.	98
35	Number of hadron tracks in p_z bins after all the track quality cuts from $p + p$ data. (–) is negatively charged tracks and (+) is positively charged tracks.	98
36	Number of hadron tracks in p_T bins after all the track quality cuts from $p + \text{Au}$ data. (–) is negatively charged tracks and (+) is positively charged tracks.	99
37	Number of hadron tracks in p_z bins after all the track quality cuts from $p + \text{Au}$ data. (–) is negatively charged tracks and (+) is positively charged tracks.	99
38	p_T dependence of A_N^B (blue beam), A_N^Y (yellow beam) and A_N (combined) with statistical uncertainty δA_N^{stat} in forward and backward rapidity for negatively charged hadrons from $p + p$ collisions. . . .	102
39	p_T dependence of A_N^B (blue beam), A_N^Y (yellow beam) and A_N (combined) with statistical uncertainty δA_N^{stat} in forward and backward rapidity for positively charged hadrons from $p + p$ collisions. . . .	103
40	x_F dependence of A_N^B (blue beam), A_N^Y (yellow beam) and A_N (combined) with statistical uncertainty δA_N^{stat} for negatively charged hadrons from $p + p$ collisions.	104

41	x_F dependence of A_N^B (blue beam), A_N^Y (yellow beam) and A_N (combined) with statistical uncertainty δA_N^{stat} for positively charged hadrons from $p + p$ collisions.	105
42	p_T dependence of A_N (blue beam) with statistical uncertainty δA_N^{stat} in forward and backward rapidity for negatively charged hadrons from $p + \text{Au}$ collision	106
43	p_T dependence of A_N (blue beam) with statistical uncertainty δA_N^{stat} for positively charged hadrons from $p + \text{Au}$ collisions.	106
44	x_F dependence of A_N (blue beam) with statistical uncertainty δA_N^{stat} for negatively charged hadrons from $p + \text{Au}$ collisions.	107
45	x_F dependence of A_N (blue beam) with statistical uncertainty δA_N^{stat} for positively charged hadrons from $p + \text{Au}$ collisions.	107
46	p_T dependence of A_N (blue beam) with statistical uncertainty δA_N^{stat} in forward and backward rapidity in the centrality range 0-30% for negatively charged hadrons from $p + \text{Au}$ collisions	109
47	p_T dependence of A_N (blue beam) with statistical uncertainty δA_N^{stat} in the centrality range 0-30% for positively charged hadrons from $p + \text{Au}$ collisions	109
48	x_F dependence of A_N (blue beam) with statistical uncertainty δA_N^{stat} in the centrality range 0-30% for negatively charged hadrons from $p + \text{Au}$ collisions.	110

49	x_F dependence of A_N (blue beam) with statistical uncertainty δA_N^{stat} in the centrality range 0-30% for positively charged hadrons from $p + \text{Au}$ collisions.	110
50	p_T dependence of A_N (blue beam) with statistical uncertainty δA_N^{stat} in forward and backward rapidity in the centrality range 50-84% for negatively charged hadrons from $p + \text{Au}$ collisions.	112
51	p_T dependence of A_N (blue beam) with statistical uncertainty δA_N^{stat} in the centrality range 50-84% for positively charged hadrons from $p + \text{Au}$ collisions.	112
52	x_F dependence of A_N (blue beam) with statistical uncertainty δA_N^{stat} in the centrality range 50-84% for negatively charged hadrons from $p + \text{Au}$ collisions.	113
53	x_F dependence of A_N (blue beam) with statistical uncertainty δA_N^{stat} in the centrality range 50-84% for positively charged hadrons from $p + \text{Au}$ collisions.	113
54	Table of Fig. 81 for negatively charged hadrons. Parent K^-/π^- ratio in bins of reconstructed p_T , p_z of muon spectrometers from hadron-cocktail simulation in $p + p$	134
55	Table of Fig. 81 for positively charged hadrons. Parent K^+/π^+ ratio in bins of reconstructed p_T , p_z of muon spectrometers from hadron-cocktail simulation in $p + p$	135

56	Systematic uncertainty of unfolded A_N in p_T bins in $p + p$ collisions.	157
57	Systematic uncertainty of unfolded A_N in x_F bins for negative charge in $p + p$ collisions	158
58	Systematic uncertainty of unfolded A_N in x_F bins for positive charge in $p + p$ collisions.	159
59	Systematic uncertainty of unfolded A_N in p_T bins in the centrality range 0-84% in $p + \text{Au}$ collisions.	160
60	Systematic uncertainty of unfolded A_N in x_F bins for positive charge in the centrality range 0-84% in $p + \text{Au}$ collisions.	161
61	Systematic uncertainty of unfolded A_N in x_F bins for positive charge in the centrality range 0-84% in $p + \text{Au}$ collisions	162
62	Systematic uncertainty of unfolded A_N in p_T bins in the centrality range 0-30% in $p + \text{Au}$ collisions.	163
63	Systematic uncertainty of unfolded A_N in x_F bins for negative charge in the centrality range 0-30% in $p + \text{Au}$ collisions.	164
64	Systematic uncertainty of unfolded A_N in x_F bins for positive charge in the centrality range 0-30% in $p + \text{Au}$ collisions.	165
65	Systematic uncertainty of unfolded A_N in p_T bins in the 50-84% in $p + \text{Au}$ collisions.	166
66	Systematic uncertainty of unfolded A_N in x_F bins for negative charge in the centrality range 50-84% in $p + \text{Au}$ collisions.	167

67	Systematic uncertainty of unfolded A_N in x_F bins for positive charge in the centrality range 50-84% in $p + \text{Au}$ collisions.	168
68	Unfolded A_N in p_T bins in $p + p$ collisions	176
69	Unfolded A_N with systematic uncertainty in x_F bins from $p + p$ data for negative charge	177
70	Unfolded A_N with systematic uncertainty in x_F bins from $p + p$ data for positive charge	178
71	Unfolded A_N in p_T bins from $p + \text{Au}$ data	179
72	Unfolded A_N with systematic uncertainty in x_F bins from $p + \text{Au}$ data for negative charge	180
73	Unfolded A_N with systematic uncertainty in x_F bins from $p + \text{Au}$ data for positive charge.	181
74	Unfolded A_N in p_T bins from $p + \text{Au}$ data in the centrality range 0-30%	182
75	Unfolded A_N with systematic uncertainty in x_F bins from $p + \text{Au}$ data in the centrality range 0-30% for negative charge.	183
76	Unfolded A_N with systematic uncertainty in x_F bins from $p + \text{Au}$ data in the centrality range 0-30% for positive charge.	184
77	Unfolded A_N in p_T bins from $p + \text{Au}$ data in the centrality range 50-84%	185

78	Unfolded A_N with systematic uncertainties in x_F bins from $p + \text{Au}$ data in the centrality range 50-84% for negative charge.	186
79	Unfolded A_N with systematic uncertainties in x_F bins from $p + \text{Au}$ data in the centrality range 50-84% for positive charge.	187
80	x_F dependence of A_N with statistical uncertainty δA_N^{stat} in $p + \text{Al}$ collisions.	189

LIST OF FIGURES

1	In the 1980s, the proton's spin was assumed to be the sum of the three valence quarks' spins (Left). It has been revealed that the spin of a proton includes contributions from gluons (Right, yellow corkscrews) and a sea of quarks and antiquarks [1].	2
2	Transverse Single Spin Asymmetry of pion production in transversely-polarized proton-proton collisions at $\sqrt{s} = 4.9$ GeV [2].	4
3	Transverse Single Spin Asymmetry of pion production in transversely-polarized proton-proton collisions at RHIC energies [3].	4
4	RHIC has six intersection points allowing the particle beams in two rings to collide.	12
5	The collision species combinations, energies and luminosities at RHIC	13
6	The collision species combination, energies and luminosities in $p, d+$ A collisions at RHIC	13
7	The energies, luminosities, and polarizations in $p^\uparrow + p$ collisions at RHIC	14
8	RHIC as the polarized proton collider.	14
9	Quarter-cut view of PHENIX detectors	17
10	PHENIX coordinate system	18

11	Side view of the PHENIX muon arms	19
12	Drawing of the Muon Tracker of the South Muon Arm.	21
13	Momentum is calculated from the trajectory of a charged particle in a magnetic field.	21
14	Layout of 6 MUID panels from A to H. The edges overlap between panels to eliminate dead areas.	23
15	Cross section of the MUID panel and 2-pack of plastic tube.	24
16	Finding a track from MUID and MUTR hits.	26
17	PHENIX Beam Beam counter. (a) A Single BBC (b) A BBC array of 64 elements (c) Installed BBC on the PHENIX nearby the beam pipe	27
18	Correlation between energy deposited in ZDC and sum of charge in BBC. The straight lines define 5% intervals in centrality, from 0-5% on the rightmost side.	27
19	(a) Top view of the PHENIX Zero Degree calorimeter. (b) Beam's eye view of ZDC	28
20	Mechanical design of a ZDC module in mm.	29
21	Symsets of the MuID trigger	33
22	MuID symset logic. The left side shows the MuID-1D logic and the right side shows the MuID-1H logic.	33
23	A schematic drawing of the Muon Trigger LL1 trigger logic [4].	34

24	p_T dependence of asymmetries for inclusive muons (Gap4) in the forward (left) and backward (right) rapidity. (–) charge	47
25	p_T dependence of asymmetries for hadrons background (Gap3) in the forward (left) and backward (right) rapidity. (–) charge	48
26	p_T dependence of physics asymmetries in the forward (left) and backward (right) rapidity, obtained by using Eq. 8 and 9 with A_N (Inclusive)= A_N (Gap4) and A_N (Background)= A_N (Gap3). (–) charge	48
27	p_T dependence of asymmetries for inclusive muons (Gap4) in the forward (left) and backward (right) rapidity. (+) charge	52
28	p_T dependence of asymmetries for hadrons background (Gap3) in the forward (left) and backward (right) rapidity. (+) charge	53
29	p_T dependence of physics asymmetries in the forward (left) and backward (right) rapidity, obtained by using Eq. 8 and 9 with A_N (Inclusive)= A_N (Gap4) and A_N (Background)= A_N (Gap3). (+) charge	53
30	x_F dependence of asymmetries for inclusive muons (Gap4). (–) charge	57
31	x_F dependence of asymmetries for hadron background (Gap3). (–) charge	58
32	x_F dependence of physics asymmetries, obtained by using Eqs. 8 and 9 with A_N (Inclusive)= A_N (Gap4) and A_N (Background)= A_N (Gap23). (–) charge	58
33	x_F dependence of asymmetries for inclusive muons (Gap4). (+) charge	61
34	x_F dependence of asymmetries for hadron background (Gap3). (+) charge	61

35	x_F dependence of physics asymmetries, obtained by using Eq. 8 and 9 with $A_N(\text{Inclusive}) = A_N(\text{Gap4})$ and $A_N(\text{Background}) = A_N(\text{Gap3})$. (+) charge	62
36	The Monte Carlo simulation test with $MCp_T \times 2\%$ ($p_T < 5 \text{ GeV}/c$), 10% for $MCp_T > 5 \text{ GeV}/c$ for injected (open circles) and reconstructed (filled circles) asymmetries of Gap4 (blue) and Gap3 (red).	71
37	Example of a fit of the cosine modulation induced by $A_N^{J/\psi}$. On the left is shown the input $A_N(J/\psi)$, where the fit result shows good agreement with input value(-0.026), justifying the procedure and fit. The right plot shows the asymmetry for the output muon, which is different from the input $A_N^{J/\psi}$.	73
38	$A_N^{J/\psi \rightarrow \mu}$ distribution (lower side) from simulated runs using six input $A_N^{J/\psi}$'s (upper side).	73
39	Cosine fit result of Gap4 inclusive tracks for 6 p_T bins, (-) charge. Rows correspond to (1) blue beam $x_F > 0$, (2) blue beam $x_F < 0$, (3) yellow beam $x_F > 0$, and (4) yellow beam $x_F < 0$.	75
40	Cosine fit result of Gap4 inclusive tracks for 6 p_T bins, (+) charge. Rows correspond to (1) blue beam $x_F > 0$, (2) blue beam $x_F < 0$, (3) yellow beam $x_F > 0$, and (4) yellow beam $x_F < 0$.	76

41	Cosine fit result of Gap4 inclusive tracks for two p_z bins (4 x_F bins), (–) charge. Rows correspond to (1) blue beam $x_F > 0$, (2) blue beam $x_F < 0$, (3) yellow beam $x_F > 0$, and (4) yellow beam $x_F < 0$	77
42	Cosine fit result of Gap4 inclusive tracks for 2 p_z bins (4 x_F bins), (+) charge. Rows correspond to (1) blue beam $x_F > 0$, (2) blue beam $x_F < 0$, (3) yellow beam $x_F > 0$, and (4) yellow beam $x_F < 0$	78
43	Comparison between the cosine fit results (blue) and the likelihood result (red) of Gap4 inclusive tracks for 6 p_T bins, (–) charge. The lower plots represent the χ^2/ndf in cosine fit, smaller than 2	79
44	Comparison between the cosine fit results (blue) and the likelihood result (red) of Gap4 inclusive tracks for 6 p_T bins, (+) charge. The lower plots represent the χ^2/ndf in cosine fit, smaller than 2	79
45	Comparison between the cosine fit results (blue) and the likelihood result (red) of Gap4 inclusive tracks for 4 x_F bins, (–) charge. The lower plots represent the χ^2/ndf in cosine fit, smaller than 2	80
46	Comparison between the cosine fit results (blue) and the likelihood result (red) of Gap4 inclusive tracks for 4 x_F bins, (+) charge. The lower plots represent the χ^2/ndf in cosine fit, smaller than 2	80

47	p_T (top) and $ x_F $ (bottom) distributions of D mesons (D^0 , \bar{D}^0 , D^+ , and D^-) decaying into μ^\pm at $1.25 < p_T^\mu < 5.0$ GeV/ c , $ x_F^\mu < 0.2$, and $1.4 < y^\mu < 2.0$, from PYTHIA. Each distribution is normalized to unity.	83
48	Theory calculations for $A_N^{D^0}$ and $A_N^{D^+}$ ($A_N^{\bar{D}^0}$ and $A_N^{D^-}$) as a function of x_F ($-0.6 < x_F^D < 0.6$, for 25 x_F values; 0.05 interval) for $p_T = 1, 2, 3, 4, 5, 6, 7, 8, 9, 10$ GeV/ c [5]	84
49	Simulation of $A_N(D \rightarrow \mu)$ for $A_N(D) = 0.1$ for low p_T muons (6 bins for $p_T < 1.0$ GeV/ c). The upper row shows the fit result for $A_N(D)$ input and the lower row shows the fit result for $A_N(D \rightarrow \mu)$	88
50	A_N of negatively-charged, heavy-flavor muons as a function of p_T in the backward ($x_F < 0$, left) and forward ($x_F > 0$, right) regions. Vertical bars (boxes) represent statistical (systematic) uncertainties. Solid and dashed lines represent twist-3 model calculations [5].	90
51	A_N of positively-charged, heavy-flavor muons as a function of p_T in the backward ($x_F < 0$, left) and forward ($x_F > 0$, right) regions. Vertical bars (boxes) represent statistical (systematic) uncertainties. Solid and dashed lines represent twist-3 model calculations [5].	91

52	A_N of negatively-charged (top) and positively-charged (bottom), heavy-flavor muons as a function of x_F , where $+x_F$ is along the direction of the polarized proton. Vertical bars (boxes) represent statistical (systematic) uncertainties. Solid and dashed lines represent twist-3 model calculations [5].	92
53	p_T dependence (left $x_F > 0$, middle $x_F < 0$) and x_F dependence (right) of asymmetries for hadrons (Gap2, 3) for negative charge. . .	101
54	p_T (left $x_F > 0$, middle $x_F < 0$) dependence and x_F dependence (right) of asymmetries for hadrons (Gap2, 3) for positive charge .	102
55	p_T dependence (left $x_F > 0$, middle $x_F < 0$) and x_F dependence (right) of asymmetries for negatively charged hadrons from $p + \text{Au}$ collisions.	108
56	p_T (left $x_F > 0$, middle $x_F < 0$) dependence and x_F dependence (right) of asymmetries for positive charged hadrons from $p + \text{Au}$ collisions.	108
57	p_T dependence (left $x_F > 0$, middle $x_F < 0$) and x_F dependence (right) of asymmetries in the centrality range 0-30% for negatively charged hadrons from $p + \text{Au}$ collisions.	111
58	p_T (left $x_F > 0$, middle $x_F < 0$) dependence and x_F dependence (right) of asymmetries in the centrality range 0-30% for positively charged hadrons from $p + \text{Au}$ collisions.	111

59	p_T dependence (left $x_F > 0$, middle $x_F < 0$) and x_F dependence (right) of asymmetries in the centrality range 50-84% for negatively charged hadrons from $p + \text{Au}$ collisions.	114
60	p_T dependence (left $x_F > 0$, middle $x_F < 0$) and x_F dependence (right) of asymmetries in the centrality range 50-84% for positive charged hadron from $p + \text{Au}$ collision.	114
61	p_T spectra of charged pions in $p + p$ collisions at $\sqrt{s} = 200$ GeV (top panel) and the ratio between data and fit functions (bottom panel).	116
62	p_T spectra of charged kaons in $p + p$ collisions at $\sqrt{s} = 200$ GeV (top panel) and the ratio between data and fit functions (bottom panel).	117
63	p_T spectra of charged pions and kaons at mid-rapidity in $p + p$ collisions at $\sqrt{s} = 200$ GeV from data and PYTHIA.	118
64	Ratio between data and PYTHIA as a function p_T at mid-rapidity in $p + p$ collisions at $\sqrt{s} = 200$ GeV.	119
65	Comparison of K/π ratio between data and tuned PYTHIA as a function of p_T in $p + p$ collisions at $\sqrt{s} = 200$ GeV.	120
66	K/π ratio in various η bins from tuned PYTHIA in $p + p$ collisions at $\sqrt{s} = 200$ GeV.	121

67	K/π ratio with fit functions in various η bins at forward rapidity from tuned PYTHIA in $p + p$ collisions at $\sqrt{s} = 200$ GeV.	121
68	p_T spectra of charged and neutral pions in d +Au collisions at $\sqrt{s_{NN}} = 200$ GeV (left) and comparison with HIJING (right).	123
69	p_T spectra of charged and neutral kaons in d +Au collisions at $\sqrt{s_{NN}} = 200$ GeV (left) and comparison with HIJING (right).	123
70	Ratio between data and fit function for pions (left) and kaons (right) in d +Au collisions at $\sqrt{s_{NN}} = 200$ GeV.	124
71	K/π ratio from a fit to data (left) and to the ratio between data and the HIJING model at mid-rapidity in d +Au collisions at $\sqrt{s_{NN}} = 200$ GeV (right).	124
72	K/π ratio of the modified HIJING model in d +Au collisions at $\sqrt{s_{NN}} = 200$ GeV.	125
73	Estimated K/π ratio for negatively (top) and positively (bottom) charged hadrons from the modified HIJING model at forward rapidity in d +Au collisions at $\sqrt{s_{NN}} = 200$ GeV.	126
74	Comparison of the K^\pm/π^\pm ratio as a function of p_T at forward and backward rapidity between $p + \text{Au}$ and d +Au collisions at $\sqrt{s_{NN}} = 200$ GeV with HIJING. Left : negative hadrons, right : positive hadrons	127

75	K/π double ratio (K/π in $p + \text{Al}$)/(K/π in $p + \text{Au}$) for comparison between $p + \text{Al}$ and $p + \text{Au}$ from the HIJING simulation. The difference is much smaller in the region of this analysis, $1.25 < p_T < 7.0 \text{ GeV}/c$ than the relative $\pm 30\%$ uncertainty assigned to this quantity.	128
76	Parent particle contributions for each p_T, p_Z bin using the QGSP-BERT package in GEANT4 simulation for $p + p$	129
77	Parent particle contributions for each p_T, p_Z bin using the FTFP-BERT package in the GEANT4 simulation for $p + p$	130
78	Parent particle contribution for each p_T, p_Z bin using QGSP-BIC package in GEANT4 simulation for $p + p$	130
79	Parent particle contribution for each p_T, p_Z bin when K/π ratio is increased by 30% relatively ($1.3 \times K/\pi$) using QGSP-BERT package in GEANT4 simulation for $p + p$	131
80	Parent particle contribution for each p_T, p_Z bin when K/π ratio is decreased by 30% relatively ($0.7 \times K/\pi$) using QGSP-BERT package in GEANT4 simulation for $p + p$	132

81	Parent K^\pm/π^\pm ratio in bins of reconstructed p_T , p_z of muon spectrometers. Black dashed lines show the K/π ratio when the initial (particle generation level in the simulation) K/π ratio is increased or decreased by 30% $((1.0 \pm 0.3) \times K/\pi)$ using the QGSP-BERT package for the hadron cocktail simulation in $p+p$. Each color corresponds to a different hadron interaction package in GEANT4. The K^\pm/π^\pm ratio in $p + \text{Au}$ collisions is shown as magenta ($x_F > 0$), or green ($x_F < 0$). QGSP-BERT is used for $p + \text{Au}$	133
82	Migration matrix used to calculate the original A_N , obtained from the full GEANT4 simulation, with the default QGSP-BERT hadronic shower package.	137
83	Migration matrices for calculating the original A_N , obtained from a full GEANT4 simulation, with the default QGSP-BERT hadronic shower package. (a) Original migration matrix in p_T . (b) Normalized migration matrix, normalized for each Reco p_T bin. (c) Inverse of normalized migration matrix in p_T . (d) Original migration matrix in x_F . (e) Normalized migration matrix. (f) Inverse of normalized migration matrix in x_F	140

84	Migration matrices for calculating the original A_N , obtained from a full GEANT4 simulation, using FTFP-BERT. (a) Original migration matrix in p_T . (b) Normalized migration matrix, normalized for each Reco p_T bin. (c) Inverse of normalized migration matrix in p_T . (d) Original migration matrix in x_F . (e) Normalized migration matrix. (f) Inverse of normalized migration matrix in x_F	141
85	Migration matrices for calculating the original A_N , obtained from a full GEANT4 simulation, using QGSP-BIC.	141
86	Toy simulation result. Linear input A_N^{True} (blue) and A_N^{Unfold} (red) on the left panel show good agreement. Right panel shows the input A_N^{True} (blue), the cosine fit result of input A_N^{True} (pink) and A_N^{Reco} (black) to cross check each step of the toy simulation. 1st, 5th, 6th, and 10th bins are overflow bins.	144
87	Statistical uncertainty calculated in the simulation. Blue is gaussian width of the A_N^{Unfold} distribution and red is the mean value of δA_N^{True} , calculated using Eq. 18 in each iteration. They are consistent with each other. 1st, 5th, 6th, and 10th bins are overflow bins.	144
88	Unfolded A_N in $p + p$ collisions using different hadron interaction packages in GEANT4. The difference is included as a source of systematic uncertainty.	145

94	Cosine fit result for 5 x_F bins for positive charge. 1st and 2nd rows are for the blue beam, 3rd and 4th rows for the yellow beam. 1st and 3rd rows are forward rapidity, 2nd and 4th rows are backward rapidity.	150
95	Comparison between the maximum likelihood method and the cosine fit method for 3 p_T bins for positive charge in $p + \text{Au}$ collisions. They agree each other. The bottom panel shows χ^2/ndf for the cosine fit; it is smaller than 2.	151
96	Comparison between the maximum likelihood method and the cosine fit method for 5 x_F bins for positive charge in $p + p$ collisions. They agree each other. The bottom panel shows χ^2/ndf for the cosine fit; it is smaller than 2.	151
97	Comparison between the maximum likelihood method and the cosine fit method for 3 p_T bins (left) and 5 x_F bins (right) for negative charge in $p + \text{Au}$ collisions. They agree each other. The bottom panel shows χ^2/ndf for the cosine fit; it is smaller than 2.	152
98	Comparison between the maximum likelihood method and the cosine fit method for 3 p_T bins (left) and 5 x_F bins (right) for positive charge in $p + \text{Au}$ collisions. They agree each other. The bottom panel shows χ^2/ndf for the cosine fit; it is smaller than 2.	153

99	The sine term in the cosine+sine fit is consistent with zero for 3 p_T bins for the blue beam for positive charge in $p + p$ collisions. The bottom panel shows χ^2/ndf for the cosine fit (filled circle) and cosine+sine (open circle) fit; it is smaller than 2.	154
100	The sine term in the cosine+sine fit is consistent with zero for 5 x_F bins for the blue beam for positive charge in $p + p$ collisions. The bottom panel shows χ^2/ndf for the cosine fit (filled circle) and cosine+sine (open circle) fit; it is smaller than 2.	154
101	Comparison of unfolded A_N for $p + p$ and $p + \text{Au}$ with systematic uncertainties as a function of p_T for negatively charged hadron. The $p + \text{Au}$ points are shifted horizontally by $+0.2 \text{ GeV}/c$ for clarity.	169
102	Comparison of unfolded A_N with systematic uncertainty as a function of x_F for $p + p$ and $p + \text{Au}$ data for negatively charged hadron. The $p + \text{Au}$ points are shifted horizontally by $+0.005$ for clarity.	170
103	Comparison of unfolded A_N with systematic uncertainty as a function of p_T for $p + p$ and $p + \text{Au}$ data for positively charged hadrons. The $p + \text{Au}$ points are shifted horizontally by $+0.2 \text{ GeV}/c$ for clarity.	170
104	Comparison of unfolded A_N with systematic uncertainty as a function of x_F for $p + p$ and $p + \text{Au}$ data for positively charged hadrons. The $p + \text{Au}$ points are shifted horizontally by $+0.005$ for clarity.	171

105	Comparison of unfolded A_N with systematic uncertainty as a function of x_F for positively charged hadrons and negatively charged hadrons for $p + p$ data. The $p + \text{Au}$ points are shifted horizontally by $+0.2 \text{ GeV}/c$ for clarity.	171
106	Comparison of unfolded A_N with systematic uncertainty as a function of x_F for positively charged hadrons and negatively charged hadrons for $p + p$ data. The netagive charge points are shifted horizontally by $+0.005$ for clarity.	172
107	Comparison of unfolded A_N with systematic uncertainty as a function of p_T for $p + p$, centrality bin 0-30%, and centrality bin 50-84% $p + \text{Au}$ result for negatively charged hadrons. The $p + \text{Au}$ points are shifted horizontally by $+0.2$ or $+0.4 \text{ GeV}/c$ for clarity.	172
108	Comparison of unfolded A_N with systematic uncertainty as a function of p_T for $p + p$, centrality bin 0-30%, and centrality bin 50-84% $p + \text{Au}$ result for negatively charged hadrons. The $p + \text{Au}$ points are shifted horizontally by $+0.005$ or $+0.010$ for clarity.	173
109	Comparison of unfolded A_N with systematic uncertainty as a function of p_T for $p + p$, centrality bin 0-30%, and centrality bin 50-84% $p + \text{Au}$ result for positively charged hadrons. $\langle p_T \rangle$ is shifted by $+0.2, +0.4 \text{ GeV}/c$ in $p + \text{Au}$ collisions for comparison.	174

110 Comparison of unfolded A_N with systematic uncertainty as a function of p_T for $p + p$, centrality bin 0-30%, and centrality bin 50-84% $p + \text{Au}$ result for positively charged hadrons. The $p + \text{Au}$ points are shifted horizontally by +0.005 or +0.010 for clarity.	175
111 Unfolded A_N in $p + \text{Al}$ collisions in the centrality range 0-72% varying the K/π ratio by $\pm 30\%$. The difference is included in the systematic uncertainty.	190
112 Unfolded A_N in $p + \text{Al}$ collisions in the centrality range 0-40% varying the K/π ratio by $\pm 30\%$. The difference is included in the systematic uncertainty.	191
113 Unfolded A_N in $p + \text{Al}$ collisions in the centrality region 41-72% varying the K/π ratio by $\pm 30\%$. The difference is included in the systematic uncertainty.	191
114 Theory predictions based on [6] for $A_N(\pi^+)$ and $A_N(K^+)$ in the $1.2 < \eta < 2.4$ range.	194
115 Theory predictions based on [6] for $A_N(\pi^-)$ and $A_N(K^-)$ in the $1.2 < \eta < 2.4$ range.	194

116 $A_N(mixture)$ are obtained for 2 models (1) theory curve from Pitonyak [6] (Model 1 on the plot) and (2) a linear extrapolation of the BRAHMS results (Model 2 on the plot), using hadron cocktail simulation for $p + p$ and $p + \text{Au(Al)}$. The upper plots (Chg0 on the plot) are for negative charge and the lower plots (Chg1 on the plot) are for positive charge.	195
117 $A^{1/3}$ -dependence of A_N of positively charged hadrons at $0.1 < x_F < 0.2$ in $p + p$, $p + \text{Al}$, and $p + \text{Au}$ collisions	197
118 Distribution of the 10000 fit results for obtaining the systematic uncertainty for α . Each fit is done for randomly selected points from a Gaussian distribution which is centered at the original data points of A_N and has a width of the systematic uncertainty of A_N	198
119 Averaged- N_{coll} -dependence of A_N of positively charged hadrons at $0.1 < x_F < 0.2$ for the centrality-categorized results in $p + p$, $p + \text{Al}$, and $p + \text{Au}$ collisions	199
120 Distribution of the 10000 fit results for obtaining the systematic uncertainty for β . Each fit is done for randomly selected points from a Gaussian distribution which is centered at the original data points of A_N and has a width of the systematic uncertainty of A_N	199

1 Introduction

1.1 Spin Structure of the Nucleon

In a constituent quark picture, the proton's spin of $\frac{1}{2}$ had been assumed to be originated from the three spin- $\frac{1}{2}$ valence quarks (uud) with two aligned quark spins and an anti-aligned one. However, in the late 1980's, the European Muon Collaboration (EMC) experiment at CERN found that only $\sim 20\%$ of the total proton spin is carried by the quarks [7, 8]. This surprising result precipitated a theoretical crisis, known as "Proton Spin Puzzle". Currently, other possible sources are included for the description of proton's spin.

$$S_p = \frac{1}{2} = \frac{1}{2}\Delta\Sigma + \Delta G + L_q + L_g, \quad (1)$$

where $\Delta\Sigma$ is the proton's spin coming from the total quark spin and ΔG is the contribution from gluons and L_q (L_g) indicates the orbital angular momentum of quarks (gluons). The complete picture of the proton's spin is changed as illustrated in Fig. 1.

In addition to the longitudinal spin structure, there is a transverse spin picture of the proton. The transverse spin structure is different from the longitudinal spin structure because the Lorentz boost and spatial rotation do not commute. Studying the transverse spin structure of the proton provides an opportunity to understand the 3-D structure of the proton.

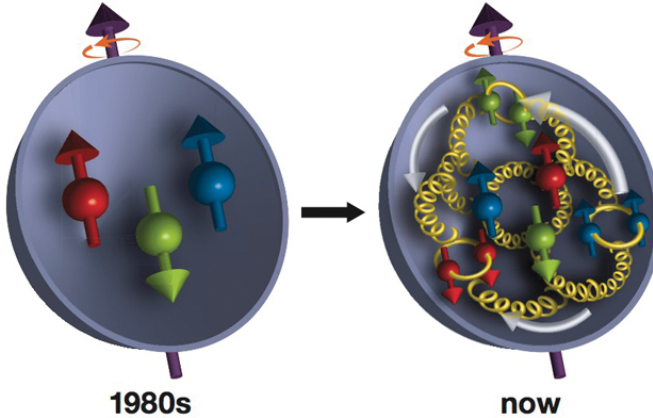


Figure 1: In the 1980s, the proton’s spin was assumed to be the sum of the three valence quarks’ spins (Left). It has been revealed that the spin of a proton includes contributions from gluons (Right, yellow corkscrews) and a sea of quarks and antiquarks [1].

1.2 Transverse Single Spin Asymmetry

Transverse Single Spin Asymmetry (TSSA) is a tool to explore the quark and gluon structure of the transversely-polarized proton. When a transversely-polarized proton beam is colliding with a unpolarized proton beam, the TSSA is defined as the azimuthal asymmetry in the yield of particles with respect to the direction of spin of the polarized proton: spin-up and spin-down perpendicular to the beam direction. The analyzing power A_N is defined as:

$$A_N = \frac{\sigma^\uparrow - \sigma^\downarrow}{\sigma^\uparrow + \sigma^\downarrow}, \quad (2)$$

where $\sigma^\uparrow(\sigma^\downarrow)$ is the cross section when the hadron’s transverse spin vector is “up” (“down”) relative to the proton’s direction.

In the mid-1970's, surprisingly large ($\sim 10^{-1}$) and oppositely-signed asymmetries were observed in π^+ and π^- production at large Feynman- x ($x_F = p_Z/p_Z(\text{max})$) where $p_Z(\text{max})$ indicates the maximum longitudinal momentum which corresponds to the center of mass energy \sqrt{s}) in transversely-polarized proton-proton collisions ($p^\uparrow + p \rightarrow \pi + X$) at $\sqrt{s} = 4.9$ GeV in the Zero Gradient Synchrotron at Argonne National Laboratory [2], shown in Figure 2. The results surprised the Quantum Chromodynamics (QCD) community because they disagreed with the expectation from the leading-twist perturbative QCD (pQCD) of very small spin asymmetries, suppressed as $\frac{\alpha_s m_q}{\sqrt{s}}$ [9], where m_q is the mass of the quark and α_s is the strong coupling constant. The existence of large TSSAs was confirmed by many experiments over 40 years from the fixed-target energy range to the collider center-of-mass energy of up to 500 GeV at the Relativistic Heavy Ion Collider (RHIC) in polarized $p + p$ collisions [10, 11, 12, 13, 14, 15, 16, 17, 18, 19]. The measured asymmetries at RHIC energies are shown in Fig. 3.

To understand the origin of large TSSAs at large x_F , two theoretical formalisms within the perturbative QCD framework have been proposed. Both formalisms connect the TSSA to the transverse motion of the partons inside the transversely-polarized nucleon and/or to spin-dependent quark fragmentation. One framework is called TMD factorization, based on the transverse-momentum-dependent (TMD) parton distribution and fragmentation functions. In 1989, Sivers proposed

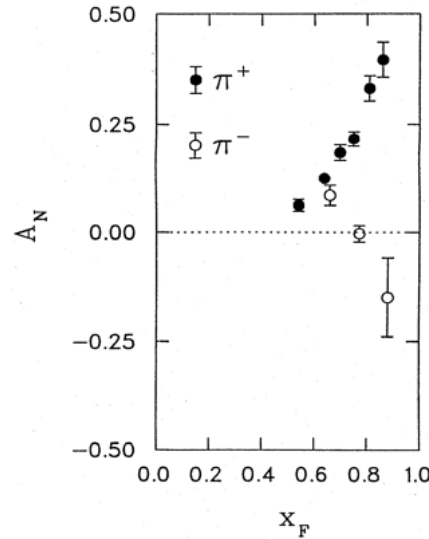


Figure 2: Transverse Single Spin Asymmetry of pion production in transversely-polarized proton-proton collisions at $\sqrt{s} = 4.9$ GeV [2].

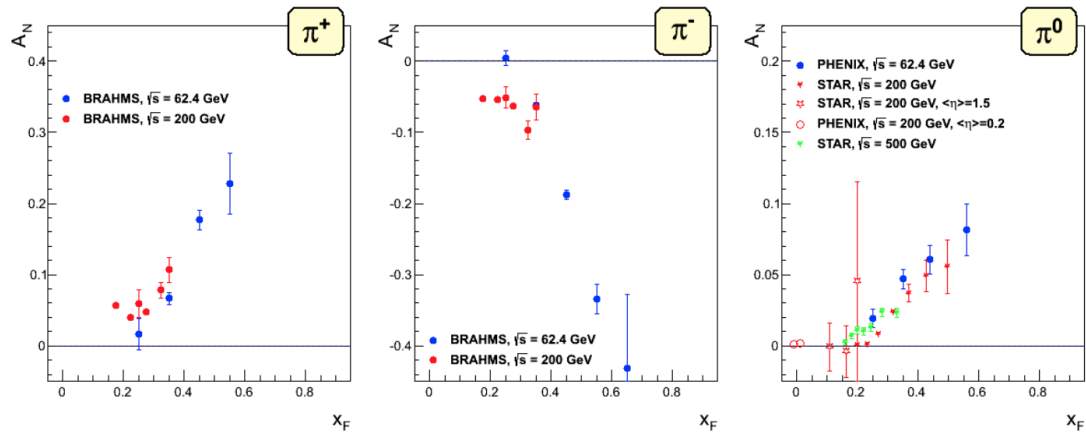


Figure 3: Transverse Single Spin Asymmetry of pion production in transversely-polarized proton-proton collisions at RHIC energies [3].

that the TSSA can be described by the correlation between the transverse spin of the nucleon and the parton transverse momentum in the initial state [20, 21]. This is known as the “Sivers effect.” The final state contribution originates from the quark transversity distribution convolved with a transverse momentum dependent fragmentation function. It is called the Collins effect [22] and it describes the fragmentation of a transversely polarized quark into a final state hadron with nonzero transverse momentum relative to the parton direction.

The TMD factorization framework needs two observed energy scale where only one needs to be hard (e.g. virtuality of the exchanged boson in semi inclusive deep inelastic scattering (SIDIS), Drell-Yan (DY) processes or $e^+ + e^-$ annihilation) while the other one is soft, of the order of Λ_{QCD} (e.g. transverse momentum of the lepton pair in DY processes, or of the final hadron in SIDIS, or the imbalance of transverse momentum in hadron-pair production in $e^+ + e^-$ collisions) [23, 24]. However, the TMD factorization cannot be used directly in the interpretation of inclusive hadron production in $p + p$ collisions as there is only one observable hard scale ($p_T \gg \Lambda_{\text{QCD}}$) [25]. A second framework, applicable to hadron-hadron collisions, follows the collinear factorization approach in perturbative quantum chromodynamics [26, 27, 28]. The collinear, higher-twist (twist-3) effects become more important in a large TSSA when there is only one observed momentum scale that is much larger than the non-perturbative hadronic scale $\Lambda_{QCD} \sim 200$ MeV. In the collinear factorization approach, a large TSSA can be generated from the

twist-3 transverse-spin-dependent, multi-parton correlation functions or twist-3 fragmentation functions.

1.3 TSSA for Light Hadron Production

The twist-3 collinear factorization framework was applied in the light hadron production at forward rapidity in proton-proton collisions [28, 29, 30, 31, 32, 33, 34, 35, 36]. In the twist-3 collinear factorization approach, the polarized differential cross-section for $A^\uparrow + B \rightarrow C + X$ can be written as

$$\begin{aligned}
 d\sigma(S_T) = & H \otimes f_{a/A(3)} \otimes f_{b/B(2)} \otimes D_{C/c(3)} \\
 & + H' \otimes f_{a/A(2)} \otimes f_{b/B(3)} \otimes D_{C/c(2)} \\
 & + H'' \otimes f_{a/A(2)} \otimes f_{b/B(2)} \otimes D_{C/c(3)},
 \end{aligned} \tag{3}$$

where $f_{a/A(t)}$ is the twist- t parton distribution function (PDF) associated with the parton a in the hadron A and $D_{C/c(t)}$ is the fragmentation function associated with the hadron C from the parton c . The factors H , H' , H'' are the hard parts and \otimes represents convolution in the appropriate parton momentum fractions. The S_T is the transverse spin direction of the hadron A . For the case of $p^\uparrow + p \rightarrow h + X$, Eq. 3 becomes

$$\begin{aligned}
d\sigma(S_T) = & H \otimes f_{a/p^\uparrow(3)} \otimes f_{b/p(2)} \otimes D_{h/c(3)} \\
& + H' \otimes f_{a/p^\uparrow(2)} \otimes f_{b/p(3)} \otimes D_{h/c(2)} \\
& + H'' \otimes f_{a/p^\uparrow(2)} \otimes f_{b/p(2)} \otimes D_{h/c(3)}. \tag{4}
\end{aligned}$$

In Eq. 4, there are three twist-3 functions: (i) twist-3 functions from the polarized proton, (ii) twist-3 functions from the unpolarized proton, and (iii) twist-3 functions from the final-state hadron. The twist-3 functions can be classified into three groups as intrinsic, kinematical, and dynamical functions and they can be 2 parton or 3 parton correlators [37, 38]. The intrinsic functions represent twist-3 Dirac projections of collinear quark-quark correlators [37, 38]. The dynamical functions are 3-parton correlators and the kinematical functions are related to the first momentum moments of TMD 2-parton functions.

The twist-3 functions (i) from the polarized proton have a soft gluon pole term and a soft fermion term. The soft gluon pole term is studied for quark-gluon-quark correlators involving the Qiu-Sterman function $F_{FT}(x, x)$ [30, 32] and tri-gluon correlators [39]. The soft fermion pole term is calculated in [34]. The Qiu-Sterman function has a relation to the Sivers function [20] $f_{1T}^\perp(x, k_T^2)$ in the TMD framework [40]. The Qiu-Sterman function has gained attention initially as a dominant source of A_N in $p^\uparrow + p \rightarrow h + X$ although later it was shown that the contribution might not be dominant [41, 42, 43]. The tri-gluon term

has been estimated to produce small effects in light hadron production at forward rapidity [39]. The soft fermion pole term is studied in [35, 36] and it cannot explain all of the asymmetry.

The twist-3 functions (ii) from the unpolarized proton connect the quark transversity PDF from the polarized proton and the dynamical term of the twist-3 function $H_{FU}(x, x)$ from the unpolarized proton [44, 45, 46, 47]. The twist-3 function from the unpolarized proton is related to the first momentum moment of the Boer–Mulders function $h_1^\perp(x, \vec{k}_T^2)$ [40, 48] and it gives a very small contribution due to its hard partonic cross section [49].

The twist-3 contribution (iii) from the fragmentation function has gained attention recently. In a recent calculation [50], the twist-3 effects from partons fragmenting into the final state hadron include the kinematical function $H^{\perp(1)(z)}$, the intrinsic function $H(z)$, and the dynamical function \hat{H}_{FU}^{\Im} . The kinematical function corresponds to the first momentum moment of the TMD Collins function $H_1^\perp(z, z^2 \vec{p}_\perp^2)$ [22]. Recently, calculation of the twist-3 contribution from parton fragmentation was carried out [50, 51, 6].

1.4 TSSA in $p + A$ Collisions

At the Relativistic Heavy Ion Collider (RHIC), gluons of small- x (where x is the longitudinal momentum fraction x -Bjorken) can be accessed at forward rapidity in $p(d) + A$ collisions which can provide an opportunity to study nuclear parton

distributions, gluon saturation, and other initial state effects [52, 53, 54, 55]. The dynamics of gluons in the small- x regime where the gluon density increases drastically can be described by the color-glass condensate (CGC) formalism [56]. In the saturation framework the multiple scatterings in the dense color fields are resummed and the small- x evolution of the color fields is incorporated. The CGC formalism successfully explained the suppression phenomena at RHIC [57]. The saturation scale Q_s is induced from this saturation framework and it demonstrates the color-charge density fluctuation within the nucleus target.

In recent years, substantial attention is given to an interplay between small- x physics and spin physics by studying TSSAs in transversely-polarized proton and ion collisions ($p^\uparrow+A$). The gluon saturation effects in a nucleus are taken into account for various calculations of TSSAs in $p^\uparrow+A$ collisions [58, 59, 60, 61, 62, 63, 64, 65, 66]. The hybrid approach [64, 65] applies the twist-3 framework for the polarized proton side and the CGC framework for the target nucleus side. In this approach, the A -dependence of A_N comes from the saturation scale Q_s by $Q_{sA}^2 \propto A^{1/3}$ in the target nucleus. A recent calculation using the hybrid approach for the A -dependence of A_N in $p^\uparrow+A \rightarrow h+X$ showed that the contribution from the twist-3 functions in the polarized proton is independent of A [67], while the fragmentation function can generate $A^{-1/3}$ -dependence for $p_T \ll Q_s$ [68] in the forward region. Therefore, A -dependence of A_N in $p^\uparrow+A \rightarrow h+X$ can be a crucial test for finding the dominant source of A_N in $p^\uparrow+p \rightarrow h+X$.

1.5 TSSA for Heavy Flavor

At RHIC energies, it is expected that heavy flavor production is dominated by gluon-gluon interactions. Any large transverse single spin asymmetry observed in heavy flavor production cannot originate from a Collins-type effect because the gluon's transversity is zero. Therefore, the production of heavy flavor particles in transversely polarized $p + p$ collisions at the PHENIX experiment offers a good opportunity to gain information on the gluon's Sivers-type effect. Furthermore, it was shown by Anselmino et al. that the single spin asymmetry in open charm production may be significant at forward rapidity which is well covered by the PHENIX muon detectors [69]. So any sizable contributions of A_N in J/ψ and open charm production can give a direct measurement of the gluon Sivers-type function. The TSSA (A_N) of J/ψ in central and forward rapidity was measured in the PHENIX experiment [70]. However, the theoretical prediction for TSSA of J/ψ is complicated due to the lack of good understanding of its production mechanism [71]. Moreover, higher resonance states give feed-down contributions to inclusive J/ψ production [72]. On the other hand, the effect of pure gluonic correlation functions on D -meson production in transversely polarized $p + p$ collisions has been studied in the twist-3 collinear factorization approach [5, 73]. However, lack of experimental results made it difficult to constrain the tri-gluon correlation functions.

2 Experimental Setup

2.1 Relativistic Heavy Ion Collider

The Relativistic Heavy Ion Collider (RHIC) is the world's first and only polarized proton collider and one of only two heavy ion colliders in the world, located at Brookhaven National Laboratory in Upton, New York. There are six interaction points where the two rings cross, called blue ring for the clockwise beam direction and yellow ring for the counterclockwise beam direction. For the collisions of heavy ions (A) and protons (p) (or deuterons (d)), the yellow ring is selected for the heavy ion beam. There were four experiments: PHENIX, STAR, BRAHMS, and PHOBOS. BRAHMS and PHOBOS stopped taking data and PHENIX at the 8 o'clock position in the ring has taken data until the 2016 run period and is preparing a new experiment, called sPHENIX.

The main physics goal is to study quark gluon plasma; a new state of matter under extreme temperature and density conditions, and to explore the spin structure of the proton. The center of mass energy in heavy ion collisions ranges from 7.7 GeV to 200 GeV per nucleon-nucleon collision pair ($\sqrt{s_{NN}}$). RHIC is capable of colliding various kinds of heavy ions and (polarized) protons and deuterons: $p+p$, $p+Al$, $p+Au$, $d+Au$, $Cu+Cu$, $Cu+Au$, $Au+Au$, $U+U$, $Ru+Ru$, $Zr+Zr$. For the polarized proton-proton collisions, the center of mass energy (\sqrt{s}) ranges from 62.4 GeV to 510 GeV. During the run in 2015, there were polarized proton and

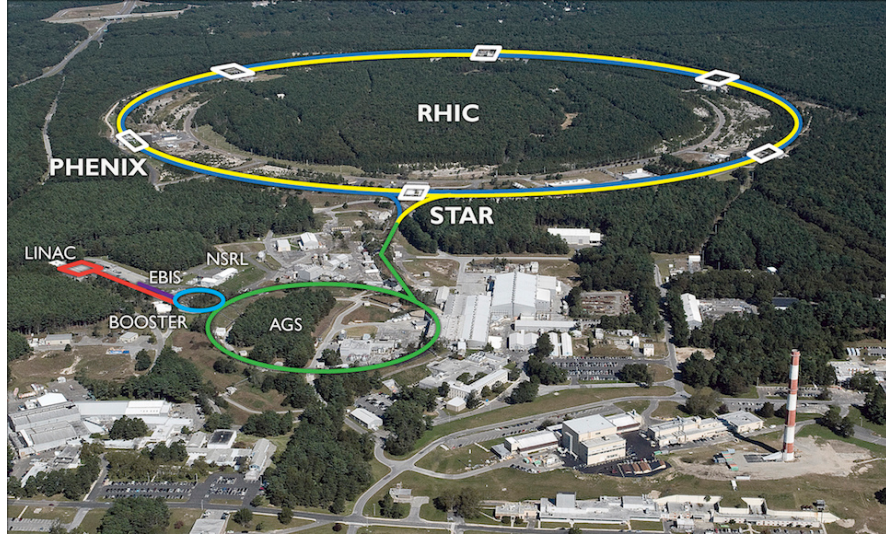


Figure 4: RHIC has six intersection points allowing the particle beams in two rings to collide.

heavy ion collisions: $p^\uparrow + \text{Al}$ and $p^\uparrow + \text{Au}$ at $\sqrt{s_{NN}} = 200$ GeV. The collision species combinations, energies and luminosities are illustrated in Figure 5, 6, 7.

2.2 Polarized Proton Acceleration for RHIC

To generate and maintain high luminosity polarized beams, various apparatuses are installed through the accelerator complex. Figure 8 shows the components for accelerating and colliding polarized proton beams [74].

2.2.1 Polarized Ion Source to RHIC

The source of polarized protons for RHIC is an optically pumped polarized H^- source [75]. 400 μs pulses of $\sim 10^{12}$ polarized H^- ions are accelerated from 35

RHIC energies, species combinations and luminosities (Run-1 to 18)

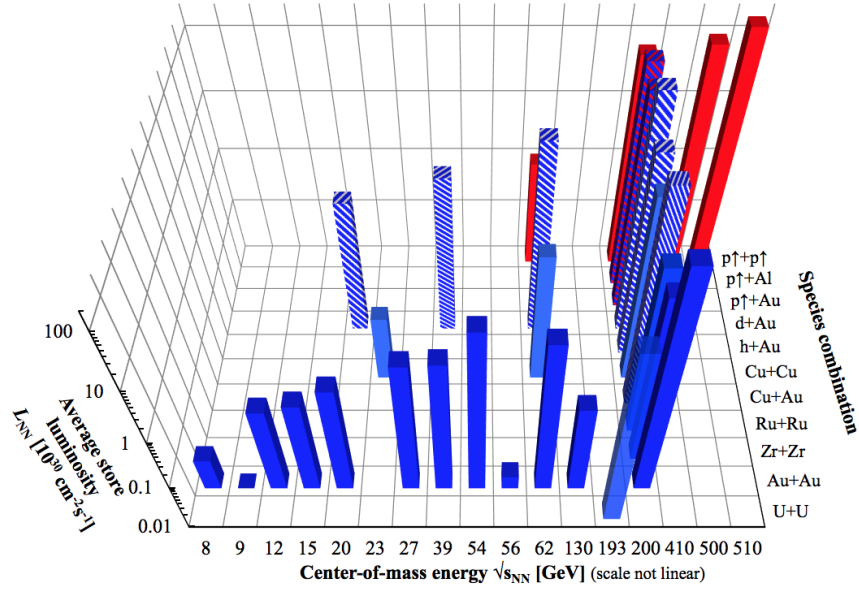


Figure 5: The collision species combinations, energies and luminosities at RHIC

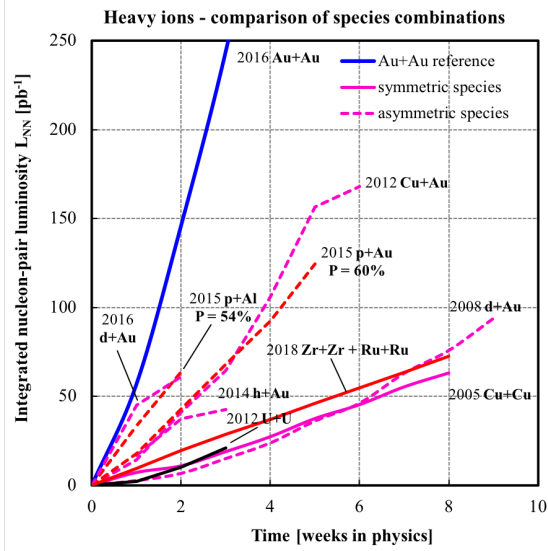


Figure 6: The collision species combination, energies and luminosities in $p, d + A$ collisions at RHIC

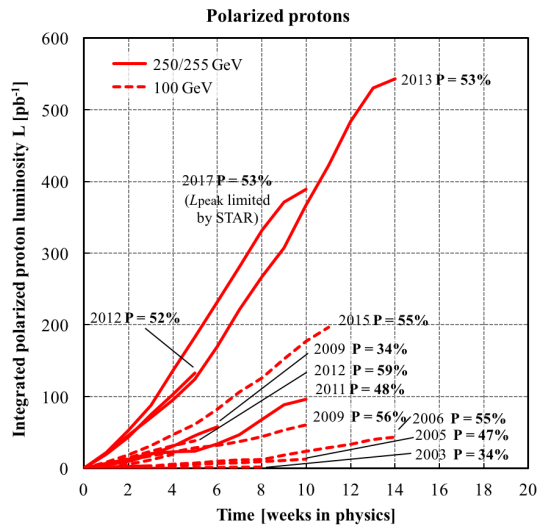


Figure 7: The energies, luminosities, and polarizations in $p^\uparrow + p$ collisions at RHIC

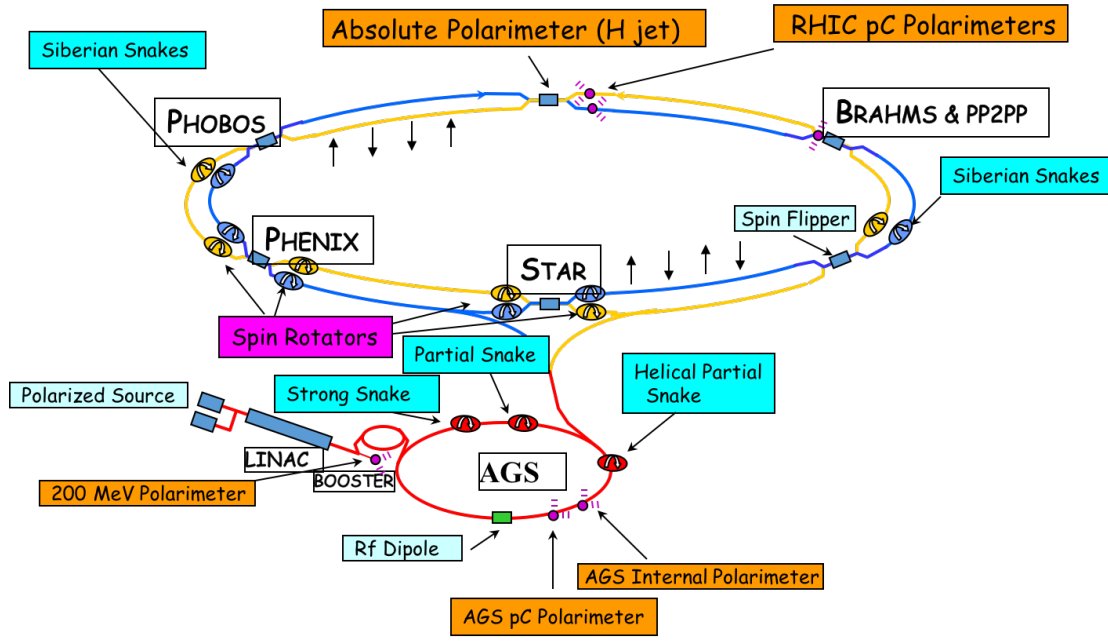


Figure 8: RHIC as the polarized proton collider.

keV to 750 keV by Radio Frequency Quadrupole (RFQ) cavities and accelerated again in the Linear Accelerator (LINAC) to 200 MeV. The Booster Synchrotron accelerates the proton bunches from the LINAC to 2.35 GeV and delivers them to the Alternating Gradient Synchrotron (AGS). The energy of the proton beam reaches 24.3 GeV in the AGS, then the proton beam is injected to RHIC for further acceleration. RHIC comprises two counter-circulating storage rings, in each of which as many as 120 polarized-proton bunches can be accelerated to a maximum energy of 255 GeV. In the collision point, two opposite direction beams collide after being made to converge by dipole magnets, named the DX dipoles, through which two beams pass. In the 2012 run, the beam injected into RHIC typically consisted of 109 filled bunches in each ring. The bunches collide with a one-to-one correspondence with a 106 ns separation. In the $\sqrt{s} = 200$ GeV proton-proton collisions during the 2012 run period, the number of ions per bunch was 160×10^9 . The peak luminosity was $46 \times 10^{30} \text{cm}^{-2}\text{s}^{-1}$, and the average luminosity was $33 \times 10^{30} \text{cm}^{-2}\text{s}^{-1}$ [76].

2.2.2 Control of Polarized Beam

To prevent depolarization of the proton beam from imperfections and intrinsic depolarizing resonances, two “Siberian Snakes” are installed on each ring [77, 78]. A Siberian Snake is composed of four superconducting magnets and is able to generate a spin rotation between vertically up and down without distorting the

trajectory of the particles. By filpping the polarization, many small effects from the RHIC magnets cancel out. In addition to the Siberian Snakes, “Spin Rotators” are constructed to rotate the spin directon from the vertical to the longitudinal direction.

Two polarimeters are used to determine the beam polarizations. One is a hydrogen-jet polarimeter, which takes several hours to measure the absolute polarization [79]. The other is a fast, proton-carbon polarimeter which measures relative changes in the magnitude of the polarization and any variations across the transverse profile of the beam several times per fill [80, 81].

2.3 PHENIX Experiment

The Pioneering High Energy Nuclear Interaction eXperiment (PHENIX) is designed to detect leptons, photons and hadrons. The experiment is capable of sampling rare events under high event rates. It rose like a phoenix from the ashes of proposals like OASIS, DIMUON, TALES, SPARC and other lepton focused proposals. Its unique hybrid design – central arms and muon arms – could be explained from this mixed origin.

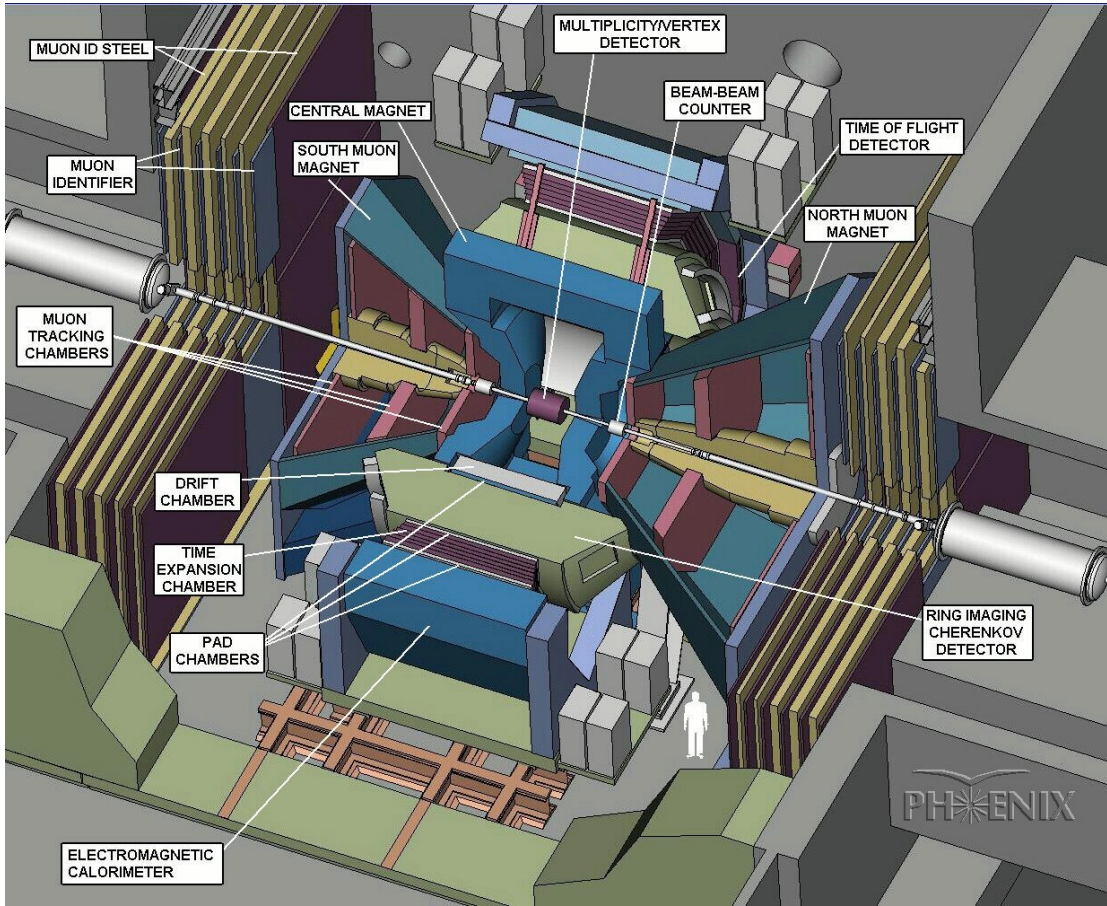
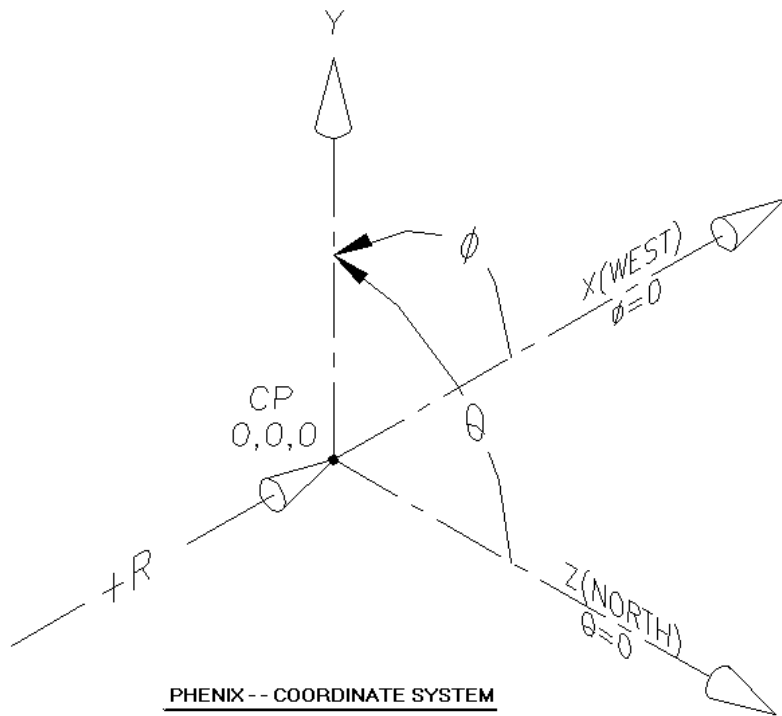


Figure 9: Quarter-cut view of PHENIX detectors

2.3.1 PHENIX Detector Overview



PHENIX local origin (0,0,0) is referenced to the RHIC secondary survey control network

Beam is on the Z axis

Position of detector assemblies in the central arms is measured in r, phi, and Z (at least most of them)

Position of detector assemblies in the muon arms is measured in X, Y, and Z

6/13/95

Figure 10: PHENIX coordinate system

2.3.2 PHENIX Muon Arms

THE PHENIX muon spectrometers (Muon arms) are built to carry out broad physics investigations such as studies of heavy quarks, vector mesons, the Drell-Yan process, and Z , W bosons by detecting muons from hadron-hadron collisions.

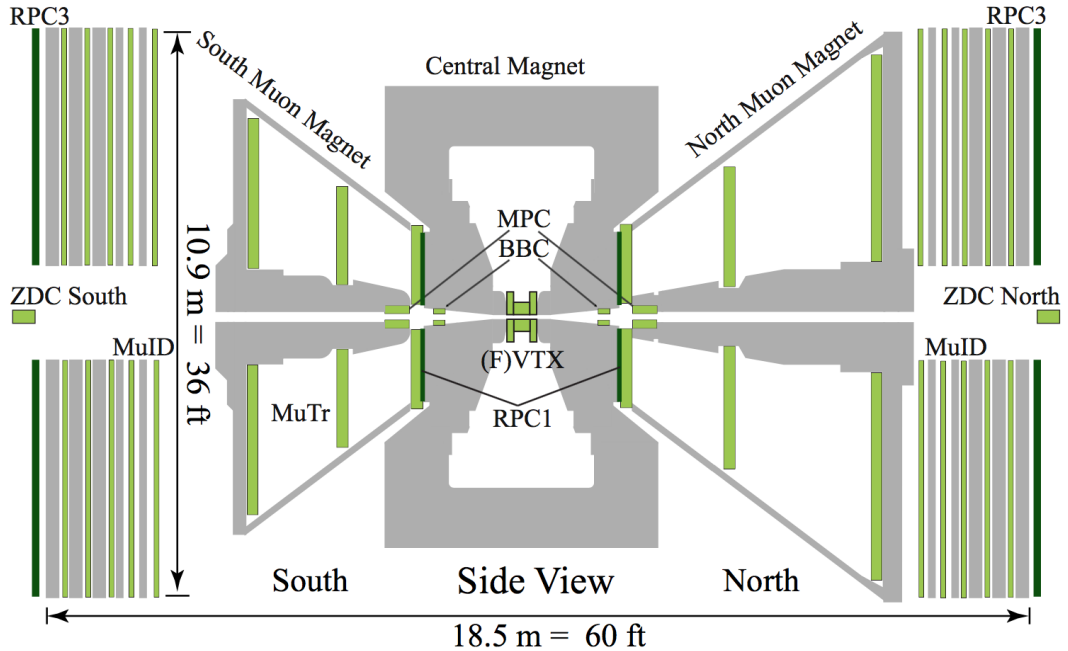


Figure 11: Side view of the PHENIX muon arms

The Muon Arms are located at forward ($1.2 < \eta < 2.4$) and backward ($-2.2 < \eta < -1.2$) rapidity regions. The North Arm is located north of the collision point, which is the going-direction of the blue beam, while the South Arm is in the going-direction of the yellow beam. For $p + A$ collisions, the blue beam contains bunches of (polarized) protons, the yellow beam has large ions such as Au or Al. Muons or hadrons from collisions pass through a hadron absorber. Surviving muons or hadrons reach the Muon Tracker which measures the momentum of the tracks and reconstructs the mass of vector mesons. Then the Muon Identifier discriminates muons from charged hadrons as described later. The drawing of the Muon Tracker is shown in the Figure 12.

Muon Tracker

The Muon Tracker (MuTr) [82] is a set of three stations of cathode-strip readout tracking chambers combined with the muon magnet to measure the momentum from a trajectory of a particle as shown in Fig. 13. It was designed to achieve requirements for separation of vector mesons (J/ψ , ψ' , Υ 's, ρ , ω , ϕ) for a large acceptance to make statistically significant measurements under high-luminosity conditions ($p + p$, $p+A$), but also to reconstruct track efficiently in central Au-Au events. The mass resolution is $\sigma(M)/M \cong 6\%/\sqrt{M}$ where M is in GeV and the spacial resolution is $100 \mu m$. There are three stations (Station-1,2,3) of cathode strip chambers in each MuTr. To produce a cathode pattern with a $25 \mu m$ accuracy, technologies like photolithography, electro-mechanical etching, and mechanical routing are used for three stations. The z -positions of the stations are at 1.80, 3.47, and 6.12 meters for the North Arm and at 1.80, 3.00, and 4.60 meters for the South Arm.

Station-1, the first station, is located at the closest position and so it has the smallest size. Therefore, highest occupancy is expected and the requirement to keep active over 95% of the station is the most stringent. Station-1 is made by putting four quadrants; each quadrant contains three cathode chamber gaps. Each chamber gap has a pair of cathode strip planes on both sides of an anode wire plane.

Station-2 and Station-3 are composed of eight octants. Station-2 is required to

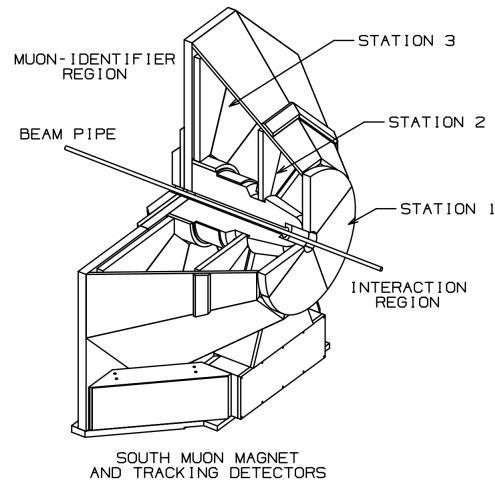


Figure 12: Drawing of the Muon Tracker of the South Muon Arm.

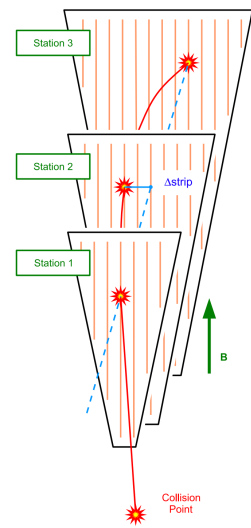


Figure 13: Momentum is calculated from the trajectory of a charged particle in a magnetic field.

be less than 0.1% of a radiation length (X_0) in order to provide decent momentum resolution down to 1.5 GeV. The cathodes were made of etched 25 mm mylar foils with 600 Angstroms of cooper coat. Also, 3.175 mm laminated frames are used for all 6 cathode foils and 3 anode wire planes. Station-3 is the largest one and consists of two gaps. Each gap contains a pair of cathode readout planes on both sides of an anode wire plane which are made by etching shallow lines on the copper planes mechanically. To obtain good momentum resolution, an optical alignment system is used for monitoring displacement at the level of $\pm 25 \mu\text{m}$ from an optical fiber light source at Station-1 through a convex lens at Station-2 to a CCD camera at Station-3 [83].

Muon Identifier

The Muon Identifier (MUID) is located behind of the Muon Tracker. The purpose of MUID is discriminating muons from hadrons. The irreducible μ/π ratio before reaching the absorber is about 1×10^{-3} . MUID can enhance this number by including additional material. The detector is designed to reduce the punch-through hadrons by 1/4. This factor of 1/4 suppresses the pair background for J/ψ by an order of magnitude. A total depth of 90 cm ($5.4\lambda_I$) steel is included to reduce the probability of punch-through to under 3% for pions up to 4 GeV/c . In the North Arm, there are 4 steel absorbers (10,10,20,20 cm) and 30 cm of

muon magnet backplane in front of them. The South Arm has a thinner (20 cm) backplane and absorbers (20,10,20,20 cm); the total thickness is the same as for the North Arm. Five gaps between the steel absorbers contain the MUID panels. Each MUID gap is composed of 6 panels named from A to H, shown in Fig. 14. In a MUID panel, 2 arrays of Iarocci tubes [84] are bundled and shifted by a half cell relative to each other for good efficiency, so that the readout of a channel is called “two pack” in Fig. 15. Each of the small panels B, G has 90 horizontal and 45 vertical tubes. There are 118 horizontal and 128 vertical tubes in each large panel (A, C, F, H).

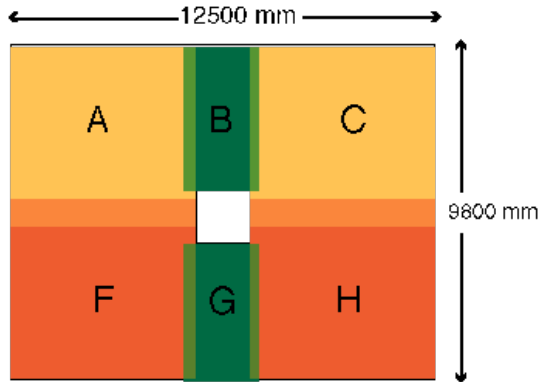
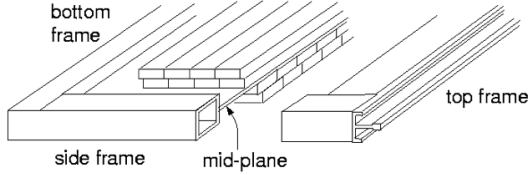
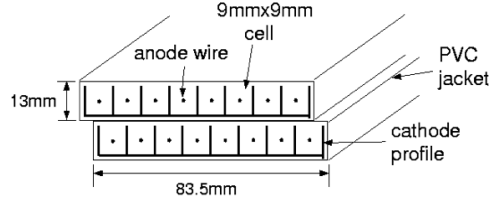


Figure 14: Layout of 6 MUID panels from A to H. The edges overlap between panels to eliminate dead areas.

Tracking in the Muon Arms



Cross section of the MUID panel



Cross section of the plastic tube(2-pack)

Figure 15: Cross section of the MUID panel and 2-pack of plastic tube.

The offline track reconstruction using MUTR and MUID starts from a MUID Road. The position resolution of MUID is 8 cm for both horizontal and vertical directions. The beginning point of the road-finding algorithm is a pair (horizontal, vertical) of clusters at 2nd and 3rd MUID Gap (called Gap-1, Gap-2 by zero-based numbering). Once a cluster is found, another cluster is searched at both sides of the 2nd and 3rd Gaps: the 1st (Gap-0) and 4th MUID Gap (Gap-3). Each one-dimensional road finally extends to the 5th Gap (Gap-4) and a fit to a straight line is done. A pair of one-dimensional roads is combined into a two-dimensional MUID Road with the following requirements:

- It needs to reach to MUID Gap-2 or deeper.
- One-dimensional road need to have hits in more than 2 MUID Gaps.

- The difference of the total number of gaps that fired between horizontal and vertical roads cannot be larger than 1.

A MUID road which meets those requirements becomes a seed of a track for MUTR. When a single charged track goes through MUTR stations, one to three adjacent cathodes can fire and those hits are combined as a cluster. In each station, two cathode strips are aligned differently, providing two-dimensional position information. Then those clusters in two or three gaps are grouped as stubs by linear fitting. The search algorithm starts from a MUID Road at Gap-0, then a search window is opened at MUTR Station-3, and the final step is finding stubs at Station-2 and Station-1. Figure 16 shows an example of track finding using MUID and MUTR hits.

2.3.3 Inner Detectors

The Beam Beam Counter (BBC) and Zero Degree Calorimeter (ZDC) provide information on events for triggering and categorizing. BBC detects charged particles while ZDC detects neutrons.

Beam Beam Counter

The Beam Beam Counter (BBC) is consist of two modules (North, South) each of which has 64 quartz Cherenkov counters, located close to the beam pipe (at $3.1 < \eta < 3.9$ rapidity), at 144 cm from the interaction point [85]. BBC detects charged particles with $\beta > 0.7$. BBC provides the timing of a collision with

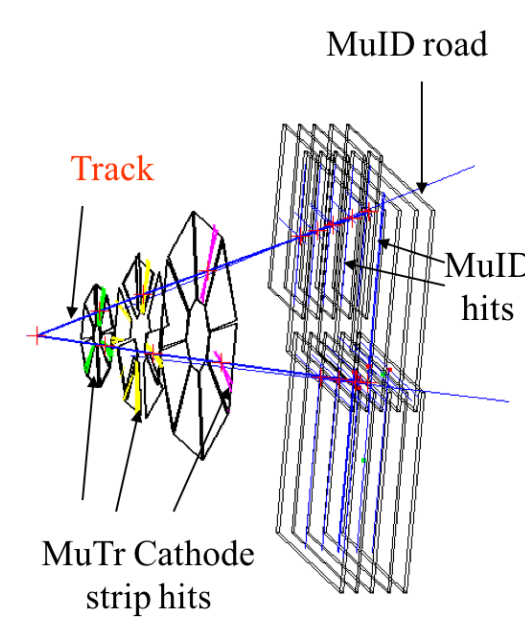


Figure 16: Finding a track from MUID and MUTR hits.

primary z-vertex information by measuring the flight-time from the interaction point to BBC. Also, BBC serves as a luminosity monitor for the PHENIX experiment. The precision of the z-vertex measurement from BBC is 2 cm. BBC also provides essential information to categorize events in terms of centrality for heavy-ion collisions, as shown in Figure 18.

Zero Degree Calorimeter

The PHENIX Zero Degree Calorimeter (ZDC) [86] is located at 18 m from the interaction point on both sides. It covers the very forward region ($\theta \leq 2.8$ mrad). From ion collisions at RHIC, neutral beam fragments, especially neutrons, are detected in this zero-degree region. ZDC is designed to detect neutrons and measure

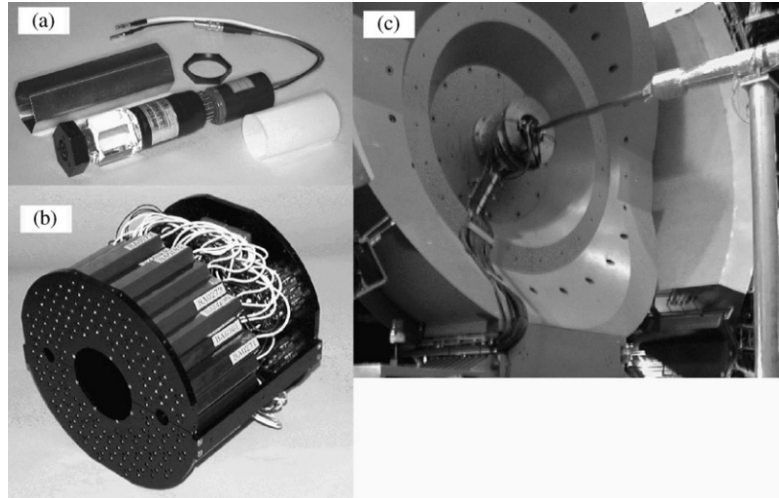


Figure 17: PHENIX Beam Beam counter. (a) A Single BBC (b) A BBC array of 64 elements (c) Installed BBC on the PHENIX nearby the beam pipe

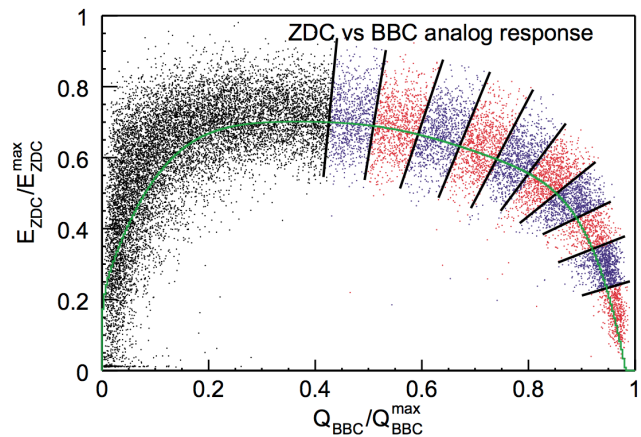


Figure 18: Correlation between energy deposited in ZDC and sum of charge in BBC. The straight lines define 5% intervals in centrality, from 0-5% on the right-most side.

the total energy. This can be used as an event trigger and a luminosity monitor. Also, centrality can be obtained from the neutron multiplicity. To detect neutrons, the DX magnets are installed in front of the ZDC and make charged particles deflect out of the ZDC acceptance as shown in Figure 19. The drawing of a ZDC module is shown in Figure 20.

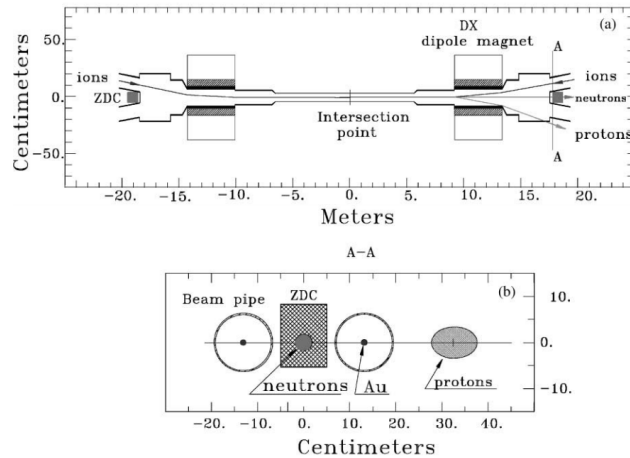


Figure 19: (a) Top view of the PHENIX Zero Degree calorimeter. (b) Beam's eye view of ZDC

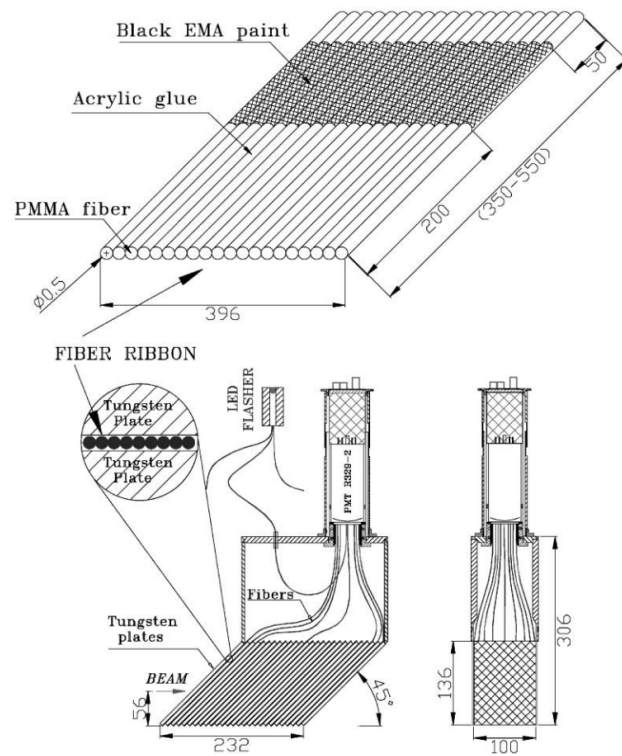


Figure 20: Mechanical design of a ZDC module in mm.

2.3.4 Event Triggering

The PHENIX level-1 trigger works in every beam crossing for efficient data-taking by selecting potentially interesting events [87]. There are two subsystems, the Local Level-1 (LL1) operates by direct communication with detector systems while the Global Level-1 (GL1) combines received data and makes a trigger decision from combined LL1 information. Table 1 shows a part of the list of trigger for Run15 $p + p$ collisions at $\sqrt{s} = 200$ GeV. In the data analysis, MUON_N_SG3&MUIDLL1_(1D||1H), MUON_S_SG3&MUIDLL1_(1D||1H) are selected. For example, MUON_N_SG3&MUIDLL1_(1D||1H)&BBCLL1novtx(nppg) is an “and” combination of MUON_N_SG3, MUIDLL1_(1D||1H), BBCLL1novtx(nppg). BBCLL1novtx(nppg) is a trigger fired by BBC. MUIDLL1_(1D||1H) means Level-1 trigger at MUID, and 1D||1H is 1D(fired MUID Gap-3 or Gap-4) or 1H(fired MUID Gap-2 or Gap-3). MUON_N_SG3 is North Arm SG-3 trigger from Muon Trigger [4]. More details are included in the following subsections. The scaledown number shows the number of dropped triggers for each recorded event. For example if the Scaledown is 25, only one event is stored (Scaled count) and 25 events are abandoned among a total of 25+1 events (Raw count). All events are saved when the scaledown is zero. Because the bandwidth of data acquisition is limited, scaledown factors are adjusted based on the physics goals of certain collisions and detector configuration.

Trigger Name	Raw count	Scaledown	Scaled count
BBCLL1(>0 tubes)	2336754137	4399	498645
MUON_N_SG3&MUIDLL1_(1D 1H)	1711981	0	1526925
&BBCLL1novtx(nppg)			
MUON_S_SG3&MUIDLL1_(1D 1H)	582035	0	525127
&BBCLL1novtx(nppg)			
MUIDLL1_N1D&BBCLL1novtx	152128067	195	727714
MUIDLL1_S1D&BBCLL1novtx	23356789	25	835617

Table 1: A part of the trigger list for Run15 $p + p$ collisions at $\sqrt{s} = 200$ GeV.

2.3.5 Minimum Bias Trigger

The minimum bias trigger provides a minimal set of requirements for the events by assuring a collision has occurred at a given time. It is also used for monitoring the luminosity. It generates trigger bits when there is more than one hit in both North and South BBC modules. There are three types of minimum bias trigger depending on the collision vertex range. The BBCLL1 (>0 tubes) is for the z vertex range ± 30 cm from the origin, BBCLL1(narrowVertex) is for ± 15 cm, and BBCLL1(noVertexCut) does not require a collision vertex range. Other triggers such as MUIDLL1 are combined with the minimum bias trigger. The BBC trigger efficiency for MB $p+p$ events (events containing muons from open heavy-flavor) is 55% (79%) [88], as measured with the van der Meer scan technique [89].

2.3.6 MUID LL1 Trigger

The MuID trigger serves to select events containing at least one MuID track reaching Gap2,3 or Gap4. For each set of x,y oriented gaps, two packs in the MUID Gap-0 are grouped virtually as “logical tube.” For each logical tube, a line is projected from the origin (0,0,0) and logical tubes are formed within a certain range along the projected line in each MUID gap. The set of logical tubes along the line is called “*symset*,” as shown in Fig. 21. Therefore it provides some power for rejecting ghost tracks. The trigger decision is made with *symsets* which satisfy the logic for MUID-1D (one-deep) for muons at Gap-4, or MUID-1H (one-hadron) for stopped hadrons at Gap2,3. The MUIDLL1 trigger can be selected separately for North or South Arm as MUIDLL1_N1D or MUIDLL1_S1D. MUIDLL1 triggers are basically combined with BBCLL1 triggers. For example, MUIDLL1_N1D&BBCLL1novtx means MUIDLL1-1D trigger for North Arm is combined with BBCLL1novtx, so that it fires when a *symset* in the North Arm passes the MUIDLL1-1D logic without any collision vertex limit.

2.3.7 MuTrg LL1 Trigger

In order for the trigger to select a specific momentum range, Muon Trigger front-end-electronics was added to the Muon Tracker. It uses about 5% of the charge from non-stereo type cathode planes. “Sagitta” is defined by the distance between the xy hit position at the MUTR station-2 and a straight line between a hit at

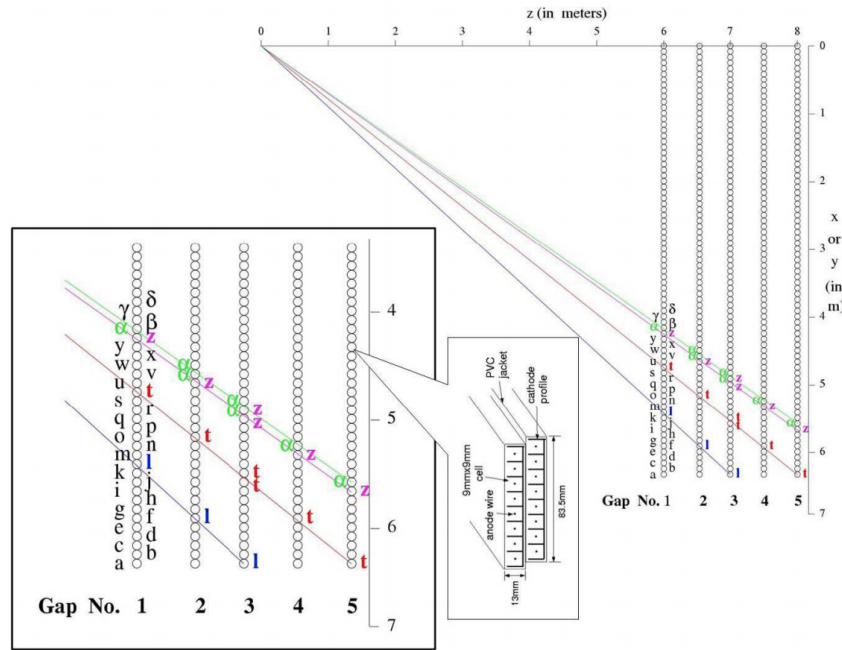


Figure 21: Symsets of the MuID trigger

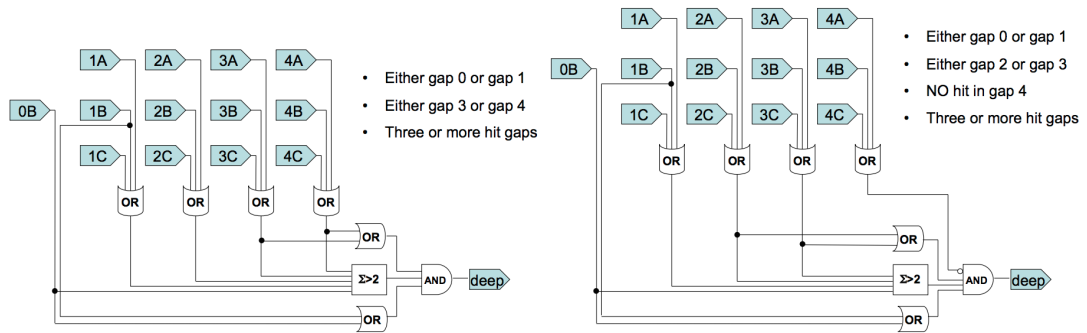


Figure 22: MuID symset logic. The left side shows the MuID-1D logic and the right side shows the MuID-1H logic.

Station-1 and Station-3. Therefore the sagitta represents the amount of bending of a charged particle's trajectory in the radial magnetic field in the MUTRs and is related to the momentum of the particle. A trigger bit is issued when the number of sagittas meets the requirements of the trigger logic. SG-N trigger allows N-strip sagitta, such as SG1 and SG3. SG1 is useful for selecting tracks with large p_z . For the charged hadron analysis in the following chapters, the SG3 trigger is used and it shows momentum-dependent efficiency. By selecting the SG trigger, it is possible to collect more statistics for high-momentum tracks within the limited bandwidth in the PHENIX data acquisition system instead of filling the disk with events dominated by low-momentum tracks.

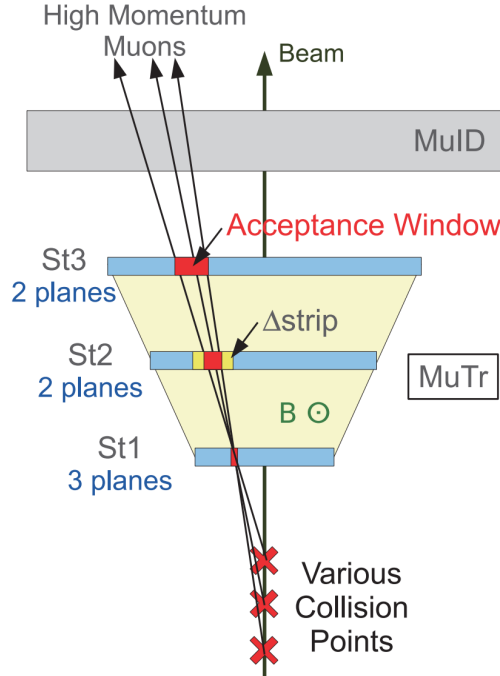


Figure 23: A schematic drawing of the Muon Trigger LL1 trigger logic [4].

2.3.8 Centrality

In heavy ion collisions, including $p + A$ collisions, the medium created in the overlapping region depends on the initial geometry. The initial energy density of the medium is determined by geometrical variables such as the number of participating nucleons (N_{part}) or the number of nucleon-nucleon collisions (N_{coll}). The collisions are grouped into *centrality* classes. For $p + A$ collisions, the value of centrality is 0 when the proton collides with the center of a heavy ion and this is the most central collision. If the proton collides with the edge of heavy ion, this is called a peripheral collision and the value of centrality is defined as 100%. The centrality is determined as the fraction of the total charge deposited into the BBC on the A -going side (South BBC in PHENIX). For example, 0-20% centrality represents the 20% of events which deposit the largest fraction of charge in the BBC on the A -going side in $p + A$ collisions. For the various centrality classes, the average number of participating nucleons ($\langle N_{part} \rangle$) or the average number of nucleon-nucleon collisions ($\langle N_{coll} \rangle$) is calculated using simulations with BBC based on the Glauber model [90].

3 Data Analysis (I) : Heavy Flavor A_N

3.1 Single Muon Measurements

This chapter contains analysis details of the study of A_N of muons from semi-leptonic decay of open heavy flavor (mainly D mesons). Data from transversely polarized $p+p$ collisions at $\sqrt{s} = 200$ GeV were collected by the PHENIX detector in 2012. The total integrated luminosity was 9.2 pb^{-1} . The MuID trigger in coincidence with the BBC trigger was used for recording the data. The BBC trigger requires at least one hit in both North and South BBCs. The BBC trigger efficiency for minimum-bias is 55% for $p+p$, 72% for $p+\text{Al}$, and 84% for $p+\text{Au}$ collisions [88], calculated using the van der Meer scan technique [89]. Events containing at least one MuID track reaching Gap3 or Gap4 are selected by the MuID trigger.

To obtain the background, the signal fraction of muon from open heavy flavor, the method of background estimation from previous PHENIC publication was used [91, 92].

Event and Track Selection

Analysis cuts are placed on a track-by-track basis. The details are shown below:

- Rapidity cut: $1.4 < |\eta| < 2.0$.
- BBC Vertex Z cut: $-25 < |BBCZ| < 25 \text{ cm}$.

- p_T range cut: $1.25 < |p_T| < 5$ GeV/ c .
- Number of MuTR hits cut: $nMutrHits \geq 13$.
- MuTR fitting $\chi^2 > 10$ for MUID last gap 2 and 3, and $\chi^2 > 8$ for last gap 4.

Other cuts :

The DG0, DDG0, VtxRad, VtxChi2, gap0 slope and $|\bar{p} \cdot \delta\theta|$ cuts are used; these are well-studied and fine-tuned transverse momentum dependent cuts which keep signal and reject backgrounds.

Other cuts used for hadron background (MuID Gap3 tracks): Minimum p_z cut $p_z > 3.4$ was used for selecting pure hadrons.

Besides muons from heavy flavor decays, other light hadrons also have finite probability to penetrate the muon spectrometers and be misidentified as muons. Even worse, since there are no experimental measurements of light hadron yields in the PHENIX muon spectrometers acceptance range, the sources of backgrounds are not well constrained. The dominant sources of backgrounds are:

(1) Muons from light hadron decays: Due to the finite distance (~ 40 cm) from the collision vertex to the muon spectrometer steel absorber, about 1% of light hadrons decay before they reach the absorber (some of them decay inside the

absorber). These decay muons are then measured by the muon spectrometers.

(2) Punch-through light hadrons: High momentum light hadrons have a finite probability (1%) to reach the last MuID panel and be mistagged as muons.

3.2 Transverse Single Spin Asymmetry

The transverse single spin asymmetry A_N is obtained for the blue and yellow beam separately by considering the polarization of only one beam and summing over the polarizations of the other beam.

3.2.1 Maximum Likelihood Method

For this measurement, the likelihood is:

$$\mathcal{L} = \prod f \cdot (1 \pm R_L \cdot P \cdot A_N \cos(\phi_i)) \quad (5)$$

where f is any correction factor, \pm depends on the spin direction, $R_L = \frac{L^\uparrow}{L^\downarrow}$ is the relative luminosity measured with BBCLL1, P is the polarization, and ϕ_i is the azimuthal angle for each track. We just look for A_N which would make $\log \mathcal{L}$ maximum. Then this A_N will be our result. For computational purposes, the likelihood function

$$\log \mathcal{L} = \sum \log(1 \pm R_L \cdot P \cdot A_N \cos(\phi_i)) + \log f; \quad (6)$$

where $\log f$ is independent of A_N , it won't affect the final A_N result and can be ignored. And if the azimuthal angle ϕ distribution does not have any cosine

modulation, R_L can be ignored too (set to be 1).

The statistical uncertainty can be derived by:

$$\sigma(A_N) = \left(-\frac{\partial^2 \mathcal{L}}{\partial A_N^2}\right)^{-1} \quad (7)$$

Since the maximum likelihood method doesn't need binning, it is reliable in low statistics situation. Because the beam polarization varies fill by fill, the asymmetry is determined fill by fill, then a fit is performed to a polynomial of degree 0 across all fills for the maximum likelihood method.

3.2.2 Inclusive and Background Asymmetry Estimations

Tracks at the last MuID gap (Gap4) consist of muons from heavy-flavor, punch-through hadrons, muons from light hadrons, and muons from J/ψ . The contribution from other sources is negligible as discussed in the previous section. In order to obtain the asymmetry of heavy-flavor muons (A_N^{HF}), the asymmetry of the background from light hadrons (A_N^h) and muons from J/ψ ($A_N^{J/\psi \rightarrow \mu}$) should be subtracted from the asymmetry of inclusive muon candidates (A_N^{incl}). The A_N^h is obtained from the asymmetry of stopped hadrons at MuID Gap3. The possible difference between the A_N of the stopped hadrons at MuID Gap3 and that of the mixture of decay muons and punch-through hadrons at MuID Gap4 is studied with the “hadron cocktail” simulation. The details are described in the following section.

For the estimation of $A_N^{J/\psi \rightarrow \mu}$, a previous PHENIX $A_N^{J/\psi}$ measurement [70] is used. The asymmetry of single muons from J/ψ decay ($A_N^{J/\psi \rightarrow \mu}$) is estimated from a decay simulation with the initial $A_N^{J/\psi}$ as measured in [70] ($A_N^{J/\psi} = -0.002 \pm 0.026$ at $x_F < 0$, and -0.026 ± 0.026 at $x_F > 0$). The initial p_T and rapidity distributions of J/ψ are from PHENIX Analysis Note 1098 [93]. The obtained $A_N^{J/\psi \rightarrow \mu}$ is $-0.002^{+0.018}_{-0.022}$ at $x_F < 0$ and $-0.019^{+0.019}_{-0.025}$ at $x_F > 0$. Details are given in the systematic uncertainty section below. Once the asymmetries of the light hadron background (A_N^h) and muons from J/ψ ($A_N^{J/\psi \rightarrow \mu}$) are determined, the A_N of heavy-flavor muons and its uncertainty can be obtained as

$$A_N^{HF} = \frac{A_N^{incl} - f_h \cdot A_N^h - f_{J/\psi} \cdot A_N^{J/\psi \rightarrow \mu}}{1 - f_h - f_{J/\psi}}, \quad (8)$$

$$\delta A_N^{HF} = \frac{\sqrt{(\delta A_N^{incl})^2 + f_h^2 \cdot (\delta A_N^h)^2 + f_{J/\psi}^2 \cdot (\delta A_N^{J/\psi \rightarrow \mu})^2}}{1 - f_h - f_{J/\psi}}, \quad (9)$$

where $f_h = (N_{hadronbackground})/N_{incl}$ is the fraction of light hadron background obtained from the number of light hadron background ($N_{hadronbackground}$) divided by the number of inclusive tracks (N_{incl}). $f_{J/\psi} = N_{J/\psi \rightarrow \mu}/N_{incl}$ is the fraction of muons from J/ψ . Both fractions (f_h and $f_{J/\psi}$) are determined from the background estimation mentioned above. $\delta A_N^{J/\psi \rightarrow \mu}$, estimated from the previous PHENIX measurement, is included only in the systematic uncertainty.

Tables 2, 3, 4, and 5 list the light hadron background fractions, calculated from the signal to (light hadron) background ratio from the Run12 $p + p$ single muon cross section analysis, described in PHENIX Analysis Note 1250 [94]. We will

Table 2: The light hadron background fraction (f_h) in p_T bins, (–) charge

p_T	South Arm			North Arm		
	GeV/c	f_h	δf_h^{syst}	δf_h^{stat}	f_h	δf_h^{syst}
(1.25,1.50)	78.15%	10.52%	0.41%	78.62%	9.35%	0.41%
(1.50,2.00)	76.88%	10.28%	0.40%	75.06%	8.72%	0.37%
(2.00,2.50)	70.36%	9.41%	0.66%	72.65%	8.36%	0.62%
(2.50,3.00)	59.10%	7.78%	0.96%	59.98%	6.80%	0.89%
(3.00,3.50)	50.06%	6.89%	1.39%	52.09%	5.17%	1.51%
(3.50,5.00)	46.11%	7.38%	1.67%	46.16%	6.03%	1.51%

Table 3: The background fraction (f_h) in x_F bins, (–) charge

$ x_F $	South Arm			North Arm		
	f_h	δf_h^{syst}	δf_h^{stat}	f_h	δf_h^{syst}	δf_h^{stat}
(0.00,0.05)	77.74%	10.46%	0.31%	77.78%	9.25%	0.30%
(0.05,0.20)	70.84%	9.47%	0.49%	69.23%	7.97%	0.44%

use these ratios to calculate our physics asymmetries. The systematic uncertainty of the light hadron background fraction was considered as a source of systematic uncertainty. Tables 6, 7, and 8 show the J/ψ fraction. It was calculated in PHENIX analysis Note 1098 [93]. $N_{HF+J/\psi}$ is the number of muons from heavy

Table 4: The background fraction (r) in p_T bins, (+) charge

p_T	South Arm			North Arm		
	GeV/c	f_h	δf_h^{syst}	δf_h^{stat}	f_h	δf_h^{syst}
(1.25,1.50)	78.17%	10.69%	0.41%	83.49%	10.60%	0.46%
(1.50,2.00)	73.03%	9.76%	0.37%	77.65%	9.15%	0.37%
(2.00,2.50)	70.97%	9.30%	0.60%	72.71%	8.14%	0.58%
(2.50,3.00)	64.97%	8.46%	0.93%	64.07%	7.07%	0.90%
(3.00,3.50)	59.21%	9.58%	1.40%	57.89%	6.78%	1.29%
(3.50,5.00)	60.23%	8.84%	1.80%	55.26%	6.27%	1.56%

 Table 5: The background fraction (r) in x_F bins, (+) charge

$ x_F $	South Arm			North Arm		
	f_h	δf_h^{syst}	δf_h^{stat}	f_h	δf_h^{syst}	δf_h^{stat}
(0.00,0.05)	76.57%	10.47%	0.30%	81.57%	10.36%	0.33%
(0.05,0.20)	70.18%	9.20%	0.44%	72.06%	8.06%	0.45%

flavor including J/ψ ; only the light hadron background is subtracted from the inclusive tracks.

Table 6: J/ψ fraction in p_T bins, (–) charge

p_T	South Arm		North Arm	
	$N_{J/\psi}/N_{HF+J/\psi}$	$f_{J/\psi}$ (absolute)	$N_{J/\psi}/N_{HF}$	$f_{J/\psi}$ (absolute)
GeV/ c	$N_{J/\psi}/N_{HF+J/\psi}$	$f_{J/\psi}$ (absolute)	$N_{J/\psi}/N_{HF}$	$f_{J/\psi}$ (absolute)
(1.25,1.50)	1.83%	0.40%	2.13%	0.46%
(1.50,2.00)	4.76%	1.10%	4.90%	1.22%
(2.00,2.50)	11.15%	3.30%	13.25%	3.62%
(2.50,3.00)	14.64%	5.99%	16.11%	6.45%
(3.00,3.50)	16.75%	8.36%	18.58%	8.90%
(3.50,5.00)	20.36%	10.97%	22.30%	12.01%

3.2.3 A_N vs. p_T

The transverse single spin asymmetries in μ^- and μ^+ production have been studied in six p_T ($1.25 < p_T < 5$ GeV/ c) bins for forward and backward rapidity separately.

To have a rough idea of the statistics, the number of tracks for inclusive muons (Gap4) and hadron background (Gap3) after all the quality cuts is listed in tables 10, 11.

Table 7: J/ψ fraction in p_T bins, (+) charge

p_T	South Arm		North Arm	
GeV/c	$N_{J/\psi}/N_{HF}$	$f_{J/\psi}$ (absolute)	$N_{J/\psi}/N_{HF+J/\psi}$	$f_{J/\psi}$ (absolute)
(1.25,1.50)	1.49%	0.32%	2.30%	0.38%
(1.50,2.00)	3.30%	0.89%	4.51%	1.01%
(2.00,2.50)	9.00%	2.61%	10.44%	2.85%
(2.50,3.00)	13.00%	4.55%	13.50%	4.85%
(3.00,3.50)	14.62%	5.96%	15.72%	6.62%
(3.50,5.00)	18.34%	7.29%	18.46%	8.26%

 Table 8: J/ψ fraction in x_F bins, (−) charge

$ x_F $	South Arm		North Arm	
	$N_{J/\psi}/N_{HF+J/\psi}$	$f_{J/\psi}$ (absolute)	$N_{J/\psi}/N_{HF+J/\psi}$	$f_{J/\psi}$ (absolute)
(0.00,0.05)	5.11%	1.14%	5.69%	1.26%
(0.05,0.20)	16.74%	4.88%	18.51%	5.69%

Table 9: J/ψ fraction in x_F bins, (+) charge

$ x_F $	South Arm		North Arm	
	$N_{J/\psi}/N_{HF+J/\psi}$	$f_{J/\psi}$ (absolute)	$N_{J/\psi}/N_{HF+J/\psi}$	$f_{J/\psi}$ (absolute)
(0.00,0.05)	3.88%	0.91%	5.00%	0.92%
(0.05,0.20)	14.79%	4.41%	15.36%	4.29%

Table 10: Number of (–) tracks in different Gaps after all the track quality cuts.

p_T (GeV/ c)	South, Gap3	South, Gap4	North, Gap3	North, Gap4
(1.25, 5.0)	32476	588964	30545	624773
(1.25, 1.5)	7750	274922	6697	264517
(1.5, 2.0)	13295	234272	12511	267715
(2.0, 2.5)	6332	55908	6238	65152
(2.5, 3.0)	2858	16181	2802	18444
(3.0, 3.5)	1241	4819	1273	5958
(3.5, 5.0)	1000	2862	1024	2987

Table 11: Number of (+) tracks in different Gaps after all the track quality cuts.

p_T (GeV/c)	South, Gap3	South, Gap4	North, Gap3	North, Gap4
(1.25, 5.0)	75195	682849	71610	298184
(1.25, 1.5)	18365	314778	15106	298184
(1.5, 2.0)	30942	270782	29372	304978
(2.0, 2.5)	14555	66768	15046	78534
(2.5, 3.0)	6431	20116	6788	23509
(3.0, 3.5)	2695	6285	2988	8026
(3.5, 5.0)	2207	4120	2399	4312

(-) Charge

Figures 24, 25, and 26 show the p_T dependence of asymmetries for single track production at Gap4 (inclusive asymmetries), Gap3 (background asymmetries) and physics asymmetries respectively. Since our p_T range of single muons is $1.25 < p_T < 5 \text{ GeV}/c$, within the limits of errors the asymmetries for Gap3 muons (mainly from light hadrons) are consistent with zero for all p_T bins, as expected from the previous experimental results. The asymmetries (blue beam, yellow beam and combined) at forward rapidity for Gap3 (background) and Gap4 (inclusive) are listed in Tables 12.

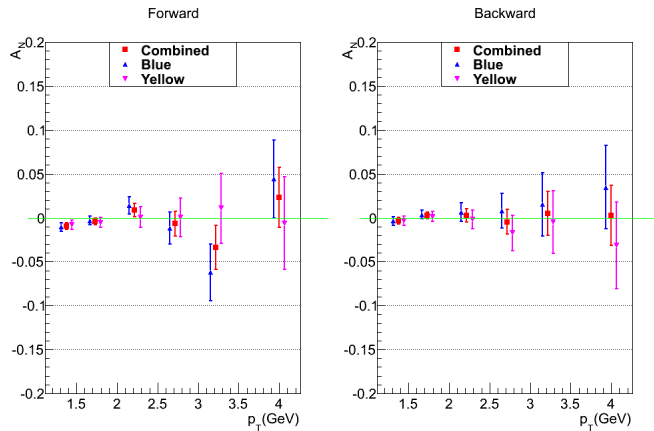


Figure 24: p_T dependence of asymmetries for inclusive muons (Gap4) in the forward (left) and backward (right) rapidity. (–) charge

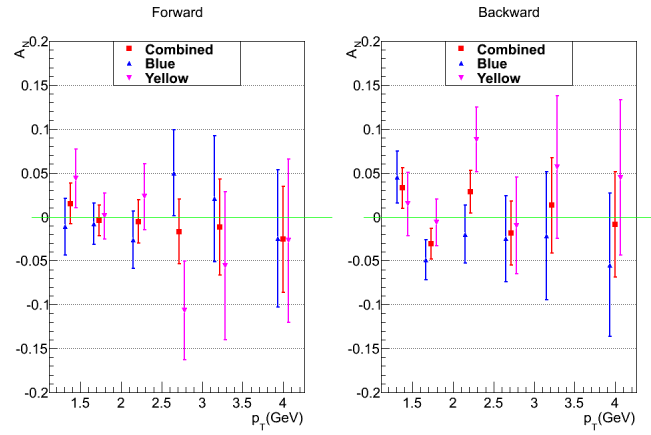


Figure 25: p_T dependence of asymmetries for hadrons background (Gap3) in the forward (left) and backward (right) rapidity. (–) charge

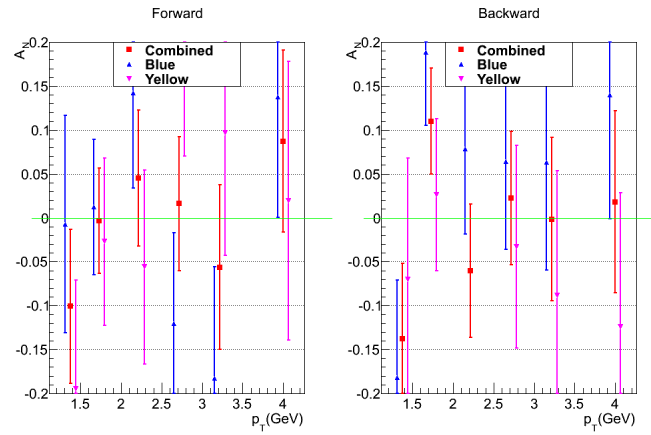


Figure 26: p_T dependence of physics asymmetries in the forward (left) and backward (right) rapidity, obtained by using Eq. 8 and 9 with $A_N(\text{Inclusive}) = A_N(\text{Gap4})$ and $A_N(\text{Background}) = A_N(\text{Gap3})$. (–) charge

Table 12: p_T dependence of A_N^B (blue beam), A_N^Y (yellow beam) and A_N (combined) in forward rapidity. (–) charge

p_T (GeV/c)	Gap4 (10^{-2})		
	A_N^B	A_N^Y	A_N
(1.25,1.50)	-1.05 ± 0.49	-0.81 ± 0.54	-0.94 ± 0.36
(1.50,2.00)	-0.31 ± 0.48	-0.55 ± 0.58	-0.41 ± 0.37
(2.00,2.50)	1.39 ± 0.98	0.07 ± 1.19	0.86 ± 0.76
(2.50,3.00)	-1.15 ± 1.83	0.05 ± 2.21	-0.66 ± 1.41
(3.00,3.50)	-6.21 ± 3.21	1.07 ± 4.00	-3.35 ± 2.50
(3.50,5.00)	4.41 ± 4.47	-0.63 ± 5.28	2.31 ± 3.41
Gap3 (10^{-2})			
(1.25,1.50)	-1.13 ± 3.23	4.33 ± 3.34	1.51 ± 2.32
(1.50,2.00)	-0.77 ± 2.34	0.09 ± 2.62	-0.39 ± 1.75
(2.00,2.50)	-2.63 ± 3.26	2.29 ± 3.78	-0.53 ± 2.47
(2.50,3.00)	5.01 ± 4.88	-10.65 ± 5.63	-1.70 ± 3.69
(3.00,3.50)	2.05 ± 7.21	-5.59 ± 8.42	-1.18 ± 5.48
(3.50,5.00)	-2.47 ± 7.84	-2.73 ± 9.33	-2.58 ± 6.00

Table 13: p_T dependence of A_N^B (blue beam), A_N^Y (yellow beam) and A_N (combined) in backward rapidity. (–) charge

p_T (GeV/c)	Gap4 (10^{-2})		
	A_N^B	A_N^Y	A_N
(1.25,1.50)	0.73±12.36	−19.51±12.43	−10.07±8.76
(1.50,2.00)	1.23±7.69	−2.72±9.52	−0.33±5.98
(2.00,2.50)	14.20±10.80	−5.61±11.07	4.54±7.73
(2.50,3.00)	−12.01±10.28	18.50±11.46	1.60±7.65
(3.00,3.50)	−18.22±12.67	9.69±13.97	−5.63±9.38
(3.50,5.00)	13.81±13.74	1.95±15.86	8.73±10.39
Gap3 (10^{-2})			
(1.25,1.50)	−18.15±11.05	−7.02±13.80	−13.80±8.63
(1.50,2.00)	18.83±8.35	2.64±8.64	11.01±6.01
(2.00,2.50)	7.88±9.72	−27.68±12.12	−6.05±7.58
(2.50,3.00)	6.45±10.03	−3.32±11.54	2.25±7.57
(3.00,3.50)	6.33±12.31	−8.81±14.18	−0.18±9.29
(3.50,5.00)	14.01±14.14	−12.41±15.27	1.81±10.38

Table 14: p_T dependence of physics asymmetries A_N^B (blue beam), A_N^Y (yellow beam) and A_N (combined). The physics asymmetries were obtained by using Eq. 8 and 9 with $A_N(\text{Inclusive}) = A_N(\text{Gap4})$ and $A_N(\text{Background}) = A_N(\text{Gap3})$. (–) charge

p_T	Forward (10^{-2})		
	A_N^B	A_N^Y	A_N
(1.25,1.50)	-0.73 ± 12.36	-19.51 ± 12.43	-10.07 ± 8.76
(1.50,2.00)	1.23 ± 7.69	-2.72 ± 9.52	-0.33 ± 5.98
(2.00,2.50)	14.20 ± 10.80	-5.61 ± 11.07	4.54 ± 7.73
(2.50,3.00)	-12.01 ± 10.28	18.50 ± 11.46	1.60 ± 7.65
(3.00,3.50)	-18.22 ± 12.67	9.69 ± 13.97	-5.63 ± 9.38
(3.50,5.00)	13.81 ± 13.74	1.95 ± 15.86	8.73 ± 10.39
Backward (10^{-2})			
(1.25,1.50)	-18.15 ± 11.05	-7.02 ± 13.80	-13.80 ± 8.63
(1.50,2.00)	18.83 ± 8.35	2.64 ± 8.64	11.01 ± 6.01
(2.00,2.50)	7.88 ± 9.72	-27.68 ± 12.12	-6.05 ± 7.58
(2.50,3.00)	6.45 ± 10.03	-3.32 ± 11.54	2.25 ± 7.57
(3.00,3.50)	6.33 ± 12.31	-8.81 ± 14.18	-0.18 ± 9.29
(3.50,5.00)	14.01 ± 14.14	-12.41 ± 15.27	1.81 ± 10.38

(+) Charge

The asymmetries (blue beam, yellow beam and combined) at backward rapidity for Gap3 (background) and Gap4 (inclusive) are listed in Table 16. The physics asymmetries listed in the table 17 were calculated by using the Eq. 8, 9, and Table 4. The asymmetries (blue beam, yellow beam and combined) at forward rapidity for Gap3 (background) and Gap4 (inclusive) are listed in table 12.

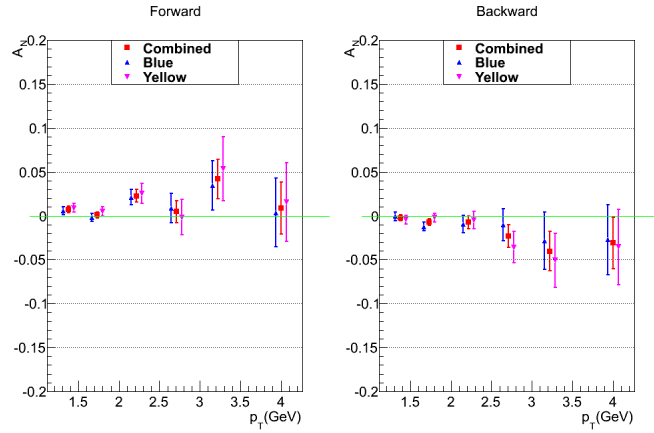


Figure 27: p_T dependence of asymmetries for inclusive muons (Gap4) in the forward (left) and backward (right) rapidity. (+) charge

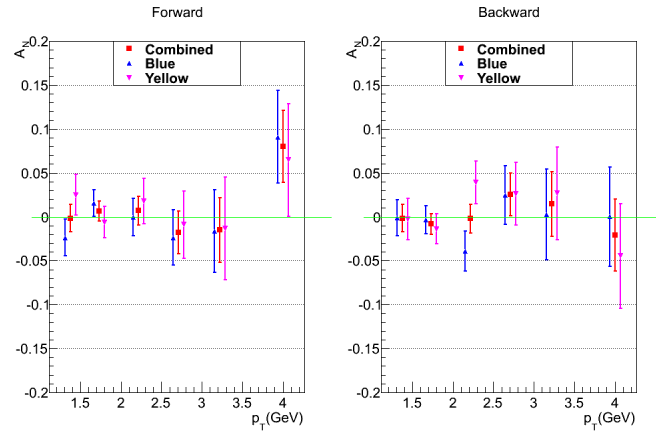


Figure 28: p_T dependence of asymmetries for hadrons background (Gap3) in the forward (left) and backward (right) rapidity. (+) charge

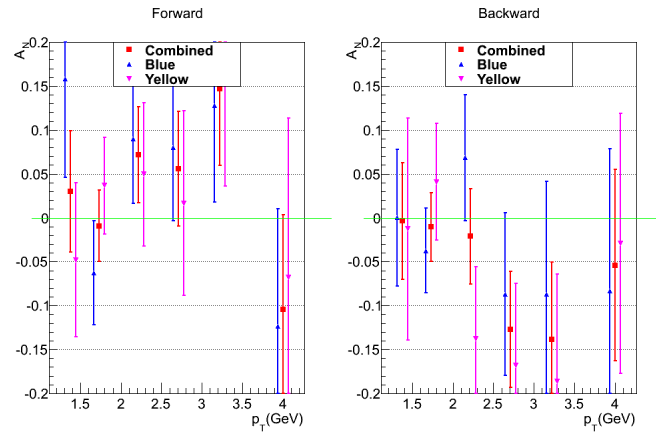


Figure 29: p_T dependence of physics asymmetries in the forward (left) and backward (right) rapidity, obtained by using Eq. 8 and 9 with $A_N(\text{Inclusive}) = A_N(\text{Gap4})$ and $A_N(\text{Background}) = A_N(\text{Gap3})$. (+) charge

Table 15: p_T dependence of A_N^B (blue beam), A_N^Y (yellow beam) and A_N (combined) in forward rapidity. (+) charge

p_T	Gap4 (10^{-2})		
	A_N^B	A_N^Y	A_N
(1.25,1.50)	0.57 ± 0.47	0.91 ± 0.53	0.72 ± 0.35
(1.50,2.00)	-0.17 ± 0.46	0.49 ± 0.56	0.09 ± 0.35
(2.00,2.50)	2.11 ± 0.90	2.53 ± 1.12	2.27 ± 0.70
(2.50,3.00)	0.87 ± 1.64	-0.17 ± 2.03	0.46 ± 1.27
(3.00,3.50)	3.47 ± 2.81	5.37 ± 3.64	4.18 ± 2.22
(3.50,5.00)	0.37 ± 3.90	1.55 ± 4.45	0.88 ± 2.93
Gap3 (10^{-2})			
(1.25,1.50)	-2.37 ± 2.11	2.49 ± 2.32	-0.17 ± 1.56
(1.50,2.00)	1.53 ± 1.52	-0.61 ± 1.80	0.64 ± 1.16
(2.00,2.50)	-0.05 ± 2.14	1.79 ± 2.60	0.69 ± 1.65
(2.50,3.00)	-2.39 ± 3.15	-0.91 ± 3.80	-1.79 ± 2.43
(3.00,3.50)	-1.63 ± 4.69	-1.33 ± 5.84	-1.51 ± 3.66
(3.50,5.00)	9.11 ± 5.31	6.47 ± 6.43	8.04 ± 4.10

Table 16: p_T dependence of A_N^B (blue beam), A_N^Y (yellow beam) and A_N (combined) in backward rapidity. (+) charge

p_T (GeV/c)	Gap4 (10^{-2})		
	A_N^B	A_N^Y	A_N
(1.25,1.50)	-0.07 ± 0.48	-0.45 ± 0.51	-0.25 ± 0.35
(1.50,2.00)	-1.23 ± 0.50	-0.21 ± 0.50	-0.72 ± 0.36
(2.00,2.50)	-0.97 ± 1.00	-0.53 ± 0.99	-0.75 ± 0.70
(2.50,3.00)	-1.05 ± 1.82	-3.57 ± 1.81	-2.32 ± 1.28
(3.00,3.50)	-2.87 ± 3.25	-5.07 ± 3.09	-4.03 ± 2.24
(3.50,5.00)	-2.71 ± 4.00	-3.55 ± 4.28	-3.10 ± 2.92
Gap3 (10^{-2})			
(1.25,1.50)	-0.09 ± 2.06	-0.29 ± 2.36	-0.18 ± 1.55
(1.50,2.00)	-0.35 ± 1.58	-1.39 ± 1.71	-0.83 ± 1.16
(2.00,2.50)	-3.91 ± 2.28	3.91 ± 2.40	-0.21 ± 1.65
(2.50,3.00)	2.47 ± 3.33	2.61 ± 3.57	2.53 ± 2.43
(3.00,3.50)	0.27 ± 5.14	2.69 ± 5.28	1.45 ± 3.68
(3.50,5.00)	0.01 ± 5.63	-4.47 ± 5.97	-2.10 ± 4.10

Table 17: p_T dependence of physics A_N^B (blue beam), A_N^Y (yellow beam) and A_N (combined). The physics asymmetries were obtained by using Eq. 8 and 9 with $A_N(\text{Inclusive}) = A_N(\text{Gap4})$ and $A_N(\text{Background}) = A_N(\text{Gap3})$. (+) charge

p_T	Forward (10^{-2})		
	A_N^B	A_N^Y	A_N
(1.25,1.50)	15.84 ± 11.29	-4.79 ± 8.78	2.99 ± 6.93
(1.50,2.00)	-6.28 ± 5.94	3.65 ± 5.49	-0.92 ± 4.03
(2.00,2.50)	9.00 ± 7.34	4.96 ± 8.17	7.20 ± 5.46
(2.50,3.00)	8.02 ± 8.36	1.67 ± 10.49	5.55 ± 6.54
(3.00,3.50)	12.79 ± 11.00	18.01 ± 14.41	14.71 ± 8.74
(3.50,5.00)	-12.36 ± 13.38	-6.80 ± 18.17	-10.40 ± 10.77
Backward (10^{-2})			
(1.25,1.50)	0.00 ± 7.80	-1.28 ± 12.61	-0.35 ± 6.63
(1.50,2.00)	-3.73 ± 4.84	4.08 ± 6.65	-1.03 ± 3.91
(2.00,2.50)	6.85 ± 7.20	-13.78 ± 8.22	-2.10 ± 5.41
(2.50,3.00)	-8.69 ± 9.27	-16.84 ± 9.39	-12.71 ± 6.60
(3.00,3.50)	-8.67 ± 12.79	-18.64 ± 12.25	-13.87 ± 8.85
(3.50,5.00)	-8.32 ± 16.15	-2.92 ± 14.82	-5.39 ± 10.92

3.2.4 A_N vs. x_F

The single spin asymmetry has also been studied in four x_F ($-0.2 < x_F < 0.2$) bins. Figures 30, 31, and 32 (for $(-)$ charge) and Figures 33, 34, and 35 (for $(+)$ charge), show the x_F dependence of asymmetries at Gap4 (inclusive asymmetries), Gap3 (background asymmetries), and physics asymmetries respectively. The physics asymmetries listed in Table 18 $((-)$ charge) and 20 $((+)$ charge) were calculated by using Eq. 8, 9 and Table 3.

$(-)$ charge

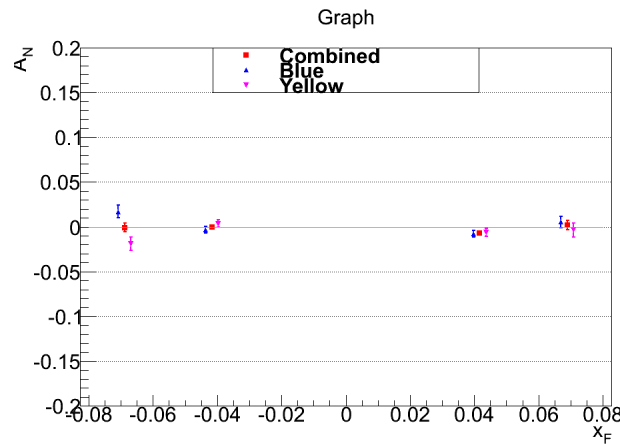


Figure 30: x_F dependence of asymmetries for inclusive muons (Gap4). $(-)$ charge

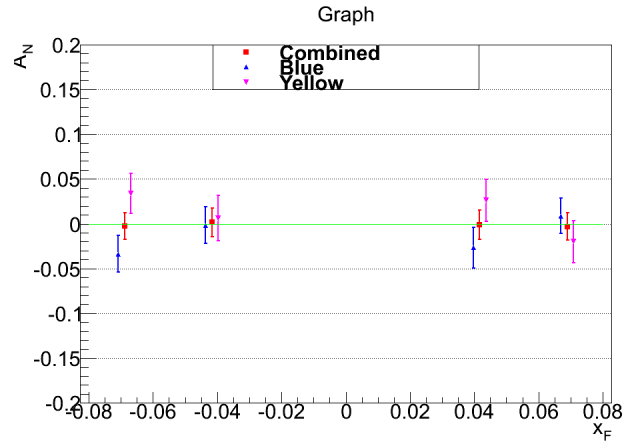


Figure 31: x_F dependence of asymmetries for hadron background (Gap3). (–) charge

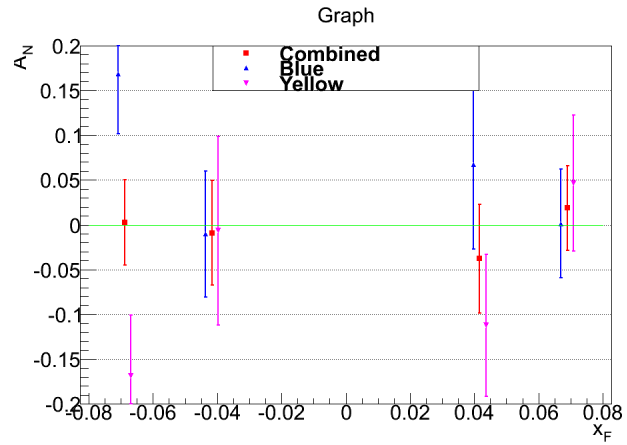


Figure 32: x_F dependence of physics asymmetries, obtained by using Eqs. 8 and 9 with $A_N(\text{Inclusive}) = A_N(\text{Gap4})$ and $A_N(\text{Background}) = A_N(\text{Gap23})$. (–) charge

Table 18: x_F dependence of A_N^B (blue beam), A_N^Y (yellow beam) and A_N (combined).

(-) charge

		Gap4 (10^{-2})		
x_F		A_N^B	A_N^Y	A_N
(-0.20,-0.05)		1.71 ± 0.72	-1.89 ± 0.72	-0.08 ± 0.51
(-0.05,0.00)		-0.35 ± 0.37	0.37 ± 0.40	-0.02 ± 0.27
(0.00,0.05)		-0.81 ± 0.36	-0.63 ± 0.41	-0.73 ± 0.27
(0.05,0.20)		0.53 ± 0.65	-0.37 ± 0.80	0.17 ± 0.51
		Gap3 (10^{-2})		
(-0.20,-0.05)		-3.35 ± 2.05	3.41 ± 2.23	-0.25 ± 1.51
(-0.05,0.00)		-0.15 ± 2.08	0.63 ± 2.54	0.16 ± 1.61
(0.00,0.05)		-2.65 ± 2.27	2.61 ± 2.34	-0.10 ± 1.63
(0.05,0.20)		0.87 ± 1.98	-1.99 ± 2.36	-0.31 ± 1.51

Table 19: x_F dependence of Physics A_N^B (blue beam), A_N^Y (yellow beam) and A_N (combined). The physics asymmetries were obtained by using Eq. 8 and 9 with $A_N(\text{Inclusive}) = A_N(\text{Gap4})$ and $A_N(\text{Background}) = A_N(\text{Gap3})$. (–) charge

x_F	$A_N^B(10^{-2})$	$A_N^Y(10^{-2})$	$A_N(10^{-2})$
(–0.20,–0.05)	16.83 ± 6.66	-16.88 ± 6.78	0.27 ± 4.75
(–0.05,0.00)	-1.02 ± 7.02	-0.65 ± 10.55	-0.91 ± 5.84
(0.00,0.05)	6.74 ± 9.43	-11.22 ± 7.92	-3.79 ± 6.06
(0.05,0.20)	0.15 ± 6.03	4.66 ± 7.61	1.89 ± 4.73

(+) Charge

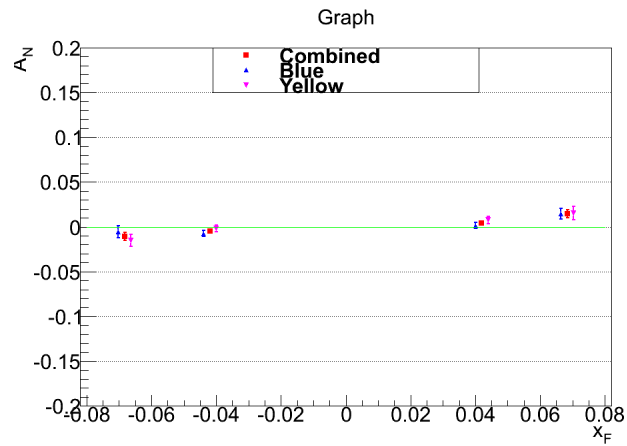


Figure 33: x_F dependence of asymmetries for inclusive muons (Gap4). (+) charge

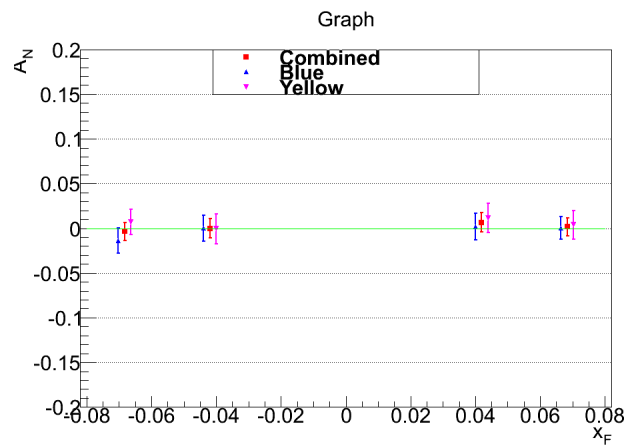


Figure 34: x_F dependence of asymmetries for hadron background (Gap3). (+) charge

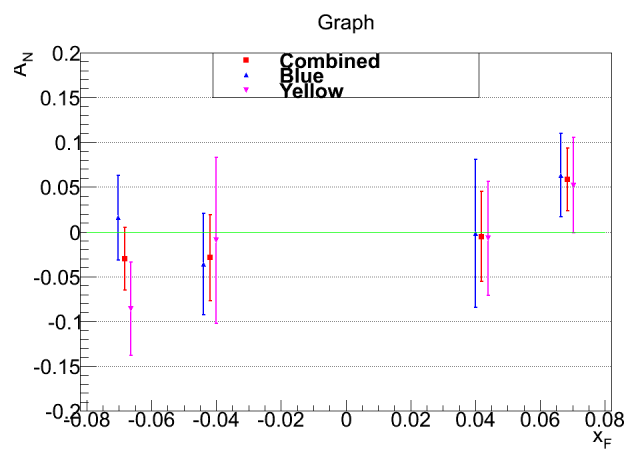


Figure 35: x_F dependence of physics asymmetries, obtained by using Eq. 8 and 9 with $A_N(\text{Inclusive}) = A_N(\text{Gap4})$ and $A_N(\text{Background}) = A_N(\text{Gap3})$. (+) charge

Table 20: x_F dependence of A_N^B (blue beam), A_N^Y (yellow beam) and A_N (combined).

(+) charge

x_F	Gap4 (10^{-2})		
	A_N^B	A_N^Y	A_N
(-0.20,-0.05)	-0.57±0.66	-1.53±0.65	-1.06±0.46
(-0.05,0.00)	-0.75±0.36	-0.19±0.38	-0.48±0.26
(0.00,0.05)	0.13±0.35	0.75±0.40	0.39±0.26
(0.05,0.20)	1.45±0.59	1.51±0.74	1.47±0.46
Gap3 (10^{-2})			
(-0.20,-0.05)	-1.37±1.42	0.71±1.44	-0.35±1.01
(-0.05,0.00)	0.01±1.43	-0.05±1.67	-0.02±1.09
(0.00,0.05)	0.21±1.49	1.17±1.62	0.65±1.10
(0.05,0.20)	0.05±1.28	0.39±1.62	0.18±1.01

Table 21: x_F dependence of Physics A_N^B (blue beam), A_N^Y (yellow beam) and A_N (combined). The physics asymmetries were obtained by using Eq. 8 and 9 with $A_N(\text{Inclusive}) = A_N(\text{Gap4})$ and $A_N(\text{Background}) = A_N(\text{Gap3})$. (+) charge

x_F	$A_N^B(10^{-2})$	$A_N^Y(10^{-2})$	$A_N(10^{-2})$
(-0.20,-0.05)	1.57 ± 4.70	-8.59 ± 5.18	-3.02 ± 3.48
(-0.05,0.00)	-3.62 ± 5.64	-0.94 ± 9.27	-2.90 ± 4.82
(0.00,0.05)	-0.19 ± 8.28	-0.72 ± 6.36	-0.52 ± 5.05
(0.05,0.20)	6.32 ± 4.63	5.19 ± 5.34	5.83 ± 3.50

3.2.5 Systematic Uncertainty

The systematic uncertainty is determined from the variation of A_N^{HF} corresponding to the upper and lower limit of each background source. Additional systematic uncertainty is determined from the comparison between two A_N^{HF} calculation methods. The final systematic uncertainty is calculated as a quadratic sum of all systematic uncertainties. The systematic bias has been checked with the bunch shuffling technique already in a previous analysis note [95]. The sources of systematic uncertainty are listed below, shown in Tables 22, 23, 24, and 25.

Table 22: Sources of $\delta A_N^{syst.}$ for μ^- as a function of p_T .

p_T bin	δf_h	$\delta A_N^{h \rightarrow \mu}$	$\delta A_N^{J/\psi \rightarrow \mu}$	δA_N^{method}
$\delta A_N^{syst.} (10^{-2})$ Forward ($x_F > 0$)				
(1.25,1.50)	+3.56 -8.96	+2.96 -2.96	+0.05 -0.04	+0.81 -0.81
(1.50,2.00)	+0.29 -0.06	+2.64 -2.64	+0.13 -0.10	+0.37 -0.37
(2.00,2.50)	+2.37 -1.20	+2.30 -2.30	+0.35 -0.26	+0.59 -0.59
(2.50,3.00)	+0.43 -0.40	+1.40 -1.40	+0.46 -0.35	+0.69 -0.69
(3.00,3.50)	+0.75 -1.06	+1.02 -1.02	+0.54 -0.41	+0.05 -0.05
(3.50,5.00)	+1.78 -1.38	+0.87 -0.87	+0.68 -0.52	+1.85 -1.85
$\delta A_N^{syst.} (10^{-2})$ Backward ($x_F < 0$)				
(1.25,1.50)	+5.37 -14.27	+2.95 -2.95	+0.04 -0.04	+0.32 -0.32
(1.50,2.00)	+7.92 -3.82	+2.67 -2.67	+0.11 -0.11	+0.69 -0.69
(2.00,2.50)	+2.24 -4.44	+2.26 -2.26	+0.30 -0.30	+1.04 -1.04
(2.50,3.00)	+0.87 -0.62	+1.39 -1.39	+0.40 -0.39	+1.00 -1.00
(3.00,3.50)	+0.28 -0.43	+1.01 -1.01	+0.47 -0.46	+0.76 -0.76
(3.50,5.00)	+0.13 -0.18	+0.87 -0.87	+0.60 -0.59	+0.74 -0.74

Table 23: Sources of $\delta A_N^{syst.}$ for μ^+ as a function of p_T .

p_T bin	δf_h	$\delta A_N^{h \rightarrow \mu}$	$\delta A_N^{J/\psi \rightarrow \mu}$	δA_N^{method}
$\delta A_N^{syst.} (10^{-2})$ Forward ($x_F > 0$)				
(1.25,1.50)	+0.71 -0.85	+3.37 -3.37	+0.05 -0.03	+0.70 -0.70
(1.50,2.00)	+0.39 -0.66	+2.55 -2.55	+0.10 -0.08	+0.11 -0.11
(2.00,2.50)	+2.81 -1.47	+2.28 -2.28	+0.27 -0.21	+0.26 -0.26
(2.50,3.00)	+2.13 -1.36	+1.67 -1.67	+0.38 -0.29	+0.57 -0.57
(3.00,3.50)	+3.49 -2.47	+1.33 -1.33	+0.45 -0.34	+0.69 -0.69
(3.50,5.00)	+3.11 -4.33	+1.31 -1.31	+0.56 -0.43	+0.79 -0.79
$\delta A_N^{syst.} (10^{-2})$ Backward ($x_F < 0$)				
(1.25,1.50)	+0.05 -0.06	+3.25 -3.25	+0.04 -0.04	+0.13 -0.13
(1.50,2.00)	+0.09 -0.34	+2.47 -2.47	+0.09 -0.08	+0.27 -0.27
(2.00,2.50)	+0.47 -1.07	+2.25 -2.25	+0.24 -0.23	+1.06 -1.06
(2.50,3.00)	+2.91 -4.57	+1.68 -1.68	+0.34 -0.33	+0.59 -0.59
(3.00,3.50)	+2.74 -4.13	+1.33 -1.33	+0.40 -0.39	+1.18 -1.18
(3.50,5.00)	+0.37 -0.39	+1.34 -1.34	+0.50 -0.49	+0.52 -0.52

Table 24: Sources of $\delta A_N^{syst.}$ for μ^- as a function of x_F .

x_F bin	δf_h	$\delta A_N^{J/\psi \rightarrow \mu}$	δA_N^{method}
(-0.20,-0.05)	$^{+0.32}_{-1.21} \times 10^{-2}$	$^{+0.48}_{-0.46} \times 10^{-2}$	$^{+0.30}_{-0.30} \times 10^{-2}$
(-0.05,0.00)	$^{+0.31}_{-0.83} \times 10^{-2}$	$^{+0.13}_{-0.12} \times 10^{-2}$	$^{+0.45}_{-0.45} \times 10^{-2}$
(0.00,0.05)	$^{+0.77}_{-1.33} \times 10^{-2}$	$^{+0.14}_{-0.11} \times 10^{-2}$	$^{+0.68}_{-0.68} \times 10^{-2}$
(0.05,0.20)	$^{+0.54}_{-0.38} \times 10^{-2}$	$^{+0.54}_{-0.41} \times 10^{-2}$	$^{+0.48}_{-0.48} \times 10^{-2}$

 Table 25: Sources of $\delta A_N^{syst.}$ for μ^+ as a function of x_F .

x_F bin	δf_h	$\delta A_N^{J/\psi \rightarrow \mu}$	δA_N^{method}
(-0.20,-0.05)	$^{+0.64}_{-1.26} \times 10^{-2}$	$^{+0.40}_{-0.38} \times 10^{-2}$	$^{+0.57}_{-0.57} \times 10^{-2}$
(-0.05,0.00)	$^{+0.88}_{-2.59} \times 10^{-2}$	$^{+0.10}_{-0.10} \times 10^{-2}$	$^{+0.17}_{-0.17} \times 10^{-2}$
(0.00,0.05)	$^{+0.42}_{-1.29} \times 10^{-2}$	$^{+0.11}_{-0.09} \times 10^{-2}$	$^{+0.29}_{-0.29} \times 10^{-2}$
(0.05,0.20)	$^{+2.25}_{-1.21} \times 10^{-2}$	$^{+0.45}_{-0.34} \times 10^{-2}$	$^{+0.46}_{-0.46} \times 10^{-2}$

δf_h Fraction of Light Hadron Background The systematic uncertainty on the fraction of light hadron background (δf_h) is an important source of systematic uncertainty on the A_N^{HF} . The upper and lower limits of A_N^{HF} are calculated using Eq. 8 with the upper and lower limits of the fraction of light hadron background ($f_h \pm \delta f_h$).

$\delta A_N^{h \rightarrow \mu}$ Difference in Gap3, Gap4 Background Asymmetry The asymmetry of light hadron background at MuID Gap4 (A_N^h) is estimated by using stopped hadrons at MuID Gap3. Since the background tracks at MuID Gap4 include decay muons and punch-through hadrons, the A_N of stopped hadrons can be different from the A_N of decay muons due to decay kinematics. In order to quantify the difference between A_N of tracks at MuID Gap3 and Gap4, a toy simulation using the hadron cocktail method and an input truth asymmetry (A_N^{true}) is performed. The A_N^{true} is taken as $0.02 \times p_T$ at $p_T < 5 \text{ GeV}/c$ and 0.1 at $p_T > 5 \text{ GeV}/c$ based on the most extreme cases of A_N^h measured at MuID Gap3 in Figs. 25 and 28. The systematic uncertainty is obtained from the difference between the mean value of Gap4 and Gap3 reconstructed asymmetries in Fig. 36, The detailed procedure is as follows:

1. Generate random spin direction (\uparrow, \downarrow) for all tracks.
2. Apply a weight $(1 \pm A_N^{true} \cdot \cos(\phi_0))$ for each track based on the manually assigned initial asymmetry (A_N^{true}). The sign is determined with the random

spin direction in step 1, and ϕ_0 is the azimuthal angle of the original particle at the collision z -vertex.

3. Extract A_N^{reco} of the tracks at MuID Gap3 and Gap4 with the azimuthal angle and momentum information at the reconstruction level.
4. Repeat 10000 times from step 1 to 3 to obtain smooth distributions of A_N^{reco} .

The largest difference between A_N^{reco} at MuID Gap3 and Gap4 in the entire p_T range is 0.008, so ± 0.008 is assigned to the systematic uncertainty. In the case of A_N^h in x_F bins, the difference of A_N^{reco} at MuID Gap3 and Gap4 is quite small, because only 2 bins are used in x_F . Therefore, the uncertainty on $A_N^h(x_F)$ is negligible.

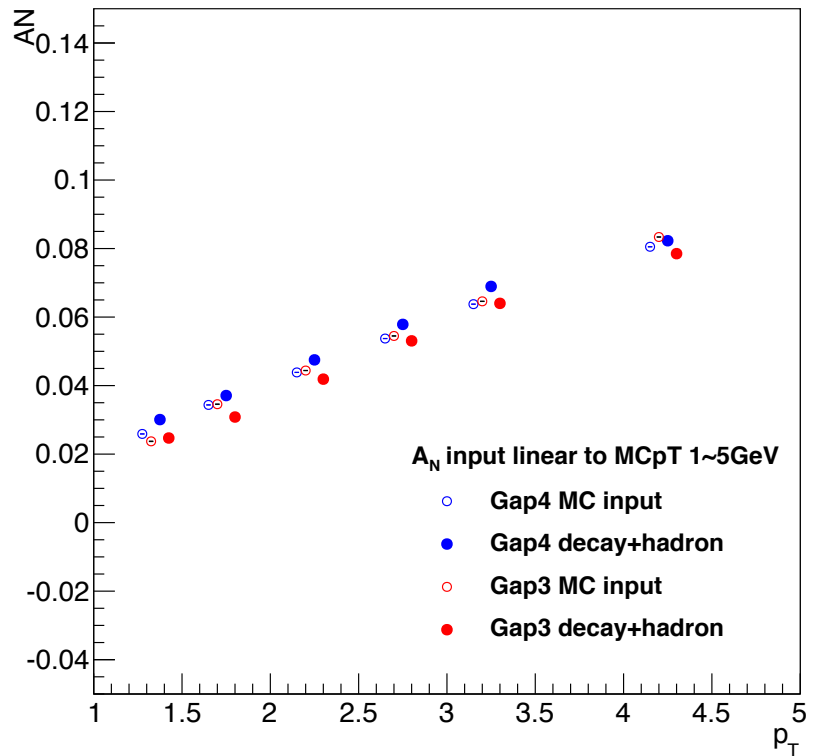


Figure 36: The Monte Carlo simulation test with $MCp_T \times 2\%$ ($p_T < 5$ GeV/c), 10% for $MCp_T > 5$ GeV/c for injected (open circles) and reconstructed (filled circles) asymmetries of Gap4 (blue) and Gap3 (red).

$\delta A_N^{J/\psi \rightarrow \mu}$, **Uncertainty in $A_N^{J/\psi \rightarrow \mu}$**

The systematic uncertainty from $A_N^{J/\psi \rightarrow \mu}$ is determined from the $J/\psi \rightarrow \mu$ simulation with the upper and lower limits of $A_N^{J/\psi}$ as given in [70]. A similar procedure for $\delta A_N^{h \rightarrow \mu}$ was used with a dimuon simulation, while $\delta A_N^{h \rightarrow \mu}$ was calculated with hadron simulation. $A_N^{J/\psi}$ in [70] is -0.002 ± 0.026 at $x_F < 0$, and -0.026 ± 0.026 at $x_F > 0$. The upper and lower limits of A_N^{HF} are calculated using Eq. 8 with the upper and lower limits of the $A_N^{J/\psi \rightarrow \mu}$. The initial p_T and rapidity distributions of J/ψ are from [93]. The obtained $A_N^{J/\psi \rightarrow \mu}$ is $-0.002^{+0.018}_{-0.022}$ at $x_F < 0$ and $-0.019^{+0.019}_{-0.025}$ at $x_F > 0$. Figure 37 shows an example of a fit of the cosine modulation generated by $A_N^{J/\psi}$. The lower side of Fig. 38 shows the distribution of $A_N^{J/\psi \rightarrow \mu}$ 1000 simulated runs using six input $A_N^{J/\psi}$'s (upper side).

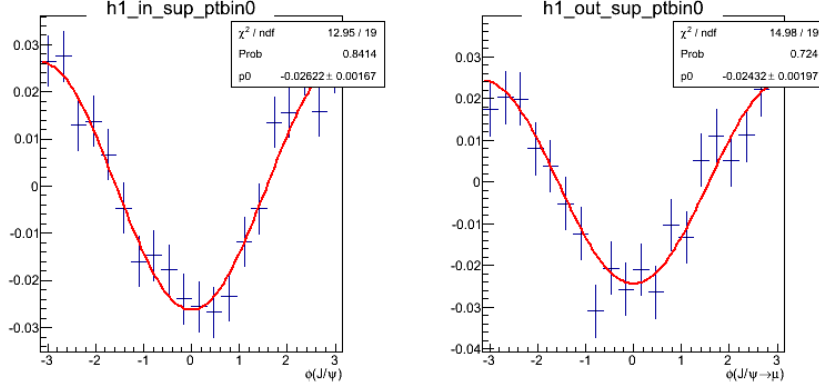


Figure 37: Example of a fit of the cosine modulation induced by $A_N^{J/\psi}$. On the left is shown the input $A_N(J/\psi)$, where the fit result shows good agreement with input value(-0.026), justifying the procedure and fit. The right plot shows the asymmetry for the output muon, which is different from the input $A_N^{J/\psi}$.

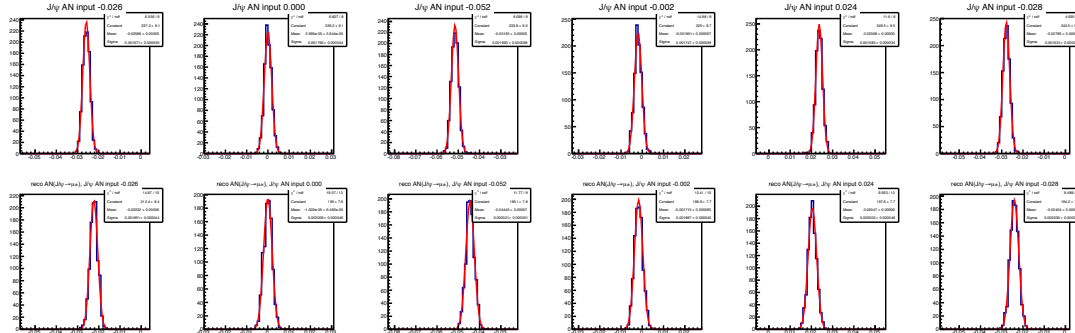


Figure 38: $A_N^{J/\psi \rightarrow \mu}$ distribution (lower side) from simulated runs using six input $A_N^{J/\psi}$'s (upper side).

δA_N^{method} , Comparison with Cosine Fit Method

The A_N^{incl} results with the maximum likelihood method are compared with another method described below. The systematic uncertainty on A_N^{HF} is evaluated by propagating variations of A_N^{incl} and A_N^h between the two methods. The difference of two methods with inclusive tracks at MuID Gap4 is used for both A_N^{incl} and A_N^h variations. The $A_N(\phi)$ of inclusive tracks for each p_T or x_F bin is calculated as,

$$\begin{aligned} A_N(\phi) &= \frac{\sigma^{\uparrow\uparrow}(\phi) + \sigma^{\uparrow\downarrow}(\phi) - \sigma^{\downarrow\uparrow}(\phi) - \sigma^{\downarrow\downarrow}(\phi)}{\sigma^{\uparrow\uparrow}(\phi) + \sigma^{\uparrow\downarrow}(\phi) + \sigma^{\downarrow\uparrow}(\phi) + \sigma^{\downarrow\downarrow}(\phi)} \\ &= \frac{1}{P} \cdot \frac{N^{\uparrow\uparrow}(\phi) + R_1 \cdot N^{\uparrow\downarrow}(\phi) - R_2 \cdot N^{\downarrow\uparrow} - R_3 \cdot N^{\downarrow\downarrow}}{N^{\uparrow\uparrow}(\phi) + R_1 \cdot N^{\uparrow\downarrow}(\phi) + R_2 \cdot N^{\downarrow\uparrow} + R_3 \cdot N^{\downarrow\downarrow}}, \end{aligned} \quad (10)$$

where P is the average beam polarization, $\sigma^{\uparrow\uparrow}$, $\sigma^{\uparrow\downarrow}$, $\sigma^{\downarrow\uparrow}$, and $\sigma^{\downarrow\downarrow}$ are cross sections for each polarization combination of the two beams, $L^{\uparrow\uparrow}$, $L^{\uparrow\downarrow}$, $L^{\downarrow\uparrow}$, and $L^{\downarrow\downarrow}$ are relative luminosities for each polarization combination, and $R_1 = L^{\uparrow\uparrow}/L^{\uparrow\downarrow}$, $R_2 = L^{\uparrow\uparrow}/L^{\downarrow\uparrow}$, and $R_3 = L^{\uparrow\uparrow}/L^{\downarrow\downarrow}$. A_N^{incl} is calculated by fitting the $A_N(\phi)$ distribution with a function of the form $\pm A_N \cdot \cos(\phi)$, where \pm depends on beam direction. Figs. 39, 40, 41, and 42 represent cosine fits of Gap4 inclusive tracks. Fit results are compared with the Maximum Likelihood method in Figs. 43, 44, 45, and 46 with χ^2/ndf from the fit results smaller than 2.

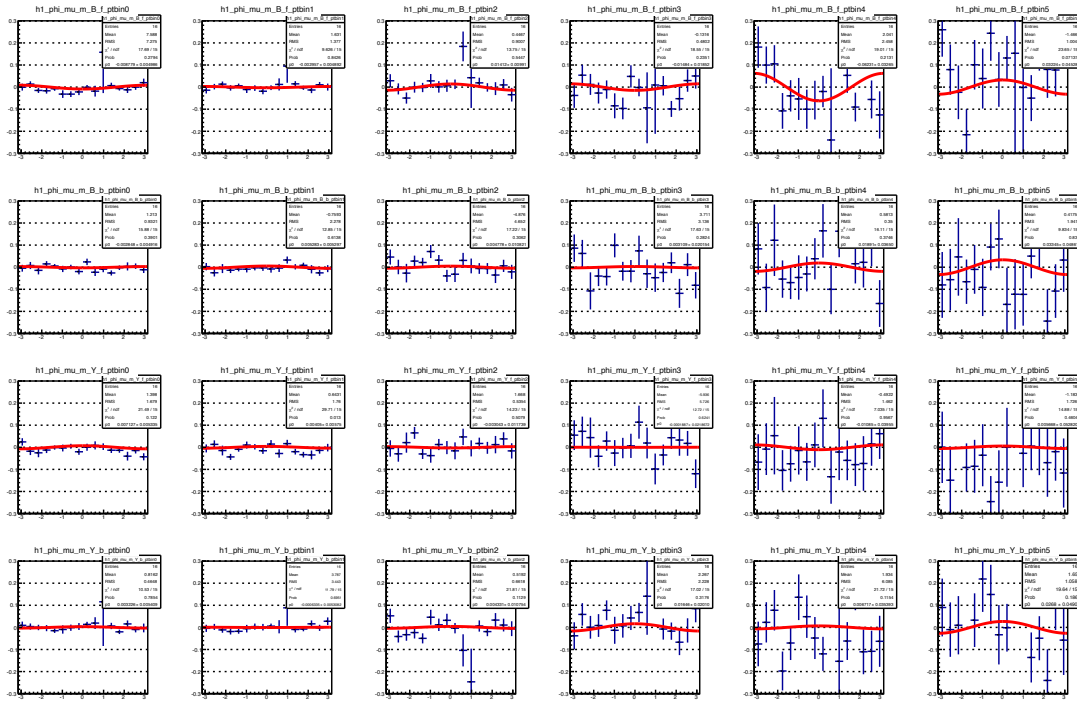


Figure 39: Cosine fit result of Gap4 inclusive tracks for 6 p_T bins, (–) charge.

Rows correspond to (1) blue beam $x_F > 0$, (2) blue beam $x_F < 0$, (3) yellow beam $x_F > 0$, and (4) yellow beam $x_F < 0$.

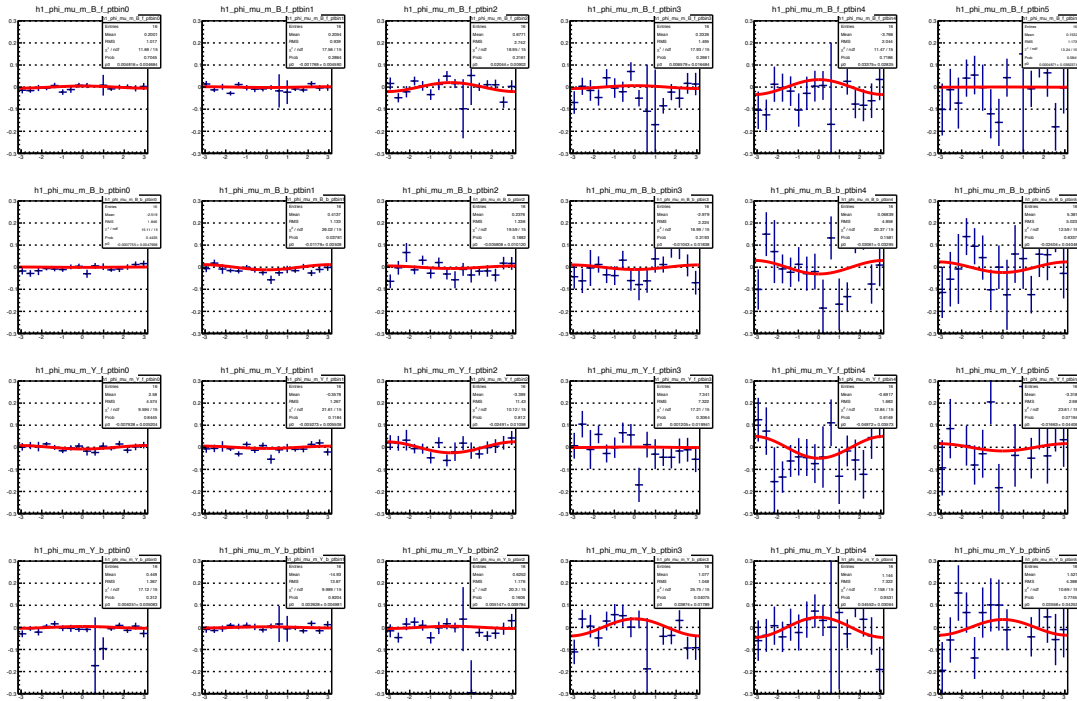


Figure 40: Cosine fit result of Gap4 inclusive tracks for 6 p_T bins, (+) charge.

Rows correspond to (1) blue beam $x_F > 0$, (2) blue beam $x_F < 0$, (3) yellow beam $x_F > 0$, and (4) yellow beam $x_F < 0$.

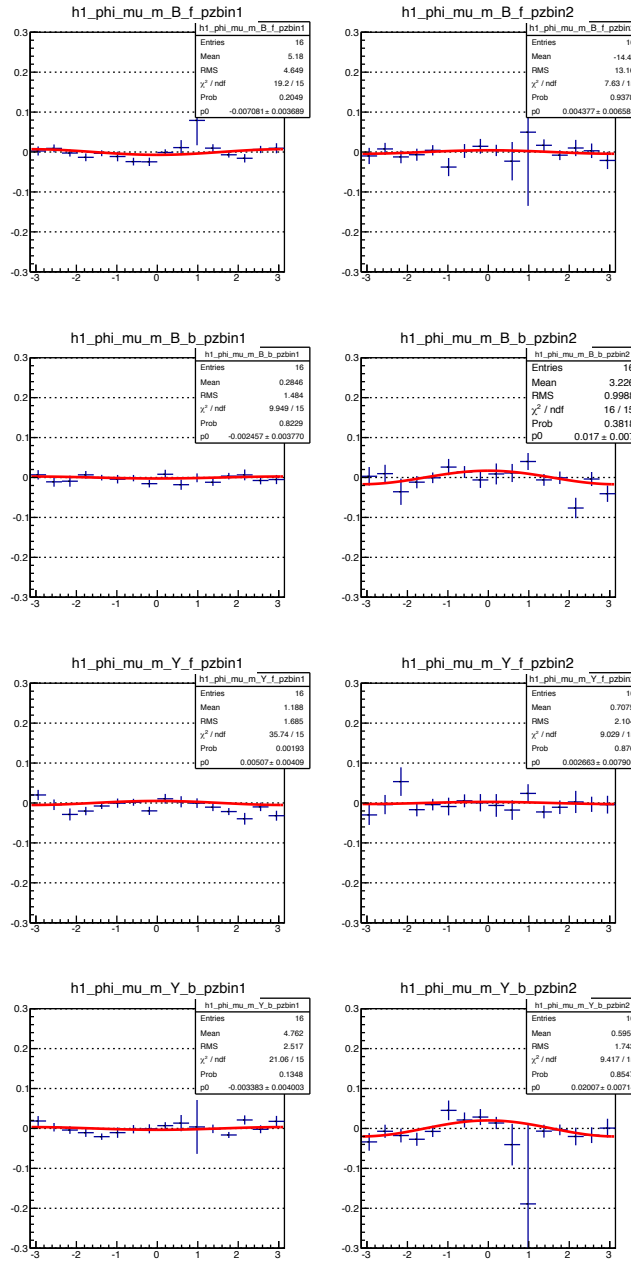


Figure 41: Cosine fit result of Gap4 inclusive tracks for two p_z bins (4 x_F bins), (–) charge. Rows correspond to (1) blue beam $x_F > 0$, (2) blue beam $x_F < 0$, (3) yellow beam $x_F > 0$, and (4) yellow beam $x_F < 0$.

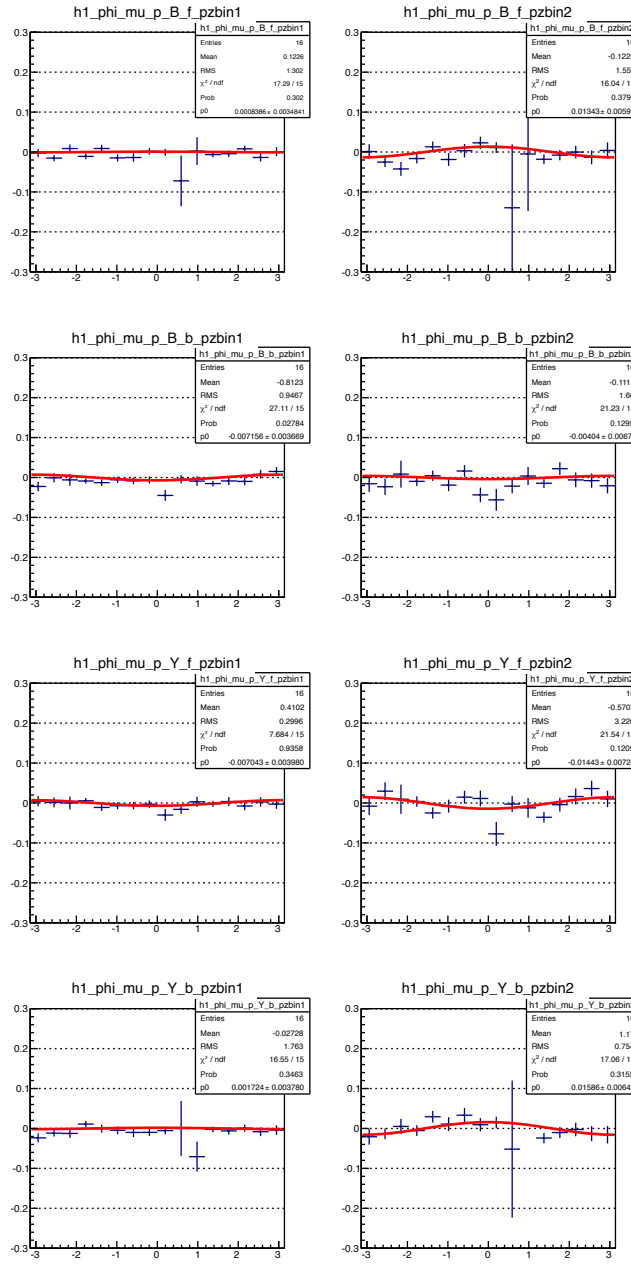


Figure 42: Cosine fit result of Gap4 inclusive tracks for 2 p_z bins (4 x_F bins), (+)

charge. Rows correspond to (1) blue beam $x_F > 0$, (2) blue beam $x_F < 0$, (3) yellow beam $x_F > 0$, and (4) yellow beam $x_F < 0$.

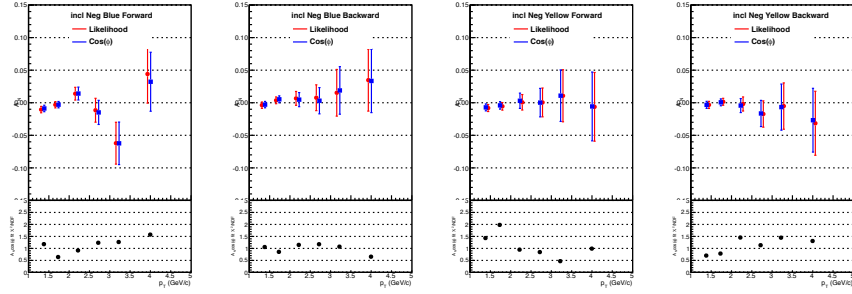


Figure 43: Comparison between the cosine fit results (blue) and the likelihood result (red) of Gap4 inclusive tracks for 6 p_T bins, $(-)$ charge. The lower plots represent the χ^2/ndf in cosine fit, smaller than 2

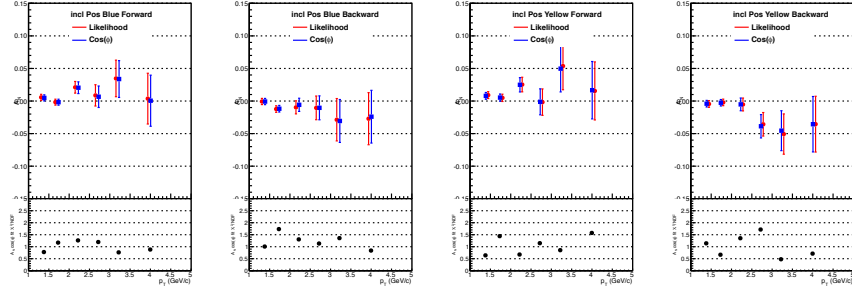


Figure 44: Comparison between the cosine fit results (blue) and the likelihood result (red) of Gap4 inclusive tracks for 6 p_T bins, $(+)$ charge. The lower plots represent the χ^2/ndf in cosine fit, smaller than 2

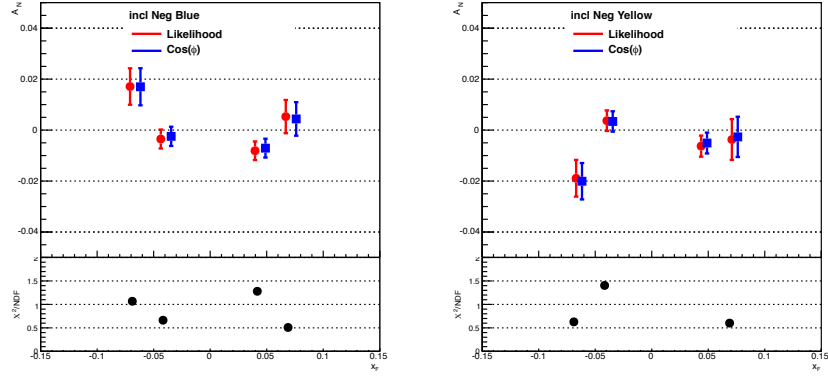


Figure 45: Comparison between the cosine fit results (blue) and the likelihood result (red) of Gap4 inclusive tracks for 4 x_F bins, $(-)$ charge. The lower plots represent the χ^2/ndf in cosine fit, smaller than 2

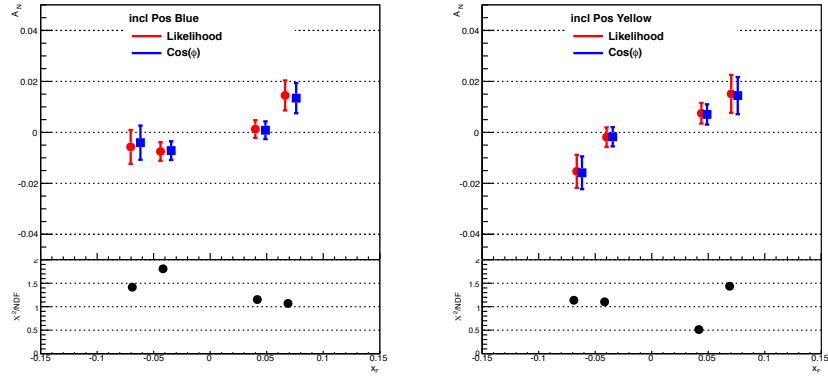


Figure 46: Comparison between the cosine fit results (blue) and the likelihood result (red) of Gap4 inclusive tracks for 4 x_F bins, $(+)$ charge. The lower plots represent the χ^2/ndf in cosine fit, smaller than 2

3.3 Simulation to Convert Theory Calculations for A_N of D Meson into A_N of Muon

A recent theory incorporating the collinear factorization framework provides a calculation of A_N for the D meson (A_N^D), produced by the $gg \rightarrow c\bar{c}$ process, which is sensitive to the three-gluon correlation function that depends on the momentum fraction of the gluon (x) [5]. Two models including x or \sqrt{x} dependence in the three-gluon correlation function are introduced to compare their behavior in the small- x region and the overall A_N^D scale is determined by assuming $|A_N^D| \leq 0.05$ in $|x_F| < 0.1$ based on the previous PHENIX preliminary results for $A_N(J/\psi)$.

In order to compare with our results for A_N^μ , the decay kinematics and cross section of $D \rightarrow \mu$ from PYTHIA [96] have been used to convert A_N^D into A_N^μ . Theory calculations of x_F and p_T dependent A_N for D^0 , \bar{D}^0 , D^+ , and D^- at $-0.6 < x_F^D < 0.6$ (25 values; 0.05 interval) and $1 < p_T^D < 10$ GeV/c (10 values; 1,2,3,4,5,6,7,8,9,10) are used as input A_N^D , as shown in Figure 48. After obtaining smooth curves for 10 p_T values for the whole x_F range, the asymmetries $A_N(p_T^D, x_F^D)$ are extrapolated linearly to adjacent p_T values. The extrapolations look reasonable for all p_T and x_F bins in the region $|x_F| < 0.2$. A similar procedure to that described in the systematic uncertainty evaluation for $\delta A_N^{h \rightarrow \mu}$ is used, but the simulation does not have to be done multiple times because the PYTHIA simulation has enough statistics while the hadron simulation was statistically lim-

ited. A weight of $(1 \pm A_N^D(p_T^D, x_F^D) \cdot \cos(\phi^D))$ is applied to each muon from a D meson and the sign is determined with a random polarization direction (\uparrow, \downarrow). Then, A_N^μ is extracted by fitting the asymmetry of two polarization cases (\uparrow, \downarrow) with $A_N^\mu \cdot \cos(\phi^\mu)$ in p_T^μ and x_F^μ regions. Nine bins in the range $0.02 < |x_F^\mu| < 0.1$, 12 bins in $1.0 < p_T^\mu < 5.0 \text{ GeV}/c$ are used to get smooth curves. $A_N(p_T^\mu, x_F^\mu)$ is rounded to three decimal places and the fit error is about 0.001, negligible. Results from the simulation are listed on Tables 26, 27, and 28.

Figure 47 shows the p_T and $|x_F|$ distributions of D mesons which decay into muons in the kinematic range of this measurement ($1.25 < p_T^\mu < 5.0 \text{ GeV}/c$, $0.0 < |x_F^\mu| < 0.2$, and $1.4 < |y^\mu| < 2.0$). Accepted charm hadrons are composed of D^0 (18.7%), \bar{D}^0 (20.3%), D^+ (24.2%), D^- (26.1%), and small fraction of others (D_s^+ , D_s^- , and baryons). Since $A_N^{D^0}$ and $A_N^{D^+}$ ($A_N^{\bar{D}^0}$ and $A_N^{D^-}$) are very close in both models, the effect of different abundances of D mesons between data and PYTHIA is negligible. In addition, the modification of A_N due to decay kinematic smearing is quite small (< 5% relative difference between A_N^D and A_N^μ). One notes that muons from charm and bottom are combined in the data, and the contribution from bottom is about 2% (55%) at $p_T = 1 \text{ GeV}/c$ (5 GeV/c) according to a “Fixed Order + Next-to-Leading Log” (FONLL) perturbative QCD calculation [94]. Therefore, the charm contribution is expected to be dominant except for the last p_T bin of A_N^μ ($3.5 < p_T < 5 \text{ GeV}/c$). The converted A_N^μ are shown in Figs. 50, 51, and 52, and both calculations agree with the data within the

statistical uncertainties. The difference between the two models becomes larger with increasing $|x_F|$, but it is hard to distinguish a favored model with the current results at $|x_F| < 0.1$.

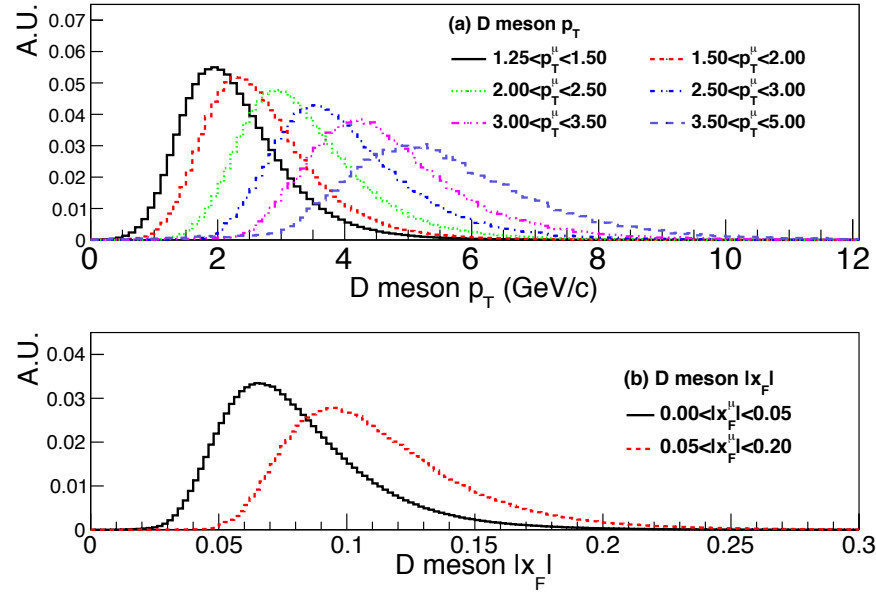


Figure 47: p_T (top) and $|x_F|$ (bottom) distributions of D mesons (D^0 , \bar{D}^0 , D^+ , and D^-) decaying into μ^\pm at $1.25 < p_T^\mu < 5.0$ GeV/ c , $|x_F^\mu| < 0.2$, and $1.4 < |y^\mu| < 2.0$, from PYTHIA. Each distribution is normalized to unity.

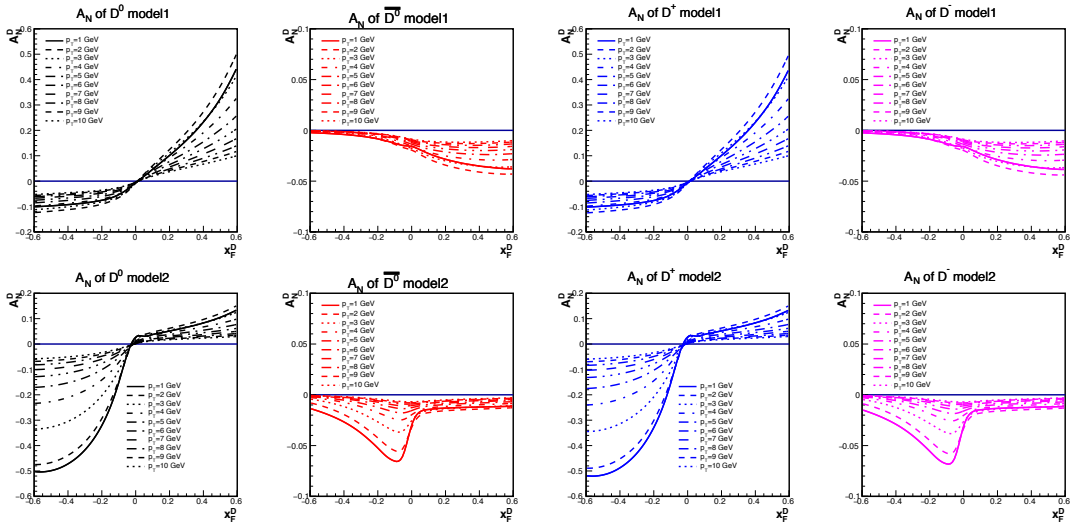


Figure 48: Theory calculations for $A_N^{D^0}$ and $A_N^{D^+}$ ($\bar{A}_N^{D^0}$ and $\bar{A}_N^{D^+}$) as a function of x_F ($-0.6 < x_F^D < 0.6$, for 25 x_F values; 0.05 interval) for $p_T = 1, 2, 3, 4, 5, 6, 7, 8, 9, 10$ GeV/c [5]

Table 26: Simulation results for A_N of μ^- ($|x_F| < 0.2$) as a function of p_T from theory input for D mesons ($\bar{D}^0, D^- \rightarrow \mu^-$).

p_T bin	Forward ($x_F > 0$)		Backward ($x_F < 0$)	
	A_N model 1	A_N model 2	A_N model 1	A_N model 2
(1.00, 1.25)	-0.020	-0.020	-0.017	-0.041
(1.25, 1.50)	-0.022	-0.021	-0.017	-0.040
(1.50, 1.75)	-0.019	-0.018	-0.015	-0.038
(1.75, 2.00)	-0.022	-0.017	-0.016	-0.035
(2.00, 2.25)	-0.022	-0.015	-0.012	-0.035
(2.25, 2.50)	-0.022	-0.015	-0.009	-0.029
(2.50, 2.75)	-0.018	-0.013	-0.011	-0.025
(2.75, 3.00)	-0.019	-0.013	-0.009	-0.023
(3.00, 3.25)	-0.017	-0.011	-0.010	-0.022
(3.25, 3.50)	-0.017	-0.011	-0.009	-0.019
(3.50, 4.00)	-0.017	-0.012	-0.008	-0.015
(4.00, 5.00)	-0.016	-0.007	-0.008	-0.011

Table 27: Simulation results for A_N of μ^+ ($|x_F| < 0.2$) as a function of p_T from theory input for D mesons ($D^0, D^+ \rightarrow \mu^+$).

p_T bin	Forward ($x_F > 0$)		Backward ($x_F < 0$)	
	A_N model 1	A_N model 2	A_N model 1	A_N model 2
(1.00, 1.25)	0.010	0.033	-0.023	-0.010
(1.25, 1.50)	0.015	0.032	-0.030	-0.017
(1.50, 1.75)	0.020	0.032	-0.032	-0.025
(1.75, 2.00)	0.024	0.033	-0.035	-0.032
(2.00, 2.25)	0.027	0.032	-0.038	-0.038
(2.25, 2.50)	0.028	0.032	-0.040	-0.045
(2.50, 2.75)	0.029	0.031	-0.039	-0.043
(2.75, 3.00)	0.035	0.031	-0.041	-0.046
(3.00, 3.25)	0.033	0.027	-0.042	-0.045
(3.25, 3.50)	0.034	0.025	-0.041	-0.042
(3.50, 4.00)	0.035	0.026	-0.039	-0.044
(4.00, 5.00)	0.033	0.022	-0.039	-0.041

Table 28: Simulation results for A_N of μ^- (μ^+) in $1.25 < p_T < 5.0$ GeV/ c as a function of x_F from theory input for D mesons ($\bar{D}^0, D^- \rightarrow \mu^-$ or $D^0, D^+ \rightarrow \mu^+$).

x_F bin	$A_N(\bar{D}^0, D^- \rightarrow \mu^-)$		$A_N(D^0, D^+ \rightarrow \mu^+)$	
	model 1	model 2	model 1	model 2
(-0.10, -0.80)	-0.010	-0.022	-0.044	-0.058
(-0.80, -0.60)	-0.013	-0.031	-0.042	-0.051
(-0.60, -0.50)	-0.014	-0.037	-0.037	-0.042
(-0.50, -0.40)	-0.015	-0.039	-0.034	-0.028
(-0.40, -0.30)	-0.016	-0.040	-0.029	-0.016
(-0.30, -0.20)	-0.017	-0.036	-0.025	-0.007
(0.20, 0.30)	-0.021	-0.021	0.011	0.032
(0.30, 0.40)	-0.019	-0.020	0.016	0.032
(0.40, 0.50)	-0.021	-0.019	0.021	0.032
(0.50, 0.60)	-0.023	-0.016	0.026	0.034
(0.60, 0.80)	-0.022	-0.018	0.034	0.033
(0.80, 1.00)	-0.019	-0.013	0.039	0.031

3.3.1 Additional Test with Flat A_N Input

There are two possible explanations for the difference between $A_N(D \rightarrow \mu)$ and $A_N(D)$. First of all, the p_T distributions of D and μ are different, as Fig. 47 shows. The asymmetry of the muon can be affected by that of the parent D meson. On the other hand, a change in azimuthal angle (ϕ) in the $D \rightarrow \mu + X$ decay may have an effect on A_N , and there may be a large effect as the momentum of the muon gets smaller. Therefore, a flat input $A_N(D)=0.1$ is tested in wide p_T ranges. $A_N(D \rightarrow \mu)$ is diluted for low p_T ($p_T < 1.0$ GeV/c) as seen in Table 29 and Fig. 49. $A_N(\mu)$ is smaller for lower $p_T(\mu)$ even though the input $A_N(D)$ is fixed as 0.10. For $p_T > 1.25$ GeV/c, the output $A_N(D \rightarrow \mu)$ are almost the same as $A_N(D \rightarrow \mu)$ for input $A_N(D \rightarrow \mu) = 0.10$. Therefore the change in azimuthal angle (ϕ) in the $D \rightarrow \mu + X$ decay did not affect the simulation result in the p_T region of this study, $p_T > 1.25$ GeV/c.

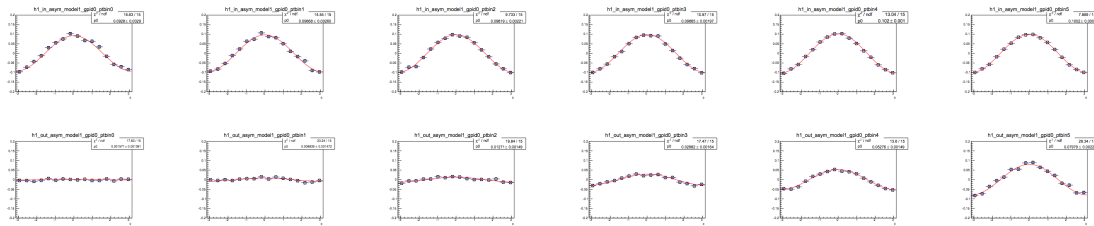


Figure 49: Simulation of $A_N(D \rightarrow \mu)$ for $A_N(D)=0.1$ for low p_T muons (6 bins for $p_T < 1.0$ GeV/c). The upper row shows the fit result for $A_N(D)$ input and the lower row shows the fit result for $A_N(D \rightarrow \mu)$.

Table 29: Fit results of the cosine modulation for simulation of $A_N(D \rightarrow \mu)$ using $A_N(D)=0.1$ for low p_T muons ($p_T < 1.0$ GeV/ c).

muon p_T (GeV/ c)	$A_N(D)$ input	fit result for $A_N(D)$	fit result for $A_N(\mu)$
(0.0, 0.2)	0.10	0.0928 ± 0.0029	0.0016 ± 0.0014
(0.2, 0.3)	0.10	0.0967 ± 0.0026	0.0088 ± 0.0015
(0.3, 0.4)	0.10	0.0989 ± 0.0022	0.0127 ± 0.0015
(0.4, 0.5)	0.10	0.0987 ± 0.0020	0.0288 ± 0.0016
(0.5, 0.7)	0.10	0.1020 ± 0.0010	0.0528 ± 0.0015
(0.7, 1.0)	0.10	0.1002 ± 0.0009	0.0798 ± 0.0022

3.4 Results

Figures 50, 51, and 52 and Table 30, 31, 32, and 33 show the results for $A_N^{HF \rightarrow \mu}$ with systematic uncertainties as well as the simulation results from theory ($D \rightarrow \mu$).

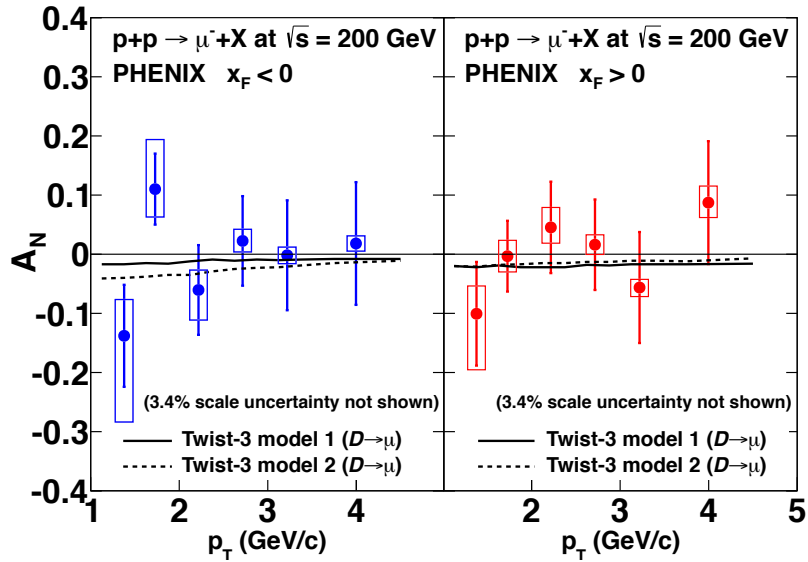


Figure 50: A_N of negatively-charged, heavy-flavor muons as a function of p_T in the backward ($x_F < 0$, left) and forward ($x_F > 0$, right) regions. Vertical bars (boxes) represent statistical (systematic) uncertainties. Solid and dashed lines represent twist-3 model calculations [5].

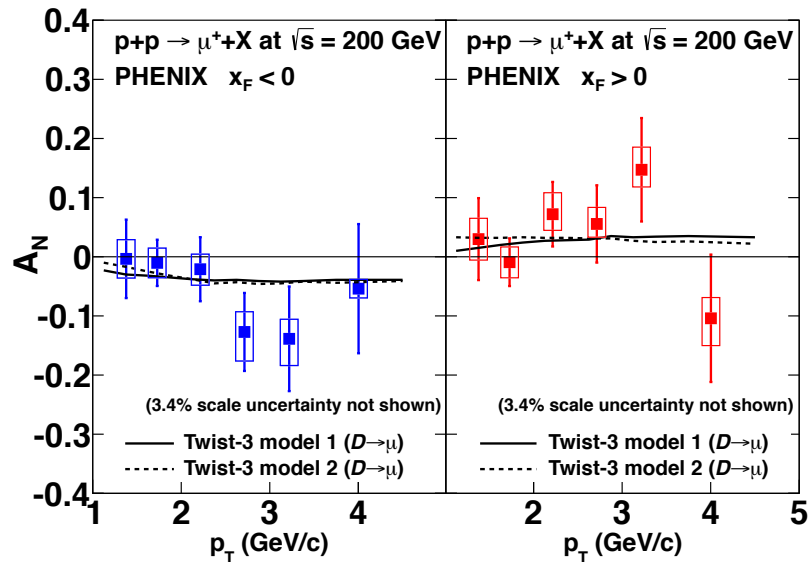


Figure 51: A_N of positively-charged, heavy-flavor muons as a function of p_T in the backward ($x_F < 0$, left) and forward ($x_F > 0$, right) regions. Vertical bars (boxes) represent statistical (systematic) uncertainties. Solid and dashed lines represent twist-3 model calculations [5].

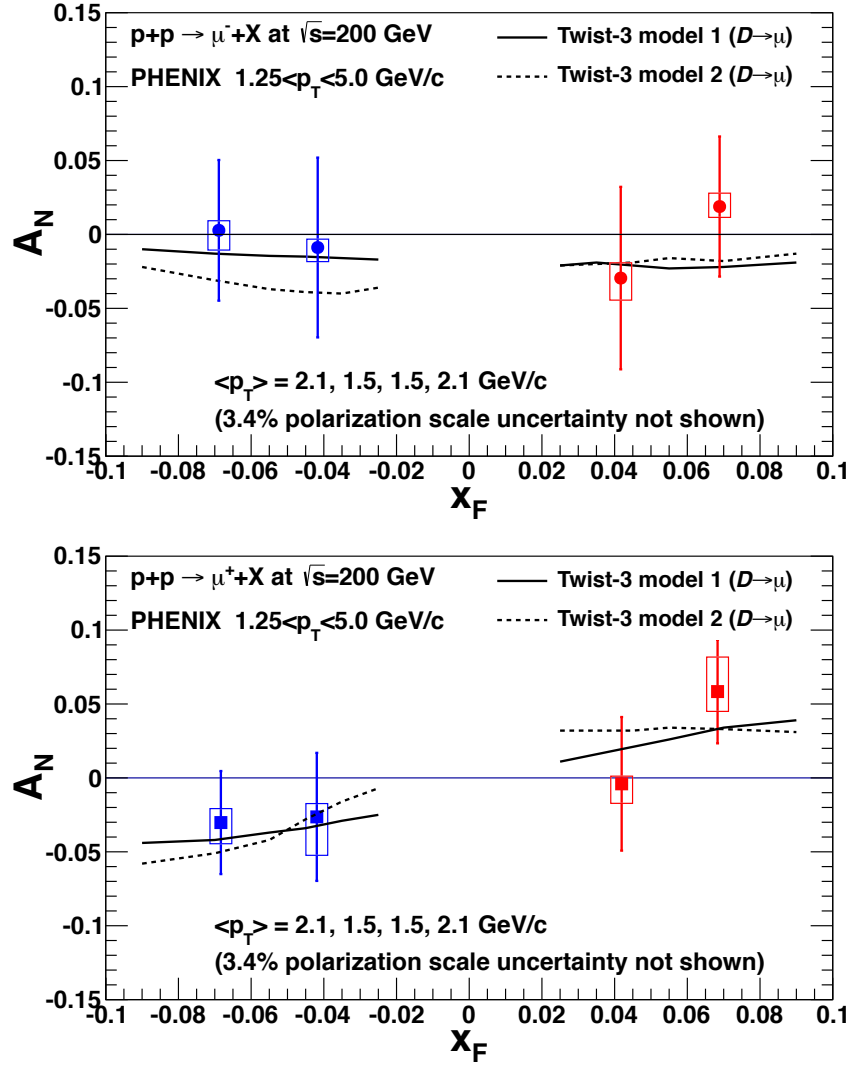


Figure 52: A_N of negatively-charged (top) and positively-charged (bottom), heavy-flavor muons as a function of x_F , where $+x_F$ is along the direction of the polarized proton. Vertical bars (boxes) represent statistical (systematic) uncertainties. Solid and dashed lines represent twist-3 model calculations [5].

Table 30: Results for A_N of heavy-flavor μ^- as a function of p_T .

p_T bin (GeV/ c)	A_N	$\delta A_N^{stat.}$	$\delta A_N^{syst.}$
Forward ($x_F > 0$)			
(1.25, 1.50)	-10.07×10^{-2}	$\pm 8.76 \times 10^{-2}$	$^{+4.49}_{-7.89} \times 10^{-2}$
(1.50, 2.00)	-0.33×10^{-2}	$\pm 5.98 \times 10^{-2}$	$^{+2.68}_{-2.66} \times 10^{-2}$
(2.00, 2.50)	4.54×10^{-2}	$\pm 7.73 \times 10^{-2}$	$^{+3.22}_{-2.65} \times 10^{-2}$
(2.50, 3.00)	1.60×10^{-2}	$\pm 7.65 \times 10^{-2}$	$^{+1.65}_{-1.63} \times 10^{-2}$
(3.00, 3.50)	-5.63×10^{-2}	$\pm 9.38 \times 10^{-2}$	$^{+1.39}_{-1.52} \times 10^{-2}$
(3.50, 5.00)	8.73×10^{-2}	$\pm 10.39 \times 10^{-2}$	$^{+2.70}_{-2.48} \times 10^{-2}$
Backward ($x_F < 0$)			
(1.25, 1.50)	-13.80×10^{-2}	$\pm 8.63 \times 10^{-2}$	$^{+5.80}_{-12.15} \times 10^{-2}$
(1.50, 2.00)	11.01×10^{-2}	$\pm 6.01 \times 10^{-2}$	$^{+7.13}_{-4.45} \times 10^{-2}$
(2.00, 2.50)	-6.05×10^{-2}	$\pm 7.58 \times 10^{-2}$	$^{+3.29}_{-4.73} \times 10^{-2}$
(2.50, 3.00)	2.25×10^{-2}	$\pm 7.57 \times 10^{-2}$	$^{+1.90}_{-1.83} \times 10^{-2}$
(3.00, 3.50)	-0.18×10^{-2}	$\pm 9.29 \times 10^{-2}$	$^{+1.38}_{-1.41} \times 10^{-2}$
(3.50, 5.00)	1.81×10^{-2}	$\pm 10.38 \times 10^{-2}$	$^{+1.30}_{-1.29} \times 10^{-2}$

Table 31: Results for A_N of heavy-flavor μ^+ as a function of p_T .

p_T bin (GeV/c)	A_N	$\delta A_N^{stat.}$	$\delta A_N^{syst.}$
Forward ($x_F > 0$)			
(1.25, 1.50)	2.99×10^{-2}	$\pm 6.93 \times 10^{-2}$	$^{+3.45}_{-3.51} \times 10^{-2}$
(1.50, 2.00)	-0.92×10^{-2}	$\pm 4.03 \times 10^{-2}$	$^{+2.58}_{-2.64} \times 10^{-2}$
(2.00, 2.50)	7.20×10^{-2}	$\pm 5.46 \times 10^{-2}$	$^{+3.33}_{-2.67} \times 10^{-2}$
(2.50, 3.00)	5.55×10^{-2}	$\pm 6.54 \times 10^{-2}$	$^{+2.57}_{-2.17} \times 10^{-2}$
(3.00, 3.50)	14.71×10^{-2}	$\pm 8.74 \times 10^{-2}$	$^{+3.39}_{-2.71} \times 10^{-2}$
(3.50, 5.00)	-10.40×10^{-2}	$\pm 10.77 \times 10^{-2}$	$^{+3.21}_{-3.99} \times 10^{-2}$
Backward ($x_F < 0$)			
(1.25, 1.50)	-0.35×10^{-2}	$\pm 6.63 \times 10^{-2}$	$^{+3.25}_{-3.25} \times 10^{-2}$
(1.50, 2.00)	-1.03×10^{-2}	$\pm 3.91 \times 10^{-2}$	$^{+2.49}_{-2.50} \times 10^{-2}$
(2.00, 2.50)	-2.10×10^{-2}	$\pm 5.41 \times 10^{-2}$	$^{+2.54}_{-2.70} \times 10^{-2}$
(2.50, 3.00)	-12.71×10^{-2}	$\pm 6.60 \times 10^{-2}$	$^{+3.21}_{-4.33} \times 10^{-2}$
(3.00, 3.50)	-13.87×10^{-2}	$\pm 8.85 \times 10^{-2}$	$^{+3.14}_{-4.12} \times 10^{-2}$
(3.50, 5.00)	-5.39×10^{-2}	$\pm 10.92 \times 10^{-2}$	$^{+1.55}_{-1.55} \times 10^{-2}$

Table 32: Results for A_N of heavy-flavor μ^- as a function of x_F .

x_F bin	$\langle x_F \rangle$	A_N	$\delta A_N^{stat.}$	$\delta A_N^{syst.}$
(-0.20, -0.05)	-0.07	0.27×10^{-2}	$\pm 4.75 \times 10^{-2}$	$^{+0.68}_{-1.32} \times 10^{-2}$
(-0.05, 0.00)	-0.04	-0.91×10^{-2}	$\pm 5.84 \times 10^{-2}$	$^{+0.55}_{-0.81} \times 10^{-2}$
(0.00, 0.05)	0.04	-3.79×10^{-2}	$\pm 6.06 \times 10^{-2}$	$^{+1.34}_{-2.89} \times 10^{-2}$
(0.05, 0.20)	0.07	1.89×10^{-2}	$\pm 4.73 \times 10^{-2}$	$^{+0.85}_{-0.71} \times 10^{-2}$

 Table 33: Results for A_N of heavy-flavor μ^+ as a function of x_F .

x_F bin	$\langle x_F \rangle$	A_N	$\delta A_N^{stat.}$	$\delta A_N^{syst.}$
(-0.20, -0.05)	-0.07	-3.02×10^{-2}	$\pm 3.48 \times 10^{-2}$	$^{+0.92}_{-1.32} \times 10^{-2}$
(-0.05, 0.00)	-0.04	-2.90×10^{-2}	$\pm 4.82 \times 10^{-2}$	$^{+1.00}_{-2.93} \times 10^{-2}$
(0.00, 0.05)	0.04	-0.52×10^{-2}	$\pm 5.05 \times 10^{-2}$	$^{+0.58}_{-1.50} \times 10^{-2}$
(0.05, 0.20)	0.07	5.83×10^{-2}	$\pm 3.50 \times 10^{-2}$	$^{+2.01}_{-1.25} \times 10^{-2}$

3.5 Discussion and Outlook for the Heavy Flavor A_N

The results for the single-spin asymmetry of muons from open heavy-flavor decays were published in Phys Rev D95, 112001 (2017). There is no clear indication of a non-zero asymmetry in the results, which have relatively large statistical uncertainties (~ 0.05). Theoretical calculations of A_N for D -meson production are converted into A_N for muons with the help of PYTHIA in order to compare with the data directly. The calculations, which take into account tri-gluon correlations in the leading order QCD, are in agreement with the data within experimental uncertainties. Future studies with improved statistics using data taken with the PHENIX detector at RHIC in 2015, could provide further constraints on the tri-gluon correlation functions.

4 Data Analysis (II) : Charged Hadron A_N

The transverse single spin asymmetry in inclusive h^- and h^+ production has been studied in 3 p_T ($1.25 < p_T < 7.0$ GeV/ c) bins and 5 $|x_F|$ ($0.035 < |x_F| < 0.020$) bins for forward and backward rapidity separately ($1.4 < |\eta| < 2.4$).

4.1 Analysis Method

Analysis cuts are placed on a track by track basis. The definition of the analysis cuts was described earlier. SG3&MuID1DH triggered events are selected. The details are shown below:

- Rapidity cut: $1.4 < |\eta| < 2.4$.
- BBC Vertex Z cut: $-30 < |BBCZ| < 30$ cm.
- p_T range cut: $1.25 < |p_T| < 7.0$ GeV/ c .
- p_Z range cut: $3.5 < |p_Z| < 20.0$ GeV/ c .
- centrality cut for $p + \text{Au}$: 0 to 84%.
- centrality cut for $p + \text{Al}$: 0 to 72%.

Other cuts :

The DG0, DDG0, VtxRad, VtxChi2, gap0 slope and $|\bar{p} \cdot \delta\theta|$ cuts that are used are well-studied and fine-tuned transverse momentum dependent cuts.

In $p + \text{Au}$, $p + \text{Al}$ data, a 3 mrad tilt angle correction is applied to p_z .

The numbers of tracks for stopped hadrons (MUID last gap = 2 or 3) after all the quality cuts are listed in Tables 34, 35, 36, and 37.

Table 34: Number of hadron tracks in p_T bins after all the track quality cuts from $p + p$ data. (–) is negatively charged tracks and (+) is positively charged tracks.

p_T (GeV/c)	N(South,–)	N(North,–)	N(South,+)	N(North,+)
(1.25, 2.50)	1115469	1332469	2093348	2805933
(2.50, 3.50)	133835	163339	274989	347710
(3.50, 7.00)	28063	32984	59440	70634
(1.25, 7.00)	1277367	1528792	2427777	3224277

Table 35: Number of hadron tracks in p_z bins after all the track quality cuts from $p + p$ data. (–) is negatively charged tracks and (+) is positively charged tracks.

$ p_z $ (GeV/c)	N(South,–)	N(North,–)	N(South,+)	N(North,+)
(3.50, 5.00)	394178	248704	728379	508147
(5.00, 7.00)	543416	551499	1025701	1203821
(7.00, 10.00)	267539	521342	527000	1085630
(10.00, 13.00)	55084	149318	110294	305409
(13.00, 20.00)	17150	57929	36403	121270
(3.50, 20.00)	1277367	1528792	2427777	3224277

Table 36: Number of hadron tracks in p_T bins after all the track quality cuts from $p + \text{Au}$ data. $(-)$ is negatively charged tracks and $(+)$ is positively charged tracks.

p_T (GeV/c)	N(South,(-))	N(North,(-))	N(South,(+))	N(North,(+))
(1.25, 2.50)	810103	618464	1228782	1307340
(2.50, 3.50)	94128	105186	164216	223456
(3.50, 7.00)	20408	24347	35549	51576
(1.25, 7.00)	924639	747997	1428547	1582372

Table 37: Number of hadron tracks in p_z bins after all the track quality cuts from $p + \text{Au}$ data. $(-)$ is negatively charged tracks and $(+)$ is positively charged tracks.

$ p_z $ (GeV/c)	N(South,(-))	N(North,(-))	N(South,(+))	N(North,(+))
(3.50, 5.00)	369713	99110	527833	202257
(5.00, 7.00)	350450	247725	551761	543141
(7.00, 10.00)	158710	271440	269265	569269
(10.00, 13.00)	34313	90414	59851	185051
(13.00, 20.00)	11453	39308	19837	82654
(3.50, 20.00)	924639	747997	1428547	1582372

A detailed discussion on the maximum likelihood method can be found in the previous chapter. The A_N results with the maximum likelihood method are compared with another method described below,:

$$A_N(\phi) = \frac{\sigma^\uparrow(\phi) - \sigma^\downarrow(\phi)}{\sigma^\uparrow(\phi) + \sigma^\downarrow(\phi)} = \frac{1}{P} \cdot \frac{N^\uparrow(\phi) - R \cdot N^\downarrow(\phi)}{N^\uparrow(\phi) + R \cdot N^\downarrow(\phi)}, \quad (11)$$

where P is the average beam polarization, σ^\uparrow , σ^\downarrow are cross sections for each polarization, N^\uparrow , N^\downarrow are the yields for the two polarizations and $R = L^\uparrow/L^\downarrow$ is the relative luminosity where the luminosity $(L^\uparrow, L^\downarrow)$ is measured by the BBC detectors. A_N^{incl} is calculated by fitting the $A_N(\phi)$ distribution with a function $\pm A_N \cdot \cos \phi$, where \pm depends on the beam direction.

4.2 Raw A_N for Charged Hadrons

The measured A_N from the hadron track detected in the muon spectrometers cannot be compared with theory or results from other experiments directly because of momentum migration and charge conversion in the detectors and absorbers. Further steps to correct these will be shown in the following sections.

4.2.1 Raw A_N in $p + p$ Collisions

The asymmetries (blue beam, yellow beam and combined) for charged hadrons stopped at MUID Gap2 or 3 are listed in Tables 38, 39, 40, and 41, and shown in Figs. 53 and 54.

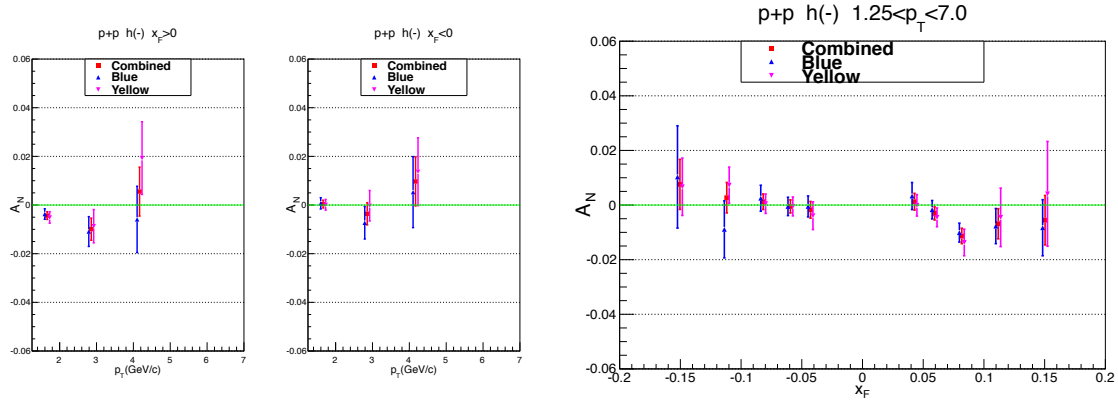


Figure 53: p_T dependence (left $x_F > 0$, middle $x_F < 0$) and x_F dependence (right) of asymmetries for hadrons (Gap2, 3) for negative charge.

Table 38: p_T dependence of A_N^B (blue beam), A_N^Y (yellow beam) and A_N (combined) with statistical uncertainty δA_N^{stat} in forward and backward rapidity for negatively charged hadrons from $p + p$ collisions.

p_T	$x_F > 0$		
(GeV/c)	$A_N^B (\times 10^{-2})$	$A_N^Y (\times 10^{-2})$	$A_N (\times 10^{-2})$
(1.25, 2.50)	-0.37±0.22	-0.51±0.24	-0.43±0.16
(2.50, 3.50)	-1.09±0.61	-0.87±0.68	-0.99±0.46
(3.50, 7.00)	-0.59±1.36	1.93±1.49	0.55±1.01
	$x_F < 0$		
(1.25, 2.50)	0.07±0.23	0.01±0.22	0.04±0.16
(2.50, 3.50)	-0.73±0.67	-0.03±0.63	-0.36±0.46
(3.50, 7.00)	0.53±1.46	1.37±1.40	0.97±1.01

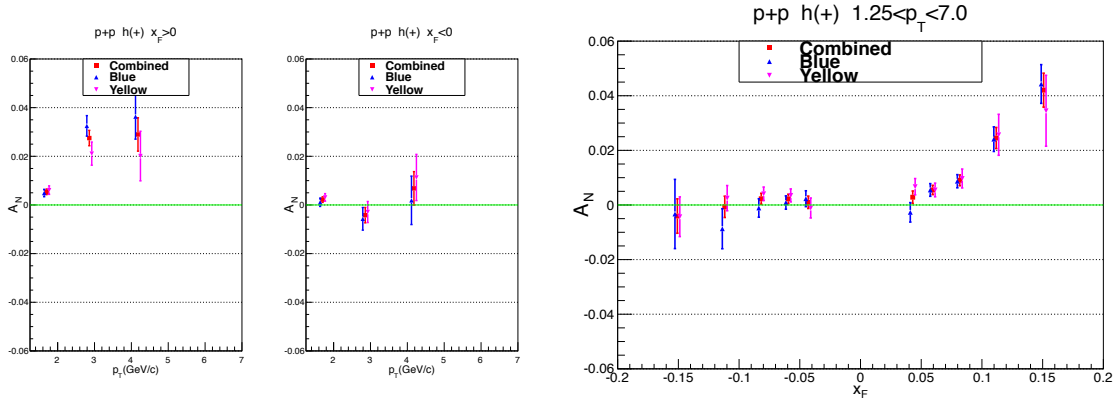


Figure 54: p_T (left $x_F > 0$, middle $x_F < 0$) dependence and x_F dependence (right) of asymmetries for hadrons (Gap2, 3) for positive charge

Table 39: p_T dependence of A_N^B (blue beam), A_N^Y (yellow beam) and A_N (combined) with statistical uncertainty δA_N^{stat} in forward and backward rapidity for positively charged hadrons from $p + p$ collisions.

p_T	$x_F > 0$		
	$A_N^B (\times 10^{-2})$	$A_N^Y (\times 10^{-2})$	$A_N (\times 10^{-2})$
(1.25, 2.50)	0.49 \pm 0.15	0.61 \pm 0.17	0.54 \pm 0.11
(2.50, 3.50)	3.25 \pm 0.42	2.11 \pm 0.48	2.75 \pm 0.32
(3.50, 7.00)	3.63 \pm 0.93	2.01 \pm 1.02	2.90 \pm 0.69
$x_F < 0$			
(1.25, 2.50)	0.11 \pm 0.17	0.31 \pm 0.15	0.22 \pm 0.11
(2.50, 3.50)	-0.57 \pm 0.47	-0.29 \pm 0.43	-0.42 \pm 0.32
(3.50, 7.00)	0.19 \pm 1.00	1.13 \pm 0.95	0.68 \pm 0.69

Table 40: x_F dependence of A_N^B (blue beam), A_N^Y (yellow beam) and A_N (combined) with statistical uncertainty δA_N^{stat} for negatively charged hadrons from $p+p$ collisions.

x_F	$A_N^B(\times 10^{-2})$	$A_N^Y(\times 10^{-2})$	$A_N(\times 10^{-2})$
(-0.20, -0.13)	1.03±1.87	0.67±1.05	0.76±0.92
(-0.13, -0.10)	-0.89±1.05	0.73±0.66	0.27±0.56
(-0.10, -0.07)	0.25±0.48	0.05±0.36	0.12±0.28
(-0.07, -0.05)	-0.05±0.34	-0.05±0.35	-0.05±0.24
(-0.05, -0.035)	-0.05±0.38	-0.39±0.51	-0.17±0.31
(0.035, 0.05)	0.33±0.49	-0.01±0.39	0.12±0.31
(0.05, 0.07)	-0.17±0.34	-0.45±0.34	-0.31±0.24
(0.07, 0.10)	-1.01±0.35	-1.37±0.49	-1.13±0.28
(0.10, 0.13)	-0.77±0.64	-0.45±1.07	-0.69±0.55
(0.13, 0.20)	-0.83±1.03	0.41±1.92	-0.55±0.91

Table 41: x_F dependence of A_N^B (blue beam), A_N^Y (yellow beam) and A_N (combined) with statistical uncertainty δA_N^{stat} for positively charged hadrons from $p+p$ collisions.

x_F	$A_N^B(\times 10^{-2})$	$A_N^Y(\times 10^{-2})$	$A_N(\times 10^{-2})$
(-0.20, -0.13)	-0.33±1.27	-0.43±0.73	-0.41±0.63
(-0.13, -0.10)	-0.87±0.73	0.25±0.46	-0.07±0.39
(-0.10, -0.07)	-0.11±0.34	0.41±0.25	0.23±0.20
(-0.07, -0.05)	0.09±0.24	0.35±0.24	0.22±0.17
(-0.05, -0.035)	0.23±0.29	-0.11±0.37	0.10±0.23
(0.035, 0.05)	-0.27±0.36	0.67±0.30	0.28±0.23
(0.05, 0.07)	0.55±0.23	0.55±0.25	0.55±0.17
(0.07, 0.10)	0.87±0.24	0.97±0.35	0.90±0.20
(0.10, 0.13)	2.41±0.45	2.57±0.75	2.45±0.39
(0.13, 0.20)	4.43±0.71	3.45±1.30	4.20±0.62
(0.20, 0.30)	4.61±2.33	9.33±4.87	5.49±2.10

4.2.2 Raw A_N in $p + \text{Au}$

The asymmetries (blue beam) for charged hadrons stopped at MUID Gap2,3 are listed in Tables 38, 43, 44, and 45, and shown in Figs. 55 and 56.

Table 42: p_T dependence of A_N (blue beam) with statistical uncertainty δA_N^{stat} in forward and backward rapidity for negatively charged hadrons from $p + \text{Au}$ collision

p_T (GeV/c)	$x_F > 0$ $A_N(\times 10^{-2})$	$x_F < 0$ $A_N(\times 10^{-2})$
(1.25, 2.50)	-0.39 ± 0.31	-0.11 ± 0.25
(2.50, 3.50)	-0.31 ± 0.74	-0.41 ± 0.75
(3.50, 7.00)	0.53 ± 1.53	0.33 ± 1.62

Table 43: p_T dependence of A_N (blue beam) with statistical uncertainty δA_N^{stat} for positively charged hadrons from $p + \text{Au}$ collisions.

p_T (GeV/c)	$x_F > 0$ $A_N(\times 10^{-2})$	$x_F < 0$ $A_N(\times 10^{-2})$
(1.25, 2.50)	0.25 ± 0.22	0.27 ± 0.21
(2.50, 3.50)	0.07 ± 0.51	-0.09 ± 0.58
(3.50, 7.00)	1.17 ± 1.05	-1.07 ± 1.23

Table 44: x_F dependence of A_N (blue beam) with statistical uncertainty δA_N^{stat} for negatively charged hadrons from $p + \text{Au}$ collisions.

x_F	$A_N^B (\times 10^{-2})$	x_F	$A_N^B (\times 10^{-2})$
(-0.20, -0.13)	-0.43±2.18	(0.035, 0.05)	-0.45±0.76
(-0.13, -0.10)	0.79±1.26	(0.05, 0.07)	-0.59±0.49
(-0.10, -0.07)	0.13±0.58	(0.07, 0.10)	-0.11±0.47
(-0.07, -0.05)	-0.37±0.38	(0.10, 0.13)	-0.21±0.81
(-0.05, -0.035)	-0.07±0.35	(0.13, 0.20)	-0.49±1.22

Table 45: x_F dependence of A_N (blue beam) with statistical uncertainty δA_N^{stat} for positively charged hadrons from $p + \text{Au}$ collisions.

x_F	$A_N^B (\times 10^{-2})$	x_F	$A_N^B (\times 10^{-2})$
(-0.20, -0.13)	-0.67±1.66	(0.035, 0.05)	0.13±0.55
(-0.13, -0.10)	1.19±0.96	(0.05, 0.07)	0.07±0.34
(-0.10, -0.07)	0.67±0.46	(0.07, 0.10)	0.55±0.33
(-0.07, -0.05)	-0.11±0.32	(0.10, 0.13)	-0.49±0.57
(-0.05, -0.035)	0.21±0.32	(0.13, 0.20)	1.43±0.84

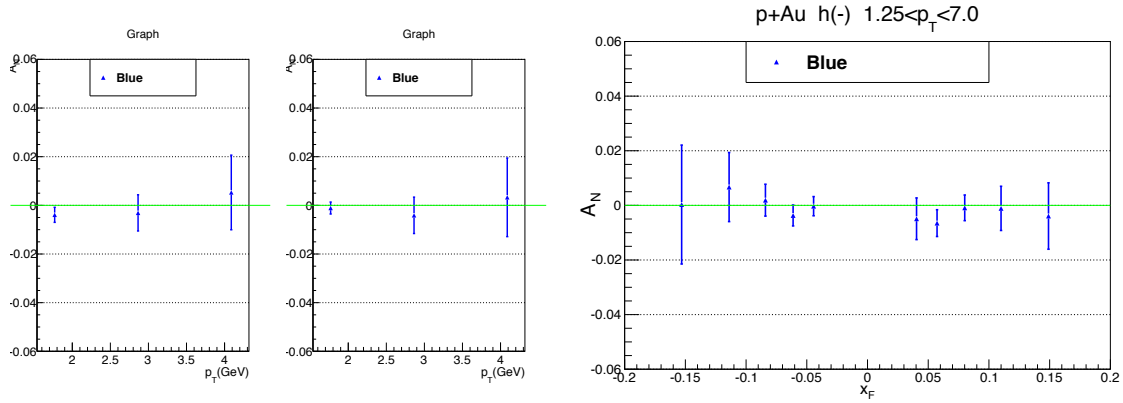


Figure 55: p_T dependence (left $x_F > 0$, middle $x_F < 0$) and x_F dependence (right) of asymmetries for negatively charged hadrons from $p + \text{Au}$ collisions.

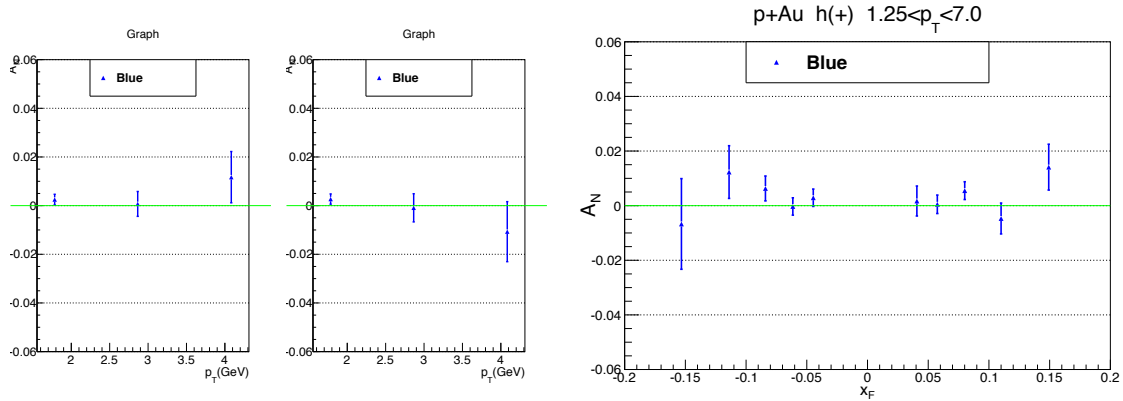


Figure 56: p_T (left $x_F > 0$, middle $x_F < 0$) dependence and x_F dependence (right) of asymmetries for positive charged hadrons from $p + \text{Au}$ collisions.

4.2.3 Measured A_N from $p + \text{Au}$ Data for Different Centrality Range

A_N results in 2 centrality bins (0-30% and 50-85%) from $p + \text{Au}$ collisions are listed in Tables 38, 43, 44, and 45, and shown in Figs. 55 and 56. Due to large statistical uncertainties, no deviation from 0 of more than 2σ is seen.

Table 46: p_T dependence of A_N (blue beam) with statistical uncertainty δA_N^{stat} in forward and backward rapidity in the centrality range 0-30% for negatively charged hadrons from $p + \text{Au}$ collisions

p_T (GeV/c)	$x_F > 0$ $A_N (\times 10^{-2})$	$x_F < 0$ $A_N (\times 10^{-2})$
(1.25, 2.50)	-0.23 ± 0.36	-0.01 ± 0.27
(2.50, 3.50)	0.19 ± 0.87	-0.47 ± 0.82
(3.50, 7.00)	1.51 ± 1.80	-0.09 ± 1.78

Table 47: p_T dependence of A_N (blue beam) with statistical uncertainty δA_N^{stat} in the centrality range 0-30% for positively charged hadrons from $p + \text{Au}$ collisions

p_T (GeV/c)	$x_F > 0$ $A_N (\times 10^{-2})$	$x_F < 0$ $A_N (\times 10^{-2})$
(1.25, 2.50)	0.11 ± 0.25	0.21 ± 0.23
(2.50, 3.50)	-0.13 ± 0.60	-0.07 ± 0.63
(3.50, 7.00)	0.33 ± 1.24	-1.15 ± 1.35

Table 48: x_F dependence of A_N (blue beam) with statistical uncertainty δA_N^{stat} in the centrality range 0-30% for negatively charged hadrons from $p + \text{Au}$ collisions.

x_F	$A_N^B (\times 10^{-2})$	x_F	$A_N^B (\times 10^{-2})$
(-0.20, -0.13)	-0.65±2.40	(0.035, 0.05)	0.37±0.89
(-0.13, -0.10)	1.05±1.38	(0.05, 0.07)	-0.57±0.58
(-0.10, -0.07)	0.15±0.64	(0.07, 0.10)	-0.03±0.55
(-0.07, -0.05)	-0.11±0.42	(0.10, 0.13)	-0.37±0.95
(-0.05, -0.035)	-0.17±0.39	(0.13, 0.20)	1.69±1.43

Table 49: x_F dependence of A_N (blue beam) with statistical uncertainty δA_N^{stat} in the centrality range 0-30% for positively charged hadrons from $p + \text{Au}$ collisions.

x_F	$A_N^B (\times 10^{-2})$	x_F	$A_N^B (\times 10^{-2})$
(-0.20, -0.13)	-1.95±1.82	(0.035, 0.05)	-0.29±0.64
(-0.13, -0.10)	1.51±1.05	(0.05, 0.07)	0.21±0.40
(-0.10, -0.07)	0.35±0.50	(0.07, 0.10)	0.37±0.38
(-0.07, -0.05)	-0.15±0.35	(0.10, 0.13)	-0.97±0.67
(-0.05, -0.035)	0.29±0.35	(0.13, 0.20)	0.49±0.99

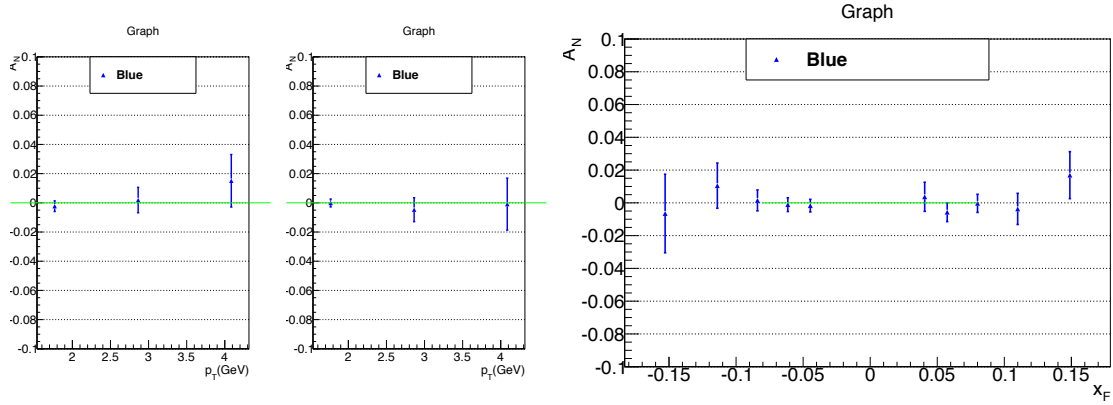


Figure 57: p_T dependence (left $x_F > 0$, middle $x_F < 0$) and x_F dependence (right)

of asymmetries in the centrality range 0-30% for negatively charged hadrons from $p + \text{Au}$ collisions.

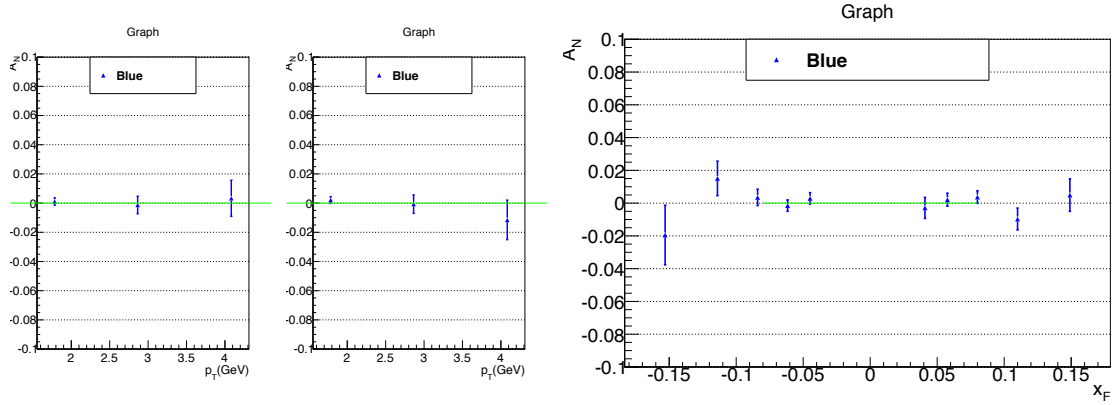


Figure 58: p_T (left $x_F > 0$, middle $x_F < 0$) dependence and x_F dependence (right)

of asymmetries in the centrality range 0-30% for positively charged hadrons from $p + \text{Au}$ collisions.

Table 50: p_T dependence of A_N (blue beam) with statistical uncertainty δA_N^{stat} in forward and backward rapidity in the centrality range 50-84% for negatively charged hadrons from $p + \text{Au}$ collisions.

p_T (GeV/c)	$x_F > 0$ $A_N(\times 10^{-2})$	$x_F < 0$ $A_N(\times 10^{-2})$
(1.25, 2.50)	-0.83 ± 0.58	-0.59 ± 0.60
(2.50, 3.50)	-1.65 ± 1.43	-0.13 ± 1.82
(3.50, 7.00)	-2.05 ± 2.93	2.21 ± 3.85

Table 51: p_T dependence of A_N (blue beam) with statistical uncertainty δA_N^{stat} in the centrality range 50-84% for positively charged hadrons from $p + \text{Au}$ collisions.

p_T (GeV/c)	$x_F > 0$ $A_N(\times 10^{-2})$	$x_F < 0$ $A_N(\times 10^{-2})$
(1.25, 2.50)	0.65 ± 0.41	0.57 ± 0.52
(2.50, 3.50)	0.59 ± 0.98	-0.17 ± 1.44
(3.50, 7.00)	3.39 ± 2.01	-0.71 ± 3.00

Table 52: x_F dependence of A_N (blue beam) with statistical uncertainty δA_N^{stat} in the centrality range 50-84% for negatively charged hadrons from $p + \text{Au}$ collisions.

x_F	$A_N^B (\times 10^{-2})$	x_F	$A_N^B (\times 10^{-2})$
(-0.20, -0.13)	-0.65±2.40	(0.035, 0.05)	0.37±0.89
(-0.13, -0.10)	1.05±1.38	(0.05, 0.07)	-0.57±0.58
(-0.10, -0.07)	0.15±0.64	(0.07, 0.10)	-0.03±0.55
(-0.07, -0.05)	-0.11±0.42	(0.10, 0.13)	-0.37±0.95
(-0.05, -0.035)	-0.17±0.39	(0.13, 0.20)	1.69±1.43

Table 53: x_F dependence of A_N (blue beam) with statistical uncertainty δA_N^{stat} in the centrality range 50-84% for positively charged hadrons from $p + \text{Au}$ collisions.

x_F	$A_N^B (\times 10^{-2})$	x_F	$A_N^B (\times 10^{-2})$
(-0.20, -0.13)	-1.95±1.82	(0.04, 0.05)	-0.29±0.64
(-0.13, -0.10)	1.51±1.05	(0.05, 0.07)	0.21±0.40
(-0.10, -0.07)	0.35±0.50	(0.07, 0.10)	0.37±0.38
(-0.07, -0.05)	-0.15±0.35	(0.10, 0.13)	-0.97±0.67
(-0.05, -0.035)	0.29±0.35	(0.13, 0.20)	0.49±0.99

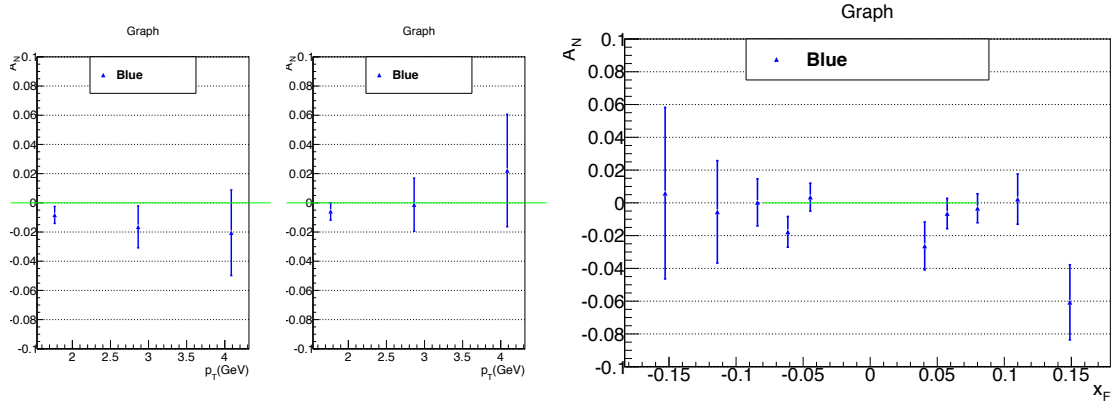


Figure 59: p_T dependence (left $x_F > 0$, middle $x_F < 0$) and x_F dependence (right)

of asymmetries in the centrality range 50-84% for negatively charged hadrons from $p + \text{Au}$ collisions.

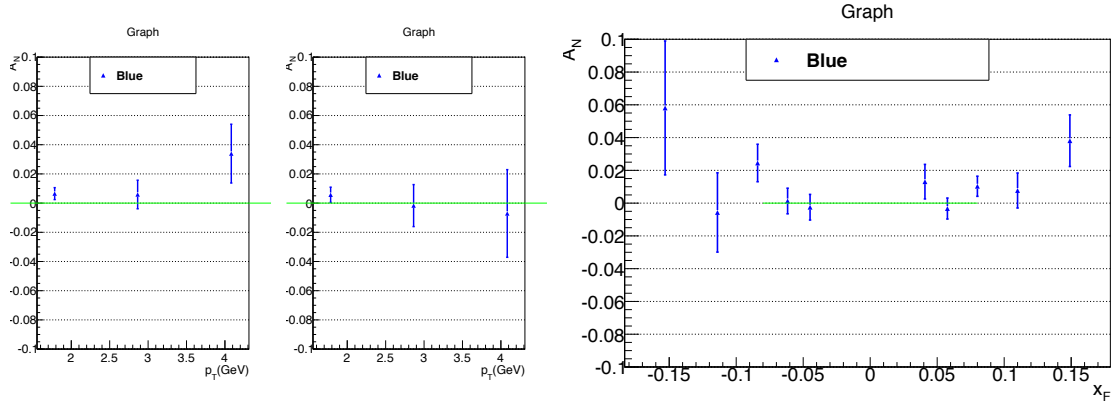


Figure 60: p_T dependence (left $x_F > 0$, middle $x_F < 0$) and x_F dependence (right)

of asymmetries in the centrality range 50-84% for positive charged hadron from $p + \text{Au}$ collision.

4.3 Estimation of Initial Charged Hadron (π^\pm, K^\pm) Spectra

4.3.1 $p + p$ Collisions

Because no identified hadron measurements at forward rapidity exist in the rapidity region of this study, it's required to estimate the hadron spectra in order to have reasonable response matrices for unfolding and the K/π ratio. There is an initial study for hadron background estimation in the heavy-flavor analysis, and a further study has been done to estimate the p_T spectra for positively and negatively charged hadrons separately. Figure 61 shows the p_T spectra of charged pions measured by PHENIX and STAR at mid-rapidity and by BRAHMS at forward rapidity, and fit functions of modified Hagedorn function [97] are also presented. In the bottom panels, the ratio between the data and the fit function is shown. Figure 62 shows the same plots for charged kaons.

The strategy to estimate p_T spectra at forward rapidity is to use measured data at mid-rapidity and extrapolation using PYTHIA. Figure 63 shows a comparison of p_T spectra between data and PYTHIA at mid-rapidity, and Fig. 64 shows their ratios as a function of p_T . PYTHIA underestimates (overestimates) the yield of charged pions (kaons). The weighting functions measured at mid-rapidity, shown in Fig. 64, are applied to all rapidity bins. Figure 65 shows the K/π ratio of data and modified PYTHIA at three rapidity ranges, and this K/π ratio agrees with the measured data within uncertainties. Figure 66 shows the K/π ratio of the

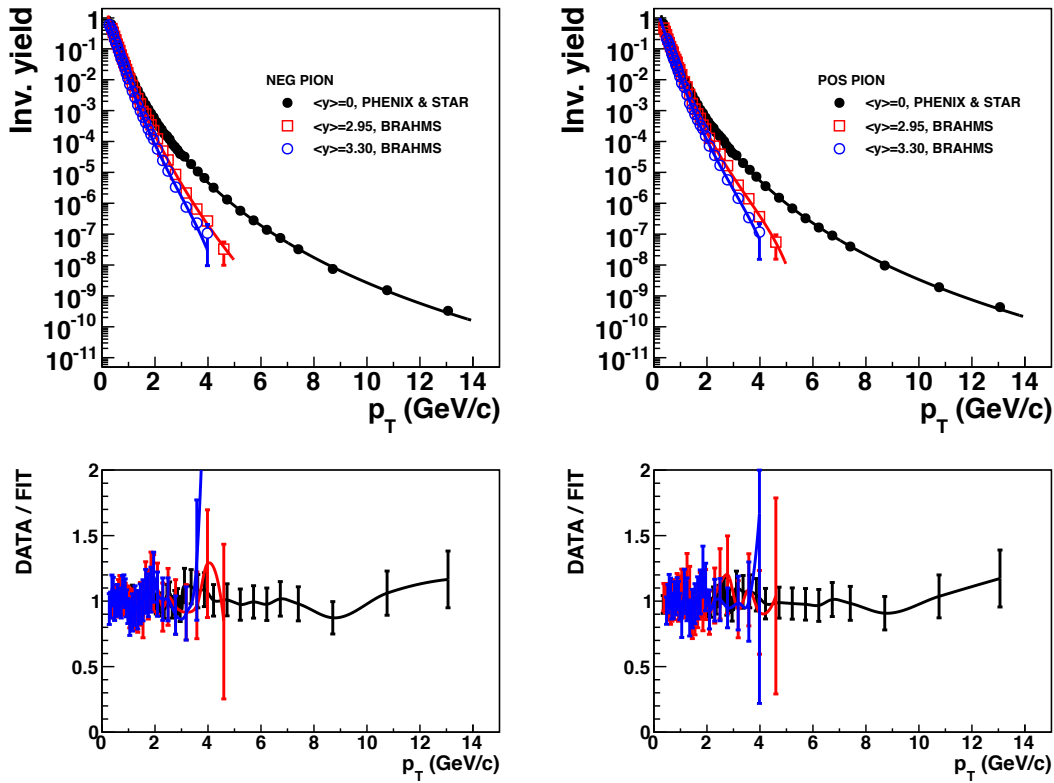


Figure 61: p_T spectra of charged pions in $p + p$ collisions at $\sqrt{s} = 200$ GeV (top panel) and the ratio between data and fit functions (bottom panel).

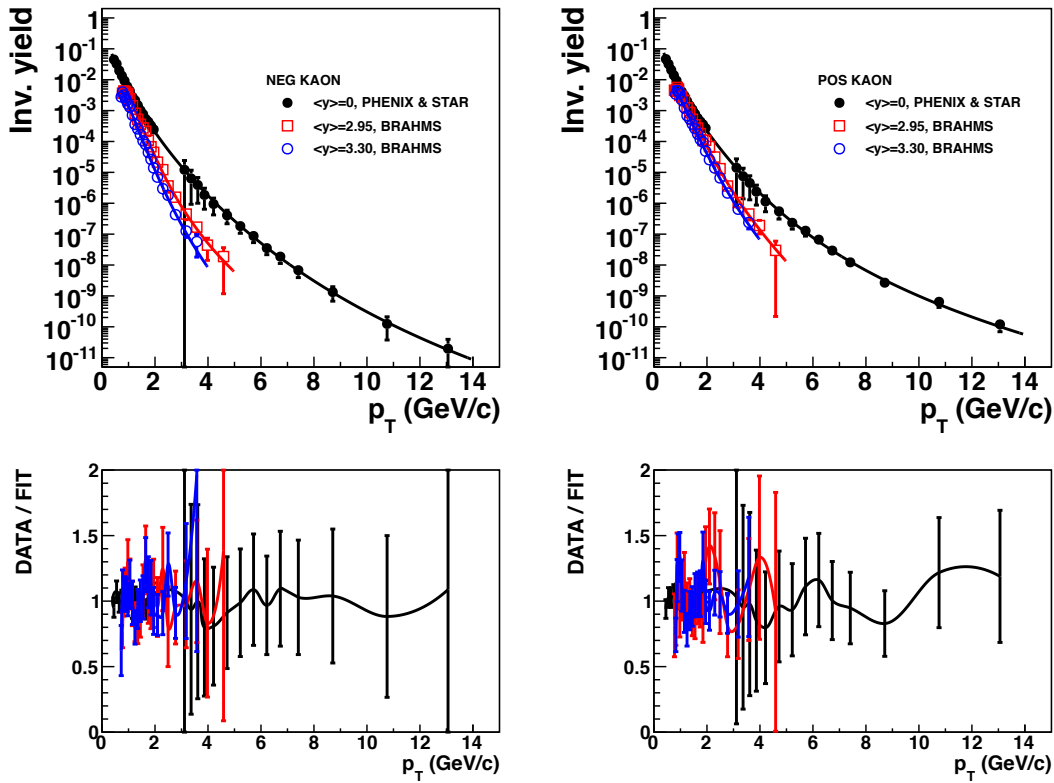


Figure 62: p_T spectra of charged kaons in $p + p$ collisions at $\sqrt{s} = 200$ GeV (top panel) and the ratio between data and fit functions (bottom panel).

modified PYTHIA in various η bins, and each line represents a 0.2 wide η bin. Figure 67 shows the K/π ratio from the fit functions to the p_T spectra of the modified PYTHIA as smoothed curves.

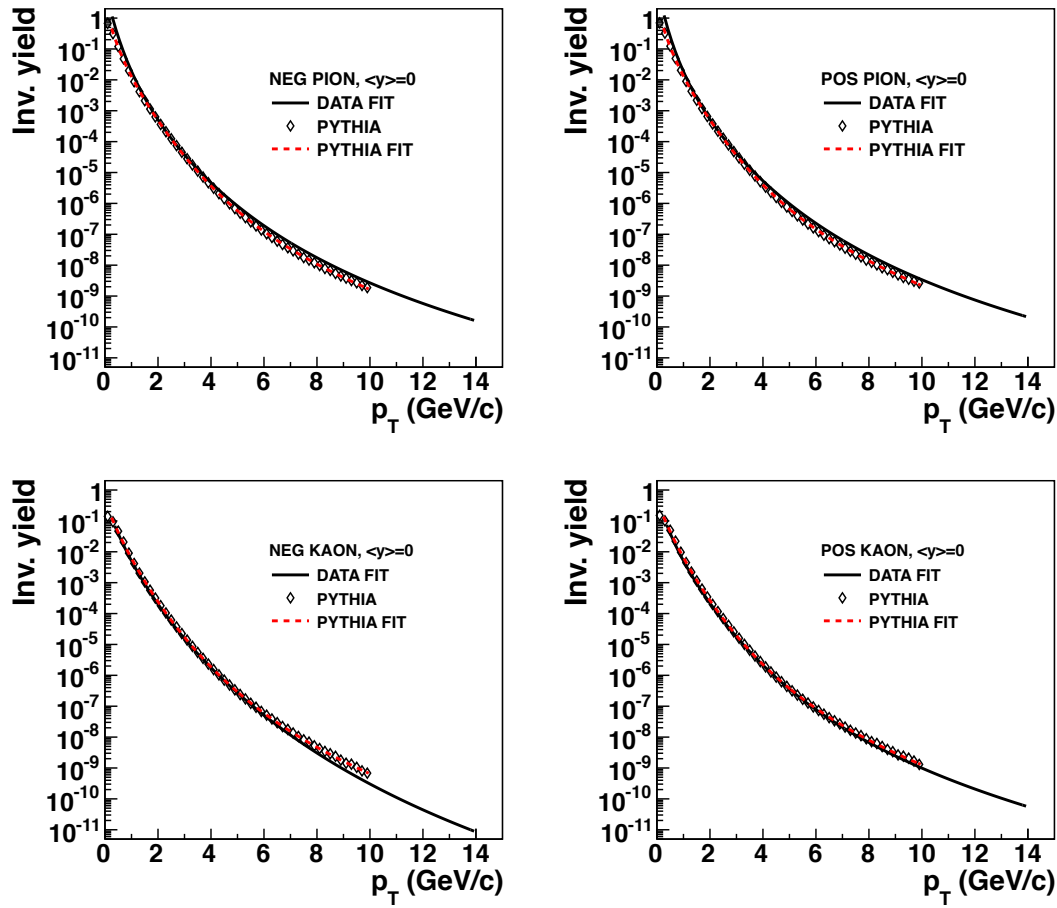


Figure 63: p_T spectra of charged pions and kaons at mid-rapidity in $p+p$ collisions at $\sqrt{s} = 200$ GeV from data and PYTHIA.

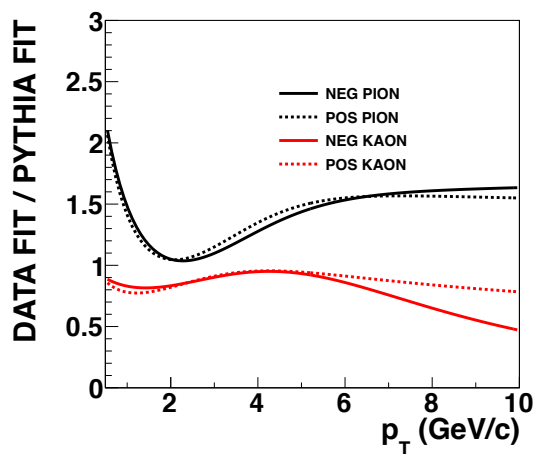


Figure 64: Ratio between data and PYTHIA as a function p_T at mid-rapidity in $p + p$ collisions at $\sqrt{s} = 200$ GeV.

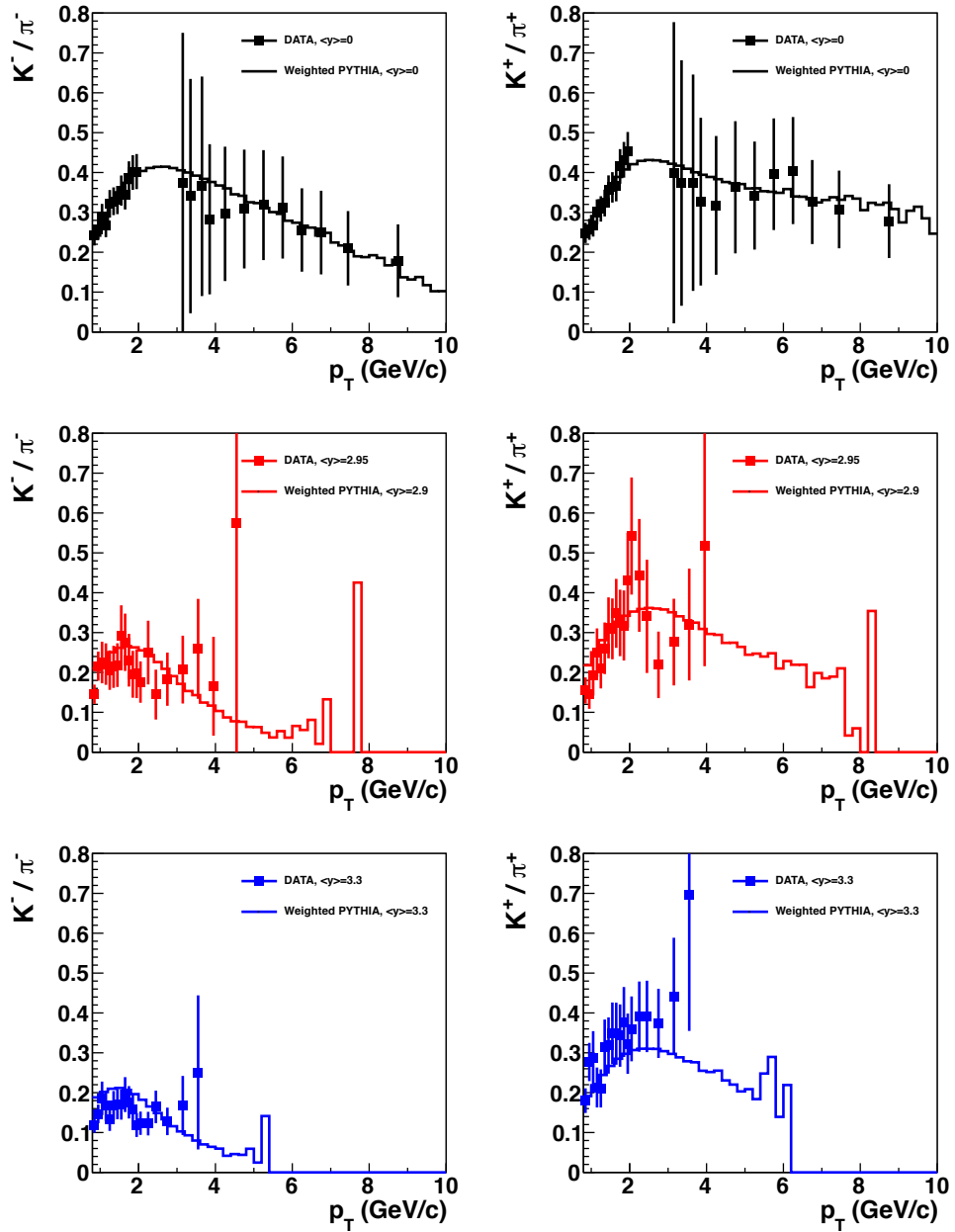


Figure 65: Comparison of K/π ratio between data and tuned PYTHIA as a function of p_T in $p + p$ collisions at $\sqrt{s} = 200$ GeV.

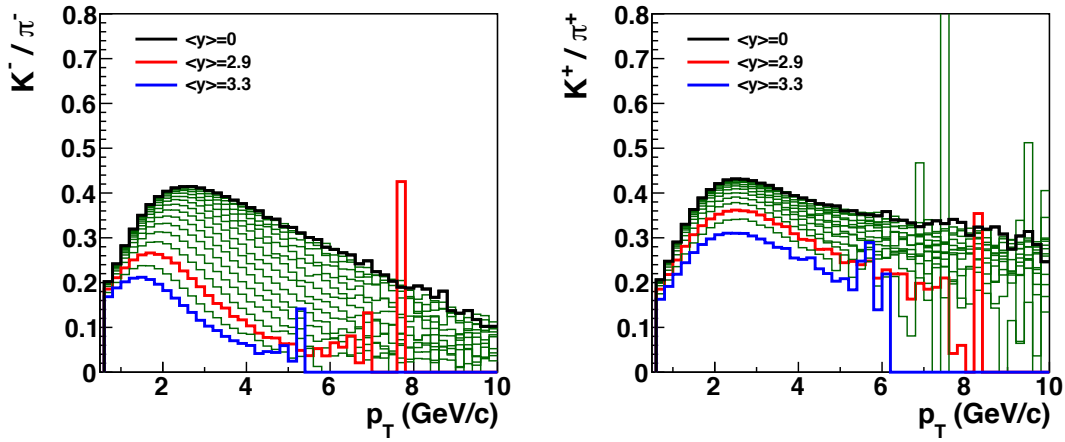


Figure 66: K/π ratio in various η bins from tuned PYTHIA in $p + p$ collisions at $\sqrt{s} = 200$ GeV.

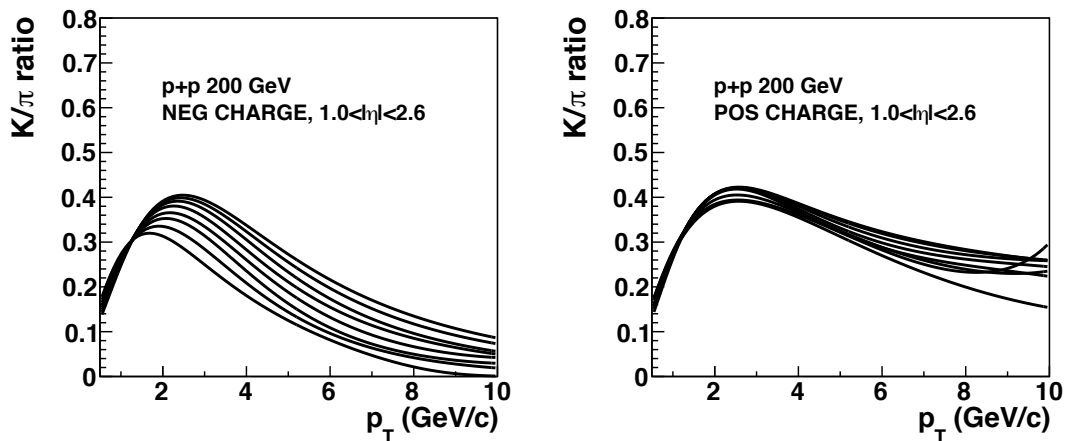


Figure 67: K/π ratio with fit functions in various η bins at forward rapidity from tuned PYTHIA in $p + p$ collisions at $\sqrt{s} = 200$ GeV.

4.3.2 d +Au Collisions

There have been no identified charged hadron measurements in $p + \text{Au}$ collisions in the rapidity range of this study. The estimation starts from d +Au collisions studied previously [92]. Figure 68 shows the p_T spectra of charged and neutral pions in d +Au collisions measured by PHENIX. In the right panel, the combined pion p_T spectrum is compared to the HIJING simulation [98], and a modified Hagedorn function [97] is used to fit the spectrum. Figure 69 shows the kaon p_T spectra, and Fig. 70 shows the ratio between the data and the fit function for pions (left) and kaons (right). Based on fits to p_T spectra of data and HIJING, the K/π ratio of charge combined data and weighting functions are obtained and are shown in Fig. 71. The weighting factors at mid-rapidity have been applied to the p_T spectra in the entire rapidity range for charge combined pions and kaons separately, and Fig. 72 shows the charge combined K/π ratio as a function of p_T from the modified HIJING model in d +Au collisions. In order to have charge separated K/π ratio, a double ratio $((K^\pm/\pi^\pm)/(K^{\text{combined}}/\pi^{\text{combined}}))$ from $p + p$ data is used to estimate $K^{\text{combined}}/\pi^{\text{combined}}$ ratio in d +Au collisions shown in Fig. 72. Figure 73 shows the estimated K^\pm/π^\pm ratios in various η bins in d +Au collisions.

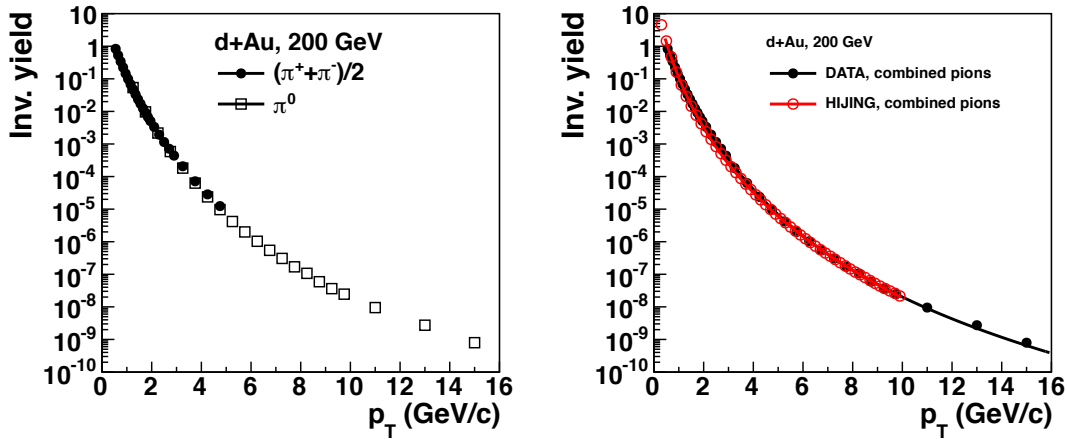


Figure 68: p_T spectra of charged and neutral pions in d +Au collisions at $\sqrt{s_{NN}} = 200$ GeV (left) and comparison with HIJING (right).

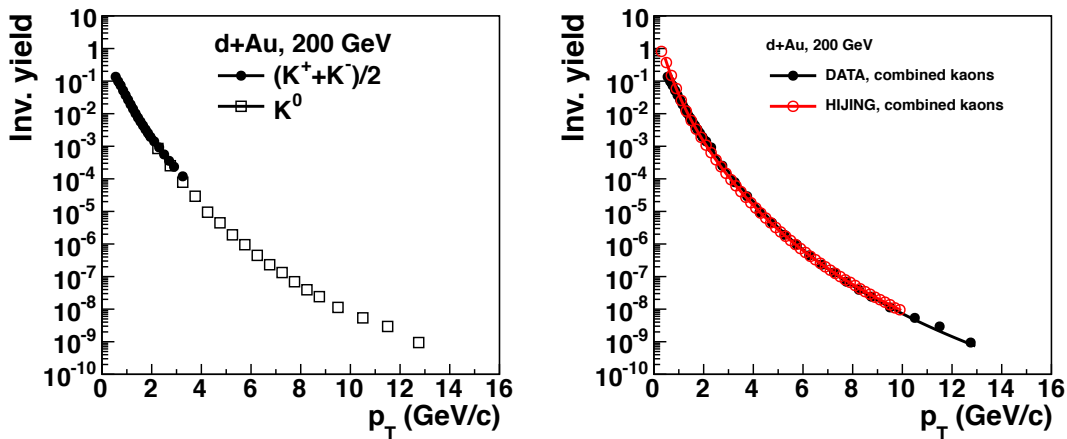


Figure 69: p_T spectra of charged and neutral kaons in d +Au collisions at $\sqrt{s_{NN}} = 200$ GeV (left) and comparison with HIJING (right).

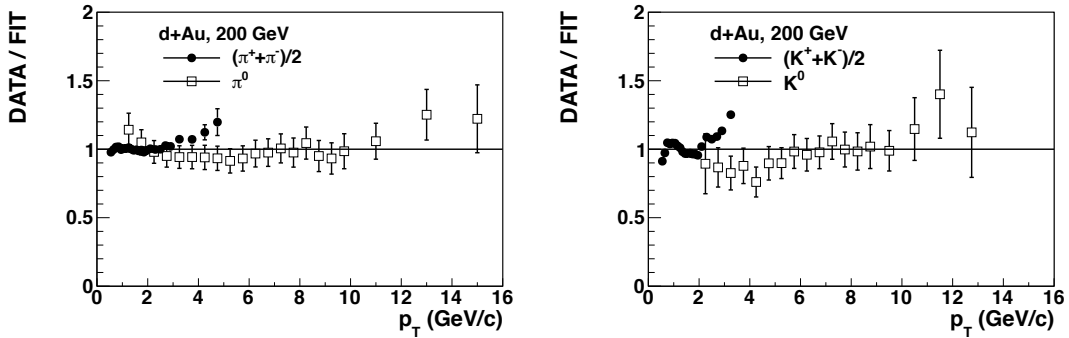


Figure 70: Ratio between data and fit function for pions (left) and kaons (right) in $d+Au$ collisions at $\sqrt{s_{NN}} = 200$ GeV.

in $d+Au$ collisions at $\sqrt{s_{NN}} = 200$ GeV.

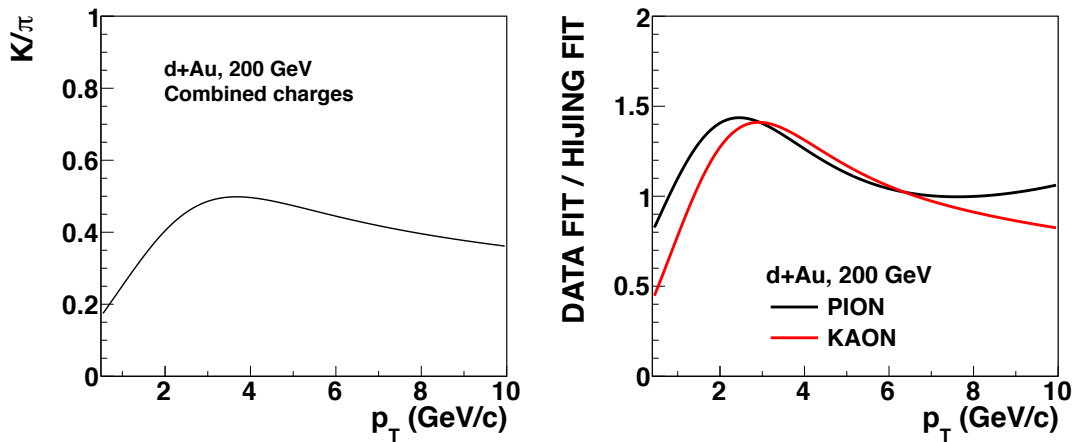


Figure 71: K/π ratio from a fit to data (left) and to the ratio between data and the HIJING model at mid-rapidity in $d+Au$ collisions at $\sqrt{s_{NN}} = 200$ GeV (right).

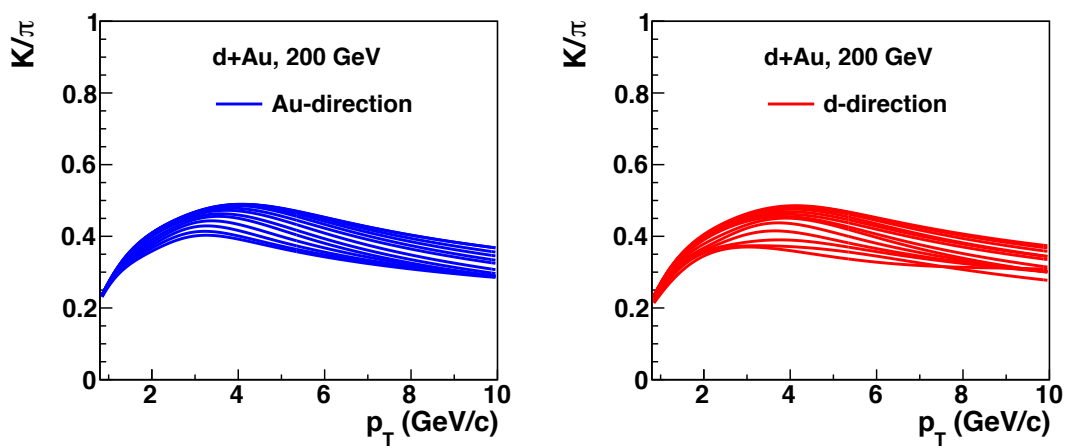


Figure 72: K/π ratio of the modified HIJING model in d +Au collisions at $\sqrt{s_{NN}} = 200$ GeV.

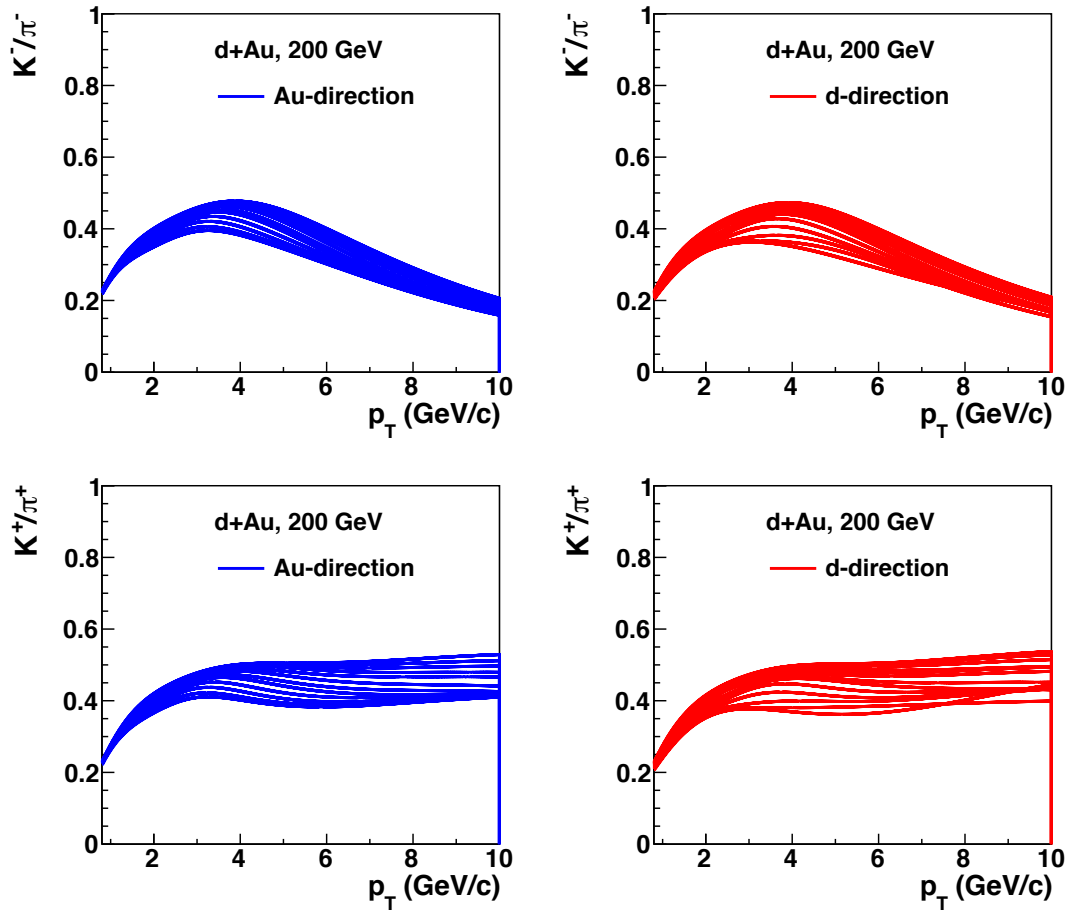


Figure 73: Estimated K/π ratio for negatively (top) and positively (bottom) charged hadrons from the modified HIJING model at forward rapidity in $d+Au$ collisions at $\sqrt{s_{NN}} = 200$ GeV.

4.3.3 $p + \text{Au}$ Collisions

In order to estimate the K^\pm/π^\pm ratio in $p + \text{Au}$ collisions, the HIJING simulation is used again. Figure 74 shows a comparison of the K^\pm/π^\pm ratios at forward and backward rapidity in $p + \text{Au}$ (dashed lines) and $d+\text{Au}$ (solid lines) collisions from HIJING. The K^\pm/π^\pm ratios for $p + \text{Au}$ and $d+\text{Au}$ collisions are similar. Therefore, it is enough to use the estimated K^\pm/π^\pm ratios in $d+\text{Au}$ collisions for $p + \text{Au}$ collisions, and a 30% uncertainty is assigned to cover the difference between $p + \text{Au}$ and $d+\text{Au}$ collisions shown in Fig. 74.

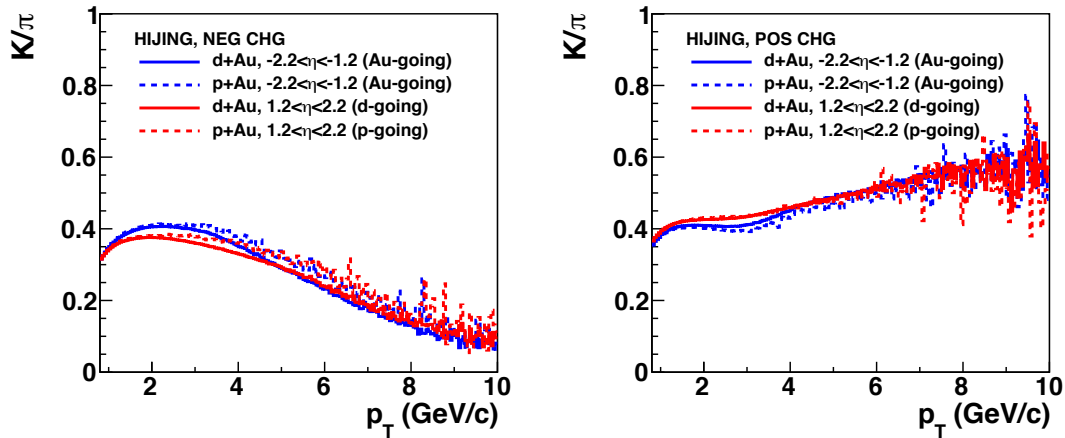


Figure 74: Comparison of the K^\pm/π^\pm ratio as a function of p_T at forward and backward rapidity between $p + \text{Au}$ and $d+\text{Au}$ collisions at $\sqrt{s_{NN}} = 200$ GeV with HIJING. Left : negative hadrons, right : positive hadrons

4.3.4 $p + \text{Al}$ Collisions

According to the HIJING simulation, the differences of the K/π ratios between $p + \text{Al}$ and $p + \text{Au}$ collisions are smaller than the systematic uncertainty assigned already ($\pm 30\%$) in the region of this analysis ($1.25 < p_T < 7.0 \text{ GeV}/c$). In Figure 75, the same K/π ratios are assumed as for $p + \text{Au}$, with the same $\pm 30\%$ systematic uncertainty.

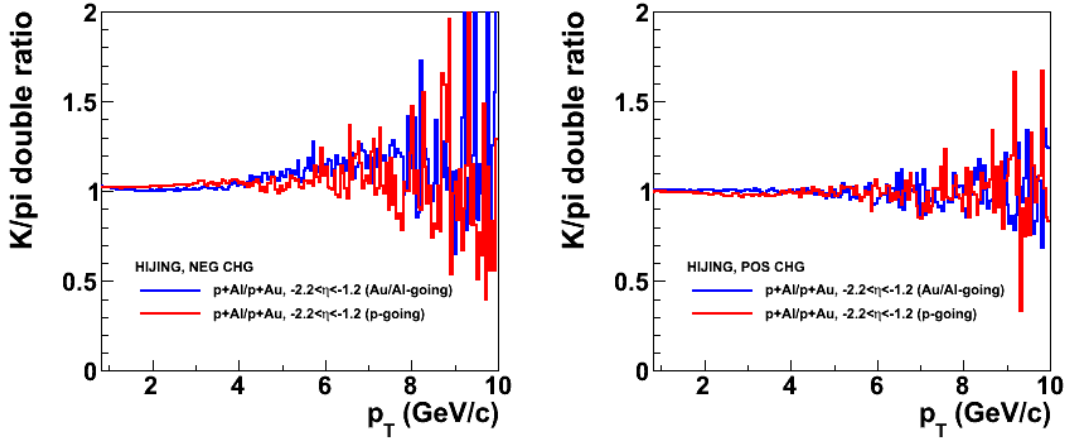


Figure 75: K/π double ratio $(K/\pi \text{ in } p + \text{Al})/(K/\pi \text{ in } p + \text{Au})$ for comparison between $p + \text{Al}$ and $p + \text{Au}$ from the HIJING simulation. The difference is much smaller in the region of this analysis, $1.25 < p_T < 7.0 \text{ GeV}/c$ than the relative $\pm 30\%$ uncertainty assigned to this quantity.

4.4 Fraction of Particles in Reconstructed Momentum Bins

Fraction of particles in reconstructed momentum bins from the GEANT4 simulation are shown in Figs. 76, 77, and 78 for a variety of hadron interaction models provided by the GEANT4 package [99, 100]: QGSP-BERT, FTFP-BERT, and QGSP-BIC in $p + p$ collisions. Figs. 79 and 79 show fraction of particles when K/π ratio is increased or decreased by 30% relatively (1.3 or $0.7 \times K/\pi$) in $p + p$ collisions. The K/π ratios in $p + p$ collisions are listed in Tables 54 and 55. K/π ratios in $p + p$ and $p + \text{Au}(\text{Al})$ collisions are compared in Fig. 81. It provides useful information for understandomg the difference between $p + p$ and $p + A$.

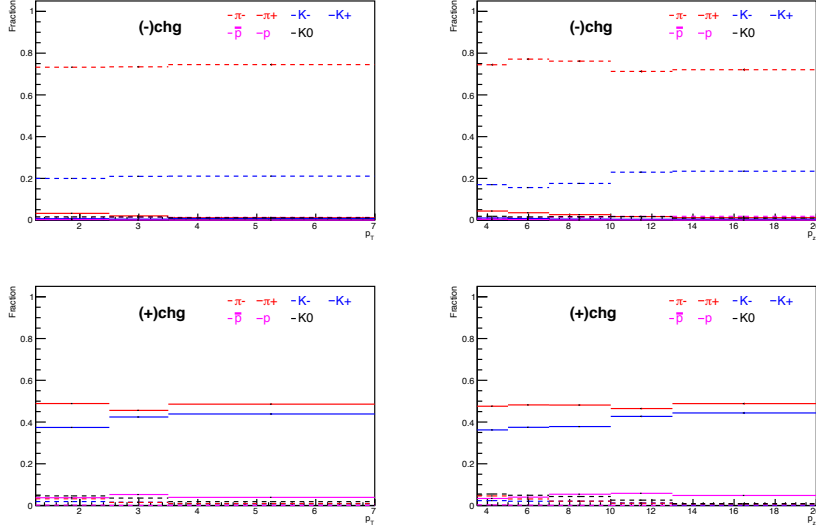


Figure 76: Parent particle contributions for each p_T , p_z bin using the QGSP-BERT package in GEANT4 simulation for $p + p$.

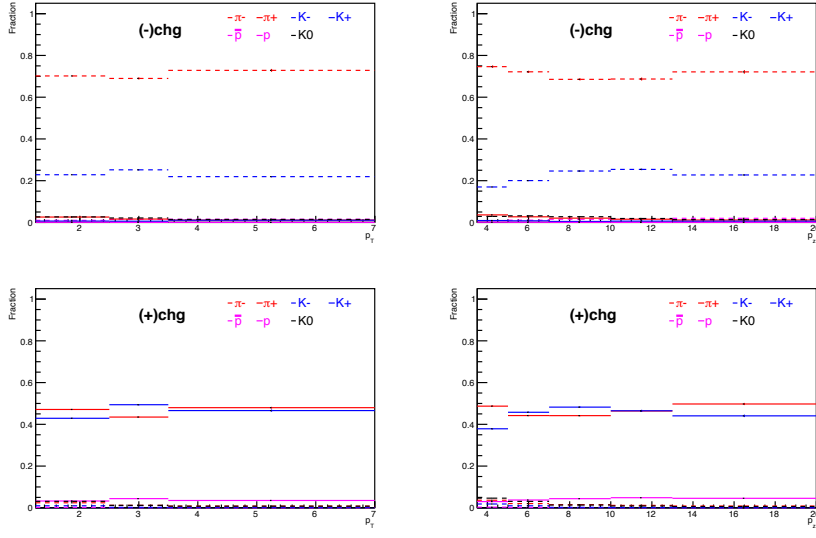


Figure 77: Parent particle contributions for each p_T , p_Z bin using the FTFP-BERT package in the GEANT4 simulation for $p + p$.

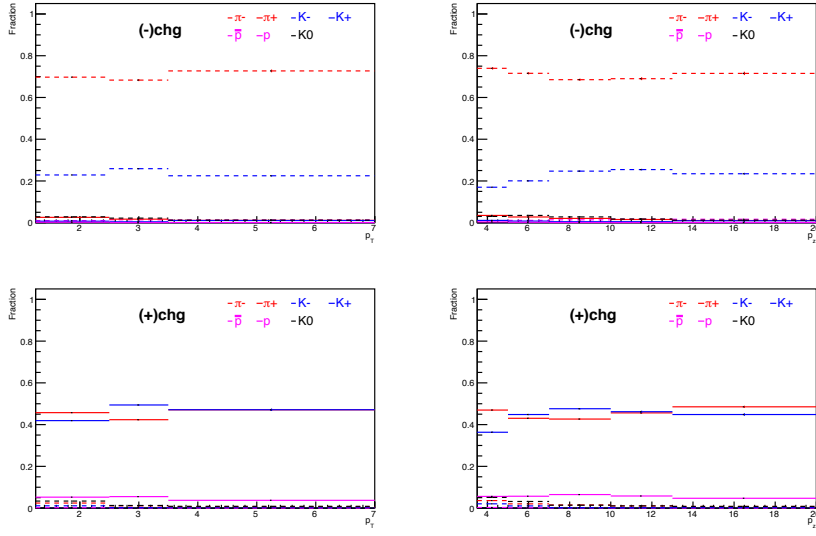


Figure 78: Parent particle contribution for each p_T , p_Z bin using QGSP-BIC package in GEANT4 simulation for $p + p$.

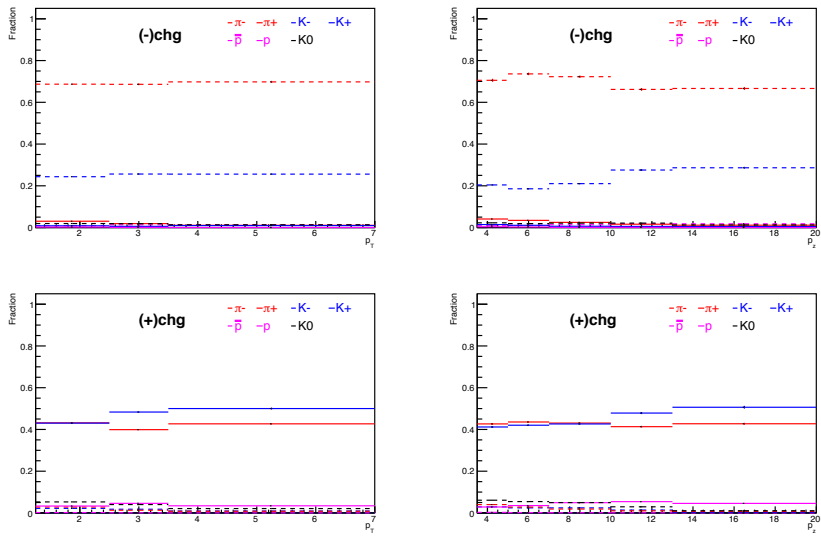


Figure 79: Parent particle contribution for each p_T , p_Z bin when K/π ratio is increased by 30% relatively ($1.3 \times K/\pi$) using QGSP-BERT package in GEANT4 simulation for $p + p$.

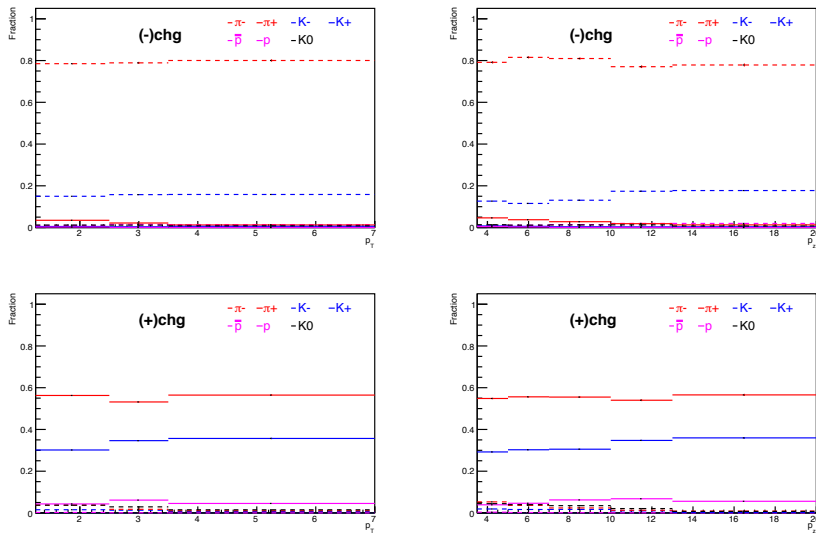


Figure 80: Parent particle contribution for each p_T , p_Z bin when K/π ratio is decreased by 30% relatively ($0.7 \times K/\pi$) using QGSP-BERT package in GEANT4 simulation for $p + p$.

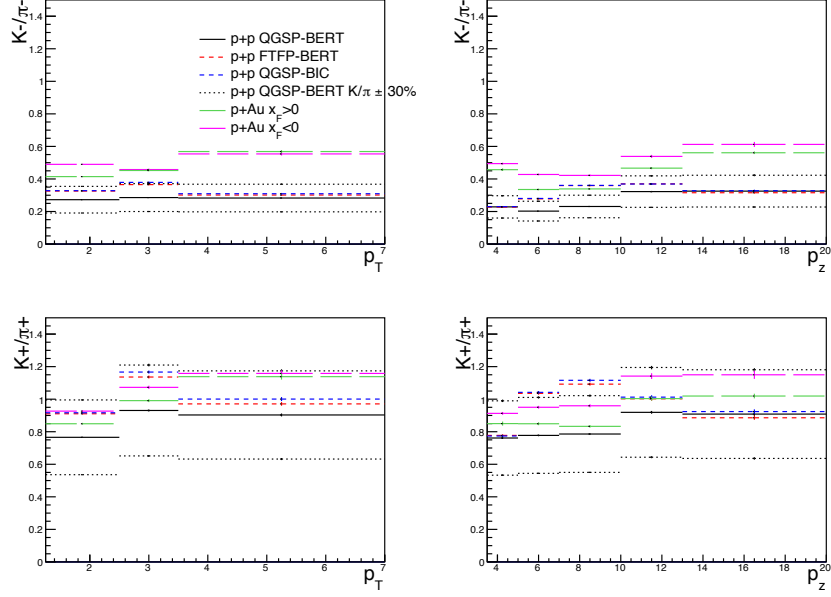


Figure 81: Parent K^\pm/π^\pm ratio in bins of reconstructed p_T , p_z of muon spectrometers. Black dashed lines show the K/π ratio when the initial (particle generation level in the simulation) K/π ratio is increased or decreased by 30% ($(1.0 \pm 0.3) \times K/\pi$) using the QGSP-BERT package for the hadron cocktail simulation in $p + p$. Each color corresponds to a different hadron interaction package in GEANT4. The K^\pm/π^\pm ratio in $p + \text{Au}$ collisions is shown as magenta ($x_F > 0$), or green ($x_F > 0$). QGSP-BERT is used for $p + \text{Au}$.

Table 54: Table of Fig. 81 for negatively charged hadrons. Parent K^-/π^- ratio in bins of reconstructed p_T , p_z of muon spectrometers from hadron-cocktail simulation in $p + p$

bin	QGSP -BERT	FTFP -BERT	QGSP -BIC	QGSP-BERT $K/\pi + 30\%$	QGSP-BERT $K/\pi - 30\%$
K^-/π^-					
p_T bin 1	0.273	0.326	0.328	0.354	0.191
p_T bin 2	0.286	0.365	0.379	0.371	0.200
p_T bin 3	0.283	0.301	0.309	0.368	0.198
p_z bin 1	0.228	0.228	0.230	0.297	0.160
p_z bin 2	0.202	0.278	0.280	0.263	0.142
p_z bin 3	0.231	0.359	0.361	0.300	0.162
p_z bin 4	0.322	0.370	0.369	0.419	0.226
p_z bin 5	0.325	0.315	0.328	0.423	0.228

Table 55: Table of Fig. 81 for positively charged hadrons. Parent K^+/π^+ ratio in bins of reconstructed p_T , p_z of muon spectrometers from hadron-cocktail simulation in $p + p$

bin	QGSP -BERT	FTFP -BERT	QGSP -BIC	QGSP-BERT $K/\pi + 30\%$	QGSP-BERT $K/\pi - 30\%$
K^+/π^+					
p_T bin 1	0.766	0.910	0.916	0.995	0.536
p_T bin 2	0.931	1.136	1.167	1.210	0.651
p_T bin 3	0.903	0.971	1.001	1.174	0.632
p_z bin 1	0.761	0.777	0.774	0.990	0.533
p_z bin 2	0.777	1.036	1.042	1.011	0.544
p_z bin 3	0.786	1.092	1.116	1.022	0.550
p_z bin 4	0.919	1.002	1.012	1.195	0.643
p_z bin 5	0.908	0.886	0.924	1.181	0.636

4.5 Momentum Migration

The GEANT4 simulation with the hadron cocktail allows us to estimate the migration from the original momentum bin to the reconstructed momentum bin for tracks reconstructed in the muon spectometers. The p_T migration matrix in Fig. 82 shows the number of tracks for each original (generated in the GEANT4 simulation) and reconstructed p_T bin. For instance, the green element on Fig. 82 represents the number of track originating in the 2nd p_T bin as negative charge, then reconstructed in the 2nd p_T bin as negative charge. In Fig. 82, both charges are considered simultaneously in order to include charge conversion in the reconstruction. Left top and right bottom sides represent charge conversion. Because the trigger efficiency is included, the matrix elements are not integer. Elements out of the red boxes are overflow bins. For example, in Fig. 82, 1 $(-)$, 5 $(-)$, 1 $(+)$, and 5 $(+)$ are overflow bins below or above the p_T range of this analysis ($1.25 < p_T < 7.0$ GeV/ c) for unfolding.

Once the momentum migration matrix is computed, it is possible to obtain A_N in the original momentum bin (A_N^{True}) from linear equations which relate A_N in reconstructed bins (A_N^{Reco}) to the A_N in the original bins. For example, 12 below is a linear equation between A_N^{True} 's, elements of migration matrix, and A_N^{Reco} at

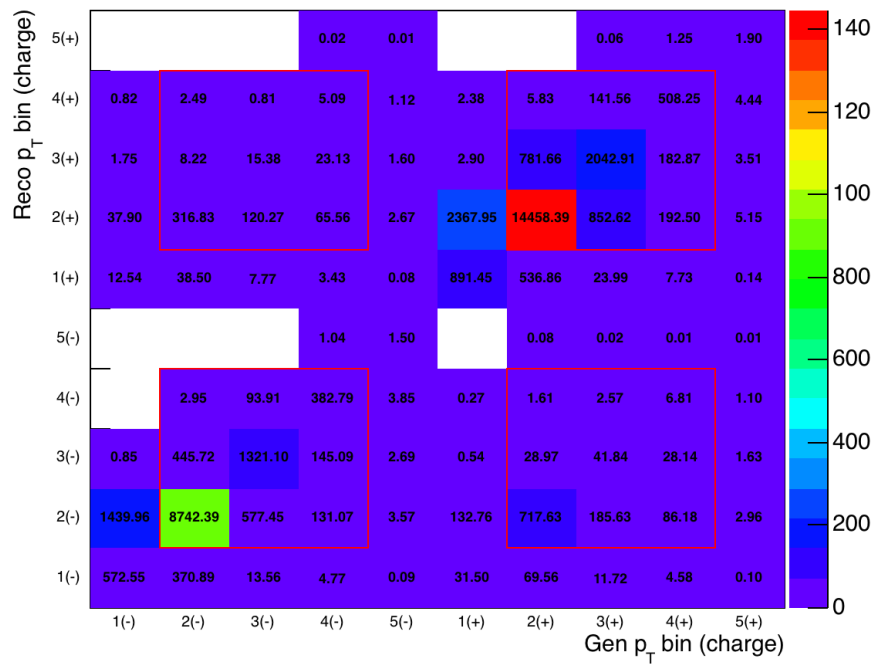


Figure 82: Migration matrix used to calculate the original A_N , obtained from the full GEANT4 simulation, with the default QGSP-BERT hadronic shower package.

1st bin:

$$\begin{aligned} & \frac{N(1_{True} \rightarrow 1_{Reco})}{N_{Reco}^1} \cdot A_1^{True} + \frac{N(2_{True} \rightarrow 1_{Reco})}{N_{Reco}^1} \cdot A_2^{True} \\ & + \frac{N(3_{True} \rightarrow 1_{Reco})}{N_{Reco}^1} \cdot A_3^{True} + \dots = A_1^{Reco} \end{aligned} \quad (12)$$

In Eq. 12, $N(2_{True} \rightarrow 1_{Reco})$ represents one of the elements of the migration matrix when the original bin is the 2nd and it is reconstructed in the 1st bin. A_2^{True} is A_N at 2nd original bin, A_1^{Reco} is A_N at 1st reconstructed bin. A series of equations like Eq. 12 become Eq. 13.

$$\begin{bmatrix} \frac{N(1_{True} \rightarrow 1_{Reco})}{N_{Reco}^1} & \frac{N(2_{True} \rightarrow 1_{Reco})}{N_{Reco}^1} & \dots & \frac{N(J_{True} \rightarrow 1_{Reco})}{N_{Reco}^1} \\ \frac{N(1_{True} \rightarrow 2_{Reco})}{N_{Reco}^2} & \frac{N(2_{True} \rightarrow 2_{Reco})}{N_{Reco}^2} & \dots & \frac{N(J_{True} \rightarrow 2_{Reco})}{N_{Reco}^2} \\ \vdots & \vdots & \ddots & \vdots \\ \frac{N(1_{True} \rightarrow J_{Reco})}{N_{Reco}^J} & \frac{N(2_{True} \rightarrow J_{Reco})}{N_{Reco}^J} & \dots & \frac{N(J_{True} \rightarrow J_{Reco})}{N_{Reco}^J} \end{bmatrix} \cdot \begin{bmatrix} A_1^{True} \\ A_2^{True} \\ \vdots \\ A_J^{True} \end{bmatrix} = \begin{bmatrix} A_1^{Reco} \\ A_2^{Reco} \\ \vdots \\ A_J^{Reco} \end{bmatrix} \quad (13)$$

This is a matrix equation now,

$$M \cdot A^{True} = A^{Reco}, \quad (14)$$

where M is the normalized migration matrix which can be calculated from the original migration matrix in Fig. 82. Each of original migration matrix element is normalized by each reconstructed bin

$$M_{ij} = \frac{N(j_{True} \rightarrow i_{Reco})}{N_{Reco}^i}. \quad (15)$$

Plot (b) in Fig. 83 is an example of normalized migration matrix when the original migration matrix is (a). Since A^{Reco} is the measured asymmetry, only A^{True} is

unknown. Eq. 14 can be converted into Eq. 16

$$M^{-1} \cdot A^{True} = A^{Reco}, \quad (16)$$

where M^{-1} is the inverse of the normalized migration matrix on the panel (b) in Fig. 83. Therefore from the matrix calculation above, we are able to access A_N^{True} for each p_T, x_F bin. This procedure is a kind of unfolding in a broad sense, however no regularization is required because the number of bins is small and crosstalk is very small. Therefore, systematic bias is minimum.

Statistical uncertainties are calculated using Eq. 17. Only diagonal terms are considered because elements of A^{Reco} are uncorrelated, as they were obtained from measurement:

$$\delta A^{Reco} = \delta M^{-1} \cdot \delta A^{Reco}, \quad (17)$$

where

$$(\delta A_j^{True})^2 = \sum_{i=1}^n ([M^{-1}]_{ji})^2 \cdot (\delta A_i^{Reco})^2. \quad (18)$$

4.5.1 Toy Simulation to Test the Unfolding Procedure

To justify the procedure, a toy simulation is performed assuming a linearly increasing input A_N which is suitable for checking migration effects qualitatively and quantitatively. Also, the measured A_N of (+) charged hadrons shows a trend of increasing at large x_F . Migration matrices for p_T, x_F are prepared from the full GEANT4 simulation using three kinds of hadron interaction packages: default

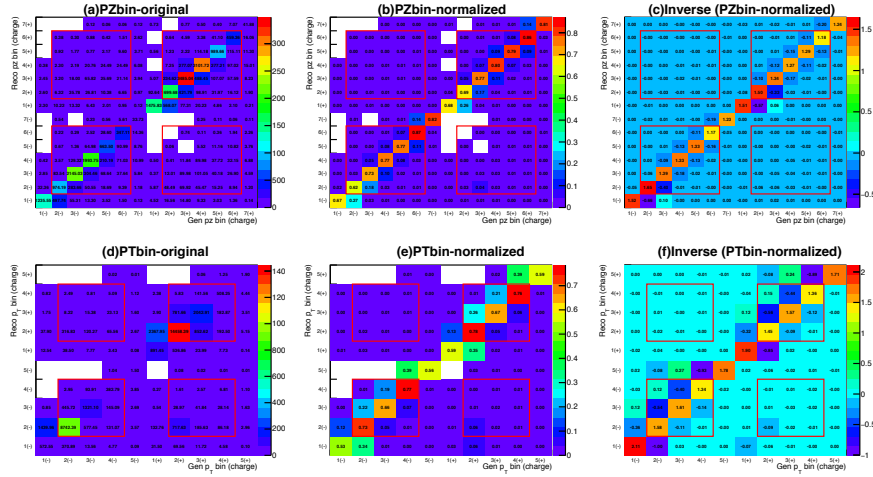


Figure 83: Migration matrices for calculating the original A_N , obtained from a full GEANT4 simulation, with the default QGSP-BERT hadronic shower package. (a) Original migration matrix in p_T . (b) Normalized migration matrix, normalized for each Reco p_T bin. (c) Inverse of normalized migration matrix in p_T . (d) Original migration matrix in x_F . (e) Normalized migration matrix. (f) Inverse of normalized migration matrix in x_F .

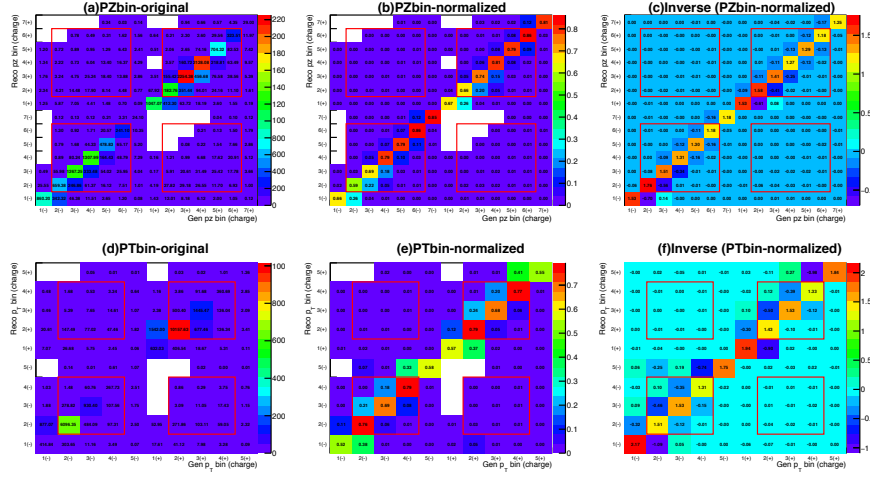


Figure 84: Migration matrices for calculating the original A_N , obtained from a full GEANT4 simulation, using FTFP-BERT. (a) Original migration matrix in p_T . (b) Normalized migration matrix, normalized for each Reco p_T bin. (c) Inverse of normalized migration matrix in p_T . (d) Original migration matrix in x_F . (e) Normalized migration matrix. (f) Inverse of normalized migration matrix in x_F .

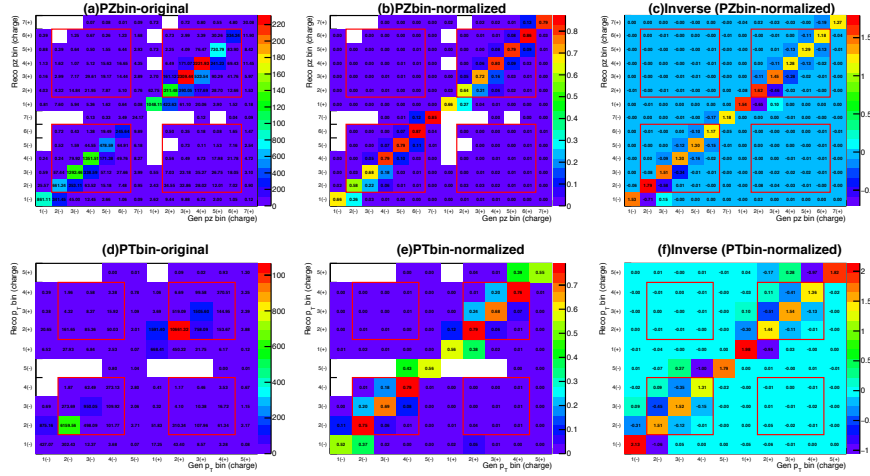


Figure 85: Migration matrices for calculating the original A_N , obtained from a full GEANT4 simulation, using QGSP-BIC.

QGSP-BERT in Fig. 83, FTFP-BERT in Fig. 84, and QGSP-BIC in Fig. 85. The default QGSP-BERT is chosen for the toy simulation.

The procedure used in [101] is the following:

1. Generate random tracks which have a p_T distribution based on the migration matrix in Fig. 82. Uniformly distributed random ϕ_0 and random spin direction (\uparrow, \downarrow) are assigned.
2. Apply a weight $(1 \pm A_N^{True} \cdot \cos(\phi_0))$ for each track based on the manually assigned initial asymmetry ($A_N^{True} = 0.05 \cdot p_T$ for $(-)$, $0.1 \cdot p_T$ for $(+)$). The sign is determined from the random spin direction in step 1 and ϕ_0 is the azimuthal angle of the track at the generation level.
3. Extract A_N^{Reco} by fitting the cosine modulation of each Reco bin
4. Obtain A_N^{Unfold} by matrix calculation using Eq. 16
5. Repeat 10000 times from step 1 to 4 to obtain smooth distributions of unfolded asymmetry A_N^{Unfold} .

The results are shown in Fig. 86. On the left panel, input A_N^{True} (blue) and A_N^{Unfold} (red) are consistent each other. The 1st, 5th, 6th, and 10th bins are overflow bins which will not be included in the result. The right panel shows that A_N^{Reco} (black) is different from A_N^{True} (blue), as a result of bin migration.

A_N^{Unfold} calculated from the A_N^{Reco} is shown on the left panel (A_N^{Unfold} (red)). The statistical uncertainty is calculated from Eq. 17 in each iteration, then compared with the width of the unfolded A_N^{True} distribution in Fig. 87. The Gaussian width of the A_N^{Unfold} distribution (blue) and the mean value of δA_N^{Unfold} (red) calculated in each iteration are consistent with each other.

4.5.2 Unfolding Result

Unfolding Result in $p + p$ collisions

The measured A_N , δA_N^{Stat} is converted into unfolded A_N , δA_N^{Stat} using the matrix calculation in Eqs. 16 and 17. Three different hadron interaction packages are used. Fig. 88 shows unfolded A_N in $p + p$ collisions using different hadron interaction packages in GEANT4. Fig. 89 shows unfolded A_N with changing the K/π ratio by $\pm 30\%$. The variation of A_N due to different hadron interaction packages and $\pm 30\%$ of K/π variation are included as a source of systematic uncertainty.

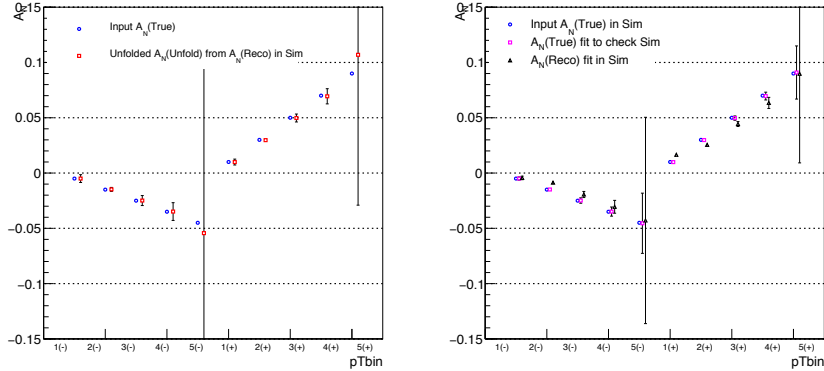


Figure 86: Toy simulation result. Linear input A_N^{True} (blue) and A_N^{Unfold} (red) on the left panel show good agreement. Right panel shows the input A_N^{True} (blue), the cosine fit result of input A_N^{True} (pink) and A_N^{Reco} (black) to cross check each step of the toy simulation. 1st, 5th, 6th, and 10th bins are overflow bins.

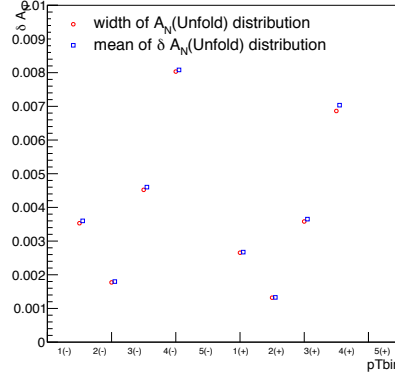


Figure 87: Statistical uncertainty calculated in the simulation. Blue is gaussian width of the A_N^{Unfold} distribution and red is the mean value of δA_N^{True} , calculated using Eq. 18 in each iteration. They are consistent with each other. 1st, 5th, 6th, and 10th bins are overflow bins.

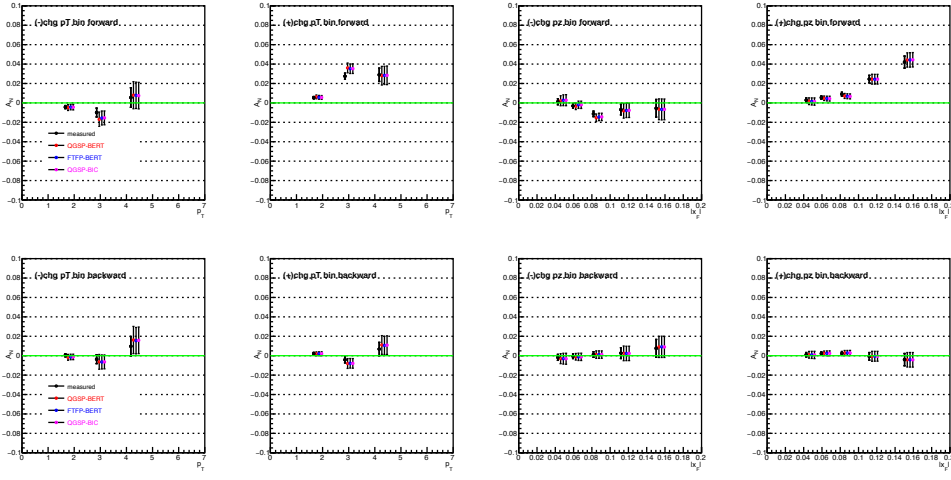


Figure 88: Unfolded A_N in $p+p$ collisions using different hadron interaction packages in GEANT4. The difference is included as a source of systematic uncertainty.

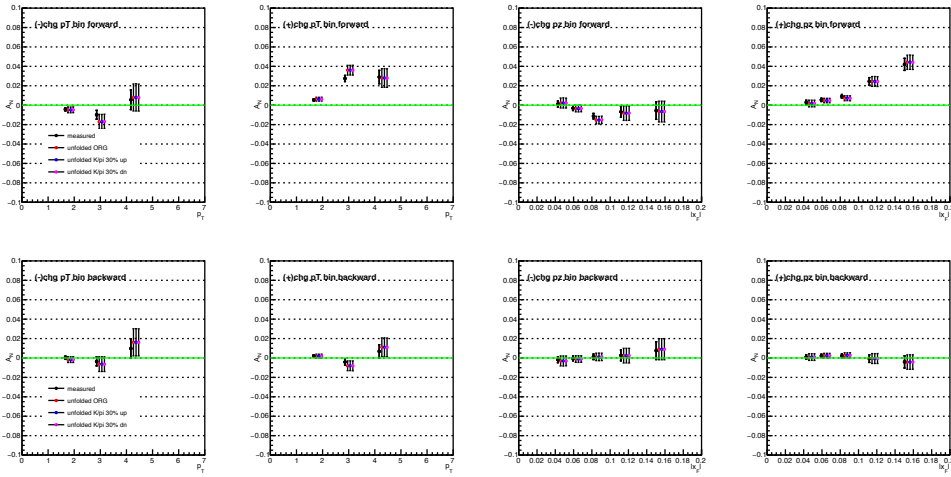


Figure 89: Unfolded A_N in $p+p$ collisions with changing the K/π ratio by $\pm 30\%$. The difference is included in the systematic uncertainty.

Unfolding Result in $p + \text{Au}$ collisions

The same method is used for $p + \text{Au}$ collisions. Fig. 90 shows the migration matrices. Fig. 91 shows unfolded A_N in $p + \text{Au}$ collisions with changing the K/π ratio by $\pm 30\%$.

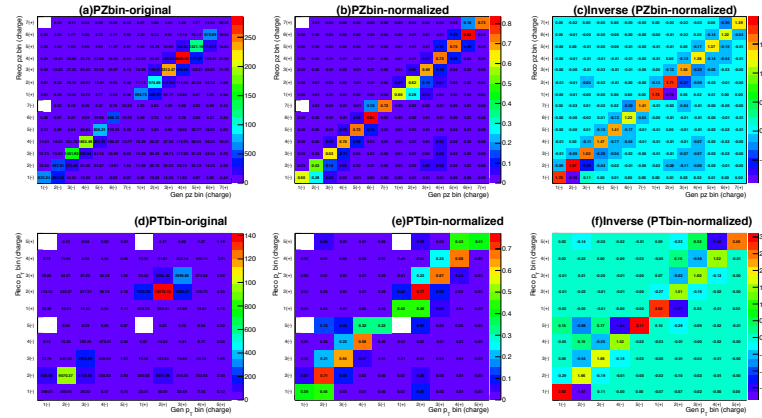


Figure 90: Migration matrices for calculating the original A_N in $p + \text{Au}$ collisions, obtained from the full GEANT4 simulation using the default QGSP-BERT hadronic shower package. (a) Original migration matrix in p_T . (b) Normalized migration matrix, normalized for each $\text{Reco } p_T$ bin. (c) Inverse of normalized migration matrix in p_T . (d) Original migration matrix in x_F . (e) Normalized migration matrix. (f) Inverse of normalized migration matrix in x_F .

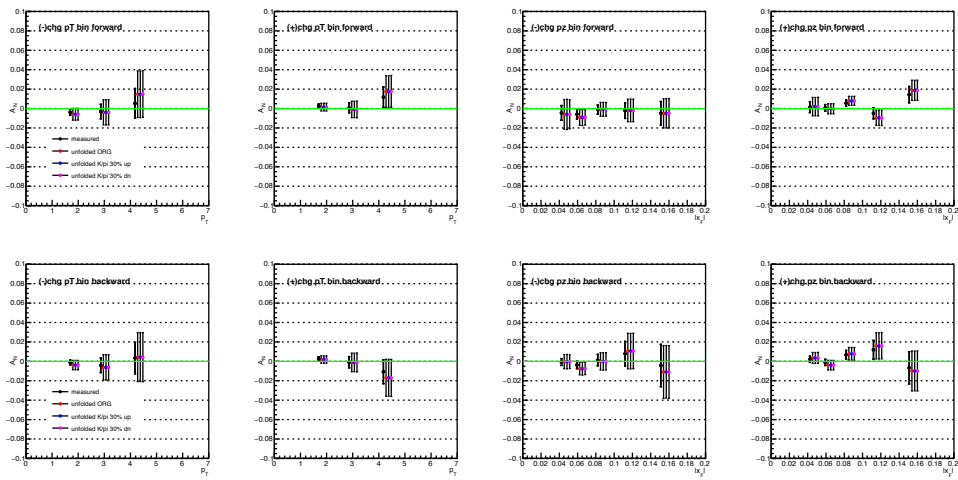


Figure 91: Unfolded A_N in $p + \text{Au}$ collisions with changing the K/π ratio by $\pm 30\%$. The difference is included in the systematic uncertainty.

4.6 Systematic Uncertainty

Systematic uncertainties for unfolded A_N are discussed in this section. Following subsections describe each source of systematic uncertainty. Systematic uncertainties are listed in Tables. 56, 57, 58, 59, 60, 61, 62, 63, 64, 65, 66, 67.

4.6.1 Analysis Method

The difference between the results with the maximum likelihood method and the cosine fit method is assigned as a source of systematic uncertainty for all results. It is listed as δA_N^{method} in the tables. Figs. 92, 93, 94 show results from the cosine fit method. The comparison with results from the maximum likelihood method is shown in Figs. 95, 96, 97, 98. The sine term is consistent with zero as shown in Figs. 99, 100.

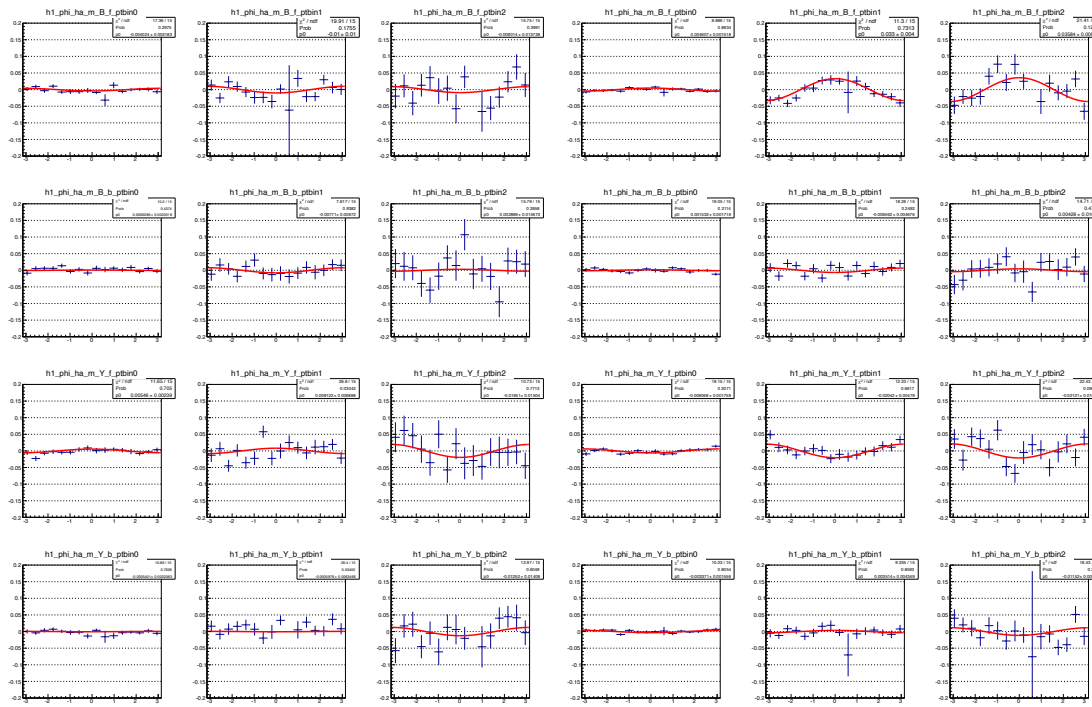


Figure 92: Cosine fit result for 3 p_T bins. Left side is negative charge, right side is positive charge. 1st and 2nd rows are for the blue beam, 3rd and 4th rows for the yellow beam. 1st and 3rd rows are forward rapidity, 2nd and 4th rows are backward rapidity.

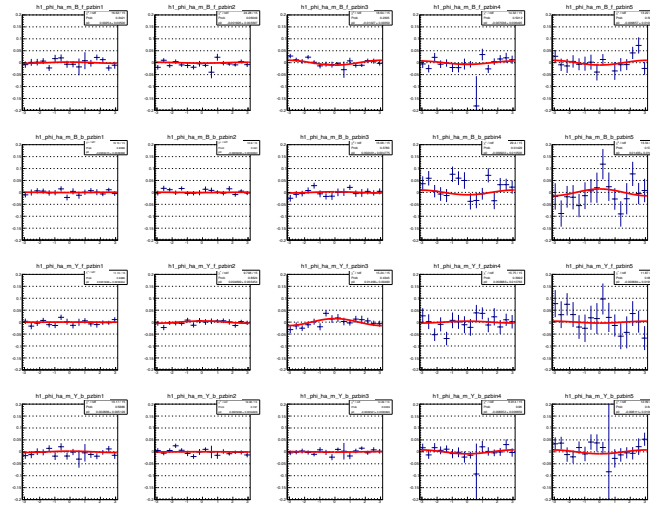


Figure 93: Cosine fit result for 5 x_F bins for negative charge. 1st and 2nd rows are for the blue beam, 3rd and 4th rows for the yellow beam. 1st and 3rd rows are forward rapidity, 2nd and 4th rows are backward rapidity.

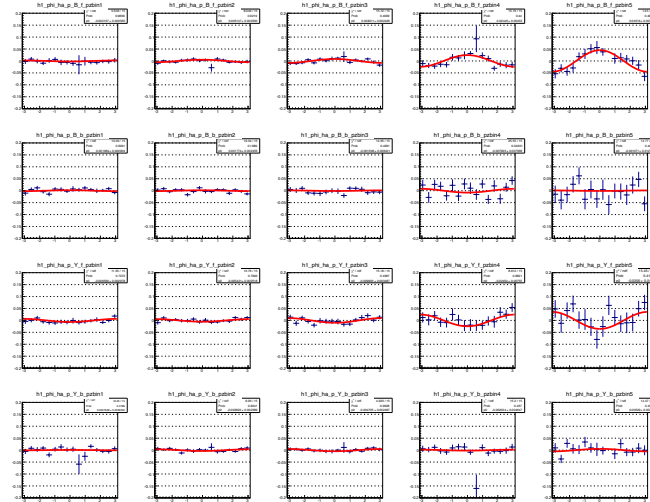


Figure 94: Cosine fit result for 5 x_F bins for positive charge. 1st and 2nd rows are for the blue beam, 3rd and 4th rows for the yellow beam. 1st and 3rd rows are forward rapidity, 2nd and 4th rows are backward rapidity.

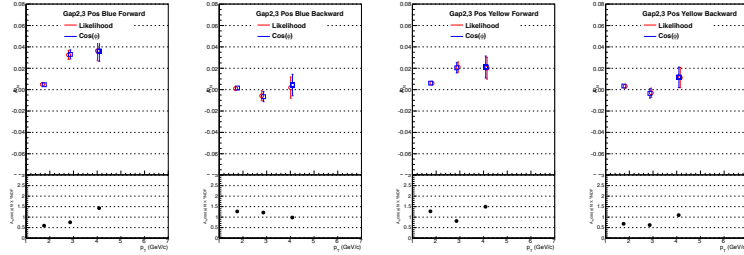


Figure 95: Comparison between the maximum likelihood method and the cosine fit method for 3 p_T bins for positive charge in $p + \text{Au}$ collisions. They agree each other. The bottom panel shows χ^2/ndf for the cosine fit; it is smaller than 2.

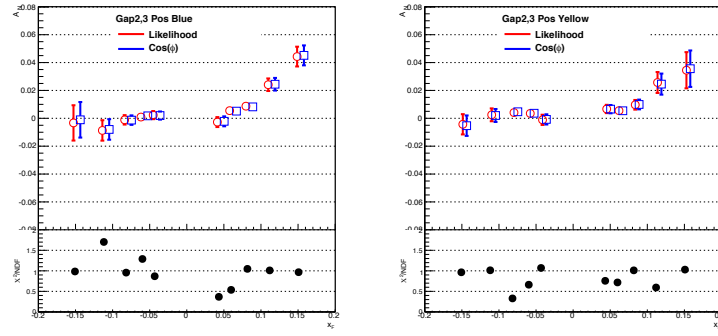


Figure 96: Comparison between the maximum likelihood method and the cosine fit method for 5 x_F bins for positive charge in $p + p$ collisions. They agree each other. The bottom panel shows χ^2/ndf for the cosine fit; it is smaller than 2.

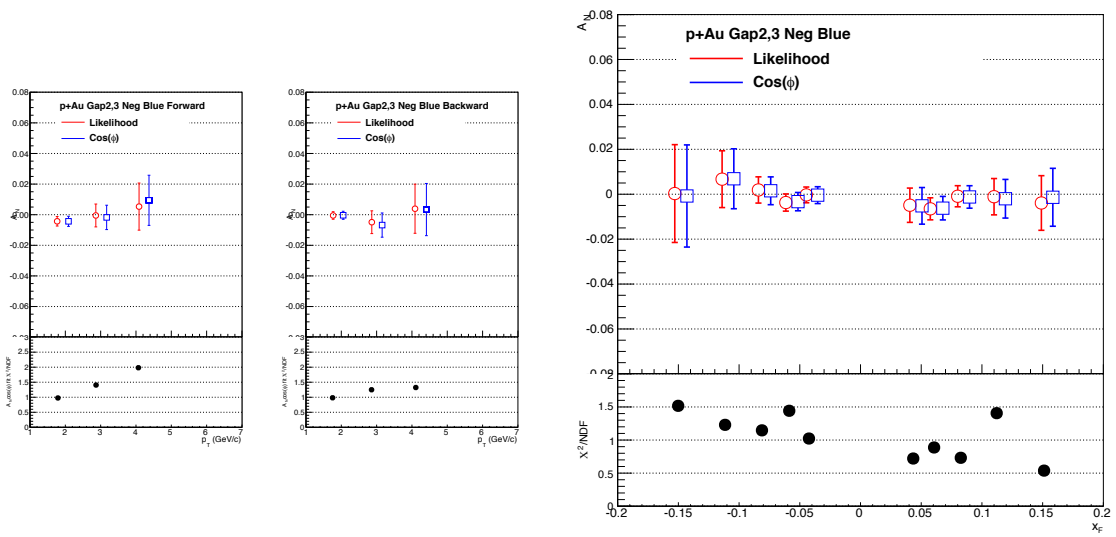


Figure 97: Comparison between the maximum likelihood method and the cosine fit method for 3 p_T bins (left) and 5 x_F bins (right) for negative charge in $p + \text{Au}$ collisions. They agree each other. The bottom panel shows χ^2/ndf for the cosine fit; it is smaller than 2.

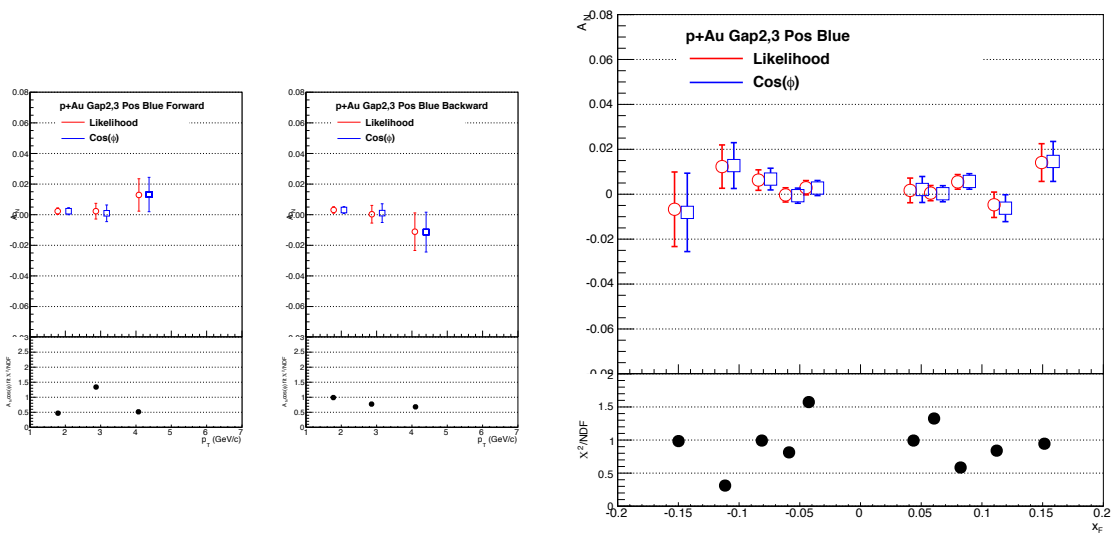


Figure 98: Comparison between the maximum likelihood method and the cosine fit method for 3 p_T bins (left) and 5 x_F bins (right) for positive charge in $p + \text{Au}$ collisions. They agree each other. The bottom panel shows χ^2/ndf for the cosine fit; it is smaller than 2.

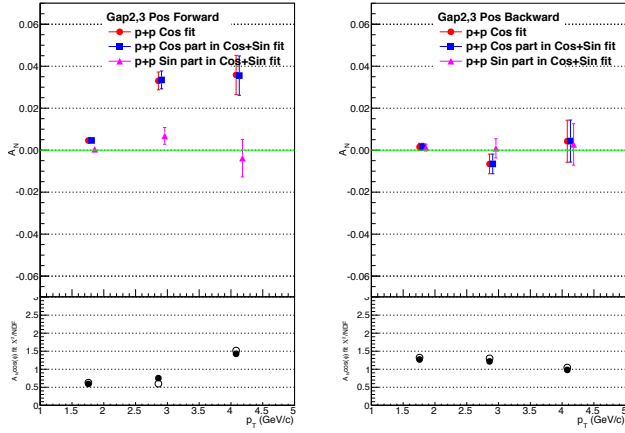


Figure 99: The sine term in the cosine+sine fit is consistent with zero for 3 p_T bins for the blue beam for positive charge in $p + p$ collisions. The bottom panel shows χ^2/ndf for the cosine fit (filled circle) and cosine+sine (open circle) fit; it is smaller than 2.

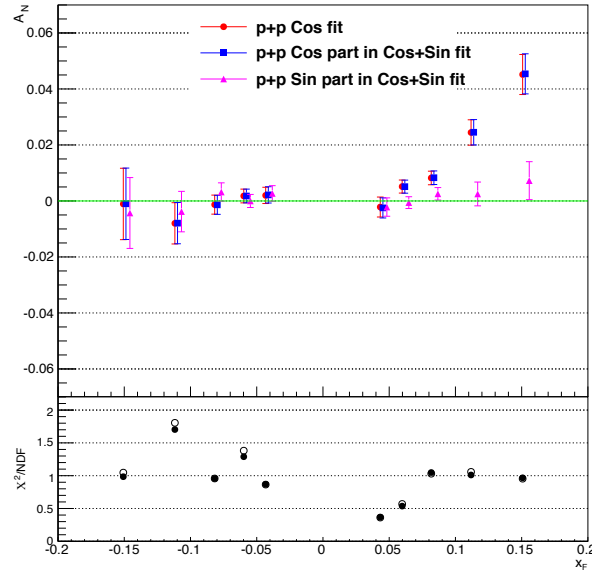


Figure 100: The sine term in the cosine+sine fit is consistent with zero for 5 x_F bins for the blue beam for positive charge in $p + p$ collisions. The bottom panel shows χ^2/ndf for the cosine fit (filled circle) and cosine+sine (open circle) fit; it is smaller than 2.

4.6.2 Difference between Unfolded and Measured Asymmetries

As mentioned in the unfolding subsection, the difference between unfolded and measured asymmetries is included as a source of systematic uncertainty. It is listed as $\delta A_N^{\text{Unfold}}$ in tables.

4.6.3 Contribution from Other Spices

K^0 , p , and \bar{p} are included in the hadron cocktail simulation, so we consider the asymmetries from those sources in the systematic uncertainty ($\delta A_N^{\text{proton}}$). We assumed that the size of A_N from K^0 is comparable to those from K^+ and K^- . Based on the previous BRAHMS result [14, 102], $A_N(p)$, $A_N(\bar{p})$, $A_N(K^0)$ are assumed to be smaller than ± 0.02 . This uncertainty is applied to both forward and backward rapidity ($x_F > 0$) and to both $p + p$ and $p + \text{Au}$. It is listed as $\delta A_N^{\text{proton}}$ in the tables.

4.6.4 Uncertainty in the Migration Matrix

We performed a hadron cocktail simulation using three hadron interaction packages in GEANT4, called QGSP-BERT, FTFP-BERT, and QGSP-BIC. These simulate different aspects of interactions between particles and material especially in the front absorber located in front of the Muon Tracker. For example, momentum migration and charge conversion can be different, so that the migration matrix in the previous section can be changed. The changes in the unfolded A_N caused by

different migration matrices in the unfolding stage in Figs. 88 and 89 are considered in the systematic uncertainty ($\delta A_N^{p_{kg}}$). Also, the K/π ratio could affect the migration matrix, so this is studied by checking the changes within the variation of K/π ratio by $\pm 30\%$. This uncertainty is very small ($< 10^{-4}$) and is included in the unfolded asymmetry ($\delta A_N^{K/\pi \pm 30}$). The following tables will list each source of systematic uncertainty for the unfolded asymmetries.

p_T (GeV/c)	$\delta A_N^{syst.}$	δA_N^{method}	δA_N^{proton}	δA_N^{pkg}	$\delta A_N^{k/\pi\pm 30}$	$\delta A_N^{\text{Unfold}}$
δA_N ($\times 10^{-2}$) for negative charge. $x_F > 0$						
(1.25, 2.50)	+0.10 -0.07	+0.03 -0.03	+0.06 -0.06	+0.05 -0.00	+0.01 -0.01	+0.05 -0.00
(2.50, 3.50)	+0.73 -0.10	+0.07 -0.07	+0.06 -0.06	+0.16 -0.00	+0.01 -0.01	+0.71 -0.00
(3.50, 7.00)	+0.17 -0.30	+0.17 -0.17	+0.05 -0.05	+0.00 -0.05	+0.01 -0.01	+0.00 -0.24
δA_N ($\times 10^{-2}$) for negative charge. $x_F < 0$						
(1.25, 2.50)	+0.21 -0.04	+0.03 -0.03	+0.02 -0.02	+0.04 -0.00	+0.00 -0.00	+0.21 -0.00
(2.50, 3.50)	+0.29 -0.07	+0.07 -0.07	+0.03 -0.03	+0.00 -0.01	+0.00 -0.00	+0.28 -0.00
(3.50, 7.00)	+0.18 -0.67	+0.18 -0.18	+0.03 -0.03	+0.00 -0.07	+0.00 -0.00	+0.00 -0.65
δA_N ($\times 10^{-2}$) for positive charge. $x_F > 0$						
(1.25, 2.50)	+0.17 -0.20	+0.02 -0.02	+0.17 -0.17	+0.00 -0.06	+0.00 -0.00	+0.00 -0.08
(2.50, 3.50)	+0.19 -0.88	+0.06 -0.06	+0.18 -0.18	+0.00 -0.08	+0.00 -0.00	+0.00 -0.85
(3.50, 7.00)	+0.17 -0.14	+0.08 -0.08	+0.12 -0.12	+0.04 -0.00	+0.00 -0.01	+0.10 -0.00
δA_N ($\times 10^{-2}$) for positive charge. $x_F < 0$						
(1.25, 2.50)	+0.09 -0.09	+0.04 -0.04	+0.08 -0.08	+0.01 -0.00	+0.00 -0.00	+0.02 -0.00
(2.50, 3.50)	+0.41 -0.13	+0.07 -0.07	+0.11 -0.11	+0.02 -0.00	+0.01 -0.01	+0.38 -0.00
(3.50, 7.00)	+0.15 -0.45	+0.13 -0.13	+0.08 -0.08	+0.00 -0.05	+0.01 -0.01	+0.00 -0.42

Table 56: Systematic uncertainty of unfolded A_N in p_T bins in $p + p$ collisions.

Table 57: Systematic uncertainty of unfolded A_N in x_F bins for negative charge in $p + p$ collisions

x_F	$\delta A_N (\times 10^{-2})$ for negative charge.					
	$\delta A_N^{syst.}$	δA_N^{method}	δA_N^{proton}	δA_N^{pkg}	$\delta A_N^{k/\pi\pm 30}$	$\delta A_N^{\text{Unfold}}$
(-0.200, -0.130)	+0.27 -0.31	+0.27 -0.27	+0.04 -0.04	+0.01 -0.00	+0.00 -0.00	+0.00 -0.15
(-0.130, -0.100)	+0.12 -0.11	+0.10 -0.10	+0.04 -0.04	+0.00 -0.01	+0.00 -0.00	+0.03 -0.00
(-0.100, -0.070)	+0.04 -0.04	+0.02 -0.02	+0.03 -0.03	+0.00 -0.00	+0.00 -0.00	+0.01 -0.00
(-0.070, -0.050)	+0.07 -0.03	+0.01 -0.01	+0.03 -0.03	+0.00 -0.01	+0.00 -0.00	+0.06 -0.00
(-0.050, -0.035)	+0.15 -0.07	+0.06 -0.06	+0.03 -0.03	+0.00 -0.01	+0.00 -0.00	+0.13 -0.00
(0.035, 0.050)	+0.08 -0.13	+0.04 -0.04	+0.06 -0.06	+0.06 -0.00	+0.00 -0.01	+0.00 -0.10
(0.050, 0.070)	+0.17 -0.06	+0.02 -0.02	+0.06 -0.06	+0.16 -0.00	+0.01 -0.00	+0.04 -0.00
(0.070, 0.100)	+0.41 -0.09	+0.06 -0.06	+0.07 -0.07	+0.08 -0.00	+0.02 -0.02	+0.39 -0.00
(0.100, 0.130)	+0.18 -0.10	+0.06 -0.06	+0.08 -0.08	+0.05 -0.00	+0.01 -0.00	+0.14 -0.00
(0.130, 0.200)	+0.15 -0.11	+0.09 -0.09	+0.06 -0.06	+0.00 -0.01	+0.00 -0.00	+0.10 -0.00

Table 58: Systematic uncertainty of unfolded A_N in x_F bins for positive charge in $p + p$ collisions.

x_F	$\delta A_N (\times 10^{-2})$ for positive charge.					
	$\delta A_N^{syst.}$	δA_N^{method}	δA_N^{proton}	δA_N^{pkg}	$\delta A_N^{k/\pi\pm 30}$	$\delta A_N^{\text{Unfold}}$
(-0.200, -0.130)	+0.19 -0.19	+0.16 -0.16	+0.10 -0.10	+0.00 -0.00	+0.00 -0.00	+0.02 -0.00
(-0.130, -0.100)	+0.14 -0.14	+0.06 -0.06	+0.12 -0.12	+0.00 -0.00	+0.00 -0.00	+0.00 -0.01
(-0.100, -0.070)	+0.12 -0.13	+0.04 -0.04	+0.11 -0.11	+0.01 -0.00	+0.00 -0.00	+0.00 -0.05
(-0.070, -0.050)	+0.10 -0.10	+0.05 -0.05	+0.08 -0.08	+0.00 -0.00	+0.00 -0.00	+0.00 -0.03
(-0.050, -0.035)	+0.08 -0.08	+0.03 -0.03	+0.07 -0.07	+0.00 -0.02	+0.00 -0.00	+0.00 -0.00
(0.035, 0.050)	+0.19 -0.18	+0.03 -0.03	+0.18 -0.18	+0.00 -0.03	+0.00 -0.00	+0.07 -0.00
(0.050, 0.070)	+0.26 -0.18	+0.02 -0.02	+0.18 -0.18	+0.00 -0.04	+0.00 -0.00	+0.19 -0.00
(0.070, 0.100)	+0.20 -0.20	+0.04 -0.04	+0.20 -0.20	+0.00 -0.05	+0.01 -0.01	+0.01 -0.00
(0.100, 0.130)	+0.19 -0.19	+0.08 -0.08	+0.18 -0.18	+0.00 -0.01	+0.01 -0.01	+0.00 -0.00
(0.130, 0.200)	+0.16 -0.27	+0.10 -0.10	+0.12 -0.12	+0.02 -0.00	+0.01 -0.01	+0.00 -0.22

Table 59: Systematic uncertainty of unfolded A_N in p_T bins in the centrality range 0-84% in $p + \text{Au}$ collisions.

p_T (GeV/c)	$\delta A_N^{syst.}$	δA_N^{method}	δA_N^{proton}	$\delta A_N^{k/\pi\pm30}$	$\delta A_N^{\text{Unfold}}$
δA_N ($\times 10^{-2}$) for negative charge. $x_F > 0$					
(1.25, 2.50)	+0.21 -0.06	+0.00 -0.00	+0.06 -0.06	+0.01 -0.01	+0.20 -0.00
(2.50, 3.50)	+0.16 -0.14	+0.13 -0.13	+0.06 -0.06	+0.00 -0.00	+0.08 -0.00
(3.50, 7.00)	+0.41 -1.04	+0.41 -0.41	+0.05 -0.05	+0.02 -0.02	+0.00 -0.95
δA_N ($\times 10^{-2}$) for negative charge. $x_F < 0$					
(1.25, 2.50)	+0.28 -0.03	+0.01 -0.01	+0.02 -0.02	+0.00 -0.00	+0.28 -0.00
(2.50, 3.50)	+0.28 -0.19	+0.19 -0.19	+0.03 -0.03	+0.00 -0.00	+0.21 -0.00
(3.50, 7.00)	+0.06 -0.12	+0.05 -0.05	+0.03 -0.03	+0.01 -0.01	+0.00 -0.10
δA_N ($\times 10^{-2}$) for positive charge. $x_F > 0$					
(1.25, 2.50)	+0.20 -0.17	+0.00 -0.00	+0.17 -0.17	+0.00 -0.00	+0.10 -0.00
(2.50, 3.50)	+0.28 -0.22	+0.14 -0.14	+0.18 -0.18	+0.00 -0.00	+0.17 -0.00
(3.50, 7.00)	+0.12 -0.60	+0.03 -0.03	+0.12 -0.12	+0.01 -0.01	+0.00 -0.59
δA_N ($\times 10^{-2}$) for positive charge. $x_F < 0$					
(1.25, 2.50)	+0.12 -0.08	+0.00 -0.00	+0.08 -0.08	+0.00 -0.00	+0.09 -0.00
(2.50, 3.50)	+0.13 -0.13	+0.07 -0.07	+0.11 -0.11	+0.00 -0.00	+0.02 -0.00
(3.50, 7.00)	+0.63 -0.08	+0.03 -0.03	+0.08 -0.08	+0.01 -0.01	+0.62 -0.00

Table 60: Systematic uncertainty of unfolded A_N in x_F bins for positive charge in the centrality range 0-84% in $p + \text{Au}$ collisions.

$\delta A_N (\times 10^{-2})$ for negative charge.					
x_F	$\delta A_N^{syst.}$	δA_N^{method}	δA_N^{proton}	$\delta A_N^{k/\pi \pm 30}$	$\delta A_N^{\text{Unfold}}$
(-0.200, -0.130)	+0.67 -0.12	+0.11 -0.11	+0.04 -0.04	+0.01 -0.01	+0.66 -0.00
(-0.130, -0.100)	+0.05 -0.27	+0.02 -0.02	+0.04 -0.04	+0.01 -0.01	+0.00 -0.27
(-0.100, -0.070)	+0.14 -0.05	+0.04 -0.04	+0.03 -0.03	+0.00 -0.00	+0.13 -0.00
(-0.070, -0.050)	+0.38 -0.05	+0.04 -0.04	+0.03 -0.03	+0.02 -0.01	+0.37 -0.00
(-0.050, -0.035)	+0.03 -0.05	+0.01 -0.01	+0.03 -0.03	+0.00 -0.00	+0.00 -0.04
(0.035, 0.050)	+0.17 -0.07	+0.03 -0.03	+0.06 -0.06	+0.01 -0.01	+0.15 -0.00
(0.050, 0.070)	+0.34 -0.07	+0.03 -0.03	+0.06 -0.06	+0.01 -0.01	+0.33 -0.00
(0.070, 0.100)	+0.07 -0.08	+0.03 -0.03	+0.07 -0.07	+0.00 -0.00	+0.00 -0.03
(0.100, 0.130)	+0.12 -0.12	+0.09 -0.09	+0.08 -0.08	+0.00 -0.00	+0.00 -0.02
(0.130, 0.200)	+0.26 -0.26	+0.25 -0.25	+0.06 -0.06	+0.00 -0.00	+0.00 -0.00

Table 61: Systematic uncertainty of unfolded A_N in x_F bins for positive charge in the centrality range 0-84% in $p + \text{Au}$ collisions

$\delta A_N (\times 10^{-2})$ for positive charge.					
x_F	$\delta A_N^{syst.}$	δA_N^{method}	δA_N^{proton}	$\delta A_N^{k/\pi\pm 30}$	$\delta A_N^{\text{Unfold}}$
(-0.200, -0.130)	+0.37 -0.17	+0.14 -0.14	+0.10 -0.10	+0.00 -0.00	+0.32 -0.00
(-0.130, -0.100)	+0.13 -0.43	+0.05 -0.05	+0.12 -0.12	+0.01 -0.01	+0.00 -0.41
(-0.100, -0.070)	+0.12 -0.16	+0.04 -0.04	+0.11 -0.11	+0.01 -0.01	+0.00 -0.11
(-0.070, -0.050)	+0.30 -0.09	+0.03 -0.03	+0.08 -0.08	+0.00 -0.00	+0.29 -0.00
(-0.050, -0.035)	+0.07 -0.16	+0.01 -0.01	+0.07 -0.07	+0.00 -0.00	+0.00 -0.14
(0.035, 0.050)	+0.18 -0.19	+0.04 -0.04	+0.18 -0.18	+0.00 -0.00	+0.00 -0.07
(0.050, 0.070)	+0.20 -0.18	+0.03 -0.03	+0.18 -0.18	+0.00 -0.00	+0.10 -0.00
(0.070, 0.100)	+0.20 -0.32	+0.02 -0.02	+0.20 -0.20	+0.00 -0.00	+0.00 -0.24
(0.100, 0.130)	+0.52 -0.23	+0.15 -0.15	+0.18 -0.18	+0.00 -0.01	+0.46 -0.00
(0.130, 0.200)	+0.13 -0.47	+0.05 -0.05	+0.12 -0.12	+0.00 -0.00	+0.00 -0.45

Table 62: Systematic uncertainty of unfolded A_N in p_T bins in the centrality range 0-30% in $p + \text{Au}$ collisions.

p_T (GeV/c)	$\delta A_N^{syst.}$	δA_N^{method}	δA_N^{proton}	$\delta A_N^{k/\pi\pm 30}$	$\delta A_N^{\text{Unfold}}$
$\delta A_N (\times 10^{-2})$ for negative charge. $x_F > 0$					
(1.25, 2.50)	+0.36 -0.06	+0.00 -0.00	+0.06 -0.06	+0.01 -0.00	+0.36 -0.00
(2.50, 3.50)	+0.14 -0.18	+0.13 -0.13	+0.06 -0.06	+0.00 -0.00	+0.00 -0.11
(3.50, 7.00)	+0.41 -1.22	+0.41 -0.41	+0.05 -0.05	+0.02 -0.01	+0.00 -1.14
$\delta A_N (\times 10^{-2})$ for negative charge. $x_F < 0$					
(1.25, 2.50)	+0.08 -0.03	+0.01 -0.01	+0.02 -0.02	+0.00 -0.00	+0.07 -0.00
(2.50, 3.50)	+0.33 -0.19	+0.19 -0.19	+0.03 -0.03	+0.00 -0.00	+0.27 -0.00
(3.50, 7.00)	+0.06 -0.06	+0.05 -0.05	+0.03 -0.03	+0.01 -0.01	+0.00 -0.01
$\delta A_N (\times 10^{-2})$ for positive charge. $x_F > 0$					
(1.25, 2.50)	+0.17 -0.30	+0.00 -0.00	+0.17 -0.17	+0.01 -0.00	+0.00 -0.24
(2.50, 3.50)	+0.32 -0.22	+0.14 -0.14	+0.18 -0.18	+0.00 -0.00	+0.23 -0.00
(3.50, 7.00)	+0.12 -0.40	+0.03 -0.03	+0.12 -0.12	+0.01 -0.01	+0.00 -0.38
$\delta A_N (\times 10^{-2})$ for positive charge. $x_F < 0$					
(1.25, 2.50)	+0.12 -0.08	+0.00 -0.00	+0.08 -0.08	+0.00 -0.00	+0.09 -0.00
(2.50, 3.50)	+0.13 -0.14	+0.07 -0.07	+0.11 -0.11	+0.00 -0.00	+0.00 -0.05
(3.50, 7.00)	+0.58 -0.08	+0.03 -0.03	+0.08 -0.08	+0.01 -0.01	+0.57 -0.00

Table 63: Systematic uncertainty of unfolded A_N in x_F bins for negative charge in the centrality range 0-30% in $p + \text{Au}$ collisions.

$\delta A_N (\times 10^{-2})$ for negative charge.					
x_F	$\delta A_N^{syst.}$	δA_N^{method}	δA_N^{proton}	$\delta A_N^{k/\pi\pm 30}$	$\delta A_N^{\text{Unfold}}$
(-0.200, -0.130)	+1.07 -0.12	+0.11 -0.11	+0.04 -0.04	+0.02 -0.02	+1.07 -0.00
(-0.130, -0.100)	+0.05 -0.37	+0.02 -0.02	+0.04 -0.04	+0.01 -0.01	+0.00 -0.37
(-0.100, -0.070)	+0.19 -0.05	+0.04 -0.04	+0.03 -0.03	+0.00 -0.00	+0.19 -0.00
(-0.070, -0.050)	+0.19 -0.05	+0.04 -0.04	+0.03 -0.03	+0.01 -0.01	+0.19 -0.00
(-0.050, -0.035)	+0.18 -0.03	+0.01 -0.01	+0.03 -0.03	+0.01 -0.01	+0.18 -0.00
(0.035, 0.050)	+0.07 -0.62	+0.03 -0.03	+0.06 -0.06	+0.02 -0.03	+0.00 -0.61
(0.050, 0.070)	+0.43 -0.07	+0.03 -0.03	+0.06 -0.06	+0.02 -0.02	+0.43 -0.00
(0.070, 0.100)	+0.07 -0.09	+0.03 -0.03	+0.07 -0.07	+0.00 -0.00	+0.00 -0.05
(0.100, 0.130)	+0.41 -0.12	+0.09 -0.09	+0.08 -0.08	+0.01 -0.01	+0.40 -0.00
(0.130, 0.200)	+0.26 -0.69	+0.25 -0.25	+0.06 -0.06	+0.01 -0.01	+0.00 -0.64

Table 64: Systematic uncertainty of unfolded A_N in x_F bins for positive charge in the centrality range 0-30% in $p + \text{Au}$ collisions.

$\delta A_N (\times 10^{-2})$ for positive charge.					
x_F	$\delta A_N^{syst.}$	δA_N^{method}	δA_N^{proton}	$\delta A_N^{k/\pi \pm 30}$	$\delta A_N^{\text{Unfold}}$
(-0.200, -0.130)	+0.70 -0.17	+0.14 -0.14	+0.10 -0.10	+0.00 -0.01	+0.67 -0.00
(-0.130, -0.100)	+0.13 -0.76	+0.05 -0.05	+0.12 -0.12	+0.02 -0.01	+0.00 -0.75
(-0.100, -0.070)	+0.12 -0.12	+0.04 -0.04	+0.11 -0.11	+0.01 -0.01	+0.02 -0.00
(-0.070, -0.050)	+0.26 -0.09	+0.03 -0.03	+0.08 -0.08	+0.00 -0.00	+0.24 -0.00
(-0.050, -0.035)	+0.07 -0.28	+0.01 -0.01	+0.07 -0.07	+0.00 -0.00	+0.00 -0.28
(0.035, 0.050)	+0.35 -0.18	+0.04 -0.04	+0.18 -0.18	+0.00 -0.00	+0.30 -0.00
(0.050, 0.070)	+0.18 -0.20	+0.03 -0.03	+0.18 -0.18	+0.00 -0.00	+0.00 -0.09
(0.070, 0.100)	+0.20 -0.30	+0.02 -0.02	+0.20 -0.20	+0.01 -0.01	+0.00 -0.23
(0.100, 0.130)	+0.55 -0.23	+0.15 -0.15	+0.18 -0.18	+0.00 -0.01	+0.50 -0.00
(0.130, 0.200)	+0.13 -0.28	+0.05 -0.05	+0.12 -0.12	+0.00 -0.00	+0.00 -0.25

Table 65: Systematic uncertainty of unfolded A_N in p_T bins in the 50-84% in $p + \text{Au}$ collisions.

p_T (GeV/c)	$\delta A_N^{syst.}$	δA_N^{method}	δA_N^{proton}	$\delta A_N^{k/\pi\pm30}$	$\delta A_N^{\text{Unfold}}$
$\delta A_N (\times 10^{-2})$ for negative charge. $x_F > 0$					
(1.25, 2.50)	+0.06 -0.19	+0.00 -0.00	+0.06 -0.06	+0.01 -0.01	+0.00 -0.18
(2.50, 3.50)	+0.59 -0.14	+0.13 -0.13	+0.06 -0.06	+0.00 -0.00	+0.57 -0.00
(3.50, 7.00)	+0.41 -0.81	+0.41 -0.41	+0.05 -0.05	+0.04 -0.04	+0.00 -0.69
$\delta A_N (\times 10^{-2})$ for negative charge. $x_F < 0$					
(1.25, 2.50)	+0.03 -1.40	+0.01 -0.01	+0.02 -0.02	+0.01 -0.01	+0.00 -1.40
(2.50, 3.50)	+0.61 -0.19	+0.19 -0.19	+0.03 -0.03	+0.01 -0.01	+0.57 -0.00
(3.50, 7.00)	+0.06 -0.06	+0.05 -0.05	+0.03 -0.03	+0.02 -0.03	+0.00 -0.00
$\delta A_N (\times 10^{-2})$ for positive charge. $x_F > 0$					
(1.25, 2.50)	+0.92 -0.17	+0.00 -0.00	+0.17 -0.17	+0.01 -0.01	+0.90 -0.00
(2.50, 3.50)	+0.23 -0.22	+0.14 -0.14	+0.18 -0.18	+0.00 -0.00	+0.03 -0.00
(3.50, 7.00)	+0.12 -1.19	+0.03 -0.03	+0.12 -0.12	+0.02 -0.01	+0.00 -1.19
$\delta A_N (\times 10^{-2})$ for positive charge. $x_F < 0$					
(1.25, 2.50)	+0.11 -0.08	+0.00 -0.00	+0.08 -0.08	+0.00 -0.00	+0.08 -0.00
(2.50, 3.50)	+0.36 -0.13	+0.07 -0.07	+0.11 -0.11	+0.00 -0.00	+0.34 -0.00
(3.50, 7.00)	+0.79 -0.08	+0.03 -0.03	+0.08 -0.08	+0.02 -0.03	+0.78 -0.00

Table 66: Systematic uncertainty of unfolded A_N in x_F bins for negative charge in the centrality range 50-84% in $p + \text{Au}$ collisions.

$\delta A_N (\times 10^{-2})$ for negative charge.					
x_F	$\delta A_N^{syst.}$	δA_N^{method}	δA_N^{proton}	$\delta A_N^{k/\pi\pm 30}$	$\delta A_N^{\text{Unfold}}$
(-0.200, -0.130)	+0.12 -1.01	+0.11 -0.11	+0.04 -0.04	+0.02 -0.01	+0.00 -1.00
(-0.130, -0.100)	+0.31 -0.05	+0.02 -0.02	+0.04 -0.04	+0.01 -0.01	+0.31 -0.00
(-0.100, -0.070)	+0.05 -0.12	+0.04 -0.04	+0.03 -0.03	+0.01 -0.01	+0.00 -0.11
(-0.070, -0.050)	+1.40 -0.05	+0.04 -0.04	+0.03 -0.03	+0.06 -0.01	+1.40 -0.00
(-0.050, -0.035)	+0.03 -1.09	+0.01 -0.01	+0.03 -0.03	+0.04 -0.01	+0.00 -1.09
(0.035, 0.050)	+2.17 -0.07	+0.03 -0.03	+0.06 -0.06	+0.10 -0.02	+2.16 -0.00
(0.050, 0.070)	+0.10 -0.07	+0.03 -0.03	+0.06 -0.06	+0.00 -0.01	+0.08 -0.00
(0.070, 0.100)	+0.09 -0.07	+0.03 -0.03	+0.07 -0.07	+0.00 -0.01	+0.05 -0.00
(0.100, 0.130)	+0.12 -1.11	+0.09 -0.09	+0.08 -0.08	+0.01 -0.06	+0.00 -1.10
(0.130, 0.200)	+1.64 -0.26	+0.25 -0.25	+0.06 -0.06	+0.01 -0.04	+1.62 -0.00

Table 67: Systematic uncertainty of unfolded A_N in x_F bins for positive charge in the centrality range 50-84% in $p + \text{Au}$ collisions.

$\delta A_N (\times 10^{-2})$ for positive charge.					
x_F	$\delta A_N^{syst.}$	δA_N^{method}	δA_N^{proton}	$\delta A_N^{k/\pi \pm 30}$	$\delta A_N^{\text{Unfold}}$
(-0.200, -0.130)	+0.17 -1.46	+0.14 -0.14	+0.10 -0.10	+0.02 -0.01	+0.00 -1.45
(-0.130, -0.100)	+1.45 -0.13	+0.05 -0.05	+0.12 -0.12	+0.02 -0.02	+1.45 -0.00
(-0.100, -0.070)	+0.12 -0.82	+0.04 -0.04	+0.11 -0.11	+0.01 -0.00	+0.00 -0.81
(-0.070, -0.050)	+0.54 -0.09	+0.03 -0.03	+0.08 -0.08	+0.01 -0.01	+0.54 -0.00
(-0.050, -0.035)	+0.62 -0.07	+0.01 -0.01	+0.07 -0.07	+0.02 -0.01	+0.62 -0.00
(0.035, 0.050)	+0.18 -1.11	+0.04 -0.04	+0.18 -0.18	+0.01 -0.01	+0.00 -1.09
(0.050, 0.070)	+0.64 -0.18	+0.03 -0.03	+0.18 -0.18	+0.01 -0.01	+0.62 -0.00
(0.070, 0.100)	+0.20 -0.37	+0.02 -0.02	+0.20 -0.20	+0.01 -0.01	+0.00 -0.31
(0.100, 0.130)	+0.43 -0.23	+0.15 -0.15	+0.18 -0.18	+0.00 -0.01	+0.36 -0.00
(0.130, 0.200)	+0.13 -0.96	+0.05 -0.05	+0.12 -0.12	+0.02 -0.01	+0.00 -0.95

4.6.5 Result with Systematic Uncertainties

The $p + p$ and $p + \text{Au}$ results are compared including systematic uncertainties in Figs. 101, 102, 103, and 104. Figs. 105 and 106 shows comparison between positive and negative charge in $p + p$ collisions. Figs. 107, 108, 109, and 110 shows centrality-categorized results in $p + \text{Au}$ collisions. The results are listed in Tables 68, 69, 70, 71, 72, 73, 74, 75, 76, 77, 78, and 79.

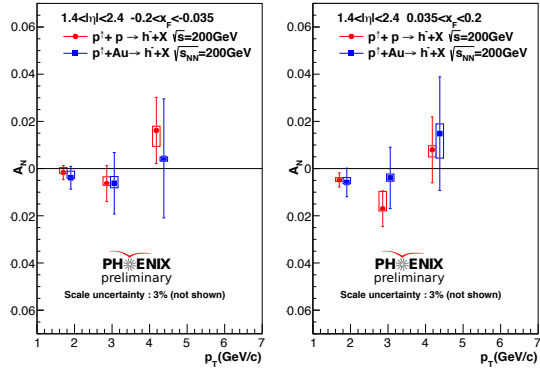


Figure 101: Comparison of unfolded A_N for $p + p$ and $p + \text{Au}$ with systematic uncertainties as a function of p_T for negatively charged hadron. The $p + \text{Au}$ points are shifted horizontally by $+0.2 \text{ GeV}/c$ for clarity.

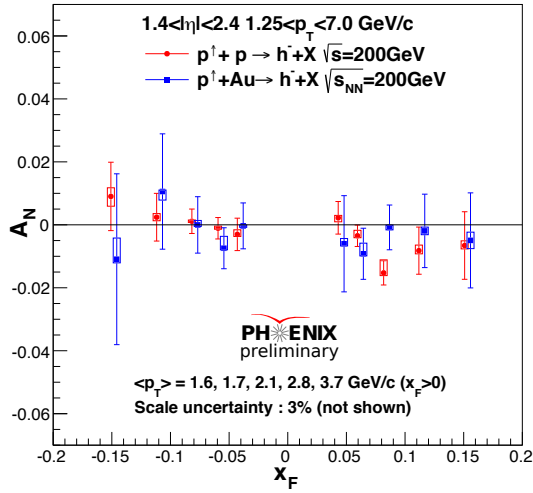


Figure 102: Comparison of unfolded A_N with systematic uncertainty as a function of x_F for $p + p$ and $p + \text{Au}$ data for negatively charged hadron. The $p + \text{Au}$ points are shifted horizontally by +0.005 for clarity.

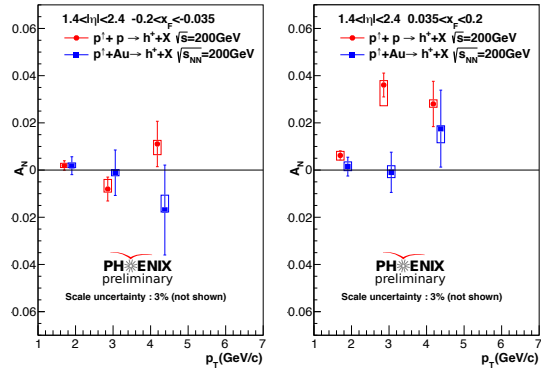


Figure 103: Comparison of unfolded A_N with systematic uncertainty as a function of p_T for $p + p$ and $p + \text{Au}$ data for positively charged hadrons. The $p + \text{Au}$ points are shifted horizontally by +0.2 GeV/c for clarity.

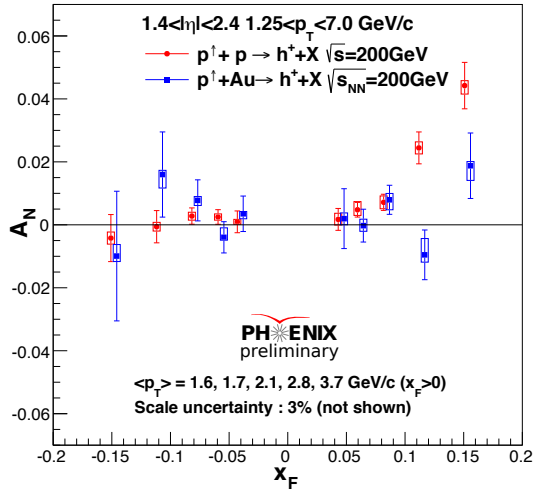


Figure 104: Comparison of unfolded A_N with systematic uncertainty as a function of x_F for $p + p$ and $p + \text{Au}$ data for positively charged hadrons. The $p + \text{Au}$ points are shifted horizontally by $+0.005$ for clarity.

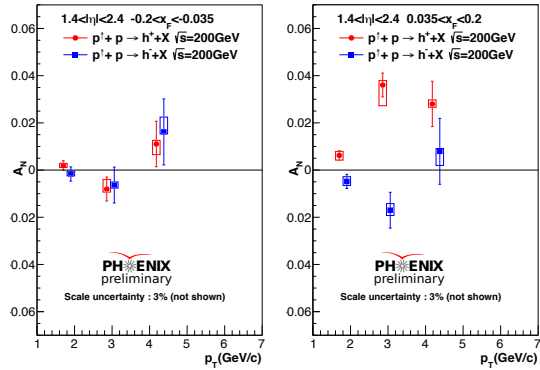


Figure 105: Comparison of unfolded A_N with systematic uncertainty as a function of x_F for positively charged hadrons and negatively charged hadrons for $p + p$ data. The $p + \text{Au}$ points are shifted horizontally by $+0.2$ GeV/c for clarity.

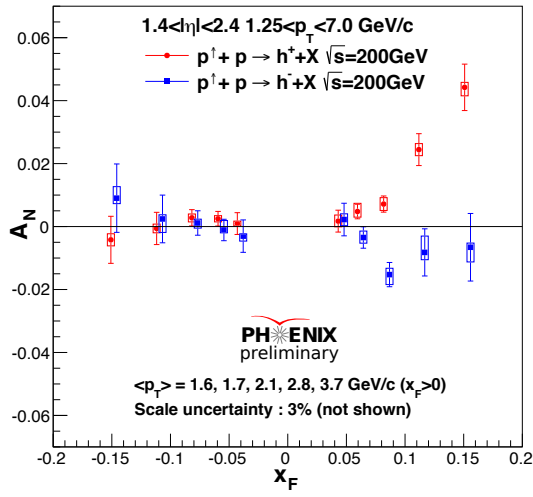


Figure 106: Comparison of unfolded A_N with systematic uncertainty as a function of x_F for positively charged hadrons and negatively charged hadrons for $p+p$ data. The netagive charge points are shifted horizontally by +0.005 for clarity.

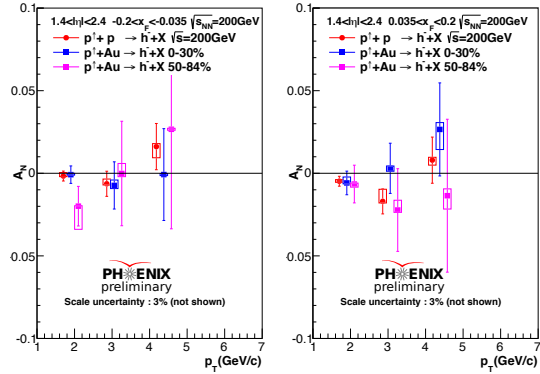


Figure 107: Comparison of unfolded A_N with systematic uncertainty as a function of p_T for $p+p$, centrality bin 0-30%, and centrality bin 50-84% $p+Au$ result for negatively charged hadrons. The $p+Au$ points are shifted horizontally by +0.2 or +0.4 GeV/c for clarity.

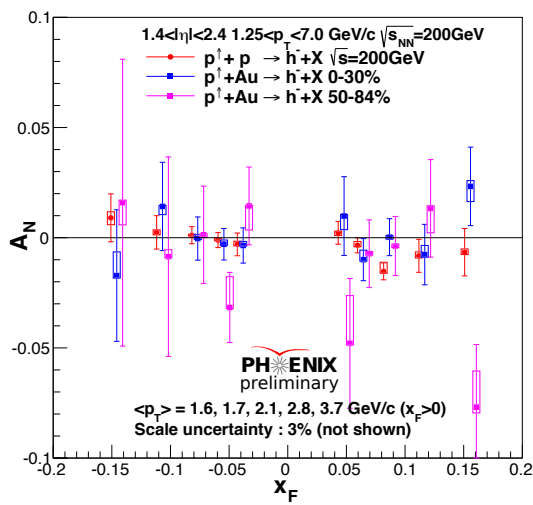


Figure 108: Comparison of unfolded A_N with systematic uncertainty as a function of p_T for $p + p$, centrality bin 0-30%, and centrality bin 50-84% $p + \text{Au}$ result for negatively charged hadrons. The $p + \text{Au}$ points are shifted horizontally by +0.005 or +0.010 for clarity.

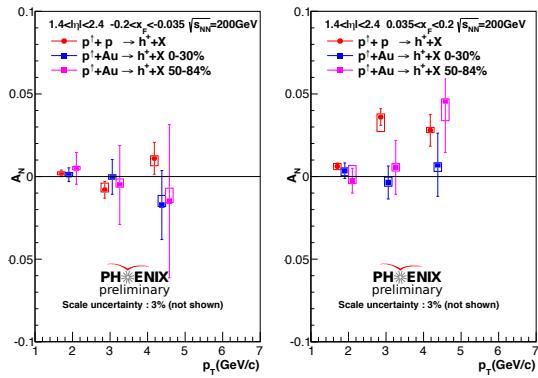


Figure 109: Comparison of unfolded A_N with systematic uncertainty as a function of p_T for $p + p$, centrality bin 0-30%, and centrality bin 50-84% $p + \text{Au}$ result for positively charged hadrons. $\langle p_T \rangle$ is shifted by $+0.2, +0.4$ GeV/ c in $p + \text{Au}$ collisions for comparison.

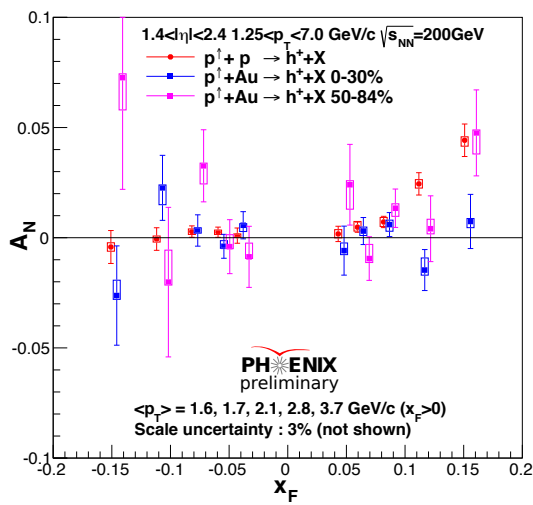


Figure 110: Comparison of unfolded A_N with systematic uncertainty as a function of p_T for $p + p$, centrality bin 0-30%, and centrality bin 50-84% $p + \text{Au}$ result for positively charged hadrons. The $p + \text{Au}$ points are shifted horizontally by +0.005 or +0.010 for clarity.

Table 68: Unfolded A_N in p_T bins in $p + p$ collisions

p_T (GeV/c)	A_N^{unfold}	$\delta A_N^{stat.}$	$\delta A_N^{syst.}$
negative charge. $x_F > 0$			
(1.25, 2.50)	-0.48×10^{-2}	0.30×10^{-2}	$^{+0.10}_{-0.07} \times 10^{-2}$
(2.50, 3.50)	-1.70×10^{-2}	0.76×10^{-2}	$^{+0.73}_{-0.10} \times 10^{-2}$
(3.50, 7.00)	0.79×10^{-2}	1.40×10^{-2}	$^{+0.17}_{-0.30} \times 10^{-2}$
negative charge. $x_F < 0$			
(1.25, 2.50)	-0.17×10^{-2}	0.30×10^{-2}	$^{+0.21}_{-0.04} \times 10^{-2}$
(2.50, 3.50)	-0.64×10^{-2}	0.76×10^{-2}	$^{+0.29}_{-0.07} \times 10^{-2}$
(3.50, 7.00)	1.61×10^{-2}	1.40×10^{-2}	$^{+0.18}_{-0.67} \times 10^{-2}$
positive charge. $x_F > 0$			
(1.25, 2.50)	0.62×10^{-2}	0.20×10^{-2}	$^{+0.17}_{-0.20} \times 10^{-2}$
(2.50, 3.50)	3.60×10^{-2}	0.51×10^{-2}	$^{+0.19}_{-0.88} \times 10^{-2}$
(3.50, 7.00)	2.80×10^{-2}	0.96×10^{-2}	$^{+0.17}_{-0.14} \times 10^{-2}$
positive charge. $x_F < 0$			
(1.25, 2.50)	0.19×10^{-2}	0.20×10^{-2}	$^{+0.09}_{-0.09} \times 10^{-2}$
(2.50, 3.50)	-0.80×10^{-2}	0.51×10^{-2}	$^{+0.41}_{-0.13} \times 10^{-2}$
(3.50, 7.00)	1.11×10^{-2}	0.96×10^{-2}	$^{+0.15}_{-0.45} \times 10^{-2}$

Table 69: Unfolded A_N with systematic uncertainty in x_F bins from $p + p$ data for negative charge

x_F	A_N^{unfold}	$\delta A_N^{stat.}$	$\delta A_N^{syst.}$
negative charge.			
(-0.200, -0.130)	0.90×10^{-2}	1.09×10^{-2}	$^{+0.27}_{-0.31} \times 10^{-2}$
(-0.130, -0.100)	0.24×10^{-2}	0.76×10^{-2}	$^{+0.12}_{-0.11} \times 10^{-2}$
(-0.100, -0.070)	0.11×10^{-2}	0.39×10^{-2}	$^{+0.04}_{-0.04} \times 10^{-2}$
(-0.070, -0.050)	-0.11×10^{-2}	0.34×10^{-2}	$^{+0.07}_{-0.03} \times 10^{-2}$
(-0.050, -0.035)	-0.30×10^{-2}	0.51×10^{-2}	$^{+0.15}_{-0.07} \times 10^{-2}$
(0.035, 0.050)	0.22×10^{-2}	0.52×10^{-2}	$^{+0.08}_{-0.13} \times 10^{-2}$
(0.050, 0.070)	-0.35×10^{-2}	0.34×10^{-2}	$^{+0.17}_{-0.06} \times 10^{-2}$
(0.070, 0.100)	-1.53×10^{-2}	0.39×10^{-2}	$^{+0.41}_{-0.09} \times 10^{-2}$
(0.100, 0.130)	-0.82×10^{-2}	0.75×10^{-2}	$^{+0.18}_{-0.10} \times 10^{-2}$
(0.130, 0.200)	-0.66×10^{-2}	1.07×10^{-2}	$^{+0.15}_{-0.11} \times 10^{-2}$

Table 70: Unfolded A_N with systematic uncertainty in x_F bins from $p + p$ data for positive charge

x_F	A_N^{unfold}	$\delta A_N^{stat.}$	$\delta A_N^{syst.}$
positive charge.			
(-0.200, -0.130)	-0.42×10^{-2}	0.75×10^{-2}	$^{+0.19}_{-0.19} \times 10^{-2}$
(-0.130, -0.100)	-0.06×10^{-2}	0.51×10^{-2}	$^{+0.14}_{-0.14} \times 10^{-2}$
(-0.100, -0.070)	0.28×10^{-2}	0.26×10^{-2}	$^{+0.12}_{-0.13} \times 10^{-2}$
(-0.070, -0.050)	0.25×10^{-2}	0.23×10^{-2}	$^{+0.10}_{-0.10} \times 10^{-2}$
(-0.050, -0.035)	0.09×10^{-2}	0.35×10^{-2}	$^{+0.08}_{-0.08} \times 10^{-2}$
(0.035, 0.050)	0.17×10^{-2}	0.35×10^{-2}	$^{+0.19}_{-0.18} \times 10^{-2}$
(0.050, 0.070)	0.48×10^{-2}	0.23×10^{-2}	$^{+0.26}_{-0.18} \times 10^{-2}$
(0.070, 0.100)	0.71×10^{-2}	0.26×10^{-2}	$^{+0.20}_{-0.20} \times 10^{-2}$
(0.100, 0.130)	2.44×10^{-2}	0.51×10^{-2}	$^{+0.19}_{-0.19} \times 10^{-2}$
(0.130, 0.200)	4.42×10^{-2}	0.74×10^{-2}	$^{+0.16}_{-0.27} \times 10^{-2}$

Table 71: Unfolded A_N in p_T bins from $p + \text{Au}$ data

p_T (GeV/c)	A_N^{unfold}	$\delta A_N^{stat.}$	$\delta A_N^{syst.}$
negative charge. $x_F > 0$			
(1.25, 2.50)	-0.59×10^{-2}	0.61×10^{-2}	$^{+0.21}_{-0.06} \times 10^{-2}$
(2.50, 3.50)	-0.39×10^{-2}	1.30×10^{-2}	$^{+0.16}_{-0.14} \times 10^{-2}$
(3.50, 7.00)	1.48×10^{-2}	2.40×10^{-2}	$^{+0.41}_{-1.04} \times 10^{-2}$
negative charge. $x_F < 0$			
(1.25, 2.50)	-0.39×10^{-2}	0.48×10^{-2}	$^{+0.28}_{-0.03} \times 10^{-2}$
(2.50, 3.50)	-0.62×10^{-2}	1.30×10^{-2}	$^{+0.28}_{-0.19} \times 10^{-2}$
(3.50, 7.00)	0.43×10^{-2}	2.52×10^{-2}	$^{+0.06}_{-0.12} \times 10^{-2}$
positive charge. $x_F > 0$			
(1.25, 2.50)	0.15×10^{-2}	0.40×10^{-2}	$^{+0.20}_{-0.17} \times 10^{-2}$
(2.50, 3.50)	-0.10×10^{-2}	0.85×10^{-2}	$^{+0.28}_{-0.22} \times 10^{-2}$
(3.50, 7.00)	1.76×10^{-2}	1.63×10^{-2}	$^{+0.12}_{-0.60} \times 10^{-2}$
positive charge. $x_F < 0$			
(1.25, 2.50)	0.18×10^{-2}	0.38×10^{-2}	$^{+0.12}_{-0.08} \times 10^{-2}$
(2.50, 3.50)	-0.11×10^{-2}	0.96×10^{-2}	$^{+0.13}_{-0.13} \times 10^{-2}$
(3.50, 7.00)	-1.69×10^{-2}	1.91×10^{-2}	$^{+0.63}_{-0.08} \times 10^{-2}$

Table 72: Unfolded A_N with systematic uncertainty in x_F bins from $p + \text{Au}$ data for negative charge

x_F	A_N^{unfold}	$\delta A_N^{stat.}$	$\delta A_N^{syst.}$
negative charge.			
(-0.200, -0.130)	-1.09×10^{-2}	2.71×10^{-2}	$^{+0.67}_{-0.12} \times 10^{-2}$
(-0.130, -0.100)	1.06×10^{-2}	1.83×10^{-2}	$^{+0.05}_{-0.27} \times 10^{-2}$
(-0.100, -0.070)	-0.00×10^{-2}	0.90×10^{-2}	$^{+0.14}_{-0.05} \times 10^{-2}$
(-0.070, -0.050)	-0.74×10^{-2}	0.65×10^{-2}	$^{+0.38}_{-0.05} \times 10^{-2}$
(-0.050, -0.035)	-0.03×10^{-2}	0.73×10^{-2}	$^{+0.03}_{-0.05} \times 10^{-2}$
(0.035, 0.050)	-0.60×10^{-2}	1.53×10^{-2}	$^{+0.17}_{-0.07} \times 10^{-2}$
(0.050, 0.070)	-0.92×10^{-2}	0.81×10^{-2}	$^{+0.34}_{-0.07} \times 10^{-2}$
(0.070, 0.100)	-0.08×10^{-2}	0.71×10^{-2}	$^{+0.07}_{-0.08} \times 10^{-2}$
(0.100, 0.130)	-0.19×10^{-2}	1.17×10^{-2}	$^{+0.12}_{-0.12} \times 10^{-2}$
(0.130, 0.200)	-0.49×10^{-2}	1.51×10^{-2}	$^{+0.26}_{-0.26} \times 10^{-2}$

Table 73: Unfolded A_N with systematic uncertainty in x_F bins from $p + \text{Au}$ data for positive charge.

x_F	A_N^{unfold}	$\delta A_N^{stat.}$	$\delta A_N^{syst.}$
positive charge.			
(-0.200, -0.130)	-0.99×10^{-2}	2.06×10^{-2}	$^{+0.37}_{-0.17} \times 10^{-2}$
(-0.130, -0.100)	1.60×10^{-2}	1.35×10^{-2}	$^{+0.13}_{-0.43} \times 10^{-2}$
(-0.100, -0.070)	0.78×10^{-2}	0.65×10^{-2}	$^{+0.12}_{-0.16} \times 10^{-2}$
(-0.070, -0.050)	-0.40×10^{-2}	0.50×10^{-2}	$^{+0.30}_{-0.09} \times 10^{-2}$
(-0.050, -0.035)	0.35×10^{-2}	0.56×10^{-2}	$^{+0.07}_{-0.16} \times 10^{-2}$
(0.035, 0.050)	0.20×10^{-2}	0.95×10^{-2}	$^{+0.18}_{-0.19} \times 10^{-2}$
(0.050, 0.070)	-0.03×10^{-2}	0.52×10^{-2}	$^{+0.20}_{-0.18} \times 10^{-2}$
(0.070, 0.100)	0.79×10^{-2}	0.46×10^{-2}	$^{+0.20}_{-0.32} \times 10^{-2}$
(0.100, 0.130)	-0.95×10^{-2}	0.79×10^{-2}	$^{+0.52}_{-0.23} \times 10^{-2}$
(0.130, 0.200)	1.88×10^{-2}	1.04×10^{-2}	$^{+0.13}_{-0.47} \times 10^{-2}$

Table 74: Unfolded A_N in p_T bins from $p + \text{Au}$ data in the centrality range 0-30%

p_T (GeV/c)	A_N^{unfold}	$\delta A_N^{stat.}$	$\delta A_N^{syst.}$
negative charge. $x_F > 0$			
(1.25, 2.50)	-0.59×10^{-2}	0.72×10^{-2}	$^{+0.36}_{-0.06} \times 10^{-2}$
(2.50, 3.50)	0.30×10^{-2}	1.52×10^{-2}	$^{+0.14}_{-0.18} \times 10^{-2}$
(3.50, 7.00)	2.65×10^{-2}	2.82×10^{-2}	$^{+0.41}_{-1.22} \times 10^{-2}$
negative charge. $x_F < 0$			
(1.25, 2.50)	-0.08×10^{-2}	0.53×10^{-2}	$^{+0.08}_{-0.03} \times 10^{-2}$
(2.50, 3.50)	-0.74×10^{-2}	1.43×10^{-2}	$^{+0.33}_{-0.19} \times 10^{-2}$
(3.50, 7.00)	-0.08×10^{-2}	2.78×10^{-2}	$^{+0.06}_{-0.06} \times 10^{-2}$
positive charge. $x_F > 0$			
(1.25, 2.50)	0.35×10^{-2}	0.47×10^{-2}	$^{+0.17}_{-0.30} \times 10^{-2}$
(2.50, 3.50)	-0.36×10^{-2}	1.00×10^{-2}	$^{+0.32}_{-0.22} \times 10^{-2}$
(3.50, 7.00)	0.71×10^{-2}	1.91×10^{-2}	$^{+0.12}_{-0.40} \times 10^{-2}$
positive charge. $x_F < 0$			
(1.25, 2.50)	0.12×10^{-2}	0.41×10^{-2}	$^{+0.12}_{-0.08} \times 10^{-2}$
(2.50, 3.50)	-0.02×10^{-2}	1.05×10^{-2}	$^{+0.13}_{-0.14} \times 10^{-2}$
(3.50, 7.00)	-1.72×10^{-2}	2.09×10^{-2}	$^{+0.58}_{-0.08} \times 10^{-2}$

Table 75: Unfolded A_N with systematic uncertainty in x_F bins from $p + \text{Au}$ data in the centrality range 0-30% for negative charge.

x_F	A_N^{unfold}	$\delta A_N^{stat.}$	$\delta A_N^{syst.}$
negative charge.			
(-0.200, -0.130)	-1.72×10^{-2}	2.99×10^{-2}	$^{+1.07}_{-0.12} \times 10^{-2}$
(-0.130, -0.100)	1.42×10^{-2}	2.00×10^{-2}	$^{+0.05}_{-0.37} \times 10^{-2}$
(-0.100, -0.070)	-0.04×10^{-2}	0.98×10^{-2}	$^{+0.19}_{-0.05} \times 10^{-2}$
(-0.070, -0.050)	-0.30×10^{-2}	0.71×10^{-2}	$^{+0.19}_{-0.05} \times 10^{-2}$
(-0.050, -0.035)	-0.35×10^{-2}	0.80×10^{-2}	$^{+0.18}_{-0.03} \times 10^{-2}$
(0.035, 0.050)	0.98×10^{-2}	1.79×10^{-2}	$^{+0.07}_{-0.62} \times 10^{-2}$
(0.050, 0.070)	-1.00×10^{-2}	0.96×10^{-2}	$^{+0.43}_{-0.07} \times 10^{-2}$
(0.070, 0.100)	0.02×10^{-2}	0.84×10^{-2}	$^{+0.07}_{-0.09} \times 10^{-2}$
(0.100, 0.130)	-0.77×10^{-2}	1.37×10^{-2}	$^{+0.41}_{-0.12} \times 10^{-2}$
(0.130, 0.200)	2.33×10^{-2}	1.78×10^{-2}	$^{+0.26}_{-0.69} \times 10^{-2}$

Table 76: Unfolded A_N with systematic uncertainty in x_F bins from $p + \text{Au}$ data in the centrality range 0-30% for positive charge.

x_F	A_N^{unfold}	$\delta A_N^{stat.}$	$\delta A_N^{syst.}$
positive charge.			
(-0.200, -0.130)	-2.62×10^{-2}	2.25×10^{-2}	$^{+0.70}_{-0.17} \times 10^{-2}$
(-0.130, -0.100)	2.26×10^{-2}	1.48×10^{-2}	$^{+0.13}_{-0.76} \times 10^{-2}$
(-0.100, -0.070)	0.33×10^{-2}	0.71×10^{-2}	$^{+0.12}_{-0.12} \times 10^{-2}$
(-0.070, -0.050)	-0.39×10^{-2}	0.54×10^{-2}	$^{+0.26}_{-0.09} \times 10^{-2}$
(-0.050, -0.035)	0.57×10^{-2}	0.62×10^{-2}	$^{+0.07}_{-0.28} \times 10^{-2}$
(0.035, 0.050)	-0.59×10^{-2}	1.11×10^{-2}	$^{+0.35}_{-0.18} \times 10^{-2}$
(0.050, 0.070)	0.30×10^{-2}	0.61×10^{-2}	$^{+0.18}_{-0.20} \times 10^{-2}$
(0.070, 0.100)	0.60×10^{-2}	0.54×10^{-2}	$^{+0.20}_{-0.30} \times 10^{-2}$
(0.100, 0.130)	-1.47×10^{-2}	0.93×10^{-2}	$^{+0.55}_{-0.23} \times 10^{-2}$
(0.130, 0.200)	0.74×10^{-2}	1.23×10^{-2}	$^{+0.13}_{-0.28} \times 10^{-2}$

Table 77: Unfolded A_N in p_T bins from $p + \text{Au}$ data in the centrality range 50-84%

p_T (GeV/c)	A_N^{unfold}	$\delta A_N^{stat.}$	$\delta A_N^{syst.}$
negative charge. $x_F > 0$			
(1.25, 2.50)	-0.65×10^{-2}	1.14×10^{-2}	$^{+0.06}_{-0.19} \times 10^{-2}$
(2.50, 3.50)	-2.22×10^{-2}	2.50×10^{-2}	$^{+0.59}_{-0.14} \times 10^{-2}$
(3.50, 7.00)	-1.36×10^{-2}	4.63×10^{-2}	$^{+0.41}_{-0.81} \times 10^{-2}$
negative charge. $x_F < 0$			
(1.25, 2.50)	-1.99×10^{-2}	1.20×10^{-2}	$^{+0.03}_{-1.40} \times 10^{-2}$
(2.50, 3.50)	-0.01×10^{-2}	3.16×10^{-2}	$^{+0.61}_{-0.19} \times 10^{-2}$
(3.50, 7.00)	2.66×10^{-2}	6.02×10^{-2}	$^{+0.06}_{-0.06} \times 10^{-2}$
positive charge. $x_F > 0$			
(1.25, 2.50)	-0.25×10^{-2}	0.75×10^{-2}	$^{+0.92}_{-0.17} \times 10^{-2}$
(2.50, 3.50)	0.56×10^{-2}	1.63×10^{-2}	$^{+0.23}_{-0.22} \times 10^{-2}$
(3.50, 7.00)	4.58×10^{-2}	3.12×10^{-2}	$^{+0.12}_{-1.19} \times 10^{-2}$
positive charge. $x_F < 0$			
(1.25, 2.50)	0.49×10^{-2}	0.96×10^{-2}	$^{+0.11}_{-0.08} \times 10^{-2}$
(2.50, 3.50)	-0.51×10^{-2}	2.39×10^{-2}	$^{+0.36}_{-0.13} \times 10^{-2}$
(3.50, 7.00)	-1.49×10^{-2}	4.64×10^{-2}	$^{+0.79}_{-0.08} \times 10^{-2}$

Table 78: Unfolded A_N with systematic uncertainties in x_F bins from $p + \text{Au}$ data in the centrality range 50-84% for negative charge.

x_F	A_N^{unfold}	$\delta A_N^{stat.}$	$\delta A_N^{syst.}$
negative charge.			
(-0.200, -0.130)	1.59×10^{-2}	6.51×10^{-2}	$^{+0.12}_{-1.01} \times 10^{-2}$
(-0.130, -0.100)	-0.86×10^{-2}	4.53×10^{-2}	$^{+0.31}_{-0.05} \times 10^{-2}$
(-0.100, -0.070)	0.14×10^{-2}	2.21×10^{-2}	$^{+0.05}_{-0.12} \times 10^{-2}$
(-0.070, -0.050)	-3.17×10^{-2}	1.59×10^{-2}	$^{+1.40}_{-0.05} \times 10^{-2}$
(-0.050, -0.035)	1.44×10^{-2}	1.77×10^{-2}	$^{+0.03}_{-1.09} \times 10^{-2}$
(0.035, 0.050)	-4.79×10^{-2}	2.95×10^{-2}	$^{+2.17}_{-0.07} \times 10^{-2}$
(0.050, 0.070)	-0.73×10^{-2}	1.54×10^{-2}	$^{+0.10}_{-0.07} \times 10^{-2}$
(0.070, 0.100)	-0.38×10^{-2}	1.34×10^{-2}	$^{+0.09}_{-0.07} \times 10^{-2}$
(0.100, 0.130)	1.33×10^{-2}	2.21×10^{-2}	$^{+0.12}_{-1.11} \times 10^{-2}$
(0.130, 0.200)	-7.69×10^{-2}	2.84×10^{-2}	$^{+1.64}_{-0.26} \times 10^{-2}$

Table 79: Unfolded A_N with systematic uncertainties in x_F bins from $p + \text{Au}$ data in the centrality range 50-84% for positive charge.

x_F	A_N^{unfold}	$\delta A_N^{stat.}$	$\delta A_N^{syst.}$
positive charge.			
(-0.200, -0.130)	7.26×10^{-2}	5.07×10^{-2}	$^{+0.17}_{-1.46} \times 10^{-2}$
(-0.130, -0.100)	-2.02×10^{-2}	3.39×10^{-2}	$^{+1.45}_{-0.13} \times 10^{-2}$
(-0.100, -0.070)	3.26×10^{-2}	1.64×10^{-2}	$^{+0.12}_{-0.82} \times 10^{-2}$
(-0.070, -0.050)	-0.41×10^{-2}	1.22×10^{-2}	$^{+0.54}_{-0.09} \times 10^{-2}$
(-0.050, -0.035)	-0.87×10^{-2}	1.39×10^{-2}	$^{+0.62}_{-0.07} \times 10^{-2}$
(0.035, 0.050)	2.40×10^{-2}	1.83×10^{-2}	$^{+0.18}_{-1.11} \times 10^{-2}$
(0.050, 0.070)	-0.95×10^{-2}	0.99×10^{-2}	$^{+0.64}_{-0.18} \times 10^{-2}$
(0.070, 0.100)	1.34×10^{-2}	0.87×10^{-2}	$^{+0.20}_{-0.37} \times 10^{-2}$
(0.100, 0.130)	0.41×10^{-2}	1.49×10^{-2}	$^{+0.43}_{-0.23} \times 10^{-2}$
(0.130, 0.200)	4.76×10^{-2}	1.95×10^{-2}	$^{+0.13}_{-0.96} \times 10^{-2}$

4.7 $p + \text{Al}$ Results in 4 x_F Bins

4.7.1 Raw A_N from $p + \text{Al}$ Data

The asymmetries for charged hadrons are listed in Tables 80. Cuts are as for $p + \text{Au}$ except for a maximum centrality cut of 72%. The centrality classes are 0-40% and 40-72%. The unfolded results are shown in Figs. 111, 112, and 113.

Table 80: x_F dependence of A_N with statistical uncertainty δA_N^{stat} in $p + \text{Al}$ collisions.

x_F	$p + \text{Al } 0\text{-}72\%$ $A_N(\times 10^{-2})$	$p + \text{Al } 0\text{-}40\%$ $A_N(\times 10^{-2})$	$p + \text{Al } 40\text{-}72\%$ $A_N(\times 10^{-2})$
negative charge. $x_F > 0$			
(0.035, 0.050)	-0.95 ± 0.91	0.03 ± 1.08	-2.83 ± 1.61
(0.050, 0.070)	-0.73 ± 0.61	-0.61 ± 0.72	-0.65 ± 1.06
(0.070, 0.100)	-0.53 ± 0.60	-0.57 ± 0.71	-0.49 ± 1.05
(0.100, 0.200)	-0.07 ± 0.90	-0.51 ± 1.07	0.71 ± 1.55
negative charge. $x_F < 0$			
(-0.035, -0.050)	0.57 ± 0.56	0.61 ± 0.64	0.35 ± 1.13
(-0.050, -0.070)	-0.39 ± 0.58	-0.05 ± 0.66	-0.63 ± 1.19
(-0.070, -0.100)	0.33 ± 0.86	0.41 ± 0.98	-0.57 ± 1.75
(-0.100, -0.200)	2.89 ± 1.63	3.57 ± 1.85	1.35 ± 3.29
positive charge. $x_F > 0$			
(0.035, 0.050)	0.85 ± 0.66	0.91 ± 0.78	1.27 ± 1.18
(0.050, 0.070)	0.05 ± 0.42	0.27 ± 0.50	-0.31 ± 0.74
(0.070, 0.100)	0.59 ± 0.42	0.47 ± 0.50	1.15 ± 0.73
(0.100, 0.200)	1.21 ± 0.63	1.27 ± 0.75	1.75 ± 1.08
positive charge. $x_F < 0$			
(-0.035, -0.050)	-0.77 ± 0.48	-0.61 ± 0.55	-1.13 ± 0.98
(-0.050, -0.070)	-1.05 ± 0.46	-1.49 ± 0.52	1.09 ± 0.95
(-0.070, -0.100)	-0.17 ± 0.66	-0.65 ± 0.74	1.31 ± 1.37
(-0.100, -0.200)	-0.43 ± 1.24	0.53 ± 1.42	-1.59 ± 2.49

4.7.2 Unfolded Result from $p + \text{Al}$ data

Figs. 111, 112, and 113, show unfolded A_N with changing the K/π ratio by $\pm 30\%$.

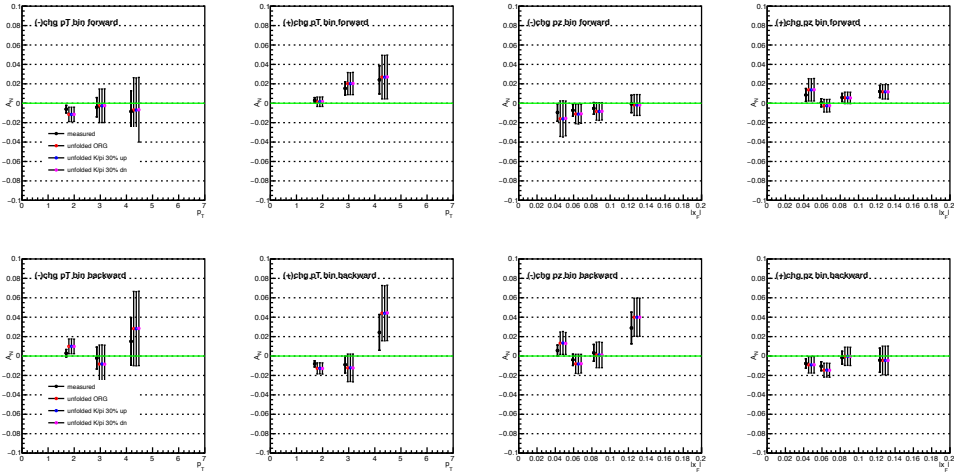


Figure 111: Unfolded A_N in $p + \text{Al}$ collisions in the centrality range 0-72% varying the K/π ratio by $\pm 30\%$. The difference is included in the systematic uncertainty.

4.8 Additional Systematic Uncertainty to Cover the K/π Ratio for Direct Comparison of $p + p$ and $p + A$ Data.

Even though changes in the migration matrix from $\delta(K/\pi)$ are very small, uncertainty in the K/π ratio can result in modification of A_N because the charged hadrons include K^\pm and π^\pm , which would have different A_N . To compare the results of $p + p$ and $p + A$ data directly, possible changes from the uncertainty in and difference of the K/π ratio are studied based on the models from the theory curve provided by Pitonyak based on a recent paper [6], shown in Figs. 114

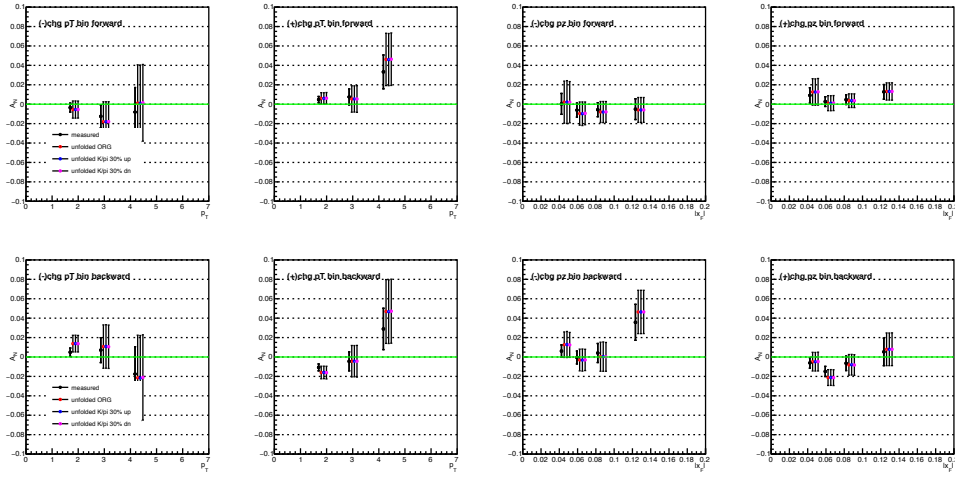


Figure 112: Unfolded A_N in $p + \text{Al}$ collisions in the centrality range 0-40% varying the K/π ratio by $\pm 30\%$. The difference is included in the systematic uncertainty.

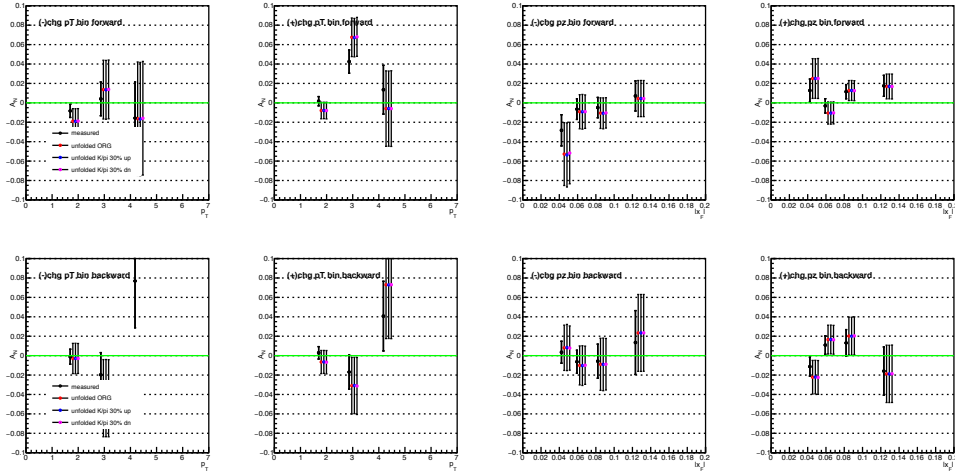


Figure 113: Unfolded A_N in $p + \text{Al}$ collisions in the centrality region 41-72% varying the K/π ratio by $\pm 30\%$. The difference is included in the systematic uncertainty.

and 115 and the BRAHMS data [102]. The theory, BRAHMS data, and many available π^0 results support a trend of increasing size of A_N for increasing x_F , at $x_F > 0$. Also, the result of this analysis agrees with this trend. From the BRAHMS results, two kinds of estimation were made. The first one is the theory curve from Pitonyak, the other one is an estimation from BRAHMS results: $A_N(\pi^+) = 0.3x_F$, $A_N(\pi^-) = -0.3x_F$, and $A_N(K^\pm) = 0.15x_F$.

With these inputs and the hadron cocktail simulation, the weighted sum of A_N for the K, π mixture is obtained. Then it is possible to quantify the effect from the $\pm 30\%$ $\delta(K/\pi)$ variation or from the different hadron interaction packages by checking the variation of A_N in each case. The systematic uncertainty for the $p + p$ result is calculated from the sum in quadrature of (1) the largest deviation of A_N for the other two hadron interaction packages and (2) the $\pm 30\%$ variation of the K/π ratio. Among two estimations explained above, the larger variation was chosen as a conservative systematic uncertainty. For $p + \text{Au}$ and $p + \text{Al}$, the same procedure and models are used, with a hadron cocktail simulation for $p + \text{Au}$ which had a different K/π ratio from $p + p$. Then, a similar sum in quadrature of (1) and (2) was made. If the deviation from the A_N mixture in the $p + p$ simulation is larger than (1) and (2), the largest deviation is selected.

Figure 116 shows the hadron cocktail simulation result of $A_N(\text{mixture})$ for $p + p$ and $p + \text{Au}(\text{Al})$ from two models. Model 1 is the calculation from Pitonyak [6] and Model 2 is a linear extrapolation of the BRAHMS results. The error bars

of the filled circles came from varying the K/π ratio by 30%. The error bars on the open circles show the final systematic uncertainties for $p + p$. These are calculated by the sum in quadrature of the errors from the K/π ratio variation and the hadron interaction packages. The open squares are the uncertainties in the $p + \text{Au(Al)}$ case. The procedure is the same, but (2) is replaced as the difference between $A_N(p + p)(\text{mixture})$ and $A_N(p + A)(\text{mixture})$ when it is larger than (2).

This systematic uncertainty covers the difference of the K/π ratio in $p + p$, $p + \text{Al}$, and $p + \text{Au}$. Eventually the results can be compared with one another on the same plot. Like for other sources of systematic uncertainty, the same uncertainty is applied to the results of different centrality bins for the same dataset ($p + \text{Au}$ or $p + \text{Al}$) based on the description in [103]: the K/π ratios are essentially identical for all centrality classes.

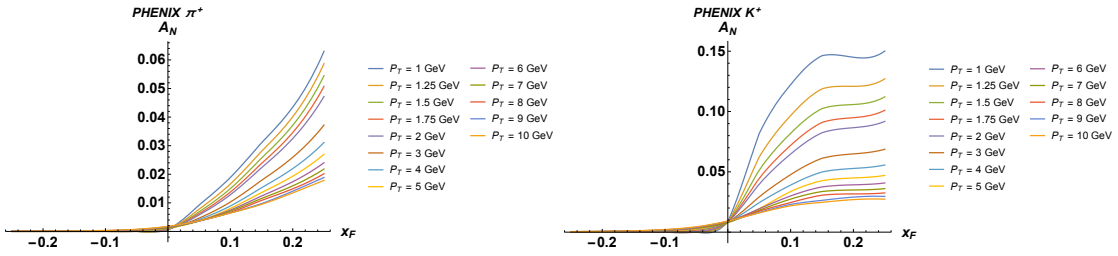


Figure 114: Theory predictions based on [6] for $A_N(\pi^+)$ and $A_N(K^+)$ in the $1.2 < |\eta| < 2.4$ range.

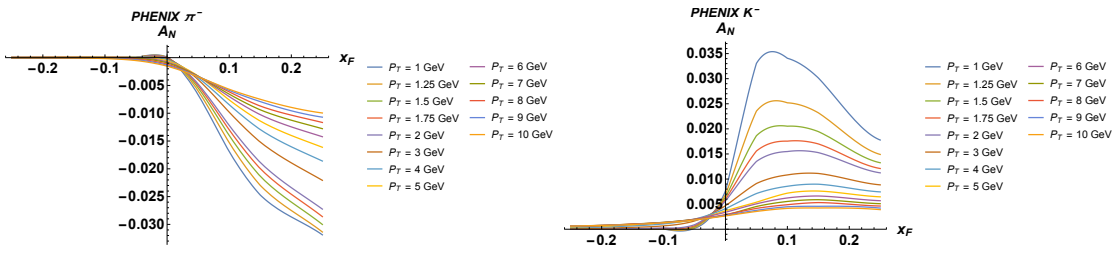


Figure 115: Theory predictions based on [6] for $A_N(\pi^-)$ and $A_N(K^-)$ in the $1.2 < |\eta| < 2.4$ range.

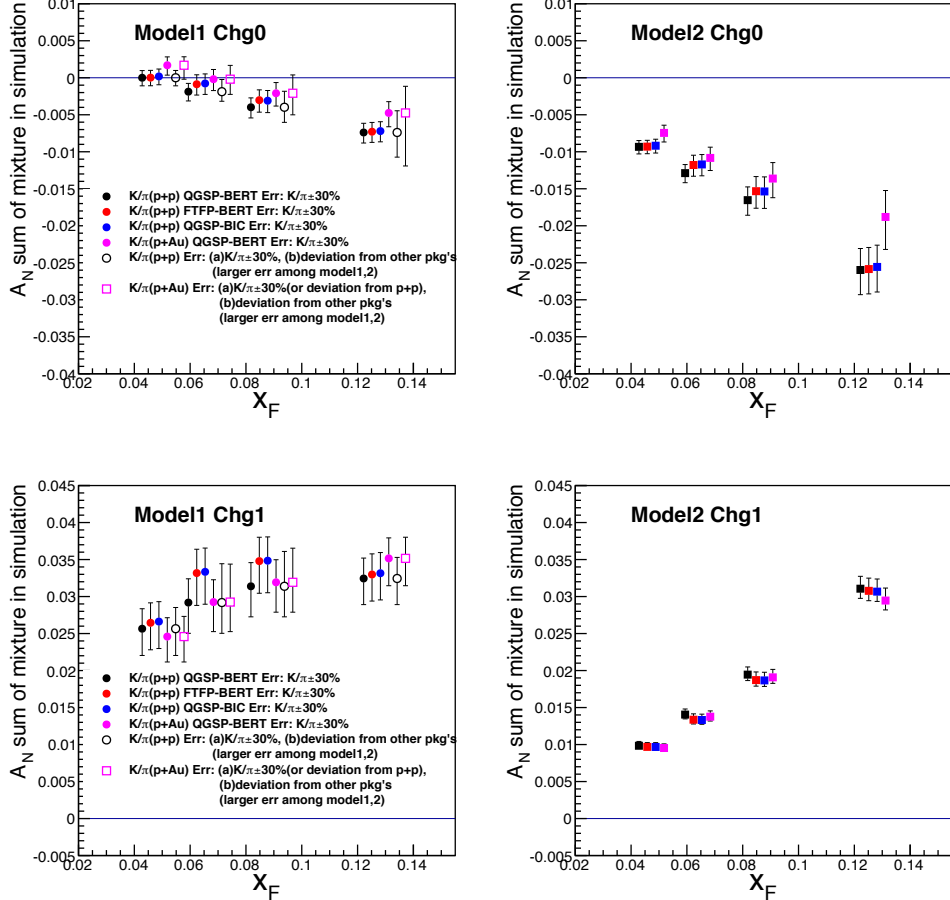


Figure 116: $A_N(mixture)$ are obtained for 2 models (1) theory curve from Pitonyak [6] (Model 1 on the plot) and (2) a linear extrapolation of the BRAHMS results (Model 2 on the plot), using hadron cocktail simulation for $p + p$ and $p + \text{Au(Al)}$. The upper plots (Chg0 on the plot) are for negative charge and the lower plots (Chg1 on the plot) are for positive charge.

4.9 A-dependence of A_N for Positively Charged Hadrons at $0.1 < x_F <$

0.2

As A_N of positively charged hadrons shows clear suppression at $0.1 < x_F < 0.2$ in $p + A$ compared with $p + p$, the A-dependence of A_N is studied in this chapter. In recent years, theory papers [67, 68, 6] proposed that measuring A_N in $p + A$ could play a critical role for finding the true source of A_N in inclusive hadron production in $p + p$ collisions. The fragmentation contribution to A_N in $p + A$ collisions is proportional to $A^{-1/3}$ while other contributions are expected to result in small or no suppression of A_N in $p + A$ collisions. To quantify this effect, fitting the results with A (atomic mass) was suggested to quantify nuclear effect. For Min-Bias events (centrality 0-84% for $p + \text{Au}$, centrality 0-72% for $p + \text{Al}$), $A^{1/3}$ is used in the horizontal axis. The fit function is shown on Fig. 117:

$$f(A^{1/3}) = \frac{A_N^0}{(A^{1/3})^\alpha}, \quad (19)$$

where α is the power parameter which indicates the nuclear dependence of A_N , scaled onto $A^{1/3}$. A_N^0 is a free parameter for the fit. As shown in Fig. 118, the systematic uncertainty of α is obtained from the $1-\sigma$ width of the 10000 fit results. Every single fit is done for randomly selected points from a Gaussian distribution which is centered at the original data points of A_N and has a width of the systematic uncertainty of A_N . If there is no A-dependence, α should be zero while α is expected to be 1.0 for the $A^{1/3}$ -dependence case. If A_N is pro-

portional to the inverse of A , α becomes 3. On the right side of Fig. 117, the χ^2 for each power parameter is shown. The range of α is from 0.79 to 2.21 for $\Delta\chi^2 < 1.0$. Even after combining the statistical uncertainty with the systematic uncertainty, $\alpha - \Delta\alpha^{total} = 0.72$, far from zero. This supports the statement that a nuclear-dependence exists for A_N in $p+A$ collisions. Moreover, $\Delta\chi^2 = 21$ (statistical uncertainty only) at $\alpha = 0$ means that the case of no-nuclear-dependence of A_N is over 4σ away from the result.

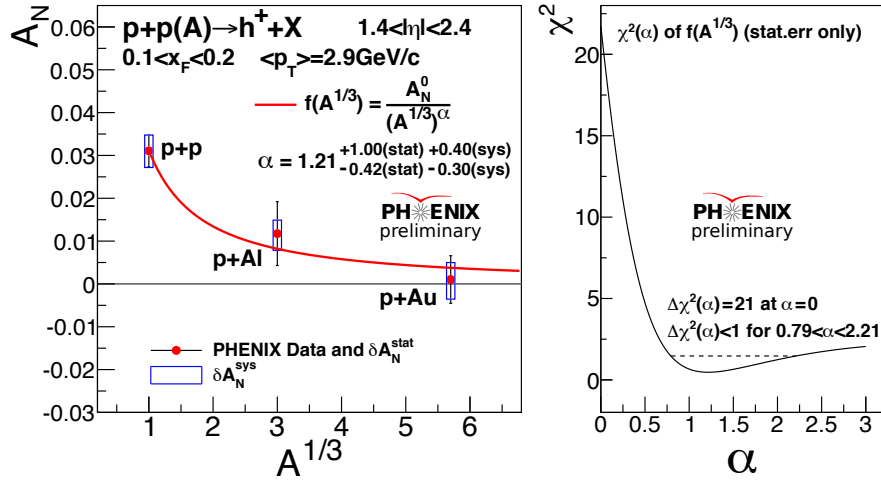


Figure 117: $A^{1/3}$ -dependence of A_N of positively charged hadrons at $0.1 < x_F < 0.2$ in $p + p$, $p + Al$, and $p + Au$ collisions

For the centrality classes, the formula is:

$$f(N_{coll}^{Avg}) = \frac{A_N^0}{(N_{coll}^{Avg})^\beta}. \quad (20)$$

Figure 119 shows the fit results for the centrality classes 0-20, 20-50, and 50-84% in $p + Au$, and 0-40 and 40-84% in $p + Al$. The averaged- N_{coll} is used on

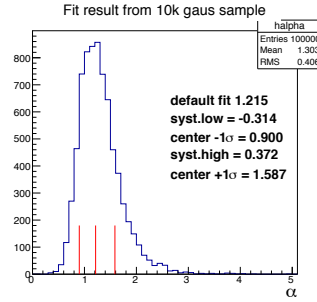


Figure 118: Distribution of the 10000 fit results for obtaining the systematic uncertainty for α . Each fit is done for randomly selected points from a Gaussian distribution which is centered at the original data points of A_N and has a width of the systematic uncertainty of A_N .

the horizontal axis because $\langle N_{coll} \rangle$ is related to the path length of nuclei in small systems. $\langle N_{coll} \rangle$ and $\delta \langle N_{coll} \rangle$ are obtained from [104, 105]. Using the same procedure, the systematic uncertainty of β is calculated from the width of the 10000 fit results. Every single fit is done for randomly selected points from a gaussian distribution which is centered at the original A_N data points and its width is the systematic uncertainty of A_N as shown in Fig. 120. In this, 2D-Gaussian is used for including the uncertainty due to the uncertainty of N_{coll} . After a test without the uncertainty of N_{coll} , the effect turned out to be very small. The result agrees with the message from the previous pages, Fig. 117: β is away from zero.

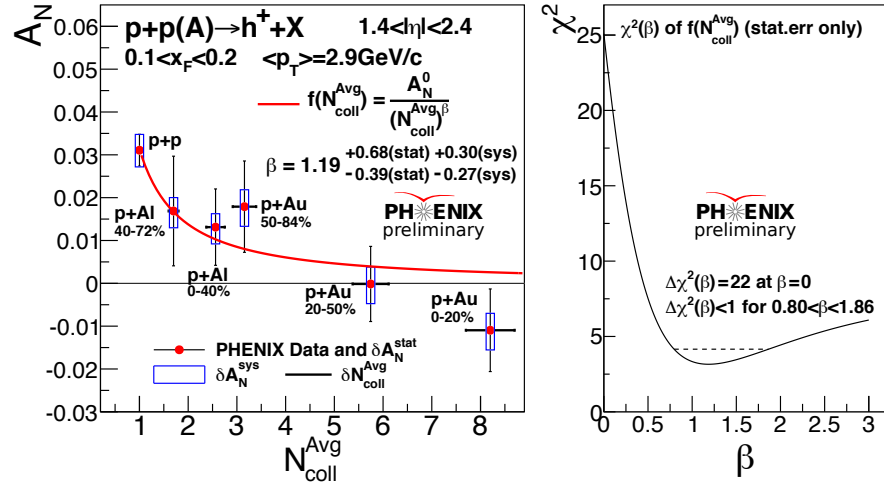


Figure 119: Averaged- N_{coll} -dependence of A_N of positively charged hadrons at $0.1 < x_F < 0.2$ for the centrality-categorized results in $p + p$, $p + Al$, and $p + Au$ collisions

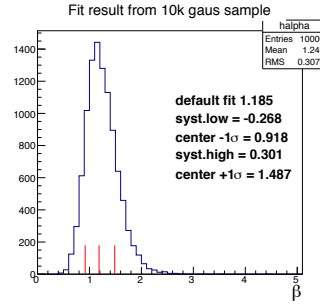


Figure 120: Distribution of the 10000 fit results for obtaining the systematic uncertainty for β . Each fit is done for randomly selected points from a Gaussian distribution which is centered at the original data points of A_N and has a width of the systematic uncertainty of A_N .

4.10 Comparison of Modulations

The nonzero A_N in $p + p$ and suppressed A_N in $p + A$ can be easily recognized when the modulations are compared. The ϕ modulations of positively charged hadrons in $p + p$, $p + \text{Al}$, and $p + \text{Au}$ collisions at $0.1 < x_F < 0.2$ are shown in Fig. 121. The results from the blue and yellow beams are combined for $p + p$ while only the blue beam was used in $p + \text{Al}$ and $p + \text{Au}$. The large statistical uncertainties in one of the bins is due to inefficiency of the detector. Modulation in $p + p$ is now showing in $p + A$. δA_N and χ^2/NDF are shown to give information on the quality of the fit.

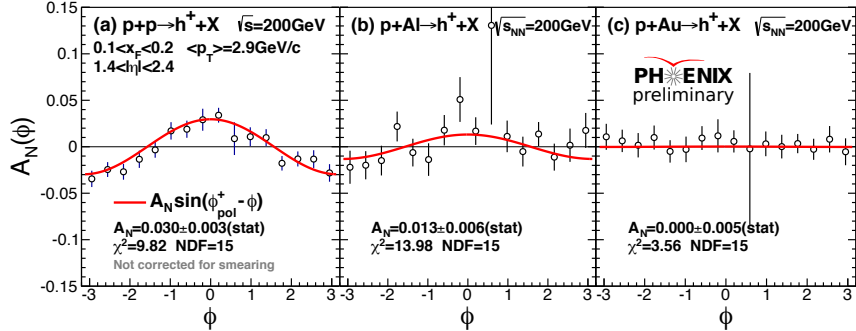


Figure 121: $\sin(\phi - \phi_{pol})$ modulation of positively charged hadrons in $p + p$, $p + \text{Al}$, and $p + \text{Au}$ collisions at $0.1 < x_F < 0.2$. The results from the blue, yellow beams are combined in $p + p$ collisions while only the blue beam was used in $p + \text{Al}$, $p + \text{Au}$.

4.11 Discussion and Outlook for the Charged Hadron A_N in $p^\uparrow+p$ and $p^\uparrow+A$

Recent calculations of the fragmentation contribution to A_N [50, 51, 6] have shown that this could be important for explaining the A_N in π and K production in $p^\uparrow+p$ collisions. Recent efforts to calculate A_N in $p^\uparrow+p$ [6] and $p^\uparrow+A$ collisions [67, 68] suggest that A_N could be A -independent or $A^{-1/3}$ -dependent for different contributions to A_N because they are affected differently by gluon saturation effects in the target nucleus. The results in this thesis strongly disfavor the A -independent scenario. This may suggest that a contribution from the A -dependent terms can be the dominant source of A_N in $p^\uparrow+p \rightarrow h + X$ in the kinematic range of this measurement. However, we note the $\langle p_T \rangle \sim 2.9$ GeV/ c in our results is larger than the saturation scale in Au nucleus [106, 107].

The $N_{\text{coll}}^{\text{avg}}$ -dependence of A_N also suggests the decrease of A_N is related to the density of nuclear matter inside the target nucleus which the projectile proton traverses. This $N_{\text{coll}}^{\text{avg}}$ -dependence of A_N could be related to novel effects in $p+A$ collisions, such as multiple scattering of partons in the initial and/or final stages of the hard scattering, which is also indicated in the recent results of the nuclear modification of single hadron production and transverse momentum broadening in dihadron correlations in $p+A$ collisions [103, 108, 109]. Another possibility is interaction of the parton with hot QCD matter produced in $p+A$ collisions,

as suggested by recent results in small systems [110, 111, 112]. We note recent preliminary results from the STAR collaboration of A_N for π^0 at $p_T > 1.5$ GeV/ c in $p^\uparrow + p$ and $p^\uparrow + \text{Au}$ collisions at $0.2 < x_F < 0.7$ and $2.6 < \eta < 4.0$ show small or no A -dependence [18]. This emphasizes the importance of more detailed studies of A_N for various particle species in wide kinematic ranges.

REFERENCES

- [1] How did the proton get its spin? <https://www.bnl.gov/newsroom/news.php?a=212163>.
- [2] R. D. Klem, J. E. Bowers, H. W. Courant, H. Kagan, M. L. Marshak, E. A. Peterson, K. Ruddick, W. H. Dragoset, and J. B. Roberts. Measurement of Asymmetries of Inclusive Pion Production in Proton Proton Interactions at 6-GeV/c and 11.8-GeV/c. *Phys. Rev. Lett.*, 36:929–931, 1976.
- [3] Elke-Caroline Aschenauer et al. The RHIC SPIN Program: Achievements and Future Opportunities. 2015.
- [4] S. Adachi et al. Trigger electronics upgrade of PHENIX muon tracker. *Nucl. Instrum. Meth.*, A703:114–132, 2013.
- [5] Yuji Koike and Shinsuke Yoshida. Probing the three-gluon correlation functions by the single spin asymmetry in $p^\uparrow p \rightarrow DX$. *Phys. Rev.*, D84 : 014026, 2011.
- [6] Leonard Gamberg, Zhong-Bo Kang, Daniel Pitonyak, and Alexei Prokudin. Phenomenological constraints on A_N in $p^\uparrow p \rightarrow \pi X$ from Lorentz invariance relations. *Phys. Lett.*, B770:242–251, 2017.
- [7] J. Ashman et al. A Measurement of the Spin Asymmetry and Determination of the Structure Function $g(1)$ in Deep Inelastic Muon-Proton Scattering. *Phys. Lett.*, B206:364, 1988. [,340(1987)].
- [8] J. Ashman et al. An Investigation of the Spin Structure of the Proton in Deep Inelastic Scattering of Polarized Muons on Polarized Protons. *Nucl. Phys.*, B328:1, 1989. [,351(1989)].
- [9] Gordon L. Kane, J. Pumplin, and W. Repko. Transverse Quark Polarization in Large $p(T)$ Reactions, $e+e-$ Jets, and Leptoproduction: A Test of QCD. *Phys. Rev. Lett.*, 41:1689, 1978.
- [10] C. E. Allgower et al. Measurement of analyzing powers of π^+ and π^- produced on a hydrogen and a carbon target with a 22-GeV/c incident polarized proton beam. *Phys. Rev.*, D65:092008, 2002.
- [11] J. Antille, L. Dick, L. Madansky, D. Perret-Gallix, M. Werlen, A. Gonidec, K. Kuroda, and P. Kyberd. Spin Dependence of the Inclusive Reaction pp (Polarized) $\rightarrow \pi^0 X$ at 24-GeV/c for High $p_T \pi^0$ Produced in the Central Region. *Phys. Lett.*, 94B:523–526, 1980.

- [12] D. L. Adams et al. Comparison of spin asymmetries and cross-sections in π^0 production by 200-GeV polarized anti-protons and protons. *Phys. Lett.*, B261:201–206, 1991.
- [13] D. L. Adams et al. Analyzing power in inclusive π^+ and π^- production at high $x(F)$ with a 200-GeV polarized proton beam. *Phys. Lett.*, B264:462–466, 1991.
- [14] I. Arsene et al. Single Transverse Spin Asymmetries of Identified Charged Hadrons in Polarized $p+p$ Collisions at $s^{**}(1/2) = 62.4$ -GeV. *Phys. Rev. Lett.*, 101:042001, 2008.
- [15] J. Adams et al. Cross-sections and transverse single spin asymmetries in forward neutral pion production from proton collisions at $s^{**}(1/2) = 200$ -GeV. *Phys. Rev. Lett.*, 92:171801, 2004.
- [16] B. I. Abelev et al. Forward Neutral Pion Transverse Single Spin Asymmetries in $p+p$ Collisions at $s^{**}(1/2) = 200$ -GeV. *Phys. Rev. Lett.*, 101:222001, 2008.
- [17] Mriganka Mouli Mondal. Measurement of the Transverse Single-Spin Asymmetries for π^0 and Jet-like Events at Forward Rapidities at STAR in $p + p$ Collisions at $\sqrt{s} = 500$ GeV. *PoS*, DIS2014:216, 2014.
- [18] Steven Heppelmann. Preview from RHIC Run 15 pp and pAu Forward Neutral Pion Production from Transversely Polarized Protons. In *Proceedings, 7th International Workshop on Multiple Partonic Interactions at the LHC (MPI@LHC 2015): Miramare, Trieste, Italy, November 23-27, 2015*, pages 228–231, 2016.
- [19] A. Adare et al. Measurement of transverse-single-spin asymmetries for midrapidity and forward-rapidity production of hadrons in polarized $p+p$ collisions at $\sqrt{s} = 200$ and 62.4 GeV. *Phys. Rev.*, D90(1):012006, 2014.
- [20] Dennis W. Sivers. Single Spin Production Asymmetries from the Hard Scattering of Point-Like Constituents. *Phys. Rev.*, D41:83, 1990.
- [21] Dennis W. Sivers. Hard scattering scaling laws for single spin production asymmetries. *Phys. Rev.*, D43:261–263, 1991.
- [22] John C. Collins. Fragmentation of transversely polarized quarks probed in transverse momentum distributions. *Nucl. Phys.*, B396:161–182, 1993.
- [23] A. Airapetian et al. Effects of transversity in deep-inelastic scattering by polarized protons. *Phys. Lett.*, B693:11–16, 2010.

- [24] C. Adolph et al. Experimental investigation of transverse spin asymmetries in muon-p SIDIS processes: Collins asymmetries. *Phys. Lett.*, B717:376–382, 2012.
- [25] Ted C. Rogers and Piet J. Mulders. No Generalized TMD-Factorization in Hadro-Production of High Transverse Momentum Hadrons. *Phys. Rev.*, D81:094006, 2010.
- [26] A. V. Efremov and O. V. Teryaev. On Spin Effects in Quantum Chromodynamics. *Sov. J. Nucl. Phys.*, 36:140, 1982. [Yad. Fiz.36,242(1982)].
- [27] A. V. Efremov and O. V. Teryaev. QCD Asymmetry and Polarized Hadron Structure Functions. *Phys. Lett.*, 150B:383, 1985.
- [28] Jian-wei Qiu and George F. Sterman. Single transverse spin asymmetries. *Phys. Rev. Lett.*, 67:2264–2267, 1991.
- [29] Jian-wei Qiu and George F. Sterman. Single transverse spin asymmetries in direct photon production. *Nucl. Phys.*, B378:52–78, 1992.
- [30] Jian-wei Qiu and George F. Sterman. Single transverse spin asymmetries in hadronic pion production. *Phys. Rev.*, D59:014004, 1999.
- [31] Hisato Eguchi, Yuji Koike, and Kazuhiro Tanaka. Single Transverse Spin Asymmetry for Large-p(T) Pion Production in Semi-Inclusive Deep Inelastic Scattering. *Nucl. Phys.*, B752:1–17, 2006.
- [32] Chris Kouvaris, Jian-Wei Qiu, Werner Vogelsang, and Feng Yuan. Single transverse-spin asymmetry in high transverse momentum pion production in pp collisions. *Phys. Rev.*, D74:114013, 2006.
- [33] Yuji Koike and Kazuhiro Tanaka. Universal structure of twist-3 soft-gluon-pole cross-sections for single transverse-spin asymmetry. *Phys. Rev.*, D76:011502, 2007.
- [34] Yuji Koike and Tetsuya Tomita. Soft-fermion-pole contribution to single-spin asymmetry for pion production in pp collisions. *Phys. Lett.*, B675:181–189, 2009.
- [35] Koichi Kanazawa and Yuji Koike. New Analysis of the Single Transverse-Spin Asymmetry for Hadron Production at RHIC. *Phys. Rev.*, D82:034009, 2010.
- [36] Koichi Kanazawa and Yuji Koike. A phenomenological study on single transverse-spin asymmetry for inclusive light-hadron productions at RHIC. *Phys. Rev.*, D83:114024, 2011.

- [37] Koichi Kanazawa, Yuji Koike, Andreas Metz, Daniel Pitonyak, and Marc Schlegel. Operator Constraints for Twist-3 Functions and Lorentz Invariance Properties of Twist-3 Observables. *Phys. Rev.*, D93(5):054024, 2016.
- [38] D. Pitonyak. Transverse spin observables in hard-scattering hadronic processes within collinear factorization. *Int. J. Mod. Phys.*, A31(32):1630049, 2016.
- [39] Hiroo Beppu, Koichi Kanazawa, Yuji Koike, and Shinsuke Yoshida. Three-gluon contribution to the single spin asymmetry for light hadron production in pp collision. *Phys. Rev.*, D89(3):034029, 2014.
- [40] Daniel Boer, P. J. Mulders, and F. Pijlman. Universality of T odd effects in single spin and azimuthal asymmetries. *Nucl. Phys.*, B667:201–241, 2003.
- [41] Zhong-Bo Kang, Jian-Wei Qiu, Werner Vogelsang, and Feng Yuan. An Observation Concerning the Process Dependence of the Sivers Functions. *Phys. Rev.*, D83:094001, 2011.
- [42] Zhong-Bo Kang and Alexei Prokudin. Global fitting of single spin asymmetry: an attempt. *Phys. Rev.*, D85:074008, 2012.
- [43] A. Metz, D. Pitonyak, A. Schafer, M. Schlegel, W. Vogelsang, and J. Zhou. Single-spin asymmetries in inclusive deep inelastic scattering and multiparton correlations in the nucleon. *Phys. Rev.*, D86:094039, 2012.
- [44] Y. Kanazawa and Yuji Koike. Chiral odd contribution to single transverse spin asymmetry in hadronic pion production. *Phys. Lett.*, B478:121–126, 2000.
- [45] Jian Zhou, Feng Yuan, and Zuo-Tang Liang. QCD Evolution of the Transverse Momentum Dependent Correlations. *Phys. Rev.*, D79:114022, 2009.
- [46] Zhong-Bo Kang and Jian-Wei Qiu. Evolution of twist-3 multi-parton correlation functions relevant to single transverse-spin asymmetry. *Phys. Rev.*, D79:016003, 2009.
- [47] Zhong-Bo Kang and Jian-Wei Qiu. QCD evolution of naive-time-reversal-odd parton distribution functions. *Phys. Lett.*, B713:273–276, 2012.
- [48] Daniel Boer and P. J. Mulders. Time reversal odd distribution functions in lepto-production. *Phys. Rev.*, D57:5780–5786, 1998.
- [49] Y. Kanazawa and Yuji Koike. Estimate of a chiral odd contribution to single transverse spin asymmetry in hadronic pion production. *Phys. Lett.*, B490:99–105, 2000.

- [50] A. Metz and D. Pitonyak. Fragmentation contribution to the transverse single-spin asymmetry in proton-proton collisions. *Phys. Lett.*, B723:365–370, 2013. [Erratum: *Phys. Lett.* B762, 549 (2016)].
- [51] Koichi Kanazawa, Yuji Koike, Andreas Metz, and Daniel Pitonyak. Towards an explanation of transverse single-spin asymmetries in proton-proton collisions: the role of fragmentation in collinear factorization. *Phys. Rev.*, D89(11):111501, 2014.
- [52] I. Arsene et al. On the evolution of the nuclear modification factors with rapidity and centrality in $d + Au$ collisions at $s(NN)^{**}(1/2) = 200$ -GeV. *Phys. Rev. Lett.*, 93:242303, 2004.
- [53] J. Adams et al. Forward neutral pion production in $p+p$ and $d+Au$ collisions at $s(NN)^{**}(1/2) = 200$ -GeV. *Phys. Rev. Lett.*, 97:152302, 2006.
- [54] Ermes Braidot. Suppression of Forward Pion Correlations in $d+Au$ Interactions at STAR. In *Proceedings, 45th Rencontres de Moriond on QCD and High Energy Interactions: La Thuile, Italy, March 13-20, 2010*, pages 355–338, 2010.
- [55] A. Adare et al. Suppression of back-to-back hadron pairs at forward rapidity in $d+Au$ Collisions at $\sqrt{s_{NN}} = 200$ GeV. *Phys. Rev. Lett.*, 107:172301, 2011.
- [56] Francois Gelis, Edmond Iancu, Jamal Jalilian-Marian, and Raju Venugopalan. The Color Glass Condensate. *Ann. Rev. Nucl. Part. Sci.*, 60:463–489, 2010.
- [57] Adrian Dumitru, Arata Hayashigaki, and Jamal Jalilian-Marian. The Color glass condensate and hadron production in the forward region. *Nucl. Phys.*, A765:464–482, 2006.
- [58] Daniel Boer, Adrian Dumitru, and Arata Hayashigaki. Single transverse-spin asymmetries in forward pion production at high energy: Incorporating small- x effects in the target. *Phys. Rev.*, D74:074018, 2006.
- [59] Zhong-Bo Kang and Feng Yuan. Single Spin Asymmetry Scaling in the Forward Rapidity Region at RHIC. *Phys. Rev.*, D84:034019, 2011.
- [60] Yuri V. Kovchegov and Matthew D. Sievert. A New Mechanism for Generating a Single Transverse Spin Asymmetry. *Phys. Rev.*, D86:034028, 2012. [Erratum: *Phys. Rev.* D86, 079906 (2012)].
- [61] Zhong-Bo Kang and Bo-Wen Xiao. Sivers asymmetry of Drell-Yan production in small- x regime. *Phys. Rev.*, D87(3):034038, 2013.

- [62] Jian Zhou. Transverse single spin asymmetries at small x and the anomalous magnetic moment. *Phys. Rev.*, D89(7):074050, 2014.
- [63] Tolga Altinoluk, Néstor Armesto, Guillaume Beuf, Mauricio Martínez, and Carlos A. Salgado. Next-to-eikonal corrections in the CGC: gluon production and spin asymmetries in pA collisions. *JHEP*, 07:068, 2014.
- [64] Andreas Schäfer and Jian Zhou. Transverse single spin asymmetry in direct photon production in polarized pA collisions. *Phys. Rev.*, D90(3):034016, 2014.
- [65] Jian Zhou. Transverse single spin asymmetry in Drell-Yan production in polarized pA collisions. *Phys. Rev.*, D92(1):014034, 2015.
- [66] Daniël Boer, Miguel G. Echevarria, Piet Mulders, and Jian Zhou. Single spin asymmetries from a single Wilson loop. *Phys. Rev. Lett.*, 116(12):122001, 2016.
- [67] Yoshitaka Hatta, Bo-Wen Xiao, Shinsuke Yoshida, and Feng Yuan. Single Spin Asymmetry in Forward pA Collisions. *Phys. Rev.*, D94(5):054013, 2016.
- [68] Yoshitaka Hatta, Bo-Wen Xiao, Shinsuke Yoshida, and Feng Yuan. Single spin asymmetry in forward pA collisions II: Fragmentation contribution. *Phys. Rev.*, D95(1):014008, 2017.
- [69] M. Anselmino, M. Boglione, U. D'Alesio, E. Leader, and F. Murgia. Accessing Sivers gluon distribution via transverse single spin asymmetries in $p^\uparrow p \rightarrow DX$ processes at RHIC. *Phys. Rev.*, D70:074025, 2004.
- [70] A. Adare et al. Measurement of Transverse Single-Spin Asymmetries for J/ψ Production in Polarized $p + p$ Collisions at $\sqrt{s} = 200$ GeV. *Phys. Rev.*, D82:112008, 2010. [Erratum: *Phys. Rev.* D86, 099904(2012)].
- [71] Feng Yuan. Heavy Quarkonium Production in Single Transverse Polarized High Energy Scattering. *Phys. Rev.*, D78:014024, 2008.
- [72] A. Adare et al. Ground and excited charmonium state production in $p + p$ collisions at $\sqrt{s} = 200$ GeV. *Phys. Rev.*, D85:092004, 2012.
- [73] Zhong-Bo Kang, Jian-Wei Qiu, Werner Vogelsang, and Feng Yuan. Accessing tri-gluon correlations in the nucleon via the single spin asymmetry in open charm production. *Phys. Rev.*, D78:114013, 2008.
- [74] I. Alekseev et al. Polarized proton collider at RHIC. *Nucl. Instrum. Meth.*, A499:392–414, 2003.

- [75] A. N. Zelenski et al. Optically pumped polarized H- ion sources for RHIC and HERA colliders. In *Polarized protons at high-energies - accelerator challenges and physics opportunities. Proceedings, Workshop, Hamburg, Germany, May 17-20, 1999*, pages 106–108, 1999. [,177(1999)].
- [76] Rhic run page. <http://www.rhichome.bnl.gov/RHIC/Runs/>.
- [77] Ya. S. Derbenev, A. M. Kondratenko, S. I. Serednyakov, A. N. Skrinsky, G. M. Tumaikin, and Yu. M. Shatunov. RADIATIVE POLARIZATION: OBTAINING, CONTROL, USING. *Part. Accel.*, 8:115–126, 1978.
- [78] S. R. Mane, Yu. M. Shatunov, and K. Yokoya. Siberian snakes in high-energy accelerators. *J. Phys.*, G31:R151–R209, 2005.
- [79] H. Okada et al. Measurement of the analyzing power in pp elastic scattering in the peak CNI region at RHIC. *Phys. Lett.*, B638:450–454, 2006.
- [80] I. Nakagawa et al. p-carbon polarimetry at RHIC. *AIP Conf. Proc.*, 980:380–389, 2008.
- [81] H. Huang and K. Kurita. Fiddling carbon strings with polarized proton beams. *AIP Conf. Proc.*, 868:3–21, 2006. [,3(2006)].
- [82] H. Akikawa et al. PHENIX muon arms. *Nucl. Instrum. Meth.*, A499:537–548, 2003.
- [83] J. Murata, A. Al-Jamel, R. L. Armendariz, M. L. Brooks, T. Horaguchi, N. Kamihara, H. Kobayashi, D. M. Lee, T. A. Shibata, and W. E. Sondheim. Optical alignment system for the PHENIX muon tracking chambers. *Nucl. Instrum. Meth.*, A500:309–317, 2003.
- [84] E. Iarocci. Plastic Streamer Tubes and their Applications in High-Energy Physics. *Nucl. Instrum. Meth.*, 217:30–42, 1983.
- [85] M. Allen et al. PHENIX inner detectors. *Nucl. Instrum. Meth.*, A499:549–559, 2003.
- [86] Clemens Adler, Alexei Denisov, Edmundo Garcia, Michael J. Murray, Herbert Strobel, and Sebastian N. White. The RHIC zero degree calorimeter. *Nucl. Instrum. Meth.*, A470:488–499, 2001.
- [87] Stephen Scott Adler et al. PHENIX on-line systems. *Nucl. Instrum. Meth.*, A499:560–592, 2003.
- [88] S. S. Adler et al. Mid-rapidity neutral pion production in proton proton collisions at $\sqrt{s} = 200\text{-GeV}$. *Phys. Rev. Lett.*, 91:241803, 2003.

- [89] A. Drees, B. Fox, Z. Xu, and H. Huang. Results from Vernier Scans at RHIC during the PP Run 2001-2002. *Conf. Proc.*, C030512:1688, 2003.
- [90] Michael L. Miller, Klaus Reygers, Stephen J. Sanders, and Peter Steinberg. Glauber modeling in high energy nuclear collisions. *Ann. Rev. Nucl. Part. Sci.*, 57:205–243, 2007.
- [91] A. Adare et al. Nuclear-Modification Factor for Open-Heavy-Flavor Production at Forward Rapidity in Cu+Cu Collisions at $\sqrt{s_{NN}} = 200$ GeV. *Phys. Rev.*, C86:024909, 2012.
- [92] A. Adare et al. Cold-Nuclear-Matter Effects on Heavy-Quark Production at Forward and Backward Rapidity in d+Au Collisions at $\sqrt{s_{NN}} = 200$ GeV. *Phys. Rev. Lett.*, 112(25):252301, 2014.
- [93] PHENIX Analysis Note 1098.
- [94] PHENIX Analysis Note 1250.
- [95] PHENIX Analysis Note 1188.
- [96] Torbjörn Sjöstrand, Stefan Ask, Jesper R. Christiansen, Richard Corke, Nishita Desai, Philip Ilten, Stephen Mrenna, Stefan Prestel, Christine O. Rasmussen, and Peter Z. Skands. An Introduction to PYTHIA 8.2. *Comput. Phys. Commun.*, 191:159–177, 2015.
- [97] Rolf Hagedorn. Multiplicities, p_T Distributions and the Expected Hadron \rightarrow Quark - Gluon Phase Transition. *Riv. Nuovo Cim.*, 6N10:1–50, 1983.
- [98] Xin-Nian Wang and Miklos Gyulassy. HIJING: A Monte Carlo model for multiple jet production in p p, p A and A A collisions. *Phys. Rev.*, D44:3501–3516, 1991.
- [99] J. Allison et al. Recent developments in Geant4. *Nucl. Instrum. Meth.*, A835:186–225, 2016.
- [100] C. Aidala et al. Measurements of $\mu\mu$ pairs from open heavy flavor and Drell-Yan in $p + p$ collisions at $\sqrt{s} = 200$ GeV. *Submitted to: Phys. Rev. D*, 2018.
- [101] A. Adare et al. Transverse energy production and charged-particle multiplicity at midrapidity in various systems from $\sqrt{s_{NN}} = 7.7$ to 200 GeV. *Phys. Rev.*, C93(2):024901, 2016.

- [102] J. H. Lee and F. Videbaek. Single spin asymmetries of identified hadrons in polarized $p + p$ at $s^{**}(1/2) = 62.4$ and 200-GeV. *AIP Conf. Proc.*, 915:533–538, 2007. [,533(2007)].
- [103] A. Adare et al. Spectra and ratios of identified particles in Au+Au and $d+Au$ collisions at $\sqrt{s_{NN}} = 200$ GeV. *Phys. Rev.*, C88(2):024906, 2013.
- [104] PHENIX Analysis Note 1265.
- [105] PHENIX Analysis Note 1290.
- [106] Henri Kowalski and Derek Teaney. An Impact parameter dipole saturation model. *Phys. Rev.*, D68:114005, 2003.
- [107] A. Accardi et al. Electron Ion Collider: The Next QCD Frontier. *Eur. Phys. J.*, A52(9):268, 2016.
- [108] Jason Bryslawskyj. PHENIX study of the initial state with forward hadron measurements in 200 GeV $p(d)+A$ and ${}^3\text{He}+Au$ collisions. 2018.
- [109] C. Aidala et al. Nonperturbative transverse momentum broadening in di-hadron angular correlations in $\sqrt{s_{NN}} = 200$ GeV proton-nucleus collisions. 2018.
- [110] Kevin Dusling, Wei Li, and Björn Schenke. Novel collective phenomena in high-energy proton–proton and proton–nucleus collisions. *Int. J. Mod. Phys.*, E25(01):1630002, 2016.
- [111] James L. Nagle and William A. Zajc. Small System Collectivity in Relativistic Hadron and Nuclear Collisions. 2018.
- [112] C. Aidala et al. Creating small circular, elliptical, and triangular droplets of quark-gluon plasma. 2018.